Fall 2014

Unsteady flamelet progress variable modeling of reacting diesel jets

Muhsin Mohammed Ameen
Purdue University

Graduate School Form 30
(Updated 11/20/2014)

PURDUE UNIVERSITY
GRADUATE SCHOOL
Thesis/Dissertation Acceptance

This is to certify that the thesis/dissertation prepared

By Muhsin Mohammed Ameen

Entitled
UNSTEADY FLAMELET PROGRESS VARIABLE MODELING OF REACTING DIESEL JETS

For the degree of Doctor of Philosophy

Is approved by the final examining committee:

John Abraham

Gregory A. Blaisdell

Carlos Corvalan

Gregory M. Shaver

To the best of my knowledge and as understood by the student in the Thesis/Dissertation Agreement, Publication Delay, and Certification/Disclaimer (Graduate School Form 32), this thesis/dissertation adheres to the provisions of Purdue University's "Policy on Integrity in Research" and the use of copyrighted material.

Approved by Major Professor(s): John Abraham

Approved by: Ganesh Subbarayan 12/09/2014

Head of the Department Graduate Program Date

UNSTEADY FLAMELET PROGRESS VARIABLE MODELING OF REACTING DIESEL JETS

A Dissertation

Submitted to the Faculty

of

Purdue University

by

Muhsin Mohammed Ameen

In Partial Fulfillment of the

Requirements for the Degree

of

Doctor of Philosophy

December 2014

Purdue University

West Lafayette, Indiana

ACKNOWLEDGEMENTS

First and foremost, I would like to express my deepest gratitude to my major advisor, Professor John Abraham. He has always been very patient and understanding with me and provided numerous critical suggestions on my research. He looks at everything from a very fundamental and physical point-of-view and this has helped me multiple times whenever I have encountered roadblocks in my research. Without his guidance and continuous help, this dissertation would not have been possible. I am thankful to him for providing an independent research environment and for numerous insightful discussions on different aspects of turbulent combustion modeling.

I am grateful to Professors Gregory Blaisdell, Carlos Corvalan and Gregory Shaver for serving on my PhD advisory committee and providing valuable suggestions. I would also like to thank Professor Vinicio Magi for his many contributions to the numerical codes employed in this work. The discussions I had with him have helped me in gaining a deeper insight into the numerical aspects of the code.

This research was supported partially by Caterpillar, Inc., and Purdue Research Foundation (PRF). Their financial support is gratefully acknowledged. I would also like to thank John Zink, Inc., for awarding me the John Zink fellowship, which funded my travel to Germany for attending the ICLASS 2012 conference. I am also indebted to the Department of Mechanical Engineering at Purdue for direct financial aid through

teaching assistantships and fellowships. I sincerely acknowledge National Institute for Computational Sciences (NICS), Texas Advanced Computing Center (TACC), and eResearch South Australia (eRSA) for providing the computational resources required for this work.

I am thankful to the past and present members of the research group for useful discussions and feedback about my work. I would also like to thank the staff at ME Graduate Office and the Purdue Graduate School for their valuable assistance during my stay at Purdue. I would especially like to thank my family in India for their continuous support throughout my stay at Purdue.

TABLE OF CONENTS

Page

Page

Page

Page

LIST OF TABLES

LIST OF FIGURES

Figure Page

Figure Page

Figure Page

Figure Page

Figure Page

Figure Page

NOMENCLATURE

Upper-Case Roman

C	Smagorinsky model constant; progress variable
C_B	vortex ring perturbation model constant
C_{st}	progress variable under stoichiometric conditions
D	diffusion coefficient (m^2/s)
$\tilde{D}_{eff}$	Favre-filtered effective diffusivity (m^2/s)
$\tilde{D}_{\mathbf{t}}$	LES subgrid-scale turbulent diffusivity(m^2/s)
D_t	turbulent diffusivity (m^2/s)
L	characteristic length (m)
L_{11}	longitudinal integral length-scale (m)
$Pr_{\mathbf{t}}$	turbulent Prandtl number
R	specific gas constant (J/kg-K)
Re	Reynolds number
R_{11}	normalized longitudinal two-point correlation
R_u	universal gas constant (J/kmol-K)

$R_{1/2}$	jet half-width based on axial velocity (m)
$\tilde{S}_{ij}$	strain rate tensor (s^{-1})
$\left\|\tilde{S}\right\|$	strain rate magnitude (s^{-1})
Sc_t	turbulent Schmidt number
T	temperature (K)
T_a	adiabatic temperature (K)
$T_{ambient}$	ambient temperature (K)
T_{fuel}	fuel temperature (K)
T_u	unburned temperature (K)
U	mean axial velocity (m/s)
U_{inj}	injection velocity of the jet (m/s)
U_j	jet centerline velocity at the inlet (m/s)
U_{cl}	jet centerline velocity (m/s)
U_{xo}, U_{ro}	axial and radial components of vortex ring velocity (m/s)
Y_i	mass fraction of the i^{th} species
Z	mixture fraction
$\tilde{Z}$	instantaneous filtered mixture fraction
$\bar{Z}$	mean mixture fraction
$\overline{Z''^2}$	mixture fraction variance
Z_{st}	mixture fraction at stoichiometric location

Lower-case Roman

a	strain rate (s^{-1})
c_p	mixture specific heat (J/kg-K)
d	jet diameter (m)
h	total enthalpy per unit mass (J/kg); grid spacing (m)
h_k	enthalpy of the k^{th} species (J/kg)
$\bar{k}$	Reynolds-averaged turbulent kinetic energy (m^2/s^2)
l_D	diffusion flame thickness (m)
m_1, m_2, m_3	momentum densities in Cartesian coordinate directions (m/s)
$p, \bar{p}$	total and filtered pressure (Pa)
r	radial distance (m)
r_o	jet radius at the inlet (m)
t	time (s)
u, v, w	Cartesian velocity components (m/s)
u_1, u_2, u_3	velocity in Cartesian coordinate directions (m/s)
$u_i, \langle u_i \rangle, u_i'$	total, mean and fluctuating velocity in the i^{th} direction (m/s)
u_e	internal energy (J/kg)
u_x, u_r	axial and radial velocities in region of vortex ring (m/s)
$\dot{w}_i$	chemical production/destruction rate of species *i* ($mol/s/m^3$)

$x_{\mathbf{i}}$	distance in the ith coordinate direction (m)

Upper-case Greek

Δ	spatial filter width; grid width (m)
$\Delta_{\mathbf{t}}$	time step (s)
$(\Delta Z)_F$	diffusion layer thickness (m)
$(\Delta Z)_R$	reaction zone thickness (m)
$\Psi_1 \cdots \Psi_5$	characteristic wave amplitudes (m)

Lower-case Greek

α, β	filter coefficients
δ	mixing layer thickness (m); Dirac-delta function
δ_{ij}	Kronecker delta function
ε	turbulent dissipation (m^2/s^3)
$\bar{\varepsilon}$	Reynolds-averaged turbulent dissipation rate (m^2/s^3)
ε_n, φ_n	uniform random numbers
η	overall reaction order; Kolmogorov length-scale
λ	thermal conductivity (W/m/K); Taylor micro-scale (m)
$\lambda_1 \cdots \lambda_5$	characteristic wave velocities (m/s)

$\tilde{\lambda}_{\mathbf{eff}}$	Favre-filtered effective conductivity (W/m/K)
$\mu_{\mathbf{lam}}$	laminar viscosity (kg/m/s)
$\tilde{\mu}_{\mathbf{eff}}$	Favre-filtered effective viscosity (kg/m/s)
$\widetilde{\mu}_{\mathrm{T}}$	subgrid-scale turbulent viscosity (kg/m/s)
ν	kinematic viscosity (m^2/s)
ν_{t}	turbulent kinematic viscosity (m^2/s)
ρ	mixture density (kg/m^3)
ρ_g	gas density (kg/m^3)
ρ_{a}	ambient gas density (kg/m^3)
ρ_{j}	injected gas density (kg/m^3)
$\rho_{\mathbf{k}}$	partial density of the k^{th} species (kg/m^3)
$\widetilde{\sigma}_{\mathrm{ij}}$	resolved stress tensor (N/m^2)
$\tilde{\sigma}_{\mathbf{SG_{ij}}}$	subgrid-scale stress tensor (N/m^2)
$\tau_{\mathbf{c}}$	characteristic chemical reaction time-scale (s)
$\tilde{\tau}_{\mathbf{ij}}$	effective stress tensor (N/m^2)
ω_k	production/destruction rate of k^{th} species ($mol/s/m^3$)
χ	instantaneous scalar dissipation rate (s^{-1})
χ_{e}	steady extinction limit (s^{-1})
$\chi_{\mathbf{st}}$	scalar dissipation rate at stoichiometric mixture fraction (s^{-1})

$\tilde{\chi}$	instantaneous filtered scalar dissipation rate (s^{-1})
$\bar{\chi}$	mean scalar dissipation rate (s^{-1})
$\bar{\chi}_{\mathbf{Z}}$	time-averaged conditional-mean scalar dissipation rate (s^{-1})
τ_c	chemical time (s)

Symbols

~	Fávre average

Acronyms

ASI	after start of injection
CFD	computational fluid dynamics
DNS	direct numerical simulation
DPF	diesel particulate filter
ECN	engine combustion network
EDM	eddy dissipation model
EGR	exhaust gas recirculation
FLEDS	flow and large eddy simulation
FPV	flamelet progress variable
GFSD	generalized flame surface density
ISAT	in-situ adaptive tabulation
LDEF	Lagrangian-drop Eulerian-fluid
LES	large-eddy simulation
PaSR	partially stirred reactor
PDF	probability density function

PM	particulate matter
PSR	perfectly stirred reactor
RANS	Reynolds-averaged Navier-Stokes
RIF	representative interactive flamelet
SCR	selective catalytic reduction
SKE	subgrid kinetic energy
SRT	strain rate tensor
TD	turbulent diffusivity
UFPV	unsteady flamelet progress variable
UHC	unburned hydrocarbons

ABSTRACT

Ameen, Muhsin Mohammed. Ph.D., Purdue University, December 2014. Unsteady Flamelet Progress Variable Modeling of Reacting Diesel Jets. Major Professor: John Abraham, School of Mechanical Engineering.

Accurate modeling of turbulence/chemistry interactions in turbulent reacting diesel jets is critical to the development of predictive computational tools for diesel engines. The models should be able to predict the transient physical and chemical processes in the jets such as ignition and flame lift-off. In the first part of this work, an existing unsteady flamelet progress variable (UFPV) model is employed in Reynolds-averaged Navier-Stokes (RANS) simulations and large-eddy simulations (LES) to assess its accuracy. The RANS simulations predict that ignition occurs toward the leading tip of the jet, followed by ignition front propagation toward the stoichiometric surface, and flame propagation upstream along the stoichiometric surface until the flame stabilizes at the lift-off height. The LES, on the other hand, predicts ignition at multiple points in the jet, followed by flame development from the ignition kernels, merger of the different flames and then stabilization. The UFPV model assumes that combustion occurs in thin zones known as flamelets and turbulent strain characterized by the scalar dissipation rate modifies the flame structure. Since the flamelet is thinner than the smallest grid size employed in RANS or LES, the effect of the turbulence is modeled through probability distribution functions of the independent variables. The accuracy of the assumptions of

the model is assessed in this work through direct numerical simulations (DNS) which resolves the flame. The DNS is carried out in turbulent mixing layers since the combustion in a diesel jet occurs in the fuel/air mixing layer surrounding the jet.

The DNS results show that the flamelet model is applicable but that its implementation in the UFPV model is flawed because the effects of expansion due to heat release and increase in diffusivity due to rise in temperature are not accounted for in the formulation of the scalar dissipation rate. A new diffusivity-corrected flamelet model is proposed which leads to an improved prediction of flame development. Furthermore, it is shown that the most commonly used approach to calculate the scalar dissipation rate in LES of reacting flows leads to large errors when the LES grid size is large. The DNS results are used to determine the best model for the filtered scalar dissipation rate and its PDF under diesel engine conditions. A new model is derived for the variance of the scalar dissipation rate. The DNS results are also used to compare the performance of the UFPV model with the Perfectly Stirred Reactor (PSR) model predictions. It is shown that the UFPV model performance is superior for turbulent intensities and grid sizes encountered in diesel engine applications.

1 INTRODUCTION

1.1 Motivation

Reducing emissions of particulate matter (PM) and nitrogen oxides (NO_x) from diesel engines is a continuing challenge that faces heavy-duty diesel engine manufacturers who, in turn, have invested significant resources to address it. Increasingly stringent regulations force engine designers to search for innovative ways to cut down emissions. Exhaust aftertreatment devices which remove the pollutants in the exhaust are effective and increasingly deployed by manufacturers. These include diesel particulate filters (DPF), selective catalytic reduction (SCR) systems, diesel oxidation catalysts (DOC), lean-NO_x catalysts, and NO_x adsorbers (Blakeman et al., 2003). Among these, the SCR and DPF are the most promising. Nevertheless these devices add to the cost and size of the engine package and are, hence, not the preferred means of achieving emissions goals. Advanced combustion engines, such as homogeneous-charge compression-ignition (HCCI) engines, are promising but have not reached a stage of development where they are practical. While progress is being made in the areas of exhaust aftertreatment and advanced combustion engines, it is imperative that any gains that can be achieved through improvements in conventional diesel engine combustion are exploited.

Making improvements in conventional diesel engine combustion can be accelerated by improving the understanding of the in-cylinder fuel/air mixing and combustion processes. One way of achieving this is to conduct experimental studies in optical engines. Isolating different processes and studying their effects on the pollutant formation through experiments alone is, however, time-consuming and expensive. The alternative approach is through the use of computational modeling and simulations. For the approach to be effective, however, the accuracy of the models is critical.

Computational simulations of different levels of complexity exist. Direct numerical simulations (DNS) are the most accurate means of modeling any fluid dynamics process, in which all the scales in the flow are completely resolved. DNS of diesel engine combustion can provide the detailed information required to understand different processes and optimize the engines. Such simulations are, however, computationally impractical and will remain so for the foreseeable future. On the other end of the spectrum are zero-dimensional (Arrègle et al., 2003; Kwon et al., 2011) and multi-zone models (Sahin and Durgun, 2008; Kuleshov, 2009) which are computationally inexpensive, but they provide few details. For many years, Reynolds-averaged Navier Stokes (RANS) models have been considered to be a reasonable compromise, and they are widely employed in the industry (Kaario, 2000; Senecal et al., 2003; Cao et al., 2009; Qi et al., 2010). In the RANS approach, the Navier Stokes equations are ensemble-averaged and solved numerically. In such simulations, only the mean flow field is captured, and the effect of all the turbulent scales is modeled. The accuracy of the RANS simulations in representing a flow field is highly dependent on the accuracy of the sub-

models employed for turbulence, chemistry, turbulence/chemistry interactions, and wall interactions.

As computational capabilities dramatically improve, large eddy simulations (LES) are becoming an increasingly viable alternative to RANS models. In LES, unlike in the RANS model, filtered equations are solved such that the small scales are filtered and the large scales are directly solved. In other words, in LES, only the small scales have to be modeled. Thus, LES strikes a balance between the DNS (all the scales are resolved) and RANS models (all scales are modeled) making them potentially more accurate but, computationally more expensive compared to RANS models. Note that LES requires the modeling of small-scale turbulence, turbulence/chemistry interactions, and wall interactions. For this reason, not all the limitations of RANS models are addressed by using LES.

Within the context of minimizing emissions from the diesel engines, one purpose of experimental and computational studies is to search for parameters which can be directly related to PM and NO_x emissions. One such parameter that has gained increasing attention in recent years is flame lift-off (Siebers and Higgins, 2001; Pickett and Siebers, 2004) It is important to point out that while the interest in flame lift-off in diesel engines is relatively more recent, it has been subject of study in turbulent reacting jets for over 30 years (Pitts, 1989; Peters, 2000; Venugopal and Abraham, 2007). This will become evident in the literature review in Sec. 2.3. Flame lift-off has been of interest because of its obvious link to heat loss from flames at flame base, understanding differences in fuel kinetics, and blow-off.

Interest in lift-off in reacting diesel jets has arisen because of its possible relation to mixing in the jets which, in turn, influences PM and NO_x formation. Higher lift-off has been suggested to be indicative of greater mixing upstream of the lift-off height. Greater mixing can influence soot and NO_x formation downstream of the lift-off height (Siebers and Higgins, 2001). LES is potentially a powerful tool to study the mechanism(s) of flame lift-off and the major factors affecting it because large-scale mixing, which is believed to play an important role in flame dynamics near the lift-off height, are resolved in LES.

1.2 Objectives

The primary objectives of this work are as follows:

1. To perform RANS and LES simulations of lifted reacting diesel jets, analyze the results to provide insights into the mechanisms leading to flame lift-off, and identify limitations of sub-models for combustion.
2. To carry out DNS of autoigniting turbulent mixing layers to assess the underlying assumptions of the Unsteady Flamelet Progress Variable (UFPV) model employed as a turbulent combustion model for RANS and LES.
3. To propose and evaluate improvements to the UFPV model.

1.3 Organization

The rest of this dissertation is organized into seven chapters. The outline of each chapter follows.

Chapter 2 presents a literature review of the topics relevant to this work. This includes a discussion of the turbulent jet and flame structures usually observed in conventional diesel engines. Prior experimental and computational work related to flame lift-off are reviewed. Proposed explanations for flame lift-off in turbulent reacting jets are discussed. Prior LES studies of turbulent reacting jets are reviewed.

Chapter 3 presents results from RANS simulations of lifted flames. The unsteady flamelet progress variable (UFPV) model, which is used as the turbulence-chemistry interaction model, is discussed. Ignition delay and flame lift-off heights predicted by RANS simulations are presented and compared with experimentally measured values. The results are examined in detail to understand the basis on which RANS simulations predict lift-off heights.

In Chapter 4, the governing equations and numerical methods adopted for DNS and LES are described. The subgrid-scale models employed for the LES are also discussed. The implementation of the UFPV turbulence/chemistry interaction model will, however, be discussed in Chapter 6.

The results from the LES simulation of transient non-reacting heptane jets are presented and discussed in Chapter 5. Some aspects of the jet structure are compared with experimental results. The energy spectrum resolved by the LES simulation is also analyzed and its dependence on grid resolution is discussed.

LES of transient reacting n-heptane jets are presented in Chapter 6. The UFPV model is employed to represent turbulence/chemistry interactions. Its implementation is, however, different from that in RANS simulations. The relevant issues are highlighted.

The transient flame development is discussed in detail, and ignition, flame development, and local extinction events and the factors affecting them are studied.

In Chapter 7, results from DNS of turbulent mixing layers are used to evaluate the various underlying assumptions and elements of the UFPV model.

Chapter 8 contains a summary of findings, concluding remarks and an outline of suggested future work.

2 LITERATURE REVIEW

2.1 Introduction

The primary objective of this work is to evaluate the applicability of the Unsteady Flamelet Progress Variable (UFPV) as a subgrid-scale combustion model for RANS and LES. A review of some of the current literature that is relevant to the present study is presented in this chapter. This review will also provide a motivation for the thesis. Section 2.2 begins the discussion by reviewing the structure of non-reacting (Sec. 2.2.1) and reacting (Sec. 2.2.2) diesel jets. The important physical processes that determine the jet and flame structure, including flame lift-off, are discussed. Possible explanations for flame lift-off are discussed briefly in Sec. 2.3. Sec. 2.4 examines the different regimes of turbulent non-premixed combustion and identifies the regimes relevant for diesel jets. A review of the prior RANS modeling work of reacting diesel jets is discussed in Sec. 2.5. Section 2.6 discusses the commonly adopted LES methodologies in modeling turbulent jets, with emphasis on modeling reacting diesel jets. The chapter concludes with a summary in Sec. 2.7. The prior work relevant to DNS of reacting flows is included in the discussion in Chapter 7.

2.2 Spray Structure in Conventional Diesel Engines

2.2.1 Vaporizing Diesel Jets

The structure of fuel jets in conventional diesel engines has been widely studied over the last few decades (Heywood, 1988; Hiroyasu and Arai, 1990; Abraham and Pickett, 2010; Lee and Abraham, 2011). The fuel is injected into the engine with a large pressure differential between the supply line and the combustion chamber. Typically, solid-cone injectors are used which operate with fuel injection pressures in excess of 2000 bar (Lee and Abraham, 2011). At the time of fuel injection, the chamber temperature is usually in the range of 800 to 1200 K and pressure in the range of 50 to 100 bar. Figure 2.1 shows a schematic of the diesel spray structure. As the liquid is injected at high velocities, it undergoes primary breakup to form ligaments and drops of different sizes in the atomizing region of the jet. This is also a region where the spray is dense and measurements and numerical simulations are very challenging. The mechanisms of primary breakup and drop formation in this atomizing region are still not well understood. It is highly likely that in the dense spray region the drops collide with each other. Furthermore, the ligaments formed during primary breakup and the larger drops undergo subsequent breakup, called as secondary breakup. Several studies have tried to model the atomization process in liquid jets (Bracco, 1985; Reitz, 1987; O'Rourke and Amsden, 1987), but it is important to point out that the accuracy of the models are generally assessed by measurements taken far downstream in the jet (Wu et al., 1986; Labs and Parker, 2003; Labs and Parker, 2006).

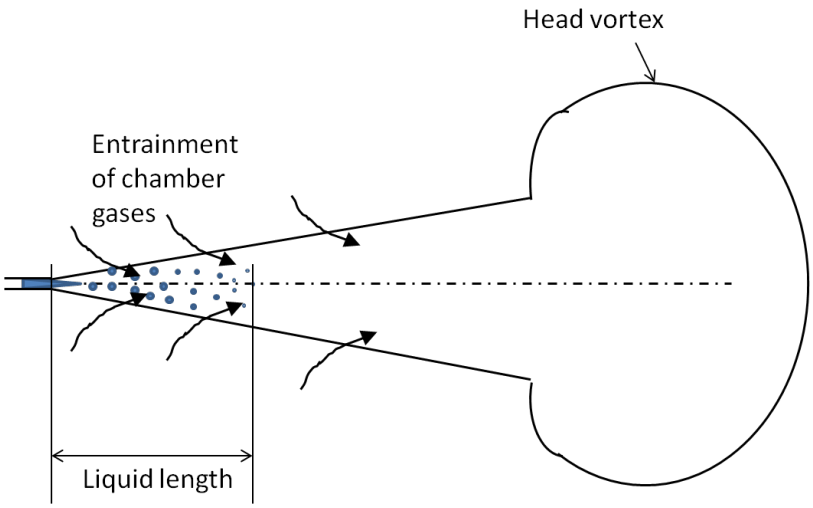

Figure 2.1. Schematic of general features of a diesel spray.

Momentum transfer between the drops and the surrounding gas takes place leading to entrainment of hot chamber air into the jet and vaporization of the liquid fuel. In conventional diesel jets, the vaporization is entrainment controlled, i.e. the liquid vaporization is limited only by the rate at which hot chamber air is entrained (Siebers, 1998; Iyer et al., 2000). In fact, previous studies have determined that the evaporation of the droplets is complete within 100 orifice diameters (Aneja and Abraham, 1998; Siebers, 1998; Iyer et al., 2000; Abraham and Pickett, 2010; Lee and Abraham, 2011). The finite length over which all the fuel droplets get vaporized, referred to as the liquid length, is also depicted in Fig. 2.1. Beyond the liquid length, the fuel penetrates as a vapor jet. The characteristics of the vapor jet are well understood as the features are close to those of transient turbulent jets, which have been studied in depth and structure reported in the literature. The figure also shows a head vortex at the leading edge of the jet where the flow is highly transient. Between the head vortex and liquid length, the non-reacting diesel jet has a structure which is reasonably well-characterized by that of a quasi-steady

turbulent jet (Abramovitz, 1981; Hinze, 1975; Schlichting, 2000). The development and evolution of the head vortex is still a subject of inquiry (Huang, 2000; Pawlak et al., 2007). The features of the head vortex become significant for diesel jets when each injection event is completed through multiple pulses (Tow et al., 1994; Han et al., 1996; Anders et al., 2008).

2.2.2 Reacting Diesel Jets

This will be discussed in greater detail in Sec. 3.4. Figure 3.3 in that section shows a schematic of a reacting diesel jet. As the fuel jet entrains and mixes with the surrounding air, low-temperature chemical reactions occur in the mixture leading to autoignition. Dec (1997) and Flynn et al. (1999) have shown that ignition typically occurs near the leading edge of the jet in the mixture where the equivalence ratio lies between 2 and 4. Other factors which strongly influence the autoignition location are the strain rate history and fuel and air temperatures. The time delay between the start of injection and the first occurrence of ignition is termed as the *ignition delay*. Subsequent to ignition in the rich mixture, Bajaj et al. (2013) has suggested that an ignition front propagates from the rich mixture to the stoichiometric mixture and a flame front then propagates upstream. The flame propagating upstream generally stabilizes some distance downstream from the orifice. The axial distance between the plane of the flame stabilization and the rim of orifice is called the *lift-off height*.

The lift-off height is an important parameter that characterizes combustion in diesel jets. Upstream of the lift-off height, entrainment of the air into the jet results in fuel/air mixing which leads to a reduction in the maximum equivalence ratios

downstream. This influences the formation of soot in the jet. Greater levels of upstream mixing lead to lower levels of soot. This suggests that a greater lift-off height would correspond to a greater degree of mixing. In fact, experimental measurements have confirmed this correlation between lift-off height and soot concentration in the jet for several parametric changes (Siebers and Higgins, 2001; Pickett and Siebers, 2004). In computational modeling of reacting diesel sprays, accurately capturing the lift-off height is critical in accurately modeling soot. Of course, other factors are also important in the modeling of soot. To accurately capture the lift-off height, the mechanism(s) which lead to flame lift-off has to be accurately represented in the model. Unfortunately, several mechanisms have been proposed to explain flame lift-off. The next section reviews the different mechanisms that have been proposed in the past to explain the mechanism of flame lift-off in turbulent reacting jets.

2.3 Possible Explanations for Flame Lift-off in Turbulent Reacting Jets

Flame lift-off in turbulent reacting jets under standard atmospheric conditions has been extensively studied over the past years. Several suggestions have been put forward to explain flame lift-off. Pitts (1989) and Peters (2000) have provided a general review of the different lift-off theories with the focus on atmospheric pressure and temperature conditions. Venugopal and Abraham (2007) have reviewed the applicability of these theories to diesel flames where the pressure and temperature are much higher than atmospheric. *Parts of the discussion from Venugopal & Abraham (2007) have been used*

with minor modifications in the following paragraphs. Results from more recent literature are added.

The premixed flame propagation model was introduced by Vanquickenborne and van Tiggelen (1969) and later investigated by Kalghatgi (1984) and Eickhoff et al. (1984). According to this theory, the fuel and air are assumed to be completely premixed at the base of the flame, and the flame stabilizes at a location where the local time-averaged downstream axial velocity, U_S, is equal to the local turbulent speed, S_t, of the flame propagating upstream The idea is depicted schematically in Fig. 2.2. Kalghatgi (1984) and Eickhoff et al. (1984) have used this model to successfully correlate their experimental findings. However, Pitts (1989) showed through measurements of concentration fluctuations in turbulent propane jets that the assumption of complete pre-mixing in the flame base may not be appropriate, and this model fails to correctly predict other experimental results.

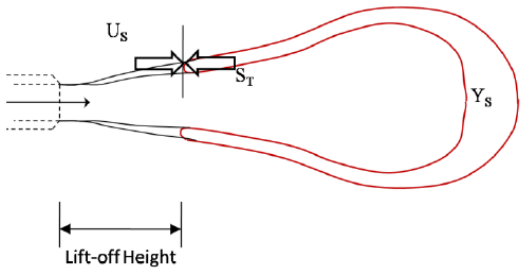

Figure 2.2. Illustration of the theory of premixedness (Venugopal and Abraham, 2007).

The theory of diffusion flamelet extinction was proposed by Peters and Williams (1983) based on the laminar flamelet concept. They disputed the validity of the theory of premixedness by showing that a fluid element does not have sufficient time to achieve the

complete molecular mixing required to reach local uniformity at the base of the flame. According to them, at the lift-off location, the flame structure can be assumed to be a stretched laminar diffusion flame. Lift-off occurs at the location where the local stoichiometric scalar dissipation rate exceeds the extinction limit. Figure 2.3 illustrates the concept behind this theory. The extinction theory for lift-off is supported by experimental results of Gunther et al. (1981), Takahashi and Goss (1992) and Clemens and Paul (1995) and numerical studies by Venugopal and Abraham (2007). However, studies by Pitts (1989) and Eickhoff et al. (1984) have shown that a certain amount of premixing occurs upstream of the lift-off height, thus questioning the validity of the assumption that the flame at the base is a diffusion flame.

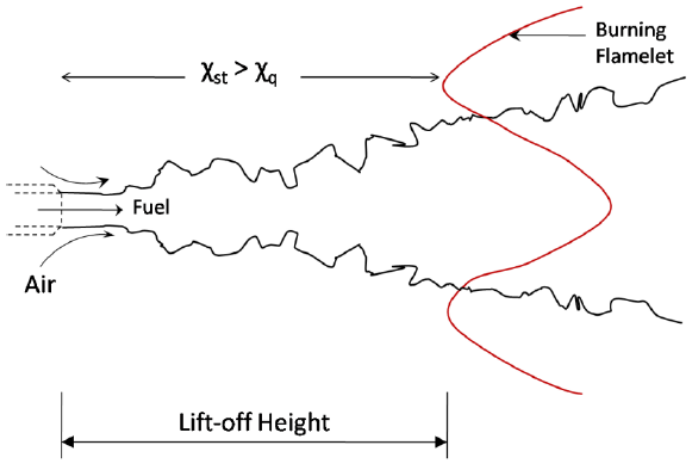

Figure 2.3. Illustration of the theory of flamelet extinction (Venugopal and Abaham, 2007).

It has also been suggested that the extinction may be of a premixed flame and not a diffusion flame. The model proposed by Byggstoyl and Magnussen (1983) assumes that the fuel and air are premixed at the base of the flame. According to them, extinction occurs when the mixing occurs on a time scale shorter than the chemical time scale. This

is equivalent to the scalar dissipation rate exceeding the extinction scalar dissipation rate in diffusion flames (as discussed earlier). In their model, stabilization is determined by extinction at the smallest turbulent scales. This method has been used for prediction of lift-off in diluted methane flames and has been shown to predict the experimental results of Horch (1978).

The suggestion has also been made that the flame stabilizes at a location where a propagating triple flame velocity is equal to the local convective velocity (Muller et al., 1994; Domingo & Vervisch, 1996; Chen & Bilger, 2000). According to this theory, a triple flame structure formed in a laminar mixing layer is suggested as the characteristic flame stabilization structure. After ignition at a downstream location, a lifted triple flame propagates upstream along the stoichiometric contour and stabilization occurs at the lift-off height. This suggestion has been supported by experiments of Muniz and Mungal (1997), Hasselbrink and Mungal (1998) and Ruetsch et al. (1995).

Oldenhof et al. (2010) studied the lift-off behavior of flames burning in hot and diluted coflow using high-speed recordings of the luminescence of the spectrum. They showed that the mechanisms governing lift-off for a jet in hot coflow is significantly different from that of conventional lifted flames. According to them, ignition kernel generation followed by convection and growth are the main factors governing flame stabilization in these flames. They also showed that use of higher alkanes had a similar effect as increasing the coflow temperature on the lift-off behavior. Related to this, it has also been suggested by Pickett et al. (2005) and Karrholm et al. (2008) that ignition has an indirect role in determining the lift-off height in diesel jets.

As the discussion above shows, the explanations for flame lift-off range from those based on premixed flame propagation to partially-premixed triple flames and non-premixed flames. In view of this, it is interesting to ask: what is the regime of turbulent combustion in diesel jets? The next section will address this question.

2.4 Modes and Regimes of Turbulent Combustion

It is important to state at the outset that it is unlikely that there is a unique mode or regime of turbulent combustion valid in all regions of the diesel jets. The interesting question is: what is the spatial distribution of these regimes? It is possible that there is premixing near the lift-off height. It is also possible that there is partial premixing in the near-field (Muller et al., 1994; Domingo & Vervisch, 1996; Chen and Bilger, 2000). Some parts of the jet are likely to be characterized by non-premixed flames. Establishing these modes of combustion in diesel jets is challenging. Optical diagnostics have not provided much guidance. Reynolds-averaged Navier-Stokes (RANS) simulations often presume a mode and regime of combustion.

The strain rate, imposed by the local flow field, which is the inverse of the characteristic flow time, is an important factor which influences the structure of a non-premixed flame. The strain rate influences the flame thickness. Higher strain leads to thinner flames and vice versa. Opposing this is the diffusivity. Increasing diffusivity increases the flame thickness and vice versa. This suggests that the strain rate, a, together with the diffusion coefficient D_{st} can be used to define a diffusion flame thickness l_D where

$$l_D = \left(\frac{D_{st}}{a} \right)^{1/2}. \tag{2.1}$$

In non-premixed flames, the mixture fraction Z can be defined as the ratio of the mass of the fuel originating from the fuel stream to the total mass of the system. It is a useful parameter to describe the mixing layer. Note that Z = 0 in the pure air stream and 1 in the pure fuel stream. A diffusion thickness in the mixture fraction space can be defined based on l_D and the gradient of the mixture fraction field, ∇Z , as

$$(\Delta Z)_F = |\nabla Z|_{st} \, l_D. \tag{2.2}$$

In addition to the diffusion thickness, $(\Delta Z)_F$, a reaction zone thickness $(\Delta Z)_R$ can also be defined in the mixture fraction space. The reaction zone thickness is defined as the region containing the fuel consumption zone and the oxidation layer in the mixture fraction space. Note that these different thicknesses in mixture fraction space are introduced to acknowledge the fact that the distribution of mixure fraction in physical space is not linear. In a turbulent diffusion flame, the characteristic thicknesses $(\Delta Z)_F$ and $(\Delta Z)_R$ in the mixture fraction space must be compared to the mixture fraction fluctuations, Z'_{st} . Here, Z'_{st} is the mixture fraction fluctuation at the mean stoichiometric mixture defined as the root mean square of the mixture fraction fluctuation at the stoichiometric boundary, i.e.,

$$Z'_{st} = \left(\widetilde{Z''^2} \right)_{st}^{1/2}. \tag{2.3}$$

The scalar dissipation rate, χ , is another important quantity related to the gradient in mixture fraction and is defined as

$$\chi = 2D\left|\nabla Z\right|^2. \tag{2.4}$$

The scalar dissipation rate enters the energy and species conservation equations when they are transformed from physical space to mixture fraction space. Its value is directly influenced by the thickness of the flame with thinner flames having higher χ. Thus, the scalar dissipation rate is related to the strain rate. The scalar dissipation rate depends on two important factors - firstly, the diffusion coefficient which is a strong function of temperature and species concentrations, and secondly, the gradient term, which is indirectly the inverse of the mixture fraction thickness. At the flame surface, the scalar dissipation rate takes on the value χ_{st}.

In the case where the mode of combustion is non-premixed, Peters (2000) represented the influence of scalar dissipation rate and turbulence intensity using a regime diagram, which is reproduced in Fig. 2.4. The effect of the turbulence intensity is characterized by the two parameters $Z''_{st}/(\Delta Z)_F$ and $Z''_{st}/(\Delta Z)_R$. The effect of scalar dissipation rate is characterized by $\chi_q / \widetilde{\chi_{st}}$, where χ_q is the extinction scalar dissipation rate and $\widetilde{\chi_{st}}$ is the conditional Fávre mean scalar dissipation rate.

Figure 2.4 shows four different regimes in non-premixed turbulent combustion. For large mixture fraction fluctuations, where $Z''_{st} > (\Delta Z)_F$, the reaction regime is composed of *separated flamelets*. The fluctuations in the mixture fraction space are large enough that they extend to sufficiently rich and lean mixtures so that the mixing layers surrounding the reaction zone are separated. For small mixture fraction fluctuations, $Z''_{st} < (\Delta Z)_F$, the reaction zones are connected leading to a regime called as the connected zone.

This zone can be divided into reaction zones based on reaction zone thickness $(\Delta Z)_R$, which is the thickness of the reaction zone composed of the fuel consumption and oxidation layer. For fluctuations greater than the reaction zone thickness, the flame falls under the *connected flame regime*, and for lower fluctuations, the flame falls under the *connected reaction regime*. In the connected reaction regime, the mixture fraction fluctuations are smaller than the reaction zone thickness and even the reaction zones are connected. This implies that the mixture fraction field is nearly homogeneous. The final regime in the regime map corresponds to regions where the scalar dissipation rate is higher than the extinction scalar dissipation rate. This corresponds to the *flame extinction regime*.

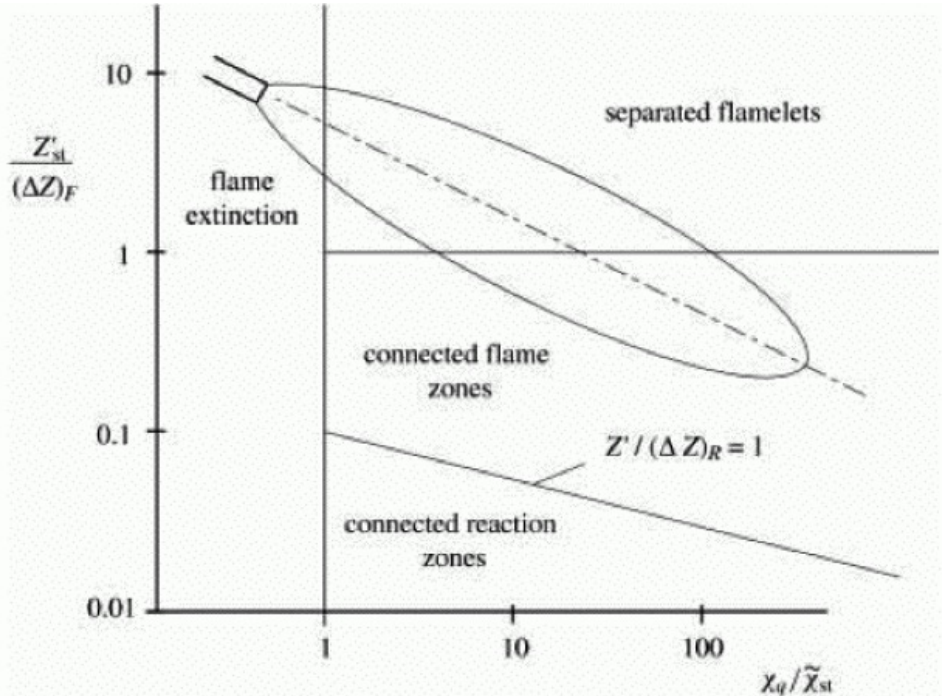

Figure 2.4. Regimes in non-premixed turbulent combustion (reproduced from Peters, 2000).

Figure 2.4 also shows the schematic of a turbulent jet diffusion flame superimposed over the regime map. The shape of the flame is determined by the local conditions along the mean stoichiometric contour. The suggestion by Peters (2000) is that for a typical turbulent jet, extinction occurs near the nozzle, separated flamelets are present near the lift-off location and a connected flame zone occurs at far downstream locations. As the earlier discussion on lift-off theories show, this is a subject of controversy.

The discussion of lift-off mechanisms, modes of combustion, and regimes of turbulent combustion, highlight the challenge in modeling reacting diesel jets. Nevertheless, progress has been made as shown below. Much of this progress has been made within the context of RANS modeling which will be reviewed in Section 2.5 below.

2.5 RANS Modeling of Reacting Diesel Jets

Numerical modeling of reacting diesel jets involves the modeling of multiple phases, atomization, vaporization, and the complex interaction of turbulence and chemistry resulting in partial premixing, quenching and flame propagation. Assumptions are always made to simplify the computational task.

2.5.1 Vaporizing Diesel Jets

One key component of modeling the reacting diesel jet involves the modeling of the vaporization in the two-phase spray. One of the most commonly used approaches to model the spray is the Lagrangian-drop Eulerian-fluid (LDEF) approach (Dukowicz,

1980; O'Rourke, 1981). This approach treats the liquid phase as a dispersed phase in a continuum of gas and solves the dispersed phase equations by employing a Lagrangian method. The liquid drops are grouped into classes (based on size, temperature, velocity) and the collection of drops is referred to as a parcel. Each parcel then represents thousands of drops with identical properties. Such parcels can be tracked as a Lagrangian entity and coupled to the gas phase through source terms. The gas which is a continuous phase can be readily represented in an Eulerian frame of reference through Navier-Stokes equations. The LDEF approach is susceptible to severe numerical challenges. Challenges with employing adequate numerical resolution in spray computations to obtain grid-independent results have been widely discussed in the literature (Iyer and Abraham, 1997; Abraham, 1997; Aneja and Abraham, 1998; Subramaniam and O'Rourke, 1998; Abraham and Pickett, 2010). Alternate approaches, for example, employing Eulerian gas and Eulerian liquid methods, which can achieve grid independence, are computationally intensive (Iyer and Abraham, 2003, 2005).

Modeling of the two-phase diesel jet is challenging. Fortunately, there is a way out of the difficulty. It has been shown by Siebers (1998) and Iyer et al. (2000) that the liquid length in vaporizing diesel jets is entrainment controlled. In other words, the drop sizes are sufficiently small that if sufficient air is entrained, they will vaporize rapidly. As a result of this fact, the liquid length in diesel jets is short and much of the jet is a vapor jet. It is important to note that recent work by Dahms et al. (2013) has suggested that the liquid may not present at all. The suggestion is that mixture is supercritical. Laying aside this possibility for the time being, and holding the conventional view that liquid does exist, the fact is that it may not be worth the effort modeling the liquid phase. In fact, it

has been shown (Iyer and Abraham, 1997; Abraham and Pickett, 2010), through detailed comparisons of computed results in vapor jets with measured results in vaporizing diesel sprays, that in the case of diesel sprays, vapor jets with the same mass and momentum flow rates as the spray jets have a very similar structure, i.e. spreading, penetration, and vapor fuel distribution, as the vaporizing spray from qualitative and quantitative viewpoints. In representing the diesel jet as a pure vapor jet, the diameter, injection density, and injection velocity of the orifice for vapor jet injection are obtained by equating the mass and momentum flow rates of the liquid spray with the vapor jet. Bajaj et al. (2013) performed numerical simulations of reacting lifted diesel jets and showed that employing the vapor jet assumption did not induce any significant differences in the ignition delay, flame lift-off and flame structure. The advantages of this formulation include significant reduction in computational time. While the challenges associated with modeling the liquid phase can be reasonably side-stepped, other challenges are not so easily addressed.

2.5.2 Modeling the Ignition

One of the major parameters whose accurate prediction is important when modeling diesel combustion is the ignition delay, i.e. the time from start of injection to the occurrence of ignition. It strongly affects thermal efficiency and the NO_x and hydrocarbon emissions. During this period, the liquid fuel is atomized, it vaporizes and mixes with the surrounding gases and low-temperature chemical reactions occur. The ignition delay is usually defined based on the time taken to attain a set temperature, the time taken for a rate-controlling radical, such as OH, to reach a set value, or related to the

rise in pressure in the chamber. Modeling of ignition within the context of detailed multidimensional computations typically requires the use of multistep chemical reaction mechanisms. The mechanism may involve artificial species and reaction steps curve-fitted to match experimental results. The multistep 'Shell' ignition model is one such model which has been developed for the autoignition of hydrocarbon fuels at high pressures and temperatures by Halstead et al. (1977) and employed to predict autoignition of fuels in engines (Natarajan and Bracco, 1984). Acceptable levels of agreement between measured and predicted ignition delay times have been observed over a wide range of operating conditions in a constant volume vessel with the Shell model. The model accounts for multistage ignition and "negative temperature" coefficient phenomena. The model has been applied to diesel combustion by many researchers, for example Kong and Reitz (1993).

These pseudo-mechanisms however lack generality. The more realistic approach is to employ multistep kinetics for surrogate fuel species. n-Heptane is often used as a single component surrogate diesel fuel since it has a comparable cetane number as diesel fuel (Heywood, 1988). Detailed chemical-kinetic mechanisms for low-, intermediate-, and high-temperature n-heptane oxidation are available (Curran et al., 1998) and several models exist that have sufficiently reduced dimensionality (number of species and reactions) to enable their use in CFD simulations (Sieser et al., 2000; Peters et al., 2002).

2.5.3 Modeling of Turbulence-Chemistry Interaction

Another challenging aspect of modeling reacting diesel jets lies in accurate representation of turbulence/chemistry interactions. Early turbulent combustion models

employed for engine applications involved a single-step reaction model with the effect of turbulence included using empirical expressions (Spalding, 1971; Magnussen and Hjertager, 1976; Marble and Broadwell, 1977) whereby the reaction time scale was assumed to be a combination of a turbulent time scale and a kinetic time scale. Along these lines, the eddy dissipation model was introduced by Magnussen and Hjertager (1976). This model assumes a one-step reaction where the fuel or reactive species and oxidizer react at a rate determined by the rate-determining species among the fuel, oxidizer and the major product, e.g. CO_2. This model further assumes that the turbulent reaction rate is directly proportional to the inverse of the turbulent time scale, i.e. the mixing time scale, and the concentrations of the reacting species. One difficulty with the application of such models is the presence of empirical constants which are generally not known á priori in cases of incomplete combustion as shown by Reitz and Bracco (1983).

Marble and Broadwell (1977) formulated the coherent flamelet model, which considers the flow field to be composed of multiple laminar flamelets stretched by the turbulent flow. In this model, the mean reaction rate is obtained as the product of the flame surface density (which is the flamelet area per unit volume) and the local strained laminar flame speed. Additional transport equations are solved to obtain the flame surface density in the solution domain. This class of flamelet models has been used for engine combustion by Veynante et al. (1992).

Another turbulent combustion model which is commonly used in engine applications is the laminar-and-turbulent characteristic-time combustion model of Abraham et al. (1985) which utilizes the eddy-breakup concept of Magnussen and Hjertager (1976) and the local equilibrium concept of Reitz and Bracco (1982). The

model has been shown to perform well in engine applications when combined with the Shell ignition model (Patterson et al., 1993). In this model, the mean reaction rate of each species due to the combined effect of turbulence and chemistry is given by

$$\frac{dY_m}{dt} = -\frac{Y_m - Y_m^*}{\tau_c}, \tag{2.5}$$

where Y_m is the mass fraction of species m, Y_m^* is the local thermodynamic equilibrium value of the mass fraction, and τ_c is the characteristic time for the achievement of equilibrium. τ_c is assumed to be the same for the seven species, *viz.* fuel, O_2, N_2, CO_2, CO, H_2, and H_2O. Among these seven species, six reactive species (i.e., all except N_2) are taken into consideration in order to solve the local and instantaneous thermodynamic equilibrium values Y_m^*. The characteristic time τ_c is assumed to be the sum of a laminar timescale and a turbulent timescale, such that the longer of the two times cales controls the combustion rate. The laminar timescale is of Arrhenius form, and the turbulent timescale is assumed to be proportional to the eddy turnover time ε/k, similar to the Magnussen and Hjertager (1976) model.

2.5.4 RANS Modeling of Flame Lift-off

RANS models have been employed to successfully model ignition and flame lift-off in diesel jets. Chomiak and Karlsson (1996) employed the partially-stirred reactor (PaSR) model, along with reduced chemical kinetics, to model turbulence/chemistry interactions and numerically investigate flame lift-off in reacting diesel sprays. In this model, each computational cell was assumed to be composed of a reacting element and a non-reacting element. The volume fraction of the reacting element was determined from

the ratio of the reaction time scale and the turbulence time scale. The computed results were in good agreement with the experimental studies of Winklhofer et al. (1992). They also observed from their studies that the ratio of the convection velocity to the turbulent triple flame velocity was close to unity. Based on their results, the authors suggested that the most plausible mechanism for flame lift-off is through stabilization of a triple-flame propagating upstream. Tao and Chomiak (2002) and Karrholm et al. (2008) also employed the PaSR model and obtained good agreement with the experimental results of Siebers and Higgins (2001) and Siebers et al. (2002).

Senecal et al. (2003) employed a perfectly-stirred reactor (PSR) model, along with detailed chemical kinetics in each computational cell, to study the spray liquid length and lift-off height for reacting diesel sprays. The computed results were found to be in good quantitative agreement with the experimental results of Siebers and Higgins (2001). The results from this study suggest that at the lift-off height, the combustion is kinetics-controlled and premixed. This model suffered from the requirement of large computational overhead due to the use of detailed kinetics and high resolution. The effect of turbulence-chemistry interaction is also not directly captured in this approach.

In the coherent flame model (CFM) (Marble and Broadwell, 1977), a balance equation for the flame surface density, measuring the available flame surface area per unit volume, is derived starting from the balance equation for the mixture fraction. The mean burning rate is then expressed as the product of the flame surface density by the reaction rate per unit flame surface, estimated from laminar flame computations. First applications to ignition problems may be found in Candel et al. (1990) and Veynante et al. (1992). This modeling approach provides local information on ignition location and delay

as well as flame development and stabilization processes under a variety of thermodynamic conditions, at low computational cost, allowing parametric design studies. Tap and Veynante (2005) introduced the generalized flame surface density (GFSD) model to study the transient combustion process from ignition to flame stabilization in diesel jets. This model is based on the concept of the flame surface density, which is the flame surface area per unit volume. In this study, the flame surface density concept was extended to incorporate two important features. First, ignition of a non-premixed flame in general, does not occur under stoichiometric conditions and hence, the flame front cannot be tracked as a given mixture fraction iso-surface. A generalized flame surface density was introduced by integration over all the possible values of the mixture fraction. Second, as ignition is a transient process between pure mixing and a well-established diffusion flame, a progress variable was introduced. This modeling approach was coupled to a mixing model and a chemistry model, based on the unsteady flamelet equations, which were solved á priori to generate a flamelet database. The ignition delay and the nature of flame development were found to be consistent with other studies. The response of the model to variations in injector diameter and ambient density were found to be in qualitative agreement with experimental results. Incidentally, the liquid lengths were not accurately captured although this is probably related to the atomization model employed. Although this model is attractive as it tries to integrate premixed flame propagation with non-premixed combustion, the implementation is more difficult than the PaSR and PSR models.

Venugopal and Abraham (2007) used a flame extinction criterion to model lift-off in diesel jets. Extinction scalar dissipation rates were computed using a flamelet model.

They showed for a range of conditions that the axial distance where the computed stoichiometric scalar dissipation rate matched the extinction scalar dissipation rate agreed with the measured value of lift-off height. Steady flamelets were employed in their work and so ignition and transient combustion processes leading to flame stabilization mechanism were not modeled.

Bajaj et al. (2013) employed the unsteady flamelet progress variable (UFPV) model (Pierce and Moin, 2004; Ihme et al., 2005; Ihme and Pitsch, 2008a; Ihme and See, 2010) to model ignition and flame lift-off in diesel jets. In this model, all thermochemical quantities are parameterized by mixture fraction, reaction progress parameter, and stoichiometric scalar dissipation rate by the solution of unsteady flamelet equations (Peters, 2000). A presumed PDF closure model was employed to evaluate Fávre-averaged thermochemical quantities. For this a beta-distribution was used for the mixture fraction, and Dirac delta function distributions for the reaction progress parameter and the stoichiometric scalar dissipation rate. These Fávre-averaged thermochemical quantities were tabulated in UFPV libraries and were used as the turbulent combustion model for the RANS simulations. Numerical simulations were conducted for a wide range of parameters including variations in chamber temperature, pressure, density, and oxygen fraction, and nozzle diameters. Good agreement was observed for the computed ignition delay and flame lift-off heights when compared to the experimental results of Pickett et al. (2005). This model also allows the use of detailed chemical kinetics through tabulation without considerably increasing the computational time. The major challenge in the application of UFPV model is the selection of appropriate probability density functions (PDF) for the independent scalars.

From this discussion, it can be concluded that if the only objective of the simulations is to predict ignition delay and model flame lift-off height, RANS models are adequate. The more important objective is, however, to also predict soot and NO_x emissions accurately. The prediction of soot and NO_x is likely to be dependent on the highly transient nature of the reacting turbulent jet. Furthermore, the transient effects of large scale turbulent structures on lift-off height are likely to influence mixing and subsequently soot and NO_x formation. The RANS models are unable to represent these effects.

2.6 Large Eddy Simulation of Turbulent Jets

Direct numerical simulation (DNS) of turbulent jets can capture all the turbulent scales in the jet unlike RANS where the flowfield is averaged and none of the turbulent scales are captured. The challenge with DNS is that the range of length and time scales increases dramatically with increase in the flow Reynolds number (Re). So, DNS is impractical for the high Re flows encountered in most practical engineering applications. Furthermore, unless the chemical scales are also resolved, the DNS will still require modeling. For reacting diesel jets, DNS is impractical and likely to remain so for the next decade until exascale resources become readily available. Meanwhile, a compromise between RANS and DNS is large eddy simulation (LES) (Pope, 2000; Lesieur et al., 2005; Sagaut and Meneveau, 2005).

In LES, the larger unsteady three-dimensional turbulent scales are resolved, whereas the effects of the smaller scales which have more universal properties, and are

easier to model, are modeled. The scalar and vector fields are divided into a resolved (filtered) component and a residual (subgrid) component corresponding to the small scales in the flow. According to Kolmogorov's theory (Pope, 2000; Davidson, 2004), the statistical properties of the small scales in a turbulent flow depend only on the kinematic viscosity and the rate at which energy is transferred down from the larger scales to the smaller scales. This theory also states that the small scales are statistically isotropic and have a statistically universal structure. The statistics of the motions of scales within the inertial subrange also have a universal form that can be uniquely determined by the rate of energy dissipation. Saddoughi and Veeravalli (1994) compiled results from several experimental measurements including those made in boundary layers, wakes, grids, jets and oceans, and showed that the errors arising from the use of this approximation are very small. The effect of the small scales is represented in LES through a subgrid scale model. Many of the LES subgrid scale models are based on the assumption of universal properties of the small scales. Regardless, the results from an LES simulation are not independent of the subgrid model, and hence the choice of the subgrid model is important. The major subgrid scale models are discussed in Section 4.3.

2.6.1 Turbulent Combustion Models for Reacting LES

Large eddy simulation of turbulent *reacting* flows is relatively new. One of the major challenges in simulating turbulent reacting flows using LES is the presence of the filtered reaction rate source term $\widetilde{\omega_k}$ which is shown in the filtered species transport equation

$$\frac{\partial}{\partial t}\left(\overline{\rho}\widetilde{Y_k}\right)+\frac{\partial}{\partial x_j}\left(\overline{\rho}\widetilde{Y_k}\widetilde{u_j}\right)=\frac{\partial}{\partial x_j}\left(\overline{\rho}\widetilde{D_{eff}}\frac{\partial\widetilde{Y_k}}{\partial x_j}\right)+\widetilde{\dot{\omega}_k}\,. \tag{2.6}$$

The term $\widetilde{\dot{\omega}_k}$ has to be modeled, as it cannot be directly expressed in terms of the resolved quantities. Turbulence/chemistry interactions are represented through its modeling. As pointed out earlier in Sec. 2.5.4, several models have been proposed to model turbulence/chemistry interactions within the context of RANS modeling. Some of these have been extended to LES. Pitsch (2006) reviewed the major models for LES of non-premixed and premixed turbulent combustion, and highlighted the major differences between RANS and LES combustion models. The rest of this section discusses the four most commonly employed models for LES of non-premixed turbulent combustion: flamelet model, flamelet/progress variable model, conditional moment closure models, and transported FDF models.

Peters (1984, 1986) introduced the flamelet model for non-premixed combustion. This model has been employed for both RANS and LES studies. Flamelet models make the assumption that a turbulent diffusion flame consists of an ensemble of stretched laminar flamelets, and the chemical reactions are confined to thin one-dimensional layers, i.e. the flamelet, at scales smaller than the turbulence length scales. The local structure of the reaction zone within the flamelet remains laminar, and the transfer of mass and energy between the flamelet and non-reacting zone is in the direction normal to the flamelet. The structure of the flamelet in a turbulent flame is shown schematically in Fig. 2.5. Turbulence wrinkles the stoichiometric mixture fraction surface. The higher the level of turbulence, the larger the strain and the thinner the flame. When the species and energy

equations are transformed from the physical space to the mixture fraction space, the flamelet equations are obtained in the form

$$\frac{\partial \phi}{\partial t} - \frac{\chi}{2}\frac{\partial^2 \phi}{\partial Z^2} = \dot{\omega}\,, \tag{2.7}$$

where the general variable ϕ represents the species and energy and $\dot{\omega}$ represents the source term. The effect of the turbulent flow field on the flamelet is captured through the scalar dissipation rate, χ, which was discussed in Sec. 2.4. χ can be thought of as a diffusivity in the mixture fraction space. The compressive strain imposed by the turbulence increases the gradient in the mixture fraction field and thus increases the scalar dissipation rate.

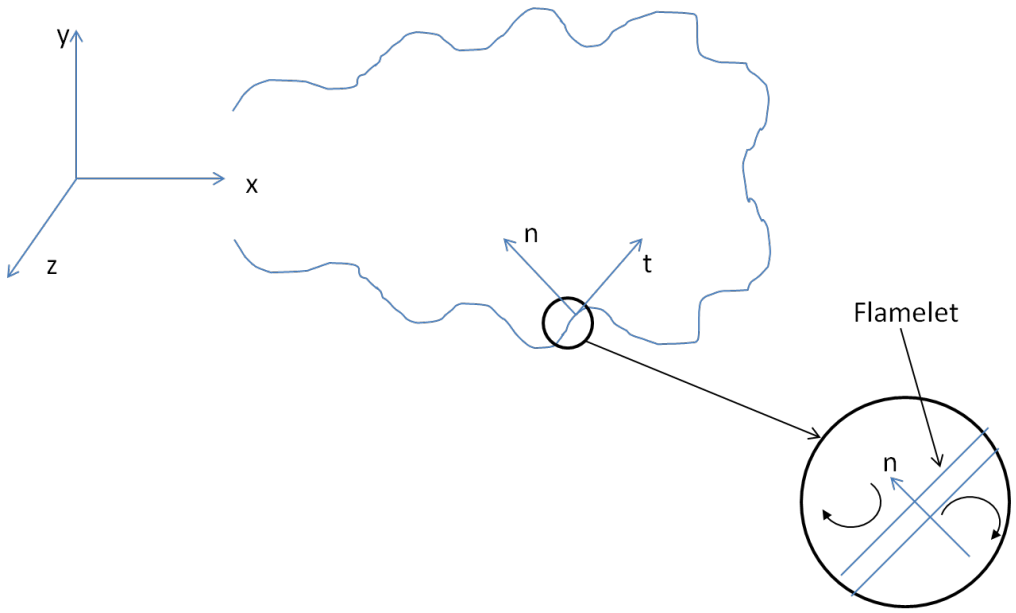

Figure 2.5. Flamelet structure in a turbulent flame.

Flamelet models can be classified as unsteady when the flame structure evolves in time and steady when only the steady flame structure is of interest. The steady flamelet equations can be derived from Eq. (2.7) under the assumption that all species are formed

on a sufficiently fast time scale, so that all species mass fractions and temperature are in quasi-steady state, i.e. Eq. (2.7) reduces to

$$-\frac{\chi}{2}\frac{\partial^2\phi}{\partial Z^2}=\dot{\omega}\,. \tag{2.8}$$

With this assumption, all the thermochemical quantities can be represented as a function of two independent variables - mixture fraction Z and the scalar dissipation rate χ. Note that the scalar dissipation rate is, in general, a function of Z. If a functional dependence of χ on Z can be assumed, then the scalar dissipation rate can, of course, be characterized by its value at one location of Z, e.g. at the stoichiometric Z location, χ_{st}. The functional form of the dependence of χ on Z is typically represented by an error function profile (Peters, 1984)

$$\chi=\chi_{st}\frac{\exp\left\{-2\left[erfc^{-1}\left(2Z\right)\right]^2\right\}}{\exp\left\{-2\left[erfc^{-1}\left(2Z_{st}\right)\right]^2\right\}}. \tag{2.9}$$

The parametrization of thermochemical variables in terms of Z and χ is not unique as it can give multiple solutions (Ihme & See, 2010). As illustrated in Fig. 2.6, which shows a typical S-curve for igniting-extinguishing flames, it is seen that three different states, a, b and c, are possible for the same values of χ_{st}. For a given value of χ and Z, it is possible that the steady solution may lie on the ignition branch or the extinction branch of the S-curve. If multiple solutions are not likely to be encountered in the problem being solved, the steady flamelet model can be successfully used for LES due to its simplicity and advantages over using direct chemistry (Cook and Riley, 1998; De Bruyn Kops et al., 1998; Kempf et al., 2003). Cook and Riley (1998) showed through comparisons with

DNS simulations with single-step chemistry that the results predicted using the steady flamelet model were substantially more accurate than assuming equilibrium chemistry. Pitsch et al. (1998) showed that the steady flamelet model is not applicable for processes like pollutant formation and radiative heat transfer which are slow The full unsteady formulation must be used for these cases.

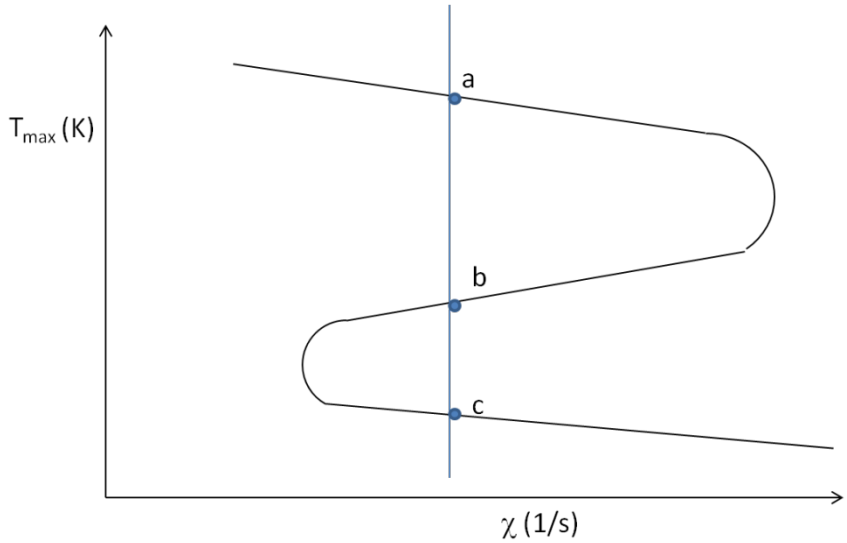

Figure 2.6. Figure illustrating multiple solutions using the steady flamelet model.

In the case of diesel combustion, the steady flamelet model is not appropriate because unsteady processes like autoignition, extinction, and re-ignition are important. In fact, multiple solutions exist because of the importance of the ignition and extinction branches of the S-curve. This problem can be addressed by introducing an additional variable called the reaction progress parameter C. Note that the reaction progress variable C is in general a function of Z. If the assumption can be made that the functional dependence is unique, i.e. multiple values of C do not exist for a given Z, C(Z) can be parameterized in terms of $\Lambda=C(Z_{st})$, i.e. the C value at the stoichiometric mixture fraction

Z_{st} A unique mapping between χ_{st} and Λ along the entire S-shaped curve is obtained. Figure 2.7 illustrates this mapping procedure. The top panel shows the temperature T_{max} and the reaction progress variable Λ as a function of χ_{st}. The bottom panel shows the corresponding data for T_{max}, obtained by remapping the solution from χ_{st} onto the reaction progress parameter Λ. The results illustrated in this figure emphasize the unique representation of each flamelet along the entire S-shaped curve. Thus, the thermochemical variables can now be expressed in the form of two independent variables - mixture fraction Z and the reaction progress parameter Λ. This model is termed as the flamelet progress variable model (FPV), and was introduced by Pierce & Moin (2001, 2004).

Note that the FPV library is generated by using steady flamelet solutions for varying values of χ, i.e., Λ for the flamelet will change when χ is varied. In this sense, the model is a "steady flamelet model", but with one additional parameter that removes the problem with multiple solutions. C can be determined from either the local temperature or the local product concentration. The advantage of this formulation is that it gives a better representation of extinction and reignition phenomena and flame lift-off. The major challenge in the FPV model is to obtain the joint PDF of the mixture fraction and reaction progress variable. Presumed PDFs are usually employed. Usually a beta function distribution is employed for mixture fraction and a Statistically Most Likely Distribution (SMLD) function for the reaction progress variable (Ihme & See, 2010). Pitsch and Ihme (2005) extended the FPV model to an unsteady flamelet library called the unsteady flamelet progress variable (UFPV) model. In this model, the thermochemical variables

are assumed to be a function of three variables: mixture fraction Z, scalar dissipation rate χ_{st} and the progress variable Λ. This model will be discussed in more detail in Chapter 3.

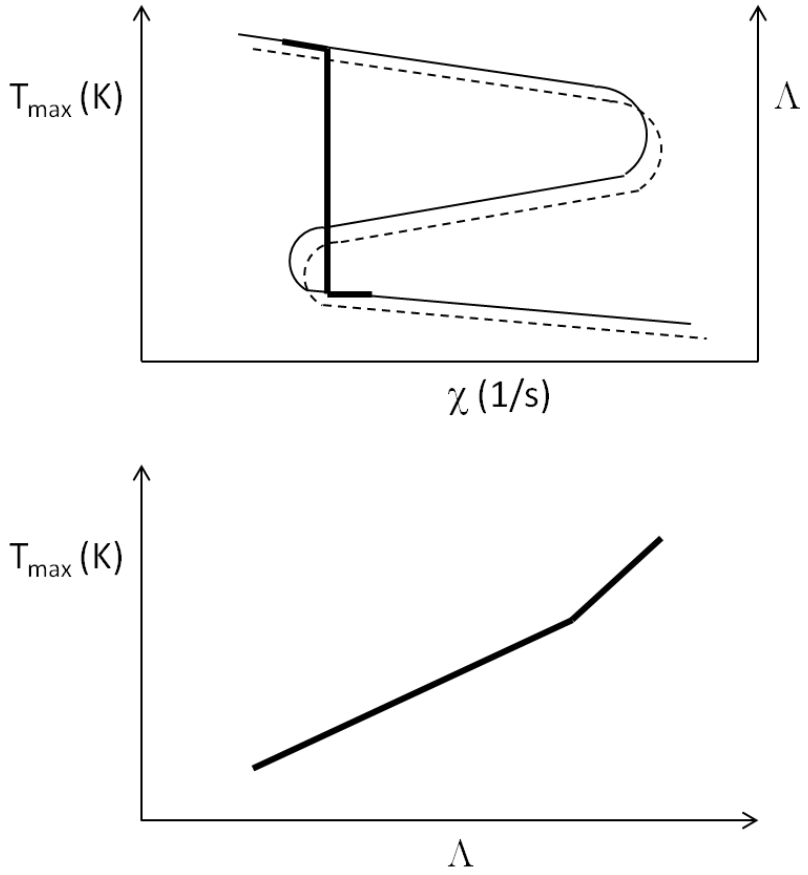

Figure 2.7. Mapping between χ and Λ. In the top panel, the solid line represents T_{max} and the dotted line represents Λ.

The conditional moment closure (CMC) model was proposed for use within the context of RANS simulations by Klimenko (1990) and Bilger (1993). Kim and Pitsch (2005) formulated the CMC model for LES. The main hypothesis behind CMC models is that the fluctuations in the scalar quantities of interest can be related to the fluctuations in the mixture fraction field. Based on this idea, transport equations are derived for the

reactive scalars which are conditionally averaged with the mixture fraction. Conditional averaging of a variable Y_i is defined as

$$\langle Y_i \,|\, \eta \rangle = \langle Y_i \,|\, Z = Z^* \rangle = \frac{P(Y_i)}{P(Z = Z^*)}. \tag{2.10}$$

In the above equation, Z^* is a particular value of the mixture fraction Z and is usually taken to be the stoichiometric value Z_{st}. The transport equation for the conditionally averaged mass fraction of species *i* is given by

$$\frac{\partial \langle Y_i \,|\, \eta \rangle}{\partial t} + \langle \mathbf{v} \,|\, \eta \rangle \cdot \nabla \langle Y_i \,|\, \eta \rangle - \frac{1}{2} \langle \chi \,|\, \eta \rangle \frac{\partial^2 \langle Y_i \,|\, \eta \rangle}{\partial \eta^2} = \langle W_i \,|\, \eta \rangle, \tag{2.11}$$

where **v** is the velocity and W_i is the source term for species *i*. Since this equation is being solved for the conditional averages, the only unclosed term in the equation is the conditionally-averaged source term. Similar equations are derived for momentum and enthalpy. Klimenko & Bilger (1999) show that the following approximation can be made with negligible errors:

$$\langle W_i(Y_i, h) \,|\, \eta \rangle \approx \langle W_i(Q_i, Q_h) \,|\, \eta \rangle = W_i(Q_i, Q_h), \tag{2.12}$$

where $Q_i = \langle Y_i \,|\, \eta \rangle$ and $Q_h = \langle h \,|\, \eta \rangle$. Here, h represents the enthalpy of the mixture. This conditional averaging makes the modeling of the averaged source term considerably easier as no closure models are required. Bilger et al. (2005) discusses that in applying the CMC model in LES of practical configurations, several challenges still exist like computational feasibility and prescribing the correct boundary conditions.

Pope (1985) discusses the use of Probability Density Function (PDF) methods for the modeling of turbulence/chemistry interactions in turbulent reactive flows in the RANS context. This method involves solving transport equations for the joint PDF of the

set of variables of interest. Lundgren (1969) derived, modeled and solved a transport equation for the joint PDF of the three velocity components. In this equation, the turbulent transport terms remain closed and do not require modeling. Pope (1976) derived the transport equation for the composition joint PDF, which was the joint PDF for the species mass fractions and enthalpy. The major advantage of this formulation is that modeling is not required for the mean reaction rate term. But, the numerical solution of the joint PDF transport equation starts to become infeasible as a larger number of variables are included, the reason being that the joint PDF is a function of all the scalars.

Pope (1981a) devised a Monte-Carlo solution technique which greatly reduced the computational expense in solving these equations for large number of independent variables. Pope (1985) derived and solved a joint velocity-composition PDF transport equation using the Lagrangian method. The advantage of having unclosed turbulent transport and mean reaction rate terms in this formulation enabled its use in premixed flames (Nguyen and Pope, 1984; Anand and Pope, 1987) and diffusion flames (Pope, 1981b; McNutt, 1981). The use of PDF for LES was suggested by Givi (1989) and its first application is due to Madnia and Givi (1993). The main challenge of using this method in LES is to properly handle the PDFs of the subgrid variables. Pope (1990) introduced the concept of ‘‘filtered density function’’, FDF, which is essentially the PDF of SGS scalar variables. Transported filtered density function (FDF) model was introduced for LES by Pope (1990). In this approach, a transport equation for the joint FDF of all independent scalars is solved. A Lagrangian approach is commonly employed by the use of a system of notional particles. The velocity, temperature and species densities of each particle are obtained by solving ordinary differential equations. Large

number of particles is required in each cell, as the accuracy of this method depends on the square root of the number of particles. This makes this method computationally intensive when the number of cells is large, as is typical for LES simulations of practical configurations. The in-situ adaptive tabulation (ISAT) method proposed by Pope (1997) considerably reduces the computational time.

2.6.2 LES of Reacting Diesel Jets

Diesel combustion is characterized by high chamber pressure and temperature, and high injection Reynolds numbers and consequently small Kolmogorov scales. Thus, the LES of diesel sprays is challenging due to the requirement of very fine grids and small numerical time steps. There have been very few applications of LES simulations to diesel jets and even fewer to reacting diesel jets.

Hori et al. (2007) performed LES of reacting diesel jets using the KIVA-LES code. Turbulent combustion was modeled using the eddy-dissipation model. Significant differences were observed in the computed heat release rates when compared to the experimental results. The jet and averaged flame structure was captured reasonably well. The reason for the discrepancy in the heat release rates was attributed to the relatively large grid sizes which were not able to capture all the energy containing scales. In other words, the LES more closely approximated RANS than “true LES”.

Recently, Bekdemir et al. (2013) performed LES of a diesel jet with tabulated chemical kinetics. The tabulated kinetics data was obtained from simulations of laminar igniting counterflow diffusion flames. Second-order centered scheme was used with a constant-coefficient Smagorinsky model. An unstructured non-uniform grid was used

which allowed the presence of fine grid near the nozzle. The ignition delay and flame lift-off heights were in good agreement with the experimental results. But the unsteady evolution of the flame could not be captured well in their study.

2.7 Summary

As evident from the discussion in this chapter, accurate numerical modeling of reacting diesel jets is a challenging task. The primary computational approach has been, and continues to be, RANS modeling. But, the main disadvantage of using RANS simulations is that unsteady effects like extinction and re-ignition and the influence of large-scale mixing and intermittency cannot be captured. These factors are expected to play important roles in the prediction of pollutants in the reacting jet. LES is promising but challenging. It can capture the unsteady physics and large-scale structures in the jet. Advances in computational power have enabled the use of LES for realistic flow configurations which could not be imagined just a few years ago. LES of reacting jets under engine conditions is, however, still in its infancy. Although some work has been done in this area (Hori et al., 2007; Bekdemir et al., 2013) much remains to be done. An important sub-model when using either RANS simulations or LES is the turbulence/chemistry interaction model (Sections 2.5.3 and 2.5.4). The accuracy of the RANS and LES predictions will depend on the accuracy of the turbulence/chemistry interaction model. One such model, the Unsteady Flamelet Progress Variable (UFPV) model, will be evaluated in detail in this work.

3 RANS SIMULATIONS OF LIFTED FLAMES IN TURBULENT REACTING JETS

3.1 Introduction

This chapter presents comparisons between computed and measured ignition delay and lift-off heights for a wide range of diesel engine conditions using RANS simulations. The details about the Unsteady Flamelet Progress Variable (UFPV) model, which is employed to model the turbulence-chemistry interaction is discussed in Section 3.2. The computational domain and conditions employed are discussed in Section 3.3. Section 3.4 discusses the experimental setup and presents the comparisons between the computed and the experimental results. This is followed by a discussion about the lift-off mechanism based on the results in Section 3.5. The chapter closes with the summary in Section 3.6. *Note that parts of this chapter have appeared in a manuscript entitled "**Evaluation Of An Unsteady Flamelet Progress Variable Model For Autoignition And Flame Lift-Off In Diesel Jets**" in Combustion Science and Technology in 2013.*

3.2 The UFPV Model

In the UFPV model, the chemical source terms obtained by solving the equations for energy and species transport in an unsteady flamelet are tabulated in look-up tables as a function of independent parameters. The unsteady flamelet equations are (Peters, 1984)

$$\frac{\partial \varphi}{\partial t} = \frac{\chi}{2}\frac{\partial^2 \varphi}{\partial Z^2} + \dot{\omega}_\varphi, \tag{3.1}$$

where φ is a vector that represents the collective set of all reactive scalars, i.e. temperature and mass fractions of the different species, and $\dot{\omega}_\varphi$ represents the corresponding source terms, and χ is the instantaneous scalar dissipation rate defined as

$$\chi = 2D\left|\nabla Z\right|^2, \tag{3.2}$$

where D is the molecular diffusivity. The functional form of the dependence of χ on Z is typically represented by an error function profile (Peters, 1984)

$$\chi = \chi_{st}\frac{\exp\left\{-2\left[erfc^{-1}\left(2Z\right)\right]^2\right\}}{\exp\left\{-2\left[erfc^{-1}\left(2Z_{st}\right)\right]^2\right\}}. \tag{3.3}$$

Note that in Eq. (3.3) the $\chi(Z)$ dependence is parameterized in terms of χ_{st}, the value of χ at the stoichiometric mixture fraction (denoted by the subscript 'st'). In RANS simulations, the instantaneous average value of scalar dissipation rate in a computational cell is obtained as

$$\widetilde{\chi} = C_\chi \frac{\varepsilon}{k}\widetilde{Z''^2}. \tag{3.4}$$

The constant C_χ is selected to have a value of 6.5 (Venugopal and Abraham, 2007). As discussed earlier in this chapter, the flamelet assumption is valid when kinetic time scale and reaction zone thickness are much smaller than the flow scales. This would imply that turbulence does not affect the reaction zone. In fact, as discussed earlier, turbulence does not influence the diffusion zone either within the framework of the flamelet model. What then is the role of χ in the flamelet model if turbulence does not affect the flame structure?

In turbulent flows, the thickness of the mixing layer (irrespective of whether there is heat release or not) varies in time and space as a result of turbulent mixing. When multiple χ values are employed, they represent the differences in thickness of the mixing layer prior to the start of combustion in that segment of the mixing layer. So, the variable χ is not modeling the influence of turbulent strain during combustion within a flamelet. In fact, in the flamelet solution, the initially specified χ does not change with time.

The solution of Eq. (3.1), with boundary conditions representing the conditions in the fuel and air streams and initial conditions representing the unburned state of the mixture, for a specified value of χ_{st}, provides the transient solution for the source terms. The measured results with which computed results are compared in this work were obtained in a constant-volume chamber where the pressure was approximately constant. For this reason, the assumption is made that the pressure is constant in the solution. The transient solutions can be obtained for a range of values of χ_{st} that are representative of the χ_{st} values encountered in the jet.

Once the solutions are obtained, they are tabulated as a function of independent variables and employed in the simulations of the reacting diesel jet. One obvious independent variable is the mixture fraction Z. The other is the stoichiometric value of

scalar dissipation rate χ_{st}. A third variable is required as a marker of progress of reaction in the unsteady flamelet during ignition and in response to transient strain effects which can lead to extinction. The progress of reaction is given by a progress variable *C* defined in this work on the basis of a normalized rise in temperature, i.e.

$$C = \frac{T - T_u}{T_a - T_u}, \tag{3.4}$$

where *T* is the instantaneous temperature at a value of Z, and the subscripts '*a*' and '*u*' indicate adiabatic and unburned conditions, respectively. There are other definitions of the progress variable, e.g. in terms of fuel or product mass fractions (Pitsch and Ihme, 2005). The progress toward steady state is likely to be dependent on the value of Z, i.e. *C* is a function of Z. To simplify the look-up table, the assumption is made that the *C*(Z) profile can be characterized by the stoichiometric value of *C*, i.e. C_{st}. This profile is obtained from a separate look-up table where C(Z) is tabulated for different values of C_{st} during the transient evolution of the flamelet. There is an implicit assumption that, given a value of C_{st}, the *C* at any Z is unique. Mukhopadhyay (2011) has assessed this uniqueness in detail and has shown that it is reasonable. This is analogous to the treatment of χ(Z) in Eq. (3) except that an analytic expression does not exist. As implied earlier, the *C*(Z) values can be tabulated for both igniting and extinguishing flames (Pitsch and Ihme, 2005; Ihme and See, 2010; Mukhopadhyay, 2011) in the look-up tables. Once the reaction source terms are tabulated as a function of the three independent variables, they can then be employed in RANS (or large-eddy) simulations. In RANS (or LES) simulations, the average source terms are required. These can be obtained by

convolving the instantaneous source terms in the look-up table with the joint probability density function (PDF), $\tilde{P}\left(Z,C_{st},\chi_{st}\right)$, of the independent variables, i.e.

$$\widetilde{\dot{\omega}_{\varphi}} = \iiint \dot{\omega}_{\varphi}\tilde{P}\left(Z,C_{st},\chi_{st}\right)\,dZdC_{st}d\chi_{st}\,, \tag{3.5}$$

where ~ denotes Fávre averaging. In the UFPV implementation reported in the literature, the assumption is made that the PDFs of the independent variables are statistically independent of each other (Pitsch and Ihme, 2005; Ihme and See, 2010). This is, of course, facilitated by the parameterization of $\chi(Z)$ and $C(Z)$ in terms of χ_{st} and C_{st}. The assumption of statistical independence has been assessed in detail by Mukhopadhyay (2011). Statistical independence converts the conditional PDFs into their respective marginal PDFs, i.e.

$$\tilde{P}\left(Z,C_{st},\chi_{st}\right)=\tilde{P}\left(Z\right)\tilde{P}\left(C_{st}\right)\tilde{P}\left(\chi_{st}\right). \tag{3.6}$$

In this work, as in all prior UFPV work, presumed functional forms will be employed to approximate the shapes of the PDFs of the three variables Z, C_{st} and χ_{st}. The β-PDF is employed for describing the mixture fraction distribution. The δ-PDF is employed for C_{st} and χ_{st}. A detailed evaluation of alternate PDFs, including the statistically-most-likely-distribution (SMLD) (Ihme and See, 2010), is presented through DNS in Mukhopadhyay (2011). The assumption of δ-PDF is generally not valid during heat release, but its use was shown not to result in significant errors in estimating *average* heat release rates. Furthermore, as will be discussed later, autoignition and flame lift-off are controlled by physics which may not be influenced significantly by these errors. Recently, Ihme and See (2010) employed the UFPV model to compute lifted autoigniting methane/air jet flames. The present work will evaluate the model for diesel jets where the

conditions are very different from those considered by Ihme and See (2010) in terms of scalar dissipation rate, temperature, pressure, and fuel.

3.3 Computational Domain and Conditions

An axisymmetric RANS code is employed in this work. Its accuracy has been assessed in prior work (see, for example, Iyer and Abraham, 1997; Abraham and Pickett, 2010). A 1-degree azimuthal slice in the spray jet is considered. The spray model treats the liquid phase as a dispersed phase in a continuum of gas and solves the dispersed phase equations employing a Lagrangian method. Challenges with employing adequate numerical resolution in spray computations to obtain grid-independent results have been widely discussed in the literature (Iyer and Abraham, 1997; Abraham and Pickett, 2010; Abraham, 1997). But, it has been shown (Iyer and Abraham, 1997; Abraham and Pickett, 2010), through detailed comparisons of computed results in vapor jets with measured results in vaporizing diesel sprays, that in the case of diesel sprays, vapor jets with the same mass and momentum flow rates as the spray jets have a very similar structure, i.e. spreading, penetration, and vapor fuel distribution, as the vaporizing spray. The diameter, injection density, and injection velocity of the orifice for vapor jet injection are obtained by equating the mass and momentum flow rates of the liquid spray with the vapor jet. Alternate approaches, for example, employing Eulerian gas-Eulerian liquid methods, which can achieve grid independence, are computationally intensive (Iyer and Abraham, 2003, 2005). Results will be shown below with both computed vapor jets and spray jets to highlight any differences that may exist.

Turbulence is modeled with the standard k-ε model and wall functions are employed to model boundary layers (Abraham and Magi, 1997; Abraham and Pickett, 2010). An RNG k-ε model was also employed, but the results showed negligible differences relative to the standard k-ε model (Abraham and Magi, 1997), and they will not be presented here. It is well known that the k- ε models over-predict the spreading rate of round jets by about 20 % (Magi et al., 2001; Wilcox, 2006). In the RANS computations, in addition to solving the governing equations of transient reacting flows, transient equations for mixture fraction $\widetilde{Z}$ and the variance of the mixture fraction ($\widetilde{Z''^2}$) are solved. The instantaneous *average* value of scalar dissipation rate $\tilde{\chi}$ in a computational cell is obtained in the RANS simulations as (Pitsch et al., 1996; Venugopal and Abraham 2007)

$$\widetilde{\chi} = C_{\chi} \frac{\varepsilon}{k} \widetilde{Z''^2}. \tag{3.7}$$

The constant C_{χ} is selected to have a value of 6.5 (Venugopal and Abraham 2007). A skeletal mechanism for n-heptane oxidation consisting of 44-species and 185 reactions is employed to represent the kinetics of n-heptane (Liu et al., 2004). This mechanism has been validated with experimental ignition delays for temperatures between 625 K and 1250 K, and pressures between 1 to 42 bar.

3.4 Results and Discussion

The measured values of ignition delay and lift-off height were obtained in a constant-volume chamber and they are available on the Engine Combustion Network

maintained by Sandia National Laboratories, Livermore, CA (http://www.ca.sandia.gov/ECN). n-Heptane was employed as the fuel in the experiments (and computations). Table 3.1 shows the details of nine cases simulated in this work. These cases represent variations in injection pressure, orifice diameter and chamber temperature, density, and oxygen mass fraction. In Case 2, the experimental results with which comparisons will be shown later are for diesel fuel injected at 432 K instead of an n-heptane jet injected at 373 K. The d_{noz} parameter in the table represents the nominal nozzle diameter, whereas d_{gas} is the equivalent nozzle diameter when the fuel is injected as a vapor jet instead of as a liquid spray jet. When the spatial resolution of the spray computations is as high as possible with the Lagrangian-drop Eulerian-gas spray model, the computed results with the vapor jet are not very dissimilar from those with sprays. This is shown with three comparisons between the two. For the computations with the spray model, the grid size stretches in the radial direction from about 0.3 mm at the injector to 2 mm at the wall. Note that the smallest grid is about three times larger than the nozzle diameter. Using even smaller grids violates the assumptions of the spray model that the liquid volume fractions in the computational cells are very small and leads to computational instabilities. In the axial direction, the grid stretches from about 0.25 mm at the injector to 4.5 mm. For the vapor jet simulations, the grid stretches from a value equal to or smaller than the nozzle radius to about 4.5 mm in the radial direction and from 0.25 to 4.5 mm in the axial direction. The injected drops sizes in the spray simulations are not known and are selected as described in Abraham and Pickett (2010). It is also important to point out that the vapor jet simulations have been assessed for grid

independence but this cannot be shown for the spray jet simulations because of the numerical constraints highlighted above.

Figure 3.1 shows the temperature contour plots for Cases 1, 3 and 5 at 2.5 ms after start of injection (ASI), when the fuel is injected as a vapor jet (denoted by g in figure) and a liquid spray (denoted by s in figure). The temperature contour plots are in fairly close agreement. The computed lift-off height in the spray case is somewhat higher than the corresponding vapor jet. It is reasonable to attribute differences observed between the two to the lack of adequate spatial resolution in the spray. Unfortunately, as indicated earlier, grid independence cannot be verified for the spray simulations but can be for the vapor jet simulations. Subsequent results will be shown with the vapor jet.

Table 3.1. Computational conditions.

Case	d_{noz} (mm)	d_{gas} (mm)	P_{inj} (MPa)	P_{amb} (bar)	T_{fuel} (K)	$T_{ambient}$ (K)	$\rho_{ambient}$ (kg/m^3)	O_2%
1	0.1	0.199	150	42.66	373	1000	14.8	21
2	0.1	0.199	60	42.66	373	1000	14.8	21
3	0.1	0.1745	150	55.45	373	1300	14.8	21
4	0.1	0.2907	150	38.39	373	900	14.8	21
5	0.1	0.199	150	43.02	373	1000	14.8	15
6	0.1	0.199	150	43.2	373	1000	14.8	12
7	0.1	0.199	150	43.45	373	1000	14.8	8
8	0.18	0.3858	140	42.66	373	1000	14.8	21
9	0.1	0.1397	150	86.47	373	1000	30.0	15

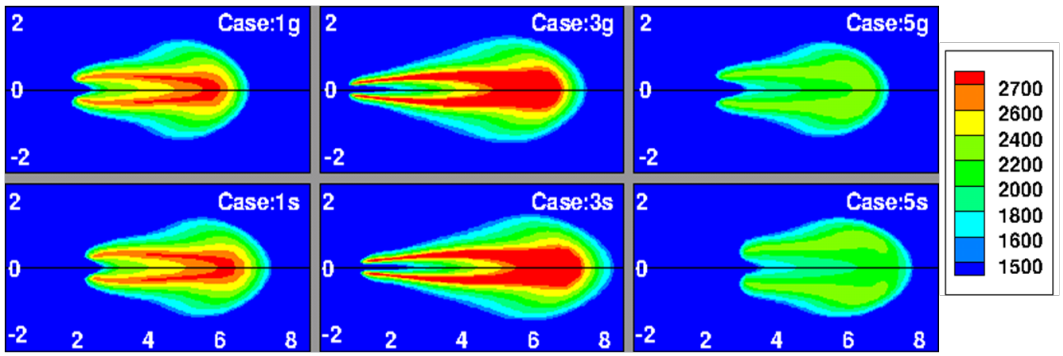

Figure 3.1. Computed temperature contours for spray and vapor jets at 2.5 ms ASI.

Recall that one of the potential strengths of the UFPV model is its ability to predict the transient evolution of reactive scalars in the jet, including during autoignition (and extinction). Figure 3.2 shows the transient evolution of the temperature contours for Case 1. Note that the temperature range shown is 1500-2700 K. The jet initially penetrates into the chamber without significant rise in temperature. This period prior to autoignition is the ignition delay period and its duration is affected by the local fuel/air mixture and scalar dissipation rate (Mukhopadhyay, 2011). Higher scalar dissipation rates are associated with higher diffusion rates of the radicals and heat which would then retard ignition. The first significant rise in temperature is observed at 0.55 ms ASI in the rich mixture (with equivalence ratio between 2 and 3) toward the leading tip of the jet (Dec, 1997). The detailed processes will be described in the next paragraph. The important point to note is that beyond about 1.2 ms, the front no longer propagates upstream, i.e. a steady lift-off height is achieved.

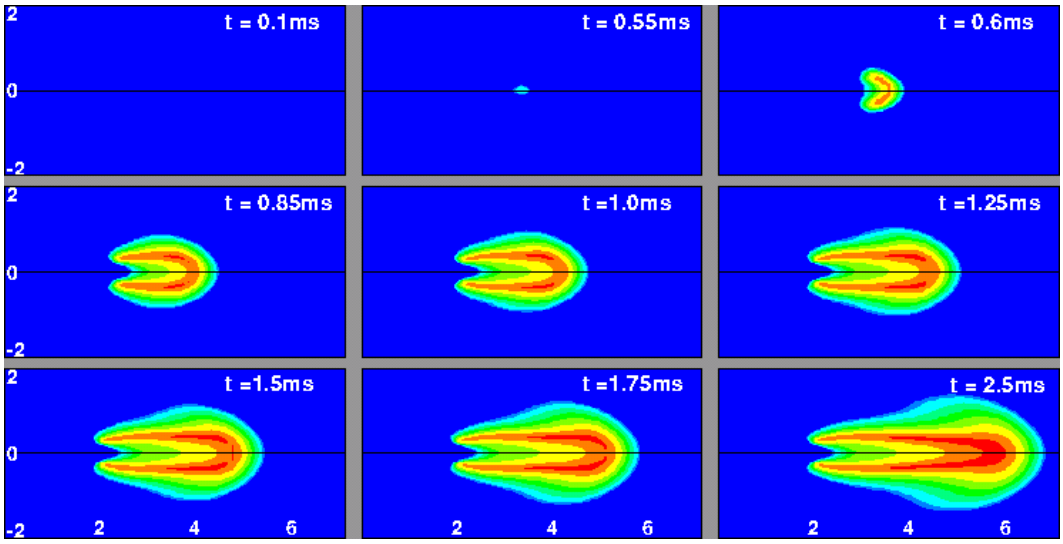

Figure 3.2. Transient development of temperature contours for the vapor jet.

Figure 3.3 shows the conceptual picture of the transient evolution of the reacting diesel spray. When liquid is injected into the domain, it atomizes, entrains hot ambient air, and vaporizes. During the early stages, the liquid and vapor penetrate into the domain but when the drops all vaporize, the liquid length reaches a steady value (Dec, 1997; Siebers, 1998; Aneja and Abraham, 1998; Iyer et al., 2000; Post et al., 2000). Subsequently, the vapor fuel continues to penetrate into the chamber. While the spray is penetrating and entraining air, low-temperature and intermediate temperature chemical reactions are in progress. These reactions lead to autoignition of the mixture. Ignition typically occurs in a richer mixture ($Z \sim 0.1$-0.2) toward the leading tip of the jet and then an ignition front propagates from the rich mixture to the stoichiometric mixture ($Z \sim 0.062$) as shown in the figure. This is consistent with the observations of Mukhopadhyay and Abraham (2011). Once the ignition front reaches the stoichiometric mixture, the flame front propagates along the stoichiometric boundary until the lift-off height is achieved. When the UFPV model is employed, the propagation of the flame is achieved by heat diffusion

and temperature rise to upstream cells. The heat diffusion raises the value of the progress variable *C*. Reaction rates corresponding to the higher value of *C* are fetched from the look-up table which accelerates the rise in temperature and so on. In this way temperature rises in upstream cells.

The process of flame propagation continues as long the scalar dissipation rate χ has a value that lies below the ignition limit. Figure 3.4 shows the typical S-curve which characterizes ignition and extinction behavior of mixtures. Also shown is the schematic of a jet. Sections A-A` and B-B` lie upstream of the lift-height, and the corresponding scalar dissipation rates are shown on the S-curve. Notice that these scalar dissipation rates are lower than the ignition limiting scalar dissipation rate. As the flame propagates upstream from section A-A` to B-B` the scalar dissipation rate increases. Section C-C` identifies the plane where the flame finally stabilizes. At this section, the scalar dissipation rate corresponds to the ignition limiting scalar dissipation rate χ_{ign}. It is interesting to note that ignition and extinction scalar dissipation rates χ_e generally correlate. In this sense, it may be possible to correlate the lift-off heights also with extinction scalar dissipation rates. In general, χ_{ign} and χ_e are sensitive to the kinetics mechanism and this can give rise to challenges in predicting the lift-off height accurately. The constant C_χ in Eq. (7) would then have to be adjusted to account for changes in χ_{ign} when employing the UFPV model.

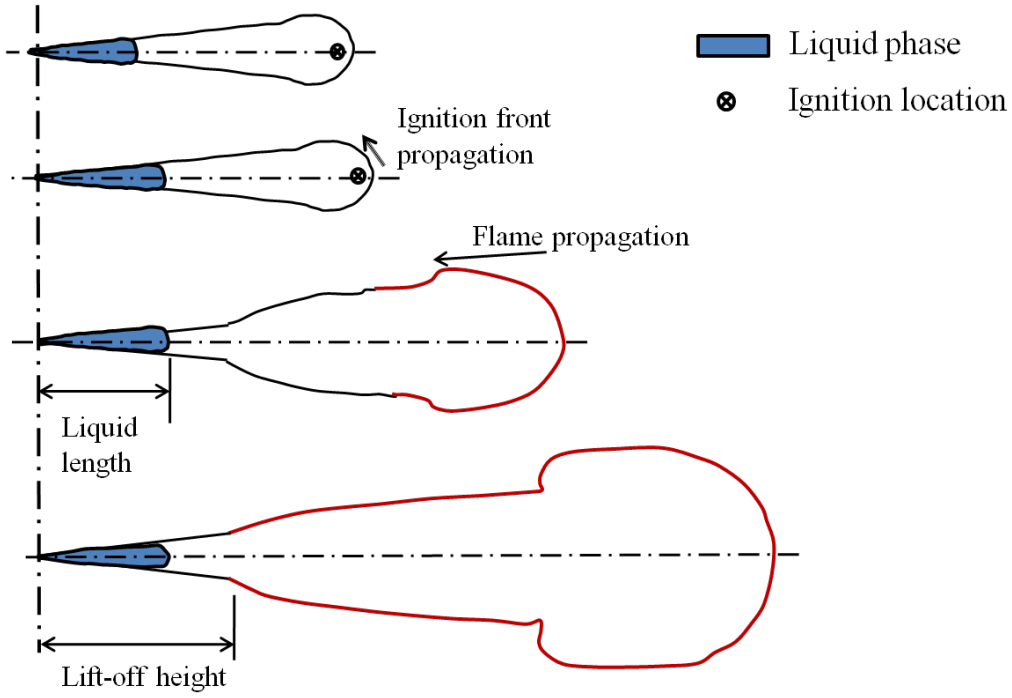

Figure 3.3. Schematic illustrating the development of a reacting diesel jet.

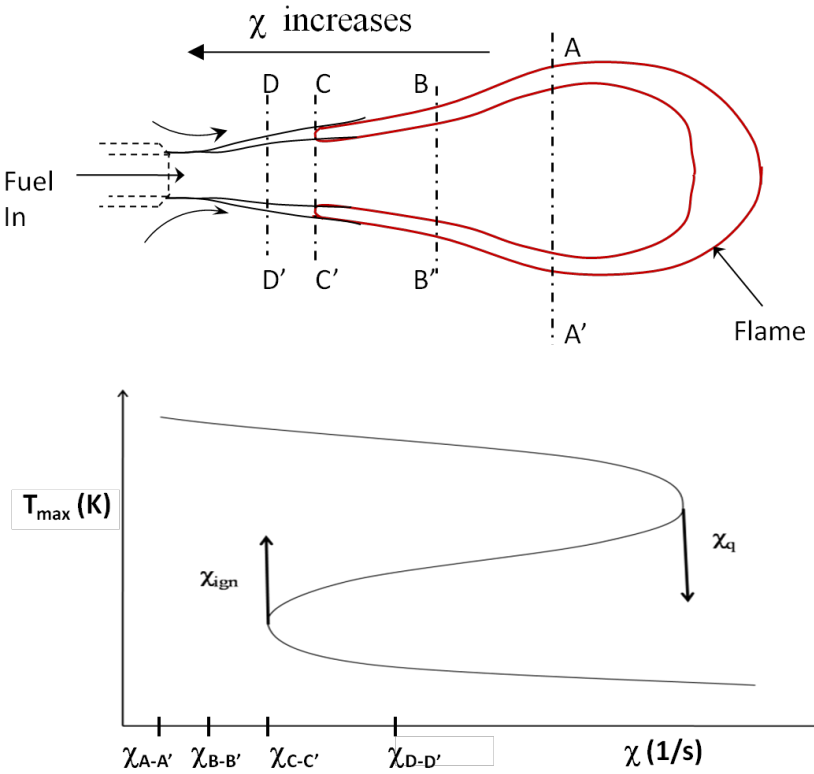

Figure 3.4. Schematic illustrating the variation of scalar dissipation rate in the jet and relation to the S-curve.

Comparisons with measured results will now be presented. The measured ignition delay is obtained as the time when the pressure in the chamber shows significant rise as a result of heat release (Siebers and Higgins, 2001). Ignition occurs on fairly short time scale and so it is not likely to be very sensitive to the measure employed to define it in the computations. In fact, several measures will be employed and will be shown to give results that are fairly close. The measured lift-off height is obtained through measurements of OH chemiluminescence though, as Siebers and Higgins (2001) discusses, the measurements may also be influenced by other factors such as soot luminosity. In fact, the quantitative value of OH at the measured lift-off height is not known. Recall that in prior work (refer to Sec. 2.5.2), time taken to reach a specified temperature and the axial location of the iso-line of a specified temperature are the most widely accepted measures of ignition delay and lift-off height, respectively, in computational studies.

Figure 3.5 shows the computed temperature contours for the nine cases, respectively, of Table 3.1 at 2.5 ms ASI when steady lift-off height is achieved for all cases. Table 3.2 presents quantitative comparisons. Ignition delay is measured as the time required for the temperature to reach 1500 K or 2000 K. For all cases except Cases 7 and 9, the differences in ignition delay between the two temperature values are relatively small suggesting that ignition occurs on a fairly short time scale. It can be seen that the differences between computed and measured results are within 30% for Cases 1 to 6 and Case 8. Recall that Cases 7 is the one with the lowest O_2 concentration, i.e. 8%. For this O_2 concentration, the peak temperature lies below 2000 K. When the O_2 concentration is this low, the temperature rises slower to steady state and inaccuracies are likely in

defining ignition. Case 9 is the one with the higher density. The kinetic mechanism has not been evaluated at the higher pressure corresponding to this higher density. This may contribute to errors, but the more likely source of error is that the rise in pressure in the chamber as a result of ignition is more difficult to identify in the measurements when the initial pressure is high. For these two cases, i.e. Cases 7 and 9, the differences between computed and measured results are as large as 50%. Differences between computed and measured lift-off heights are within 15 % for all cases except Case 7, i.e. the case with lowest O_2 concentration. It is encouraging that the computed and measured trends in both ignition delay and lift-off heights are consistent with measured trends. Next the sensitivity of the computed ignition delay and lift-off height to the criteria employed to define them will be assessed.

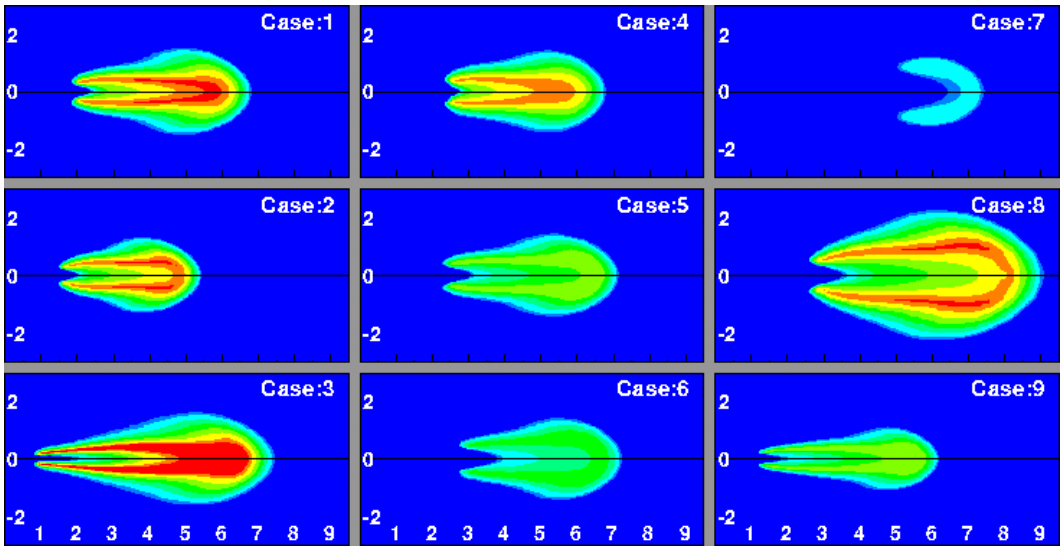

Figure 3.5. Temperature contours showing lift-off heights for nine cases of Table 3.1 employing T_1500 criterion.

Table 3.3 shows computed ignition delays and lift-off heights when other criteria are employed to define them. For each of the seven cases studied, the peak (adiabatic)

temperature and the peak OH concentration were obtained. The ignition delay was identified as the time when the temperature had risen by a certain percentage, say x, of the difference between the initial and peak temperature. Values of 5% and 10% for x were selected. In the case of the lift-off height, percentage rise in temperature and OH concentration (1% and 5%) were both employed. The differences in ignition delay between measured and computed results vary from about 2% for Case 1 to about 30% for Case 5 when a percentage rise in temperature of 5% is considered. Case 6 is an outlier in that the difference is about 60%. In the case of lift-off heights, the differences vary from about 2% in Case 1 to about 12% in Case 4. Notice that the differences are generally smaller than when absolute cut-off values were used earlier.

Table 3.2. Computed and measured ignition delay and lift-off height.

Case	Ignition Delay τ_{id} (ms)			Lift-off Height L_F (mm)		
	Measured	Computed		Measured	Computed	
		T_1500	T_2000		T_1500	OH_0.001
1	0.53	0.542	0.55	17	18.5	18
2	-	0.615	0.63	13.5[a]	15.05	14.8
3	0.26	0.209	0.213	7.7	8.05	8.25
4	0.79	0.89	0.91	25.5	23.3	22.8
5	0.73	0.56	0.593	23.2	22.9	22.9
6	0.947	1.225	1.26	29.2	27.3	----
7	1.52	2.17	----	42.3	52.88	----
8	0.57	0.65	0.662	23.97	25.8	25.31
9	0.38	0.175	0.22	11.9	12	12.8

Without dwelling on the details of the results, what this discussion shows is that the measure employed to quantify ignition delay and lift-off height does make a difference. *Most importantly, for all measures considered, the UFPV model predicts the trends (changes) in the two parameters accurately for the wide range of conditions considered.* Putting the results in perspective, it is difficult to conclude if the differences noted above are a result of inaccuracies in the UFPV model, the chemical kinetics mechanism, the turbulence model, or the measures used to identify lift-off height and ignition delay – perhaps, it is some combination of all four.

Table 3.3. Results based on alternate criteria defining ignition delay and lift-off height.

Case	Ignition Delay τ_{id} (ms)			Lift-off Height L_F (mm)				
	Measured	Computed		Measured	Computed			
		T_5%	T_10%		T_5%	T_10%	OH_1%	OH_5%
1	0.53	0.522	0.532	17	17.4	17.8	16.39	17.26
2	---	0.595	0.602	13.5[a]	14.33	14.73	13.28	14.16
3	0.26	0.205	0.212	7.7	7.98	8.16	7.36	8.03
4	0.79	0.86	0.89	25.5	22.2	22.7	20.63	21.88
5	0.73	0.522	0.55	23.4	21.6	22.8	20.36	21.4
6	0.947	1.18	1.19	29.2	25.93	26.3	24.11	25.37
7	1.52	1.55	1.69	42.3	43.96	47.17	43.28	45.89
8	0.57	0.624	0.634	23.97	24.76	25.19	22.81	24.21
9	0.38	0.145	0.156	11.9	11.2	11.5	10.46	11.16

In prior work (Mukhopadhyay, 2011) it has been shown through DNS that the assumptions that the scalar dissipation rate can be represented by Eq. (3) and the independent parameters are statistically independent, as discussed earlier, are not

generally applicable for reacting diesel jets because of the influence of heat release. Yet, computed ignition delay and lift-off results show reasonable agreement with measured results. In the case of ignition delay, an argument can be made that since there is no heat release prior to autoignition, it will not be affected by the errors in the assumptions. Furthermore, after the onset of autoignition, heat release will be accelerated by the decreasing scalar dissipation rate. In the case of lift-off, the explanation is less obvious. One possible explanation is that near and upstream of the lift-off height the scalar dissipation rate is not influenced significantly by the combustion downstream. In fact, Venugopal and Abraham (2007) made this assumption in estimating lift-off heights employing scalar dissipation rate values in non-reacting diesel jets. Figure 3.6 shows the radial variation of the scalar dissipation rate at different axial locations in the jet of Case 1 at 1.5 ms ASI. The axial locations shown are 15, 17, and 20 mm in the jet. Results are shown for reacting and non-reacting jets. Recall that the lift-off height for this case is about 17 mm and this is reached at about 1.0 ms ASI. Figure 3.6 (a) shows that the reacting and non-reacting results are almost the same upstream of the lift-off height. Figure 3.6 (b) shows that at the lift-off height there is a small decrease in the scalar dissipation rate of the reacting jet relative to the non-reacting jet. The differences between the reacting and non-reacting cases become greater at 20 mm downstream (see Fig. 3.6 (c)) where the peak temperature is over 2500 K. It appears from these results that the diffusion of heat upstream is balanced by convection of heat downstream at the lift-off height and the field upstream is not significantly modified. This may explain the reasonable agreement between computed and measured results notwithstanding the

finding of Mukhopadhyay (2011) that heat release can invalidate the assumptions of the UFPV model.

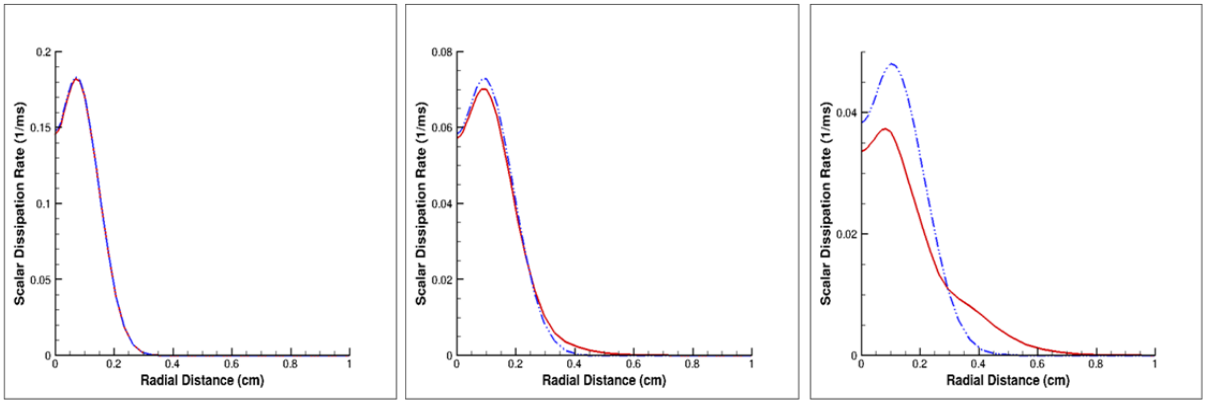

Figure 3.6. Radial variation of scalar dissipation rate at axial distances of (a) 15 mm, (b) 17 mm, and (c) 20 mm at 1.5 ms after start of injection (solid line: reacting jet; dot-dash line: non-reacting jet).

3.5 Inferences about Lift-off Mechanism

Based on the results from the RANS simulations, a conceptual picture can be formulated about the mechanism of lift-off in reacting diesel jets. The baseline case (Case 1) will be used to aid the discussion. Figure 3.7 shows that ignition occurs in the rich mixture (Z ~ 0.1 to 0.12) and then an ignition front propagates from the rich mixture to the stoichiometric mixture (Z~0.062). This is in accordance with the recent observations of Mukhopadhyay and Abraham (2011). Figure 3.8 shows this process in the physical space where the ignition front is tracked with time in the physical space. It is clear from the picture that the ignition occurs in the richer mixture (Z~0.1) and then an ignition front propagates from richer to stoichiometric location. Once the flame reaches the

stoichiometric location, a flame front propagates upstream through the stoichiometric mixture towards the orifice.

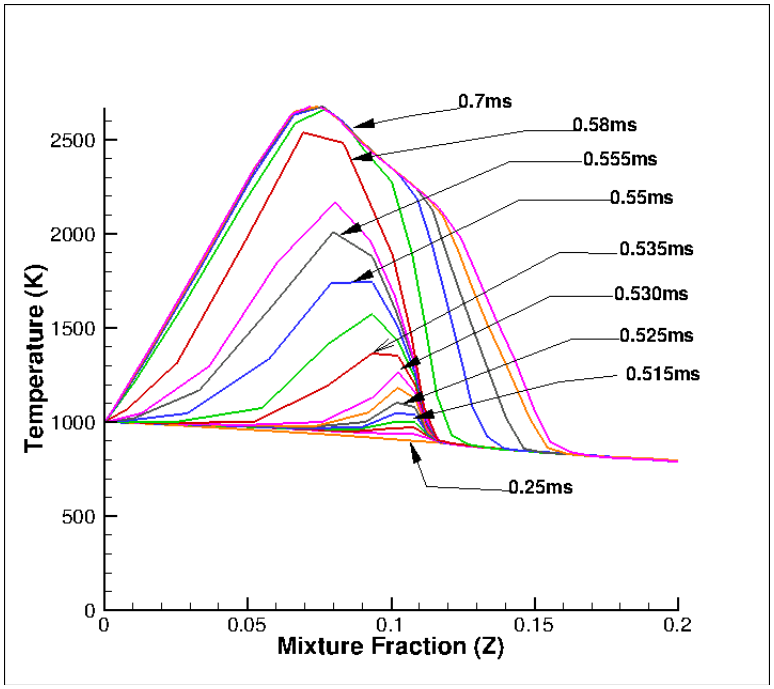

Figure 3.7. Evolution of temperature as a function of Z during ignition and flame development.

The flame front that propagates upstream stabilizes at the lift-off location. To analyze the reasons as to why the flame stops propagating further upstream once it reaches the lift-off location, the conditions of the mixture at the lift-off location have to be analyzed. Figure 3.9 shows the ignition and extinction scalar dissipation iso-lines overlaid on the temperature and mixture fraction iso-lines for Case 1. It can be seen that the location of the lift-off height coincides approximately with the intersection of the ignition scalar dissipation rate with the stoichiometric mixture fraction contour. Similar profiles were observed for other cases too. These results validate the claims made in the previous section regarding the mechanism of flame lift-off. The flame front propagates upstream until it stabilizes at a location where the scalar dissipation rate equals the

ignition scalar dissipation rate. Flame cannot propagate any further as the strain rates are high enough that it prevents ignition.

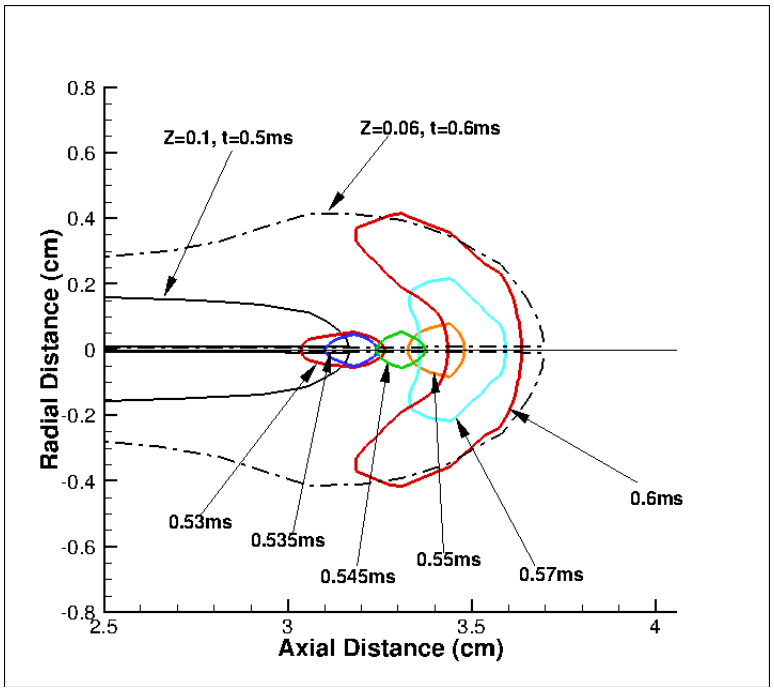

Figure 3.8. Iso-lines of temperature and mixture fraction showing ignition location and ignition front propagation.

3.6 Conclusions

An unsteady flamelet progress variable (UFPV) model is employed in Reynolds-averaged Navier-Stokes (RANS) simulations to predict ignition delay and flame lift-off in diesel jets over a range of conditions which include changes in injection pressure, and ambient temperature, density, and ambient oxygen concentration, and nozzle diameter. For the range of conditions considered, ignition delay and flame lift-off heights are generally predicted within 25% of experimental values. Recognizing that these are RANS simulations and there are uncertainties in different aspects of the models employed,

including the UFPV model, *the most important conclusion is that the simulations reproduce the measured trends in ignition delay and flame lift-off height accurately for a wide range of conditions.* It appears that ignition delay and flame lift-off are controlled by processes which are not significantly influenced by the potential shortcomings of the UFPV model identified in earlier work. Flame stabilization is achieved at the axial location where the scalar dissipation rate in the stoichiometric mixture is equal to the ignition limiting scalar dissipation rate. The UFPV model is able to model multistep chemistry, turbulence-chemistry interactions, and is computationally less expensive than directly employing multistep kinetics in RANS simulations.

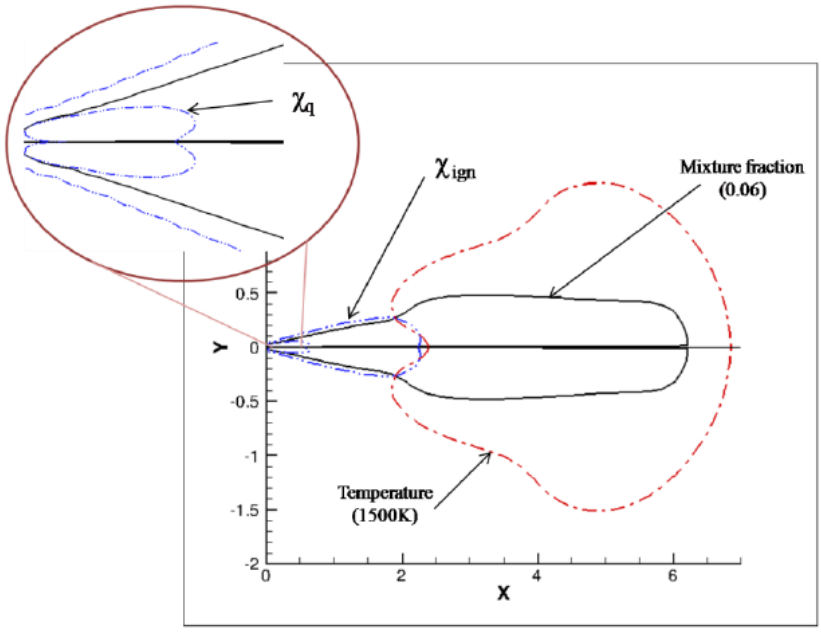

Figure 3.9. Iso-lines of temperature and mixture fraction showing ignition location and ignition front propagation.

The RANS simulations have shown that the UFPV model is a very good framework for modeling turbulence-chemistry interactions for lifted flames. A mechanism of flame stabilization was proposed based on the results from these

simulations. However, the results from these simulations may not be able to give the complete picture as the transient physics predicted by RANS simulations are known to be not very accurate. More time-accurate simulations such as LES or DNS will have to be performed to verify the validity of this mechanism. In the present study, the reacting diesel jet would be simulated using LES. DNS studies would also be performed at the critical locations (ignition location, flame stabilization location etc.) to see whether the proposed flame stabilization mechanism is valid. The additional advantage in employing LES is that it would enable us to study other critical phenomenon in lifted flames such as soot and pollutant formation. Unlike the prediction of lift-off height, soot and pollutant formation are highly dependent on the transient flame development, and thus the LES studies are expected to be significantly more accurate than RANS in predicting soot and pollutants.

4 DNS AND LES COMPUTATIONAL METHOD

4.1 Introduction

The in-house developed Flow, Large-Eddy, Direct-Simulation (FLEDS) code is employed in this work. The governing equations solved in the direct numerical simulation (DNS) and large eddy simulation (LES) of non-reacting and reacting flows are presented in this chapter. In DNS, all the length and time scales are completely resolved, whereas in LES, only the large scales are completely resolved and the effects of the unresolved smaller scales on the large scales are modeled using subgrid-scale modeling. In LES, the variables are considered to be the sum of filtered and unfiltered, or resolved and unresolved, parts. In terms of computational demands, LES falls somewhere between RANS and DNS. Since only the subgrid scales are modeled, LES approaches DNS as the resolution is increased. This is not the case for RANS, where all turbulence scales are modeled and modeling inaccuracies will be present regardless of the resolution employed. While LES approaches DNS as resolution is increased, at practical resolution it is much less computationally intensive than DNS because the small scales, which require most of the computational time in DNS, are modeled.

Two publications which describe portions of the code used in this study are Abraham and Magi (1997) and Anders et al. (2007). *Note that parts of this chapter are*

similar to the discussion given in Anders (2006). The primary difference in this work from those of Anders (2006) is that the simulations of this present work are for transient reacting jets which require the implementation and evaluation of a turbulence/chemistry interaction model. Section 4.2 reviews the governing equations for DNS. The synthetic turbulence generation scheme employed to generate the velocity field for DNS is discussed in Sec. 4.3. Section 4.4 reviews the formulation of the conservation equations for LES. Section 4.5 presents the subgrid-scale models in the code, which include both the Smagorinsky model and the Artificial Diffusivity Scheme (ADS) (Kawai and Lele, 2008). The numerics, including the discretization of first and second derivatives as well as the time integration technique are given in Section 4.6. Filtering is discussed in Section 4.7. The section includes a discussion of the spatial filtering to prevent the growth of instabilities, and the approximate truncated Gaussian filter which is used in the ADS model. Section 4.8 discusses the boundary conditions that are implemented in the code and Section 4.9 discusses the perturbation used to trigger transition to turbulence. Section 4.10 briefly addresses coding and parallelization. The chapter closes with the summary in Sec. 4.11.

4.2 DNS Equations

The governing equations for DNS will be presented in this section. In the notations, a repeated index denotes summation from 1 to 3 unless otherwise noted. For example, $u_i u_i$ denotes $u_1 u_1 + u_2 u_2 + u_3 u_3$. The DNS governing equations consist of

conservation equations for mass, momentum, energy, and species mass fractions. The continuity equation is given by

$$\frac{\partial \rho}{\partial t} + \frac{\partial}{\partial x_j}\left(\rho u_j\right) = 0, \tag{4.1}$$

where ρ is the density and u_j is the velocity in the j (j=1, 2, or 3) direction. The momentum conservation equation is given by

$$\frac{\partial}{\partial t}\left(\rho u_i\right) + \frac{\partial}{\partial x_j}\left(\rho u_i u_j\right) = -\frac{\partial p}{\partial x_i} + \frac{\partial \sigma_{ij}}{\partial x_j}, \tag{4.2}$$

where p is the pressure and σ_{ij} is the viscous stress tensor which is given by

$$\sigma_{ij} = \mu\left[\left(\frac{\partial u_i}{\partial x_j} + \frac{\partial u_j}{\partial x_i}\right) - \frac{2}{3}\frac{\partial u_k}{\partial x_k}\delta_{ij}\right]. \tag{4.3}$$

The total energy E is defined as the sum of the kinetic energy and internal energy, i.e.

$$E = \frac{1}{2}u_i u_i + e. \tag{4.4}$$

In Eq. (4.4), e is the internal energy. The conservation equation for the total energy is given by

$$\begin{aligned}\frac{\partial}{\partial t}\left(\rho E\right) + \frac{\partial}{\partial x_j}\left[\left(\rho E + p\right)u_j\right] = \frac{\partial}{\partial x_j}\left(\sigma_{ij}u_j\right) + \\ \frac{\partial}{\partial x_j}\left(\lambda\frac{\partial T}{\partial x_j}\right) + \frac{\partial}{\partial x_j}\left[\rho\sum_k\left(h_k D_k\frac{\partial Y_k}{\partial x_j}\right)\right],\end{aligned} \tag{4.5}$$

where T is the temperature, λ is the thermal conductivity of the mixture, Y_k, h_k and D_k are the mass fraction, enthalpy and molecular diffusivity of species k, respectively. The conservation equations for the species mass fractions are given by

$$\frac{\partial}{\partial t}\left(\rho Y_k\right)+\frac{\partial}{\partial x_j}\left[\rho Y_k u_j\right]=\frac{\partial}{\partial x_j}\left(\rho D_k \frac{\partial Y_k}{\partial x_j}\right)+\dot{\omega}_k, \tag{4.7}$$

where $\dot{\omega}_k$ is the chemical source term for species *k*. Note that the summation rule does not apply for the species index k in Eq. (4.7). The pressure *p* is obtained using the ideal gas equation of state

$$p=\rho T\sum_k R_k Y_k, \tag{4.8}$$

where R_k is the gas constant for species *k*.

The DNS computational methodology consists of solving Eqs. (4.1) to (4.8) simultaneously for ρ, u_i, E, Y_k, and p. The temporal and spatial discretization of the DNS governing equations will be discussed in Sec. 4.6. The method for generating the initial turbulent flow field is discussed in the next section.

4.3 Synthetic Turbulence Generation

In Chapter 7, the effect of turbulence on the flame development in reacting mixing layers will be studied using DNS and the results will be used to analyze LES subgrid-scale models. One commonly used approach in DNS is to generate the turbulent flow field á-priori using a synthetic turbulence generation scheme. This approach is discussed in this section. *Note that parts of this section are similar to the discussion given in Reddy (2011).*

There are several approaches to generate the turbulence. Lee et al. (1992) developed a method to generate a turbulent velocity field with a prescribed energy spectrum by doing an appropriate re-scaling of a random white noise field in the wave

number space. During the process of generating the turbulent velocity field using this method, there is a loss of directional and phase information regarding the correlation of different velocity components. However, this method is able to reproduce the energy content of the coherent turbulent structures as the energy spectrum is used to generate the turbulent flow field.

Hoshiya (1972) and Shinozuka (1970) developed a procedure that can be used to generate a turbulent flow field by a linear transformation of multiple sets of uncorrelated random data. The kernel function used for the linear transformation is dependent on the prescribed correlation function between the various velocity components. This method can be used to generate a turbulent flow field that has the appropriate correlation between different velocity components. However, the amount of initial statistical information required to develop the linear transformation kernel is prohibitively large. Lund et al. (1998) proposed a method to generate the turbulent flow field on the basis of a prescribed mean velocity profile and Reynolds stresses. The basic premise of the method is similar to Hoshiya (1972) and Shinozuka (1972), i.e. the turbulent flow field is generated through a linear transformation of the uncorrelated random data set. However, in this method, the transformation kernel is generated by decomposing the Reynolds stress tensor. Although, the statistical information required for this method is less than the previous method, the energy spectrum of the resulting flow field has a flat profile in wave number space which is inconsistent with the theoretical turbulent energy spectrum. Klein et al. (2003) proposed a new method for generating turbulent velocity fields by modifying the procedure used by Lund et al. (1998). This method generated the linear transformation kernel by using prescribed Reynolds stresses. However, the decomposition of the

Reynolds stress tensor was carried out by assuming a prescribed shape of the auto-correlation function between different velocity components. Thus, by utilizing second-order two-point turbulent statistics, this method was able to generate turbulent flow fields with coherent structures that had the appropriate energy spectrum profile.

Fathali et al. (2008) further modified the procedure proposed by Klein et al. (2003). Their procedure was able to provide a more accurate description of the coherent structures. They generated the turbulent flow field by a linear combination of uncorrelated random fields. These uncorrelated random fields were generated by applying a spherically symmetric Gaussian filter function. A Gaussian filter function is appropriate as the isotropic turbulence in its final period of decay shows Gaussian statistics. The coefficients for linear combination and the filter width for the Gaussian filter function were then computed from the prescribed integral length scales and Reynolds stresses. The method was then validated by simulating homogeneous turbulent shear flow and then comparing the results with a reference simulation.

In this work, the procedure followed by Fathali et al. (2008) will be used to generate turbulent flow fields. The mathematical details, along with the relevant assumptions and limitations, of this method are provided next. The “synthetic” turbulent flow fields are then used to generate initial conditions for studying the influence of turbulent spectrum on unsteady flame development in reacting mixing layers in Chapter 7. This method generates a turbulent flow field with a prescribed set of Reynolds stresses and integral length scales. The Reynolds stresses are the apparent stress terms arising from the fluctuating velocity field. They are obtained by taking the covariance of the

fluctuating velocity components and is given by $\langle u_i' u_j' \rangle$, where u_i' is the fluctuating velocity component in the *i* direction. The integral length scale is a measure of the distance over which the correlation between the velocity components is significant. Integral length scales can be defined as

$$l_{ij}(\mathbf{x}) = \int_0^\infty \frac{R_{ij}(\mathbf{x}, r\mathbf{e})}{R_{ij}(\mathbf{x}, 0)} dr, \tag{4.9}$$

where $\boldsymbol{e}$ is the unit vector in an arbitrary direction, and R_{ij} is the two-point velocity correlation which is given by

$$R_{ij}(\mathbf{x}, \mathbf{r}) = \langle u_i(\mathbf{x}) u_j(\mathbf{x}+\mathbf{r}) \rangle \tag{4.10}$$

The methodology developed by Fathali et al. (2008) leads to a turbulent velocity flow field determined based on the Reynolds' stresses, $\langle u_i' u_j' \rangle$, and the integral length scales, l_{ij}. The derivation is explained in the paper, only the final results will be presented here. The procedure starts with white noise fields, ξ_{ij}, which have zero mean and uncorrelated with each other, i.e.,

$$\langle \xi_{ij} \rangle = 0, \qquad \langle \xi_{ij} \xi_{mn} \rangle = \delta_{im} \delta_{jn}, \tag{4.11}$$

where δ_{ij} is the Kronecker delta. The velocity components are then given by

$$u_i = \sum_{j=1}^{3} a_{ij} f_{ij}, \tag{4.12}$$

where f_{ij} are obtained by filtering the white noise fields with a Gaussian filter and is given by

$$f_{ij}(\mathbf{x}) = \int_{-\infty}^{\infty} \xi_{ij}(\mathbf{x}') \exp\left(-\frac{(\mathbf{x}-\mathbf{x}')^2}{\sigma_{ij}^2} \right) d\mathbf{x}' \tag{4.13}$$

a_{ij} and σ_{ij} are obtained as follows.

$$a_{ij} = \sqrt{\frac{\left|\langle u_i' u_j' \rangle\right|}{l_{ij}}} \qquad (i \neq j)$$
$$a_{ii} = \frac{\langle u_i' u_i' \rangle - \sum_{k \neq i} \left|\langle u_i' u_k' \rangle\right|}{\sqrt{l_{ii}\langle u_i' u_i' \rangle - \sum_{k \neq i}\left[l_{ik}\left|\langle u_i' u_k' \rangle\right|\right]}} \tag{4.14}$$

$$\sigma_{ij} = \left(\sqrt{\frac{2}{\pi}}\right) l_{ij} \qquad (i \neq j)$$
$$\sigma_{ii} = \left(\sqrt{\frac{2}{\pi}}\right) \frac{l_{ii}\langle u_i' u_i' \rangle - \sum_{k \neq i}\left[l_{ik}\left|\langle u_i' u_k' \rangle\right|\right]}{\langle u_i' u_i' \rangle - \sum_{k \neq i}\left|\langle u_i' u_k' \rangle\right|} \tag{4.15}$$

The turbulent velocity field, $u_i(\mathbf{x})$ is obtained by using Eqs. (4.12) – (4.15). In this work, this method was implemented in a MATLAB code, and can be used to generate both 2-D and 3-D turbulent flow fields. Figure 4.1 shows the velocity vectors and vorticity contours for a 2-D domain obtained using this method. The integral length scales were chosen to be $l_{11}=l_{22}$=500 μm and $l_{12}=l_{21}$=0. The Reynolds stresses were chosen to be $\langle u_1' u_1' \rangle = \langle u_2' u_2' \rangle$=1.0 m^2/s^2 and $\langle u_1' u_2' \rangle = \langle u_2' u_1' \rangle$=0. This flow field has coherent vortex structures which are observed in a repeatable pattern throughout the domain. Similar flow structures were observed for a range of turbulent length scales and Reynolds stresses.

It should be noted at the outset that although the initial turbulent flow field is isotropic and homogenous, the presence of chemical reactions cause the flow to become inhomogeneous and anisotropic. Additionally, viscous dissipation at the smallest scales causes the total turbulent kinetic energy in the domain to dissipate with time. Rosales et al. (2005) performed DNS of forced homogenous isotropic turbulence where energy is

added at the smallest scales to conserve the kinetic energy in the domain. The present DNS code is validated by repeating the simulations of Rosales et al. (2005). The computational setup and results are discussed later in Section 7.3.

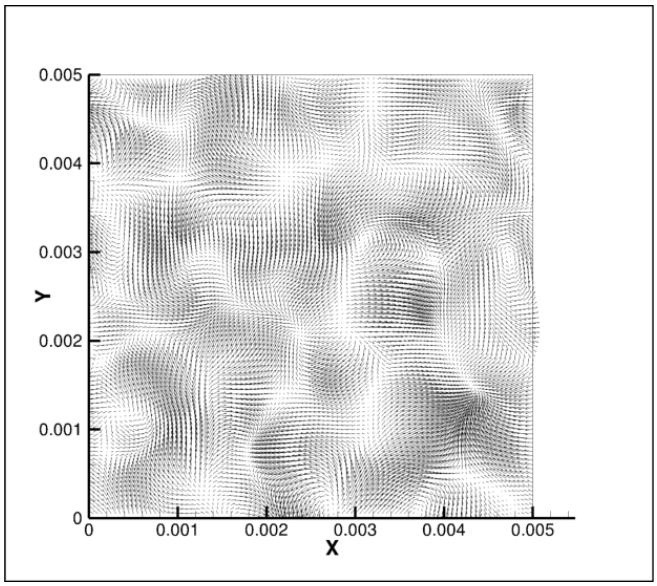

(a)

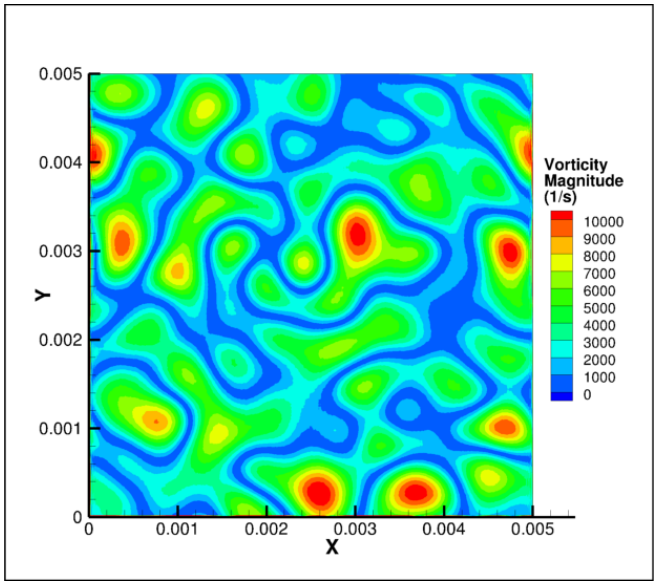

(b)

Figure 4.1. (a) Velocity vectors and (b) vorticity contours for a 2-D flow field generated by the synthetic turbulence method.

4.4 LES Equations

LES is based on the principle that only the large energy-containing scales of the flow are important and are directly resolved whereas the effects of the smaller scales can be modeled. Based on this principle, each variable f in LES is divided into two parts, the filtered (resolved) component $\overline{f}$ and the residual (subgrid) component, f' as

$$f = \overline{f} + f'. \tag{4.16}$$

The filtered component $\overline{f}$ is obtained by applying a spatial filtering operation on each variable f, i.e.,

$$\overline{f}(\mathbf{x},t) = \int G(\mathbf{r},\mathbf{x}) f(\mathbf{x}-\mathbf{r},t) d\mathbf{r}, \tag{4.17}$$

where integration is over the entire flow domain, and $G(\mathbf{r},\mathbf{x})$ is a high-pass filter which filters out all the small scales in the flow. For compressible flow, the focus of this study, Fávre filtering (density-weighted filtering) is employed. In this scheme, the variables are split into a density-weighted filtered component $\widetilde{f}$ and the residual component f'' by the following operation:

$$f = \widetilde{f} + f''. \tag{4.18}$$

Here, $\widetilde{f}$ is obtained as

$$\widetilde{f} = \frac{\overline{\rho f}}{\overline{\rho}}, \tag{4.19}$$

where ρ is the density. The details about the spatial filter are discussed in Sec 4.7.

4.4.1 Filtered Mass and Momentum Equations

The filtered mass and momentum equations are obtained by applying the filtering described in the previous section to Eqs. (4.1) and (4.2) to obtain

$$\frac{\partial \overline{\rho}}{\partial t} + \frac{\partial}{\partial x_j}\left(\overline{\rho}\widetilde{u_j}\right) = 0\,, \tag{4.20}$$

$$\frac{\partial}{\partial t}\left(\overline{\rho}\widetilde{u_i}\right) + \frac{\partial}{\partial x_j}\left(\overline{\rho}\widetilde{u_i u_j}\right) = -\frac{\partial \overline{p}}{\partial x_i} + \frac{\partial \overline{\sigma_{ij}}}{\partial x_j}\,, \tag{4.21}$$

where,

$$\overline{\sigma_{ij}} = \overline{\mu\left[\left(\frac{\partial u_i}{\partial x_j} + \frac{\partial u_j}{\partial x_i}\right) - \frac{2}{3}\frac{\partial u_k}{\partial x_k}\delta_{ij}\right]}\,. \tag{4.22}$$

In Eqs. (4.20) – (4.22), the implicit assumption is made that the operations of filtering and partial differentiation are commutative. This is not true when considering non-uniform grids. Ghosal and Moin (1995) investigated the errors introduced by making this assumption for cases with nonuniform grids. They found that the errors could be as high as that produced by a second-order discretization scheme for the LES equations, and could thus be undesirable if higher order schemes are used.

The filtered viscous stress in Eq. (4.22) can be rewritten in terms of the Favre-averaged variables as

$$\begin{aligned}\overline{\sigma_{ij}} &= \overline{\rho\nu\left[\left(\frac{\partial u_i}{\partial x_j} + \frac{\partial u_j}{\partial x_i}\right) - \frac{2}{3}\frac{\partial u_k}{\partial x_k}\delta_{ij}\right]} \\ &\approx \overline{\rho}\widetilde{\nu}\left[\left(\frac{\partial \widetilde{u_i}}{\partial x_j} + \frac{\partial \widetilde{u_j}}{\partial x_i}\right) - \frac{2}{3}\frac{\partial \widetilde{u_k}}{\partial x_k}\delta_{ij}\right] = \widetilde{\sigma_{ij}}.\end{aligned} \tag{4.23}$$

In Eq. (4.23), the approximation is made that the contribution of subgrid terms to the viscous stress term is negligible. This approximation has been used by prior authors, e.g. Moin et al. (1991), Erlebacher et al. (1990), and Gago et al. (2003). The only term that requires modeling in Eq. (9) is the Reynolds stress term $\overline{\rho u_i u_j}$. This term can be divided into resolved and subgrid components by the following decomposition:

$$\overline{\rho u_i u_j} = \overline{\rho}\widetilde{u_i}\widetilde{u_j} + \left[\overline{\rho u_i u_j} - \overline{\rho}\widetilde{u_i}\widetilde{u_j}\right] = \overline{\rho}\widetilde{u_i}\widetilde{u_j} - \widetilde{\sigma_{SG_{ij}}}, \tag{4.24}$$

where $\widetilde{\sigma_{SG_{ij}}}$ is the subgrid scale Reynolds stress. Rewriting the filtered momentum equation (Eq. (4.21)) using Eq. (4.22), the following equation is obtained:

$$\frac{\partial}{\partial t}\left(\overline{\rho}\widetilde{u_i}\right) + \frac{\partial}{\partial x_j}\left(\overline{\rho u_i u_j}\right) = -\frac{\partial \overline{p}}{\partial x_i} + \frac{\partial \widetilde{\tau_{ij}}}{\partial x_j}, \tag{4.25}$$

where,

$$\widetilde{\tau_{ij}} = \widetilde{\sigma_{ij}} + \widetilde{\sigma_{SG_{ij}}}. \tag{4.26}$$

The most common way of modeling the subgrid scale Reynolds stress is using the turbulent viscosity model given by

$$\widetilde{\sigma_{SG_{ij}}} = \widetilde{\mu_t}\left[\left(\frac{\partial \widetilde{u_i}}{\partial x_j} + \frac{\partial \widetilde{u_j}}{\partial x_i}\right) - \frac{2}{3}\frac{\partial \widetilde{u_k}}{\partial x_k}\delta_{ij}\right] - \frac{1}{3}\widetilde{\sigma_{SG_{kk}}}\delta_{ij}. \tag{4.27}$$

In Eq. (4.27), $\widetilde{\mu_t}$ is the subgrid-scale turbulent viscosity. The details about its modeling is described in Section 4.3.

The filtered pressure obtained by filtering Eq. (4.8) is given by

$$\overline{p} = \widetilde{T}\sum_k \overline{\rho_k} R_k, \tag{4.28}$$

where R_k is the gas constant and $\overline{\rho_k}$ is the filtered species partial density for species *k*.

4.4.2 Filtered Energy Equation

The filtered form of the conservation equation for the total energy is given by

$$\frac{\partial}{\partial t}\left(\overline{\rho}\widetilde{E}\right)+\frac{\partial}{\partial x_j}\left[\overline{\left(\rho E+p\right)u_j}\right]=\frac{\partial}{\partial x_j}\left(\overline{\sigma_{ij}u_j}\right)+ \frac{\partial}{\partial x_j}\left(\overline{\lambda\frac{\partial T}{\partial x_j}}\right)+\frac{\partial}{\partial x_j}\left[\overline{\rho\sum_k\left(h_k D_k\frac{\partial Y_k}{\partial x_j}\right)}\right]. \tag{4.29}$$

where λ is the thermal conductivity of the mixture, and h_k and D_k are the enthalpy and diffusivity of species *k*, respectively. The subgrid scale correlations resulting from the filtering of the right hand side terms are neglected in this study, and the subgrid correlations arising from the convection term will be modeled. Similar to the turbulent viscosity model discussed in Section 4.4.1, the filtered convection term is modeled as

$$\begin{aligned}\overline{\rho Eu_j}&=\overline{\rho}\widetilde{E}\widetilde{u}_j+\overline{\rho}\left(\widetilde{Eu_j}-\widetilde{E}\widetilde{u}_j\right)\\&=-\widetilde{\lambda_T}\frac{\partial\widetilde{T}}{\partial x_j}-\overline{\rho}\sum_k\left(\widetilde{h_k}\widetilde{D_T}\frac{\partial\widetilde{Y_k}}{\partial x_j}\right)-\widetilde{\sigma_{SG_{ij}}}\widetilde{u}_j.\end{aligned} \tag{4.30}$$

In Eq. (4.30), $\widetilde{\lambda_T}$ is the subgrid-scale turbulent conductivity and $\widetilde{D_T}$ is the subgrid-scale turbulent diffusivity. These are obtained directly from the subgrid-scale turbulent viscosity using a constant turbulent Prandtl or Schmidt numbers as in the case of the Smagorinsky model or determined independently as in the artificial diffusivity scheme (ADS) model described in Section 4.5. Making these approximations, Eq. (4.29) can be rewritten as

$$\frac{\partial}{\partial t}\left(\overline{\rho}\widetilde{E}\right)+\frac{\partial}{\partial x_j}\left[\left(\overline{\rho}\widetilde{E}+\overline{p}\right)\widetilde{\left\{u_j\right\}}\right]=\frac{\partial}{\partial x_j}\left(\widetilde{\tau_{ij}}\widetilde{u_j}\right)+ \frac{\partial}{\partial x_j}\left(\widetilde{\lambda_{eff}}\frac{\partial\widetilde{T}}{\partial x_j}\right)+\frac{\partial}{\partial x_j}\left[\overline{\rho}\sum_k\left(\widetilde{h_k}\widetilde{D_{eff}}\frac{\partial\widetilde{Y_k}}{\partial x_j}\right)\right]. \tag{4.31}$$

where $\widetilde{\lambda_{eff}}$ and $\widetilde{D_{eff}}$ are the effective conductivity and effective diffusivity, respectively, and they are obtained by adding the molecular values with subgrid-scale turbulent values.

4.4.3 Filtered Species Transport Equations

The filtered species transport equations are obtained by making similar assumptions as in Section 4.4.2. The final form of the filtered species transport equation is

$$\frac{\partial}{\partial t}\left(\overline{\rho}\widetilde{Y_k}\right)+\frac{\partial}{\partial x_j}\left[\overline{\rho}\widetilde{Y_k}\widetilde{u_j}\right]=\frac{\partial}{\partial x_j}\left(\overline{\rho}\widetilde{D_{eff}}\frac{\partial\widetilde{Y_k}}{\partial x_j}\right)+\widetilde{\dot{\omega}_k} \tag{4.32}$$

where $\widetilde{\dot{\omega}_k}$ is the filtered chemical source term for species *k*. The details about the modeling of the filtered chemical source term are discussed in Chapter 6.

4.5 Subgrid-Scale Modeling

As discussed in Section 4.4, one of the main challenges in LES modeling is the need to model the subgrid turbulent viscosity μ_t. Constant-coefficient Smagorinsky model and the Artificial Diffusivity Scheme (ADS) are used to compute μ_t.

The first subgrid model used for LES simulations, which is still widely employed was the constant-coefficient Smagorinsky model. Much of the early use of this model

was for meteorological applications (Smagorinsky, 1963; Deardoff, 1966). Deardoff (1971) was the first person to use this model for engineering applications. He carried out a simulation of the flow in a channel at infinite Reynolds number without computing the dynamics of the wall layer. The mean velocity and Reynolds stress profiles were found to be within 30-50 % of the experimental values. Moin and Kim (1982) showed that the results are closer to the experimental results when wall layer is resolved. Germano et al. (1991) and Lilly (1992) extended the constant-coefficient Smagorinsky model to a dynamic-coefficient model. In this method, the Smagorinsky constant is allowed to vary in space and time. The constant is obtained by applying a test filter in addition to the primary filter. They carried out LES simulations of transitional and fully developed turbulent channel flows, and showed that the results were in closer agreement to the experimental results compared to the constant-coefficient Smagorinsky model.

Considerable effort in subgrid scale model development has been directed toward turbulent incompressible flows. For compressible flows, the subgrid scale models were usually generalized forms of the models which have been tested for incompressible flows. Yoshizawa (1986) generalized the standard Smagorinsky model for compressible flows. Moin et al. (1991) formulated the dynamic Smagorinsky model for compressible LES. The other subgrid scale models which have been used for compressible LES include dynamic mixed model and scale similarity models. The formulations from Moin et al. (1991) for constant coefficient and dynamic Smagorinsky models are described next.

In the Smagorinsky class of models, the subgrid turbulent viscosity (symbol) is directly related to the grid size Δ and the magnitude of the strain tensor $\left|\tilde{S}\right|$ by

$$\widetilde{\mu_T} = C\overline{\rho}\Delta^2\left|\widetilde{S}\right|, \tag{4.33}$$

where C is a model constant and $\overline{\rho}$ is the filtered density. $\left|\widetilde{S}\right|$ is determined using

$$\left|\widetilde{S}\right| = 2\left(\widetilde{S_{ij}}\widetilde{S_{ij}}\right)^{1/2}, \text{ where} \tag{4.34}$$

$$\widetilde{S_{ij}} = \frac{1}{2}\left(\frac{\partial\widetilde{u_i}}{\partial x_j} + \frac{\partial\widetilde{u_j}}{\partial x_i}\right) \tag{4.35}$$

The effective stress tensor symbol, discussed in Eq. (4.26), is modeled as

$$\widetilde{\tau_{ij}} = \widetilde{\mu_{eff}}\left[2\widetilde{S_{ij}} - \frac{2}{3}\widetilde{S_{kk}}\delta_{ij}\right] - \frac{2}{3}C_I\overline{\rho}\Delta^2\left|\widetilde{S}\right|^2\delta_{ij}, \tag{4.36}$$

where C_I is a model constant and $\widetilde{\mu_{eff}}$ is the effective viscosity, i.e. the sum of the molecular and subgrid-scale viscosities.

The constant-coefficient and dynamic-coefficient Smagorinsky models differ in the determination of the two model constants, C and C_I. In the constant-coefficient Smagorinsky model, the values of the constants are prescribed. The selected values for these model constants are C = 0.012 and C_I = 0.0066. (Moin et al., 1991). The subgrid scale turbulent conductivity and diffusivity are computed using the turbulent Prandtl number and turbulent Schmidt number which are assumed to be equal to 0.7 and 0.9, respectively based on the suggestions of Moin et al. (1991). In the dynamic-coefficient Smagorinsky model, C and C_I vary across the domain and are determined during the computation. The model constants are calculated by applying a test filter to the resolved flow field. Providing the essential ideas behind the formulation would show that you understand what is done. More details of this formulation are given in Moin et al. (1991).

4.5.1 Artificial Diffusivity Scheme (ADS)

When central differencing schemes, such as high-order compact differencing schemes, are applied to solve flows that involve steep gradients, non-physical spurious oscillations that make the simulation unstable are generated. To overcome this, Kawai et al. (2010) proposed the use of an artificial diffusivity scheme (ADS) to capture the discontinuities in the flow. The main idea behind ADS is to artificially augment the viscosity, conductivity and mass diffusivity based on the gradients in velocity, internal energy and species densities, respectively. The main difference between ADS and the Smagorinsky based models is that the turbulent Prandtl and Schmidt numbers are not used in ADS. Each artificial diffusivity is computed solely based on the gradients of the corresponding variable.

The artificial diffusivities are modeled such that they automatically vanish in well-resolved regions where the grid sizes are fine enough to resolve the gradients accurately. The artificial viscosity μ^* is modeled based on the gradients of the magnitude of the strain tensor S as

$$\mu^* = C_\mu \rho \overline{\left| \sum_{l=1}^{3} \frac{\partial^4 S}{\partial x_l^4} \right|}. \tag{4.37}$$

Here, the overbar denotes an approximate truncated Gaussian filter (Cook and Cabot, 2004), which is discussed in Section 4.7.2, and C_μ is a model constant. The artificial conductivity, k^*, and mass diffusivity, D_i^*, are modeled as

$$k^* = C_k \overline{\frac{\rho c_s}{T} \left| \sum_{l=1}^{3} \frac{\partial^4 e}{\partial x_l^4} \right|}, \text{ and} \tag{4.38}$$

$$D_i^* = C_D c_s \overline{\left| \sum_{l=1}^{3} \frac{\partial^4 Y_i}{\partial x_l^4} \right|}, \tag{4.39}$$

respectively. In Eqs. (4.38) and (4.39), c_s is the speed of sound, e is the internal energy, and Y_i is the mass fraction of species i. C_k and C_D are model constants. In the present study, the model constants are selected as C_μ = 0.002, C_k = 0.05 and C_D = 0.01. Increasing the model constants increases the artificial diffusivity, thus reducing the nonphysical discontinuities, but also leads to reduction in accuracy. So, the selected model constants are the lowest values which lead to stable solutions without numerical oscillations arising in the variables.

4.6 The Numerical Scheme

4.6.1 Spatial Discretization

In this study, the spatial discretization of the governing equations is performed using a compact finite difference scheme, which is a generalized version of the classical Pade scheme (Lele, 1992; Poinsot & Lele, 1992; Abraham and Magi, 1997). The spatial derivative of a variable f at each computational grid point is expressed as a function of the values of f and its derivatives at the neighboring grid points. This leads to a set of simultaneous linear equations for the spatial derivatives, which can be solved numerically to obtain the spatial derivatives. The major reason for using this numerical scheme for LES is because this scheme has a formal accuracy comparable to that of spectral methods (Lele, 1992). Thus, this scheme is expected to reproduce the spectral properties of the

flow accurately. For a uniform mesh with size h, the first and second derivative expressions along direction *i* of a variable *f* are given by

$$\beta_1 f'_{i-2} + \alpha_1 f'_{i-1} + f'_i + \alpha_1 f'_{i+1} + \beta_1 f'_{i+2} = a_1 \frac{f_{i+1} - f_{i-1}}{2h} + b_1 \frac{f_{i+2} - f_{i-2}}{4h} + c_1 \frac{f_{i+3} - f_{i-3}}{6h} \tag{4.40}$$

$$\beta_2 f''_{i-2} + \alpha_2 f''_{i-1} + f''_i + \alpha_2 f''_{i+1} + \beta_2 f''_{i+2} = a_2 \frac{f_{i+1} - 2f_i + f_{i-1}}{h^2} + b_2 \frac{f_{i+2} - 2f_i + f_{i-2}}{4h^2} + c_2 \frac{f_{i+3} - 2f_i + f_{i-3}}{9h^2} \tag{4.41}$$

Note that these equations are also valid for non-uniform meshes, in which case the local mesh size h_i is employed instead of h. By enforcing sixth-order accuracy for both the derivatives by using the Taylor series expansion, the following relations are obtained for the coefficients:

First Derivative:

$$\begin{aligned} &a_1 + b_1 + c_1 = 1 + 2\alpha_1 + 2\beta_1 \\ &a_1 + 4b_1 + 9c_1 = 6(\alpha_1 + 4\beta_1) \\ &a_1 + 16b_1 + 81c_1 = 10(\alpha_1 + 16\beta_1) \end{aligned} \tag{4.42}$$

Second Derivative:

$$\begin{aligned} &a_2 + b_2 + c_2 = 1 + 2\alpha_2 + 2\beta_2 \\ &a_2 + 4b_2 + 9c_2 = 12(\alpha_2 + 4\beta_2) \\ &a_2 + 16b_2 + 81c_2 = 30(\alpha_2 + 16\beta_2) \end{aligned} \tag{4.43}$$

There are 3 relations above for the five parameters of each of the equations above. For a tridiagonal scheme ($b_1 = b_2 = 0$), and limiting the size of the right hand stencil to 5 ($c_1 = c_2 = 0$), the following values are obtained for the parameters.

$$\begin{aligned}&\text{First Derivative: } \alpha_1 = \frac{1}{3}, \beta_1 = 0, a_1 = \frac{14}{9}, b_1 = \frac{1}{9}, c_1 = 0 \\ &\text{Second Derivative: } \alpha_2 = \frac{2}{11}, \beta_2 = 0, a_2 = \frac{12}{11}, b_2 = \frac{3}{11}, c_2 = 0\end{aligned} \tag{4.44}$$

Near the boundaries, the above equations cannot be used and hence a fourth-order scheme is used. More details of the formulation are available in Lele (1992).

4.6.2 Time integration

The governing equations for density, momentum, energy and species mass fractions are advanced in time by using an explicit compact storage fourth-order Runge-Kutta (RK) scheme (Gill, 1951) for the convective and diffusive terms, while the source term is solved implicitly. Hence, the time marching for a general variable $\boldsymbol{W}$ can be written as

$$\frac{\partial \mathbf{W}}{\partial t} = f(\mathbf{W}). \tag{4.45}$$

The RK scheme computes the $\mathbf{W}$ value at the new time step, $\mathbf{W}^{n+1}$, from the value at the old time step, $\mathbf{W}^{n}$, through 4 stages. In each stage, the computation of f is performed by using an implicit method for the source term, as described in Abraham and Magi (1997) and Viggiano and Magi (2004).

4.7 Filtering Schemes

In this study, two separate filters are used - a spatial filter to prevent instabilities and an approximate truncated Gaussian filter to determine the artificial diffusivities for the ADS scheme discussed in Section 4.5.1. These filters are described below.

4.7.1 Spatial Filtering

Spatial filtering is used to prevent the growth of instabilities by removing fluctuations at the small scales that are close to the computational grid size. By removing these fluctuations, the spatial filter indirectly adds extra amount of dissipation to the overall numerical scheme. In this way the spatial filter, like the subgrid-scale model, prevents the accumulation of energy at the small scales. The use of this filter reduces the accuracy by increasing the artificial dissipation, but increases the stability of the simulation by removing the small fluctuations arising out of numerical inaccuracies.

In this work, a spatial filtering scheme proposed by Lele (1992) is implemented. Letting f represent a flow variable, which is a solution to the governing equations, and $\overline{f}$ represent a filtered value for that variable, a general expression for the filter is

$$\beta\overline{f_{i-2}} + \alpha\overline{f_{i-1}} + \overline{f_i} + \alpha\overline{f_{i+1}} + \beta\overline{f_{i+2}} = af_i + \frac{d}{2}\left(f_{i+3} - f_{i-3}\right) + \frac{c}{2}\left(f_{i+2} - f_{i-2}\right) + \frac{b}{2}\left(f_{i+1} - f_{i-1}\right) \tag{4.46}$$

For sixth-order accuracy, and using a tridiagonal scheme ($\beta = 0$), all the parameters in Eq. (4.46) become a function of a single parameter α, i.e.

$$
\begin{aligned}
a &= \frac{1}{16}(11+10\alpha), \\
b &= \frac{1}{32}(15+34\alpha), \\
c &= \frac{1}{16}(-3+6\alpha), \\
d &= \frac{1}{32}(1-2\alpha).
\end{aligned}
\tag{4.47}
$$

A value of α = 0.45 is used in the present study. Lower values of α filter longer wavelengths and values of α closer to 0.5 filter shorter wavelengths. A value of α= 0.5 provides no filtering. Since the implemented filter uses a seven-point stencil, different expressions must be used near the boundary. These are discussed in more detail in Lele (1992).

4.7.2 Approximate Truncated Gaussian Filter

As discussed in Section 4.5.1, to determine the artificial diffusivities using ADS, an additional filter has to be applied for the spatial derivatives of strain rate, internal energy and mass fractions. The purpose of using this filter is to reduce numerical oscillations in regions of large gradients. In this study, the approximate truncated Gaussian filter described by Cook and Cabot (2004) and used by Kawai and Lele (2008, 2010) is used. In this method, the following filtering expression is used to derived the filtered quantity $\overline{f_i}$ from the unfiltered quantity f_i.

$$\overline{f_i} = \frac{3565}{10368} f_i + \frac{3091}{12960}\left(f_{i+1} - f_{i-1}\right) + \frac{1997}{25920}\left(f_{i+2} - f_{i-2}\right) + \frac{149}{12960}\left(f_{i+3} - f_{i-3}\right) + \frac{107}{103680}\left(f_{i+4} - f_{i-4}\right) \tag{4.48}$$

This is an 8th-order accurate filtering scheme and is applied at all interior points in the computational domain. Filtering is not performed at points near the boundary.

4.8 Boundary Conditions

The treatment of the boundary conditions in this study follows the formulation of Poinsot and Lele (1992). This formulation takes advantage of the hyperbolic nature of the Euler equations by considering the different characteristic waves crossing the boundary. Applying characteristic analysis to the Navier-Stokes equations using waves traveling in the x_1-direction gives the following expressions for the continuity, energy, and momentum conservation equations:

$$\frac{\partial \rho_k}{\partial t} + d_1^k + \frac{\partial m_2}{\partial x_2} + \frac{\partial m_3}{\partial x_3} = 0. \tag{4.49}$$

$$\frac{\partial \rho E}{\partial t} + \frac{1}{2}\left(u_l u_l\right)\sum_k d_1^k + \frac{d_2}{\kappa} + m_1 d_3 + m_2 d_4 + m_3 d_5 - \frac{1}{\kappa}\sum_k \chi_k d_1^k + \frac{\partial}{\partial x_2}\left[\left(\rho E + p\right)u_2\right] + \frac{\partial}{\partial x_3}\left[\left(\rho E + p\right)u_3\right] = \frac{\partial}{\partial x_i}\left(u_j \tau_{ij}\right) - \frac{\partial q_i}{\partial x_i}. \tag{4.50}$$

$$\frac{\partial m_1}{\partial t} + u_1 \sum_k d_1^k + \rho d_3 + \frac{\partial}{\partial x_2}\left(m_1 u_2\right) + \frac{\partial}{\partial x_3}\left(m_1 u_3\right) = \frac{\partial \tau_{1j}}{\partial x_j}. \tag{4.51}$$

$$\frac{\partial m_2}{\partial t} + u_2 \sum_k d_1^k + \rho d_4 + \frac{\partial}{\partial x_2}\left(m_2 u_2\right) + \frac{\partial}{\partial x_3}\left(m_2 u_3\right) + \frac{\partial p}{\partial x_2} = \frac{\partial \tau_{2j}}{\partial x_j}. \tag{4.52}$$

$$\frac{\partial m_3}{\partial t} + u_3 \sum_k d_1^k + \rho d_5 + \frac{\partial}{\partial x_2}\left(m_3 u_2\right) + \frac{\partial}{\partial x_3}\left(m_3 u_3\right) + \frac{\partial p}{\partial x_3} = \frac{\partial \tau_{3j}}{\partial x_j}. \tag{4.53}$$

In the above set of equations, p is the thermodynamic pressure, q_i is the heat flux along the i-direction, and the pressure derivatives κ and χ_κ are defined as

$$\kappa = \left(\frac{\partial p}{\partial \rho u_e}\right)_{\rho_k} = \frac{\sum_k \rho_k R_k}{\sum_k \rho_k c_{v,k}}, \tag{4.54}$$

and

$$\chi_k = \left(\frac{\partial p}{\partial \rho_k}\right)_{\rho e} = R_k T - \kappa u_e^k, \tag{4.55}$$

where u_e^k is the internal energy of the k^{th} species. The continuity, momentum, and energy equations from the characteristic wave analysis can be advanced in time to determine the boundary conditions at the next time step for the species densities ρ_k, the momentum densities m_i and the total energy density ρ_e provided the vector $\boldsymbol{d}$ is known. From the characteristic wave analysis, the vector $\boldsymbol{d}$ is given by

$$d_1^k = \frac{1}{c^2}\left[\Psi_2^k + \frac{Y_k}{2}\left(\Psi_5 + \Psi_1\right)\right] = \frac{\partial m_1}{\partial x_1}, \tag{4.56}$$

$$d_2 = \frac{1}{2}\left(\Psi_5 + \Psi_1\right) = u_1 \frac{\partial p}{\partial x_1} + \frac{\partial\left(c^2 m_1\right)}{\partial x_1}, \tag{4.57}$$

$$d_3 = \frac{1}{2\rho c}\left(\Psi_5 - \Psi_1\right) = u_1 \frac{\partial u_1}{\partial x_1} + \frac{1}{\rho}\frac{\partial p}{\partial x_1}, \tag{4.58}$$

$$d_4 = \Psi_3 = u_1 \frac{\partial u_2}{\partial x_1}, \tag{4.59}$$

$$d_5 = \Psi_4 = u_1 \frac{\partial u_3}{\partial x_1}, \tag{4.60}$$

where the amplitudes of five characteristic waves Ψ_1 to Ψ_5 must be calculated. Each wave has a characteristic velocity λ_1 to λ_5. As an example, for the *x*-direction which has a fluid velocity u , the five characteristic velocities are the velocity of sound waves moving in the negative *x*-direction (λ_1), the convection velocity or the speed of entropy waves (λ_2), the velocity of *v* advection (λ_3), the velocity of *w* advection (λ_4), and the velocity of sound waves moving in the positive *x*-direction (λ_5). The five characteristic velocities are

$$\lambda_1 = u_1 - c, \tag{4.61}$$

$$\lambda_2 = \lambda_3 = \lambda_4 = u_1, \tag{4.62}$$

and

$$\lambda_5 = u_1 + c, \tag{4.63}$$

where c is the frozen speed of sound. Expressions for the wave amplitudes are

$$\Psi_1 = \lambda_1 \left(\frac{\partial p}{\partial x_1} - \rho c \frac{\partial u_1}{\partial x_1} \right), \tag{4.64}$$

$$\Psi_2^k = \lambda_2 \left(c^2 \frac{\partial \rho_k}{\partial x_1} - Y_k \frac{\partial p}{\partial x_1} \right), \tag{4.65}$$

$$\Psi_3 = \lambda_3 \frac{\partial u_2}{\partial x_1}, \tag{4.66}$$

$$\Psi_4 = \lambda_4 \frac{\partial u_3}{\partial x_1}, \tag{4.67}$$

and

$$\Psi_5 = \lambda_5 \left(\frac{\partial p}{\partial x_1} + \rho c \frac{\partial u_1}{\partial x_1} \right). \tag{4.68}$$

4.8.1 Navier-Stokes Characteristic Boundary Conditions (NSCBC)

The characteristic amplitudes for waves traveling from the inside of the domain to the outside are computed using one-sided differences. Poinsot and Lele (1992) present a method for determining characteristic wave amplitudes at boundaries when they cannot be calculated from information at interior points. Their approach infers wave amplitudes determined from local one-dimensional inviscid relations (LODI). Neglecting the transverse and viscous terms in the conservation equations results in the local one-dimensional relations. These relations are not physical but should be viewed as compatibility conditions between choices made for the physical boundary conditions and the amplitudes of waves crossing the boundary, as also pointed out by Poinsot and Lele (1992). The conditions differ depending on the choice of variables, but one set are

$$\frac{\partial \rho}{\partial t} + \frac{1}{c^2}\left[\sum_n \Psi_2^k + \frac{1}{2}\left(\Psi_5 - \Psi_1\right)\right] = 0, \tag{4.69}$$

$$\frac{\partial p}{\partial t} + \frac{1}{2}\left(\Psi_5 + \Psi_1\right) = 0, \tag{4.70}$$

$$\frac{\partial u_1}{\partial t} + \frac{1}{2\rho c}\left(\Psi_5 - \Psi_1\right) = 0, \tag{4.71}$$

$$\frac{\partial u_2}{\partial t} + \Psi_3 = 0, \tag{4.72}$$

$$\frac{\partial u_3}{\partial t} + \Psi_4 = 0. \tag{4.73}$$

4.8.2 Subsonic Inflow Boundary

For subsonic inflow boundary, Eqs. (4.61) to (4.63) show that only λ_5 is negative whereas the other wave speeds are positive. This means that four waves are entering the

domain and one wave is exiting the domain. The amplitudes of the waves entering the domain can be determined using the prescribed boundary conditions, whereas the amplitude of the wave moving out of the domain has to determined based on the interior points according to Eq (4.64). The prescribed values of three velocity components, the species mass fractions and the temperature at the boundary are used to calculate the amplitude of the incoming waves based on Eqs (4.65) to (4.67). Once all of the characteristic wave amplitudes are determined, Eqs. (4.49) to (4.53) can be advanced in time to estimate the boundary conditions at the next time step. With the velocity vector and temperature specified, only Eq. (4.69) for the density needs to be used.

4.8.3 Supersonic Inflow Boundary

For a supersonic inflow boundary, Eqs. (4.61) to (4.63) show that all the wave speeds are positive and hence all the waves are entering the domain. Thus, the amplitudes of all the waves can be determined based on the prescribed quantities at the boundary. Thus, prescibing a boundary as a supersonic inflow boundary is the same as equating the values of all the variables at the boundary to be the prescribed boundary values.

4.8.4 Subsonic Non-reflecting Outflow Boundary

For a subsonic outflow boundary, Eqs. (4.61) to (4.63) again show that only λ_5 is negative whereas the other wave speeds are positive. Theoretical analysis for a subsonic outflow boundary condition requires one inviscid and four viscous conditions in order to be well-posed for the Navier-Stokes equations. Following Poinsot and Lele (1992), the conditions imposed are the pressure at infinity, and that the tangential stresses and normal

heat flux have zero spatial derivatives along the direction normal to the boundary. Since there are no variables specified on the boundary, the complete set of equations (4.49) to (4.53) must be advanced in time to determine the boundary conditions at the next time step. For the outflow boundary condition, the characteristic wave amplitudes for the entropy wave, the velocity advection waves, and the sound wave exiting the domain can be calculated using information at interior points according to equations (4.64) to (4.68). The only characteristic wave amplitude which requires external information is that corresponding to the sound waves entering the domain. A perfectly non-reflecting boundary would set the amplitude of these waves to zero. Poinsot and Lele show that this results in an ill-posed problem because the mean pressure for the flow is not determined. Instead, a partially nonreflecting boundary, or corrected non-reflecting boundary, is used. This boundary condition allows waves reflected from infinite external regions at a specified pressure to determine the mean pressure for the flow. The amplitude of the incoming characteristic wave determined as a function of the difference between the outlet pressure and the specified pressure at infinity is

$$\Psi_1 = K\left(p - p_\infty\right). \tag{4.74}$$

This wave will ensure that the outlet pressure remains close to the specified pressure at infinity and will regulate the mean pressure in the flow. The constant in Eq. (4.74) is

$$K = \sigma\left(1 - M^2\right)c / L, \tag{4.75}$$

where M is the maximum Mach number for the flow, L is a characteristic length, and σ is a constant. Poinsot and Lele indicate that a range of values for σ will produce acceptable results. Outside of that range, the boundary either causes oscillation because it is too

reflective or it fails to regulate the mean flow pressure because it is not reflective enough. Poinsot and Lele show reasonable results for a ducted shear layer using $\sigma = 0.25$, which is the value used in the present study. The characteristic lengths used for the outflow boundary conditions in the jet computations presented here are the entire axial domain length for the waves entering through the end outflow boundary, and the distance from the jet centerline to the wall for waves entering though the side boundaries.

4.9 Flow Perturbation

The random perturbation used to trigger transition to turbulence is that of Bogey et al. (2003). Rather than generating a random perturbation at the inlet, this method imposes a vortex ring in the jet shear layer a short distance into the domain. This method was proposed by Bogey et al. (2003) as a means to minimize acoustic waves produced by the perturbation. The vortex ring is located 0.4 jet diameters into the domain. The axial and radial velocity components of the vortex ring given by Bogey et al. (2003) are

$$U_{xo} = 2\frac{r_0}{r}\frac{r - r_0}{\Delta_0}\exp\left(-\ln(2)\left(\frac{\Delta(x,r)}{\Delta_0}\right)^2\right), \tag{4.76}$$

and

$$U_{ro} = -2\frac{r_0}{r}\frac{x - x_0}{\Delta_0}\exp\left(-\ln(2)\left(\frac{\Delta(x,r)}{\Delta_0}\right)^2\right), \tag{4.77}$$

where,

$$r = \sqrt{y^2 + z^2}, \tag{4.78}$$

and

$$\Delta\left(x,r\right)^2 = \left(x - x_0\right)^2 + \left(r - r_0\right)^2 . \tag{4.79}$$

The axial position of the vortex ring is defined based on the inlet jet radius as $x_0 = 0.8r_0$. Following Bogey et al. (2003), the vortex ring velocity is added to the flow field at each time step as an azimuthal function with ten modes. The axial and radial ring velocities are constructed according to

$$u_x = u_x + \sum_{n=0}^{9} C_B \varepsilon_n \cos\left(n\theta + \phi_n\right) U_{x0} U_j, \text{ and} \tag{4.80}$$

$$u_r = u_r + \sum_{n=0}^{9} C_B \varepsilon_n \cos\left(n\theta + \phi_n\right) U_{r0} U_j, \tag{4.81}$$

where U_j is taken to be the jet centerline velocity at the inlet. The variables ε_n and φ_n are uniform random numbers which are updated each time step. The random amplitude *n* e is restricted to be between -1 and 1 and the random phase *n* j is restricted to be between 0 and 2π. Again following Bogey et al, a value of 0.01 is used for C_B.

4.10 Code Parallelization and Scaling

FLEDS is written in Fortran 90 and parallelized using the MPI library. The FLEDS application has been ported and optimized to run efficiently on several platforms. Sayeed et al. (2011) analyzed the speedup of the code on the CRAY XT4 and IBM Blue GeneIP architectures and showed that FLEDS is highly scalable to up to 4096 processors. Recently, the scalability of FLEDS was also verified on Fujitsu and SGI architectures.

4.11 Summary

The formulation of the DNS and LES equations, the LES subgrid-scale models and a description of the numerical methods and boundary conditions are provided in this chapter. The code parallelization and scaling performance of the FLEDS code are also discussed. The next chapter presents results from LES of non-reacting n-heptane jets.

5 LARGE EDDY SIMULATION OF NON-REACTING JETS

5.1 Introduction

The FLEDS code will be employed to carry out LES of reacting jets to assess the capability of the unsteady flamelet progress variable (UFPV) model. Chapter 6 will discuss the results from the reacting jet simulations. In this chapter, results from LES of non-reacting jets will be presented and compared with experimental correlations. The objective is to assess the accuracy of the LES methodology described in Chapter 4. Section 5.2 discusses some of the challenges in the LES of diesel jets. Section 5.3 discusses results from a simulation of an isothermal non-reacting heptane jet with an inlet Reynolds number of about 60,000. The results from this simulation will be used to benchmark the LES code with experimental results for non-reacting round jets. In typical engine combustion systems, the fuel jet typically has a temperature lower than the ambient and the injection Reynolds number is much higher than 60,000. In Section 5.4, non-isothermal jets with jet diameter similar to that of a typical diesel injector, with inlet Reynolds numbers of 250,000 and 375,000 are simulated. The computed energy spectrum is discussed in Section 5.5. The chapter ends with summary and conclusions in Section 5.6.

5.2 Challenges in the LES of Diesel Jets – A Critical Discussion

Under diesel engine conditions, the maximum penetration of the liquid phase in the vaporizing diesel spray is found to be short compared to the overall spray penetration length. This is because of the rapid vaporization of the liquid sprays due to the entrainment of the hot ambient air into the spray (Siebers, 1998; Iyer et al., 2000). In fact, ignition and flame lift-off typically occur downstream of the maximum liquid penetration length. It has been shown conclusively that within the context of RANS simulations, diesel jets can be modeled as vapor jets (Abraham and Pickett, 2010). Within the RANS context, the turbulent jet structure is momentum-controlled and the turbulent diffusivity scales with the injection velocity and the jet half-width. It has also been shown that RANS simulations employing the standard k-ε model can predict the measured jet penetration within 10% and the spreading rate within 25% (Iyer and Abraham (1997, 2005); Bajaj et al., 2011). The diesel jet can be approximated as a vapor jet by assuming that the mass and momentum flow rates of the liquid and vapor jets are identical, i.e.,

$$\begin{aligned} \rho_v \left(\pi d_v^{\,2} / 4\right) V_v &= \rho_l \left(\pi d_l^{\,2} / 4\right) V_l, \\ \rho_v \left(\pi d_v^{\,2} / 4\right) V_v^{\,2} &= \rho_l \left(\pi d_l^{\,2} / 4\right) V_l^{\,2}. \end{aligned} \tag{5.1}$$

In the above equations, ρ, d and V represent the density, diameter and velocity and the subscripts, v and l represent the vapor jet and liquid jet respectively. This assumption leads to the following relations between the injection velocity and injector diameter of the two jets:

$$V_v = V_l,$$
$$d_v = d_l\left(\frac{\rho_l}{\rho_v}\right)^{1/2}. \tag{5.2}$$

Consider Case 1 of Table 3.1 in Chapter 3 with an injection velocity of approximately 630 m/s. For the liquid jet, using the properties of liquid n-heptane at 373 K, the injection Reynolds number, Re_{il}, is about 125,000. For the vapor jet, using the properties of vapor n-heptane at 370 K, the injection Reynolds number, Re_{iv}, is about 10^6. The injection Mach number (Ma) is about 3.0 for the vapor jet. The high Ma at the orifice and the reduction of this Ma to values much smaller downstream in the jet poses a numerical challenge when computing the vapor jet. Of course, treating the injected fluid as liquid introduces its own challenges. The high Re implies that the turbulent scales in the jet vary by 3 orders of magnitude because the Kolmogorov and integral scales are related by $Re^{3/4}$. If the turbulent length scales are to be captured down to the scales that are close to being isotropic, this would require grid sizes that are about 10 times the Kolmogorv scale (Pope, 2000). This suggests that the LES of Case 1 would require approximately 100 million grid points. If the numerical time step is selected to capture the acoustic waves, it would have to of the order of 1e-8 s. If the jet is computed for about 3 ms as was done in Chapter 3 with the RANS, it would require about 300,000 steps. Based on computations with FLEDS, the computational time required on 10,000 cores would be 2000 hours. When multi-step kinetics is included, the complexity increases dramatically.

There is also another interesting point that arises from the discussion above. The liquid and vapor jets are equated on the basis of mass and momentum flow rates, but this

does not preserve Re equality between the jets. This implies that the small-scale turbulent structures are likely to be different. That this difference does not influence the overall jet characteristics including lift-off and ignition delay, suggests that the overall structure of the reacting diesel jet is momentum controlled. The influence of sub-grid scale physics on trace species, e.g. NO, and soot precursors, may, however, not be independent.

5.3 LES of Re=60,000 Non-Reacting Jet

Initial LES simulations were performed for a round gaseous isothermal n-heptane jet issuing into a co-flow of air and transiently developing as opposed to the earlier steady-state simulations of Venugopal (2008) in a smaller domain. The jet diameter d is 1 mm and the Reynolds number based on d and the injection velocity U of 42.5 m/s is about 70,000. Gaseous n-heptane at 1000 K is injected into an ambient comprising 21% O2 and 79% N2 by mole fraction at 1000 K. A relatively small co-flow velocity of 0.425 m/s is employed. The computations are carried out on a 3-D stretched Cartesian grid in a domain measuring 50x25x25 in terms of jet exit diameters with 601x151x151 grid points. The grid spacing in terms of the nozzle diameter, D, is 0.08D in the axial direction and stretches from 0.035D at the axis to 0.57D at the side boundaries in the radial direction. Figure 5.1 shows the computational domain and the developing jet. With the exception of the inlet boundary which is a subsonic inflow condition, all of the domain boundaries are implemented as subsonic non-reflecting outflow conditions.

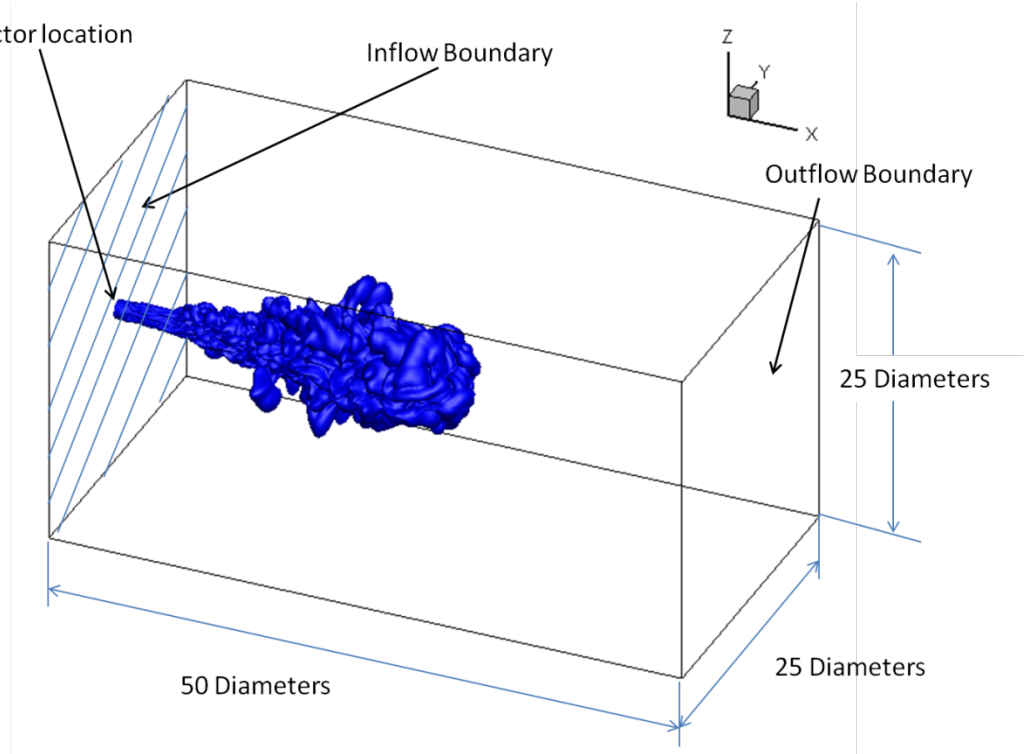

Figure 5.1. Computational domain for the isothermal jet.

Figure 5.2 shows the contours of the instantaneous mixture fraction field $\tilde{Z}$ on the central X-Y plane. Any axisymmetric round jet can be thought to be composed of 3 major regions (Fellouah et al., 2009) - the near-field (potential core) region, the intermediate-field region and the far-field (self-similar) region. Very close to the nozzle exit, the jet appears laminar, and there is minimal radial dispersion for the jet. This region is termed as the potential core region. Fiedler (1998) and Bogey *et al.* (2003) reports that the potential core is usually found in the region $0 \le x/D \le 6$. Figure 5.2 shows that in the present study, the potential core extends to an axial distance of x/D = 6, which is within the experimentally found range. The self-similar region, which is also called as the fully-developed region, is found to be located beyond x/D of 30. In this region, the velocity profiles are all self-similar. The region between the potential core and the fully-developed

regions is termed as the intermediate-field region. Figure 5.2 shows that the jet is still in the developing phase, as only the developing region of the jet, comprising of the near-field and intermediate field regions are evident.

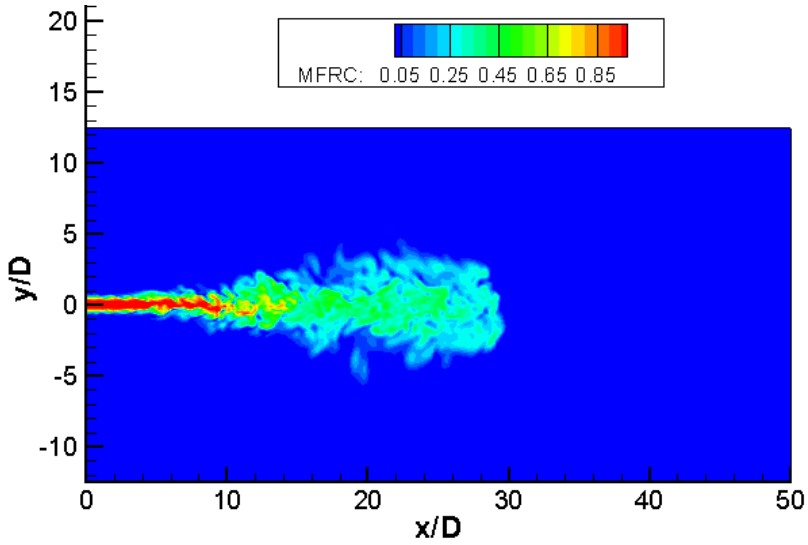

Figure 5.2. Contours of $\tilde{Z}$ in the central X-Y plane at t=2.2 ms after start of injection (ASI).

Figure 5.3 shows the transient development of the mixture fraction ($\tilde{Z}$) and vorticity (Ω) fields within the jet. The iso-contours of $\tilde{Z}$ 0.05 and Ω 10,000 s^{-1} are shown at 3 different times (0.3 ms, 1.0 ms and 2.0 ms). As was discussed in Section 4.7, in the present study, turbulence is induced in the flow by employing random vortex perturbations at a location close to the inlet boundary. At 0.3 ms, the jet seems completely undisturbed. A head vortex forms at the leading tip of the jet, which is generated by pressure difference at the tip as the jet penetrates. The vortical flow also results in entrainment of ambient air into the jet. As the jet penetrates into the domain, the induced disturbances grow in time and space, and the mixture fraction and vorticity

surfaces become highly wrinkled as shown in the figure (see figures at time of 1.0 ms and higher).

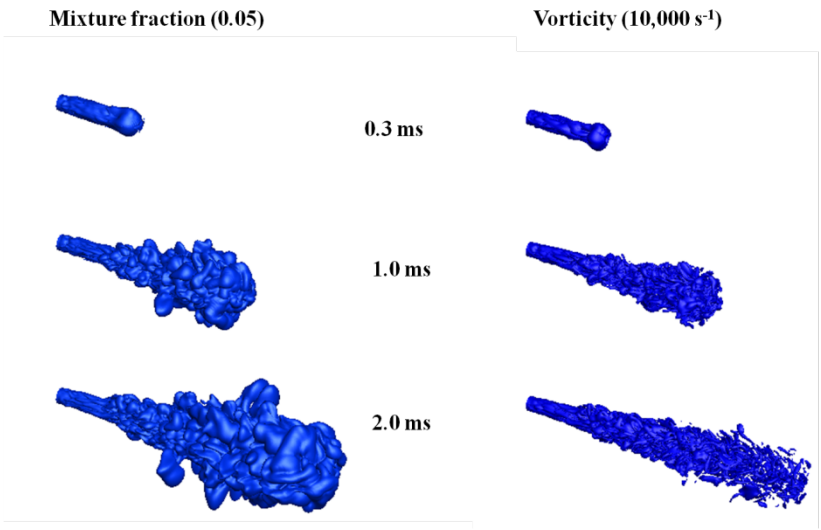

Figure 5.3. Iso-contours of mixture fraction and vorticity at 0.3 ms, 1.0 ms and 2.0 ms.

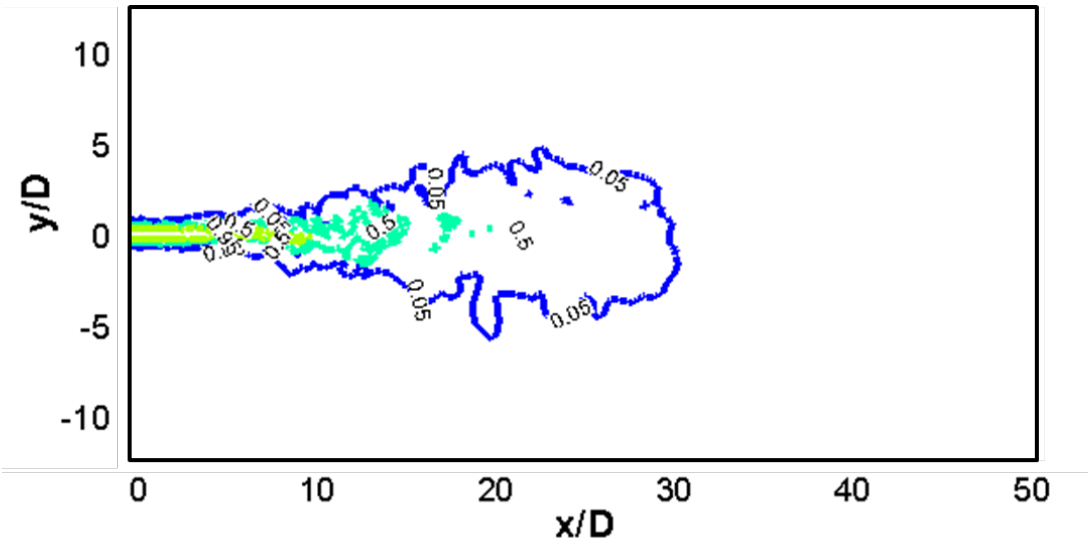

Figure 5.4. Instantaneous iso-contours of $\tilde{Z}$ in the central X-Y plane at 2.45 ms ASI.

Figure 5.4 shows three iso-contours of $\tilde{Z}$ field in the axial X-Y plane at 2.45 ms ASI. The $\tilde{Z}$= 0.05 contour appears significantly wrinkled in the figure. The potential core region (region where the $\tilde{Z}$ contours do not change significantly in the axial direction) is

observed to extend up to about 6 diameters. There is significant breakup of the jet beyond the initial 8 diameters.

An important variable in the modeling of turbulence/chemistry interactions in non-premixed combustion is the scalar dissipation rate χ (see discussion in Section 2.4). Recall that the χ is indirectly a measure of scalar gradients and of strain induced by turbulence. In RANS simulations, the mean χ is defined in terms of the turbulent kinetic energy and its dissipation through an empirical constant C_χ (Section 3.2). The reason for this definition is due to the inability of RANS simulations to resolve the gradients in mixture fraction field at the molecular scale. In the present study, the scalar dissipation rate is modeled as

$$\widetilde{\chi} = 2\left(D + D_t\right)\left|\nabla Z\right|^2, \tag{5.3}$$

where D is the molecular diffusivity of the mixture and D_t is the turbulent mass diffusivity of the mixture which is computed from the eddy viscosity ν_t and the turbulent Schmidt number Sc_t as

$$D_t = \frac{\nu_t}{Sc_t}. \tag{5.4}$$

Sc_t is assumed to be 0.9 in this study. ∇Z is computed from the resolved component of Z. The expression given in Eq. (5.3) above accounts for the effects of the sub-grid scales on χ but not for interactions between the resolved and the sub-grid (unresolved) scales of turbulent motion. Furthermore, ∇Z does not include the effects of small-scale turbulence. Figure 5.5 shows two iso-contours of the scalar dissipation rate χ = 50 s^{-1} and χ = 500 s^{-1} in the axial X-Y center plane. The figure shows that relatively high values of χ are

interspersed between relatively low values. Recall from the discussion in Chapter 3 that for n-heptane, χ of 50 s^{-1} is close to the ignition scalar dissipation rate and χ of 500 s^{-1} is close to the extinction scalar dissipation rate. The patchy distribution of the high χ highlights the possibility of local extinction at different points within the domain if a reacting simulation were to be carried out.

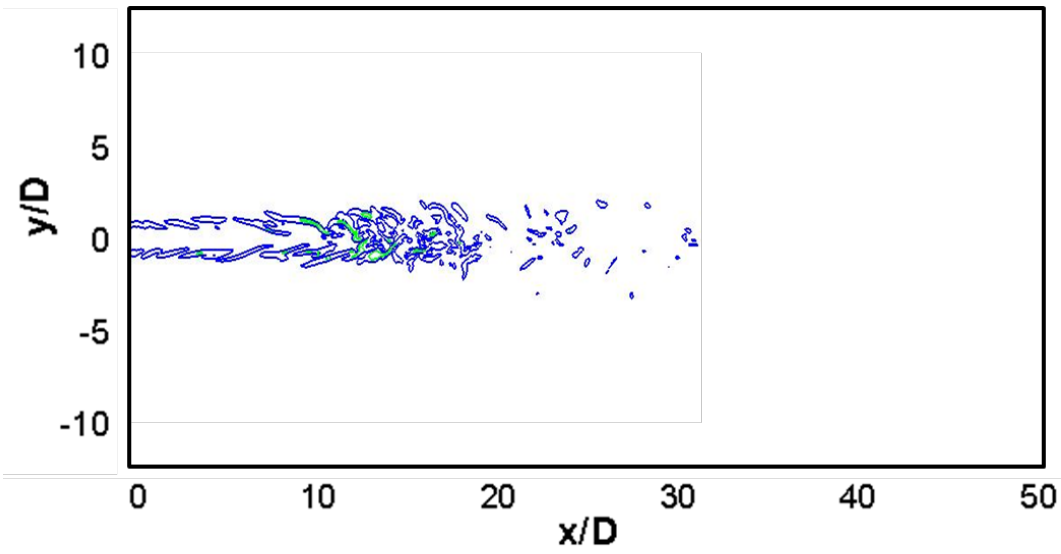

Figure 5.5. Instantaneous iso-contours of of χ in the central X-Y plane (Blue - scalar dissipation rate of 50 s^{-1} ; Green - scalar dissipation rate of 500 s^{-1}).

All the results presented until this point have been for the instantaneous fields of Z and χ. To compare these results with experimental observations in round jets, averaging of the instantaneous results have to be carried out because the experimental results are time-averaged. For a spatially inhomogeneous flow field, the two ways of averaging are ensemble averaging, in which averaging is done over multiple simulations performed with the same boundary and initial conditions, and time averaging, in which the averaging is done over time. Time averaging is the preferred way as it is

computationally infeasible to repeat the simulations multiple times to obtain the average. Time averaging is accurate only if the flow is statistically stationary. In the present study, time-averaged radial profiles of the axial velocity at different axial locations are computed by averaging the axial velocities azimuthally and in time. The averaging is done for a time duration of 0.05 ms. The results are shown in Fig. 5.6. Two sets of averaging are done - at 0.5 ms (from 0.475 to 0.525 ms) and at 1 ms (from 0.975 to 1.025 ms). Both results are shown in the figure. It can be seen from the figure that, as expected, the spreading of the jet increases along the axis. The fluctuations seen for the x/d=15 profile are thought to be because of the lack of statistics in the average. It is expected that if the averaging is done over a longer time, say 2.0 ms, the fluctuations will decrease.

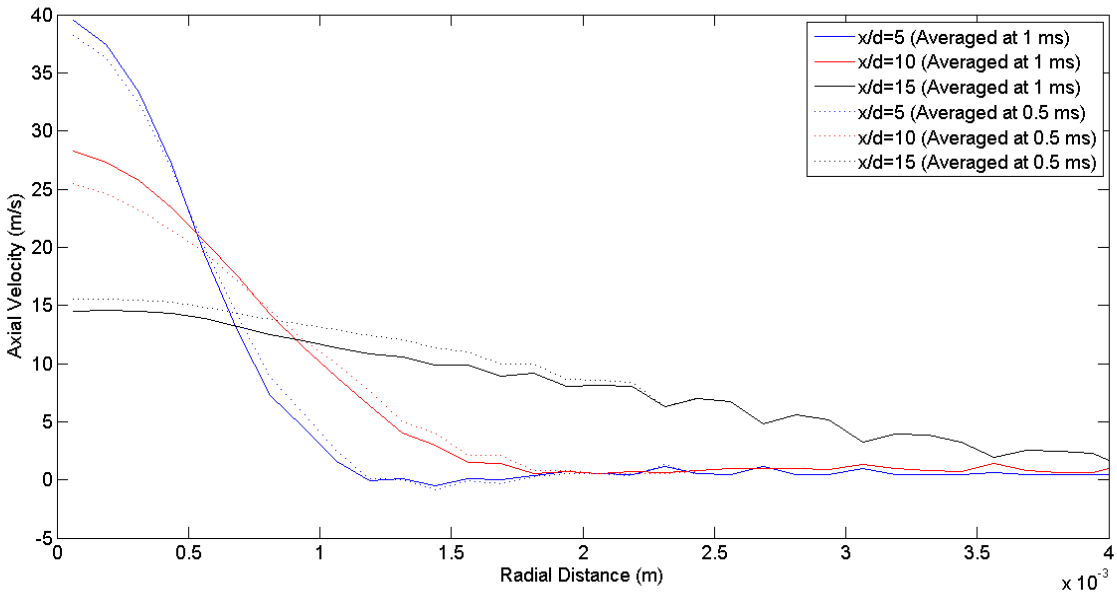

Figure 5.6. Time-averaged radial profiles of axial velocity at three different axial locations.

When the time-averaged radial velocities are scaled with the jet half-width, it is seen that the radial profiles collapse on top of each other, as shown in Fig. 5.7. This

figure also shows that the velocity profiles match closely with the experimental measurements of Hussein et al. (1994). Hussein et al. (1994) made hot-wire and laser doppler anemometry (LDA) velocity measurements for a turbulent jet of $Re=10^5$ exhausting into a large room.

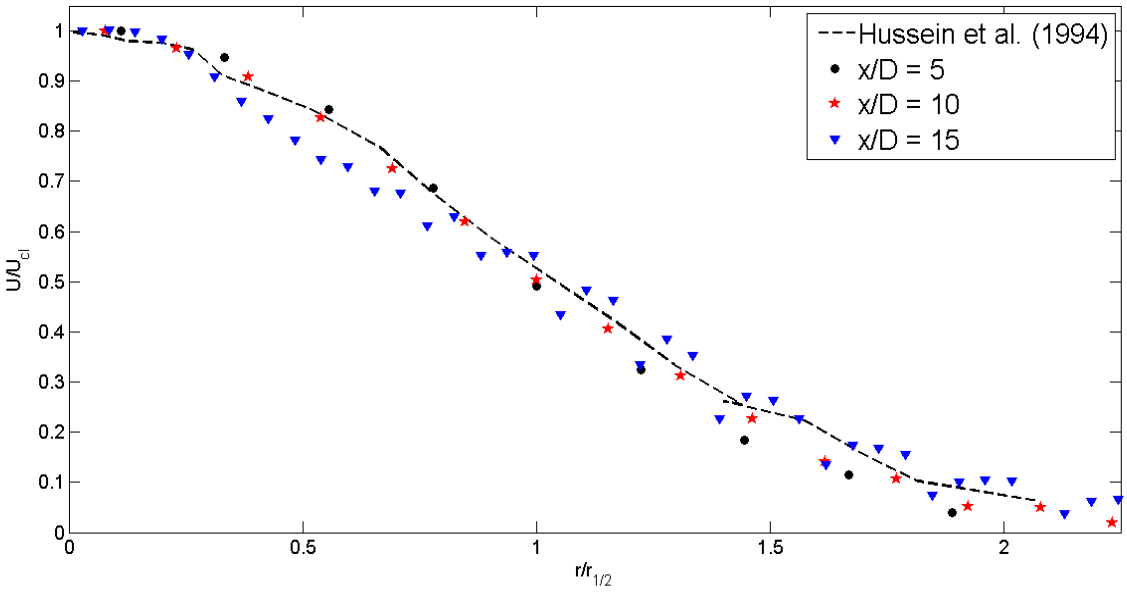

Figure 5.7. Computed and measured radial profiles of the axial velocity.

5.4 LES of Re=250,000 and 375,000, Non-Isothermal, Non-Reacting Jets

In the simulations discussed in the previous section, the injection velocity is a factor of 10 lower and the orifice diameter a factor of 5 higher than in typical engine combustion systems. Higher injection velocities make the flow more turbulent, and impact the small-scale structures and the spread of scales. Furthermore, the injected fuel and air are at different temperatures in combustion engines. The use of higher velocity and smaller orifice increases the computational overhead because of the need to capture

smaller turbulent length scales. In the simulations discussed below, n-heptane fuel at 373 K is injected into air at 1000 K and pressure of 40 bars with an inlet velocity of 150 m/s (corresponding to Re=250,000) and an inlet velocity of 250 m/s (corresponding to an Re=375,000) from an orifice of diameter 200 μm. The computations are performed in a three-dimensional domain which extended 150 diameters in the axial direction and 75 diameters in the radial direction. Recall that 50 diameters were considered in the last simulation. The computational grid consists of approximately 7.9 million grid points (350 x 150 x 150). The grid is stretched in both the axial and radial directions with the maximum resolution located along the jet centerline. Figure 5.8 shows a representation of the grid, with every third point shown. The grid spacing in the axial direction varies from 0.25 jet diameters near the inlet boundary to 0.50 jet diameters near the outlet boundary, and the grid spacing in the radial direction varies from approximately 0.10 jet diameters at the jet axis to 1.70 jet diameters at the side boundaries. The grid used in this section is coarser than the one used in the Section 5.3 due to the computational expense. Except for the inlet boundary, all of the domain boundaries are implemented as subsonic non-reflecting outflow conditions. The implementation details of these boundary conditions were discussed in Section 4.6. Due to the presence of the higher velocity, temperature, and density gradients, the Artificial Diffusivity Scheme (ADS) sub-grid scale model (Section 4.4), was employed to obtain stable results.

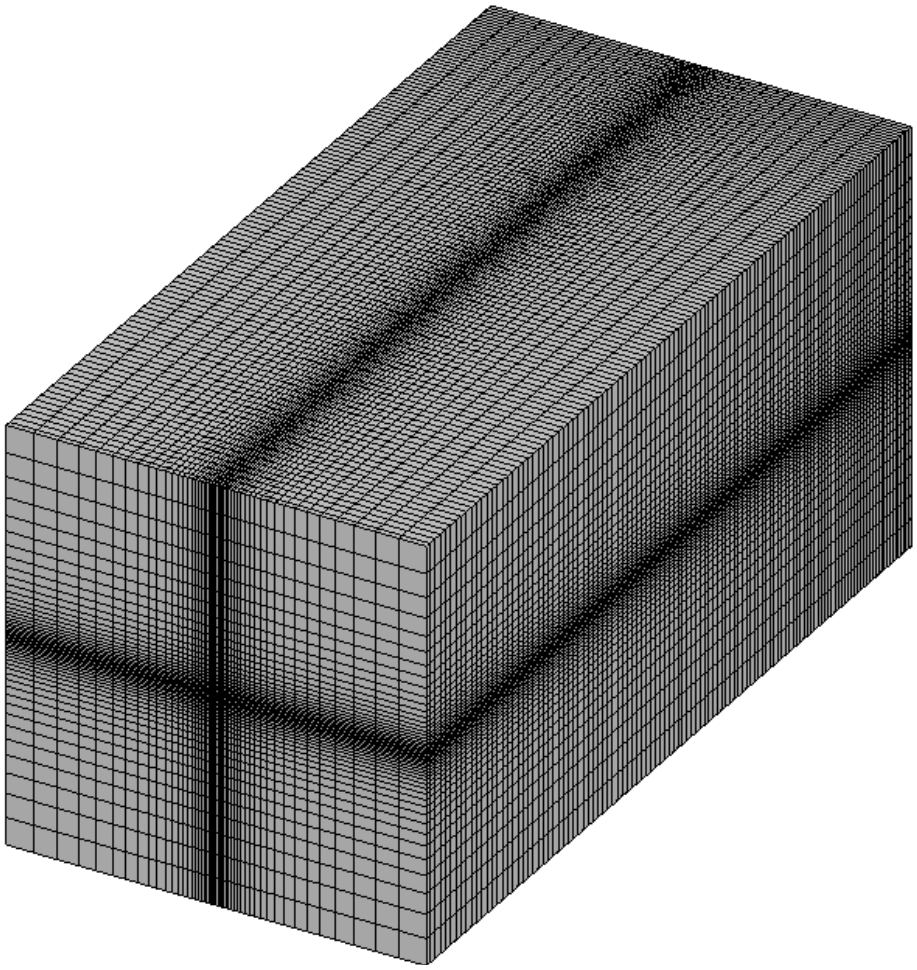

Figure 5.8. Computational grid used for LES computations with Re=250,000 and 375,000; every 3rd grid point is shown.

The instantaneous iso-surface of stoichiometric mixture fraction for this jet at 0.5 ms is shown in Fig. 5.9. The jet structure is very similar to that of the isothermal jet. The major features of the jet include a potential core region where the flow is approximately laminar, and formation, growth and eventual breakup of eddies. The potential core for this case is seen to extend approximately 25 diameters, as opposed to 8 diameters for the isothermal jet. The length of the potential core is found to be the same for both the inflow conditions (subsonic and supersonic). The reason for this difference is that the density ratio between the fuel and air for the non-isothermal jet is about 3 times higher than the

density ratio in the case of the isothermal jet. Experimental studies by Kyle and Srinivasan (1993) have shown that the length of the potential core increases as the density ratio between the jet and the ambient increases. Though their experiments were conducted for density ratios much lower than the ones employed in this study, the reason for the increased potential core length can be attributed to the higher density ratio.

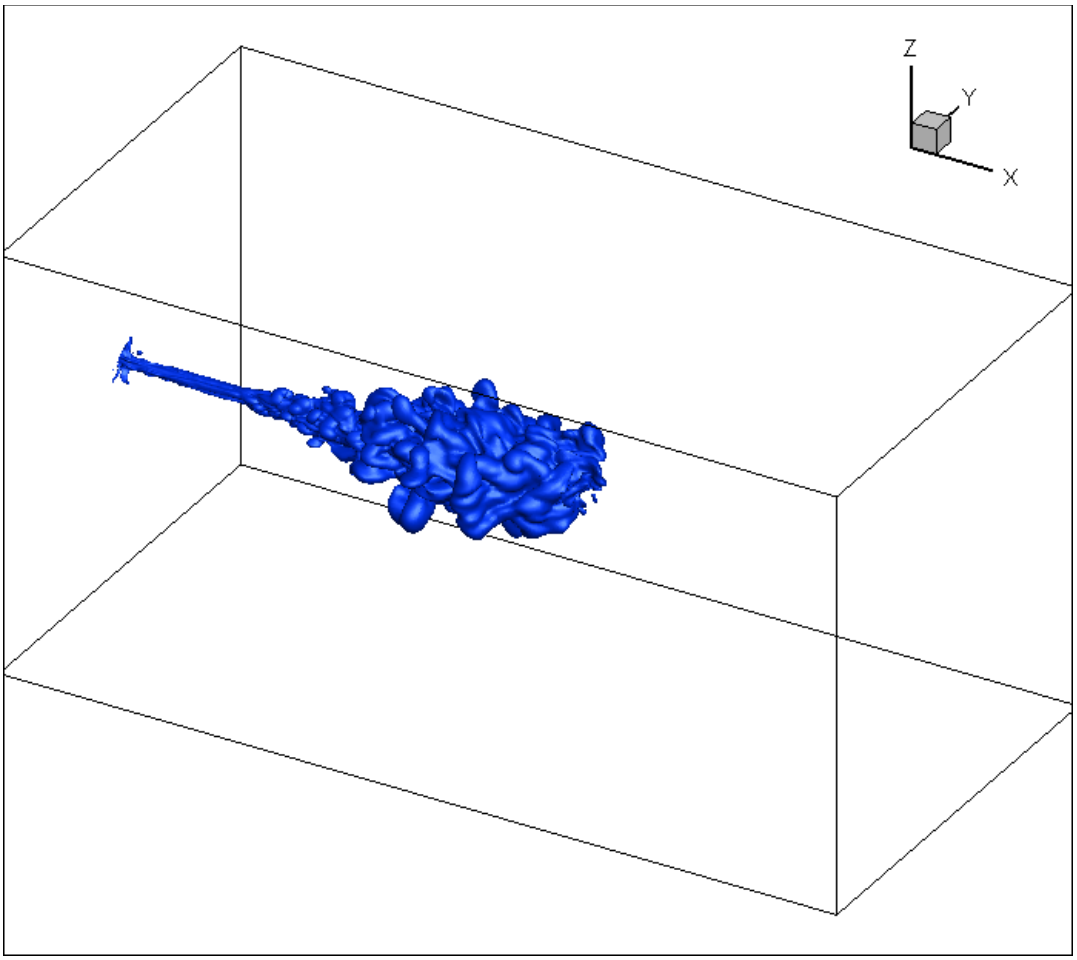

Figure 5.9. Mixture fraction iso-surface ($\widetilde{Z}$ = 0.062) at 0.5 ms.

Figure 5.10 shows the unsteady evolution of the mixture fraction contours ($\widetilde{Z}$) in the central X-Y plane at five different time instants for the subsonic inlet case. During the early injection period (t < 0.05 ms), the jet structure appears undisturbed. Similar to the

results presented in Section 5.3, a head vortex is visible at the edge of the jet in Fig 5.10(a). Figure 5.10(b) shows the early onset of turbulence. Large eddies have been generated towards the tips of the jet. These eddies grow and break up with time. Figures 5.10 (c) - (e) show the growth of the disturbances as time progresses. It can be seen that the range of length-scales found in the turbulent jet increases at longer times.

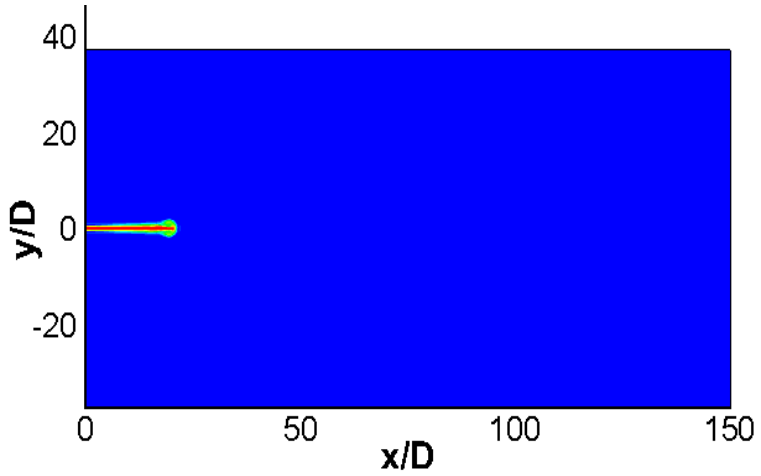

(a)

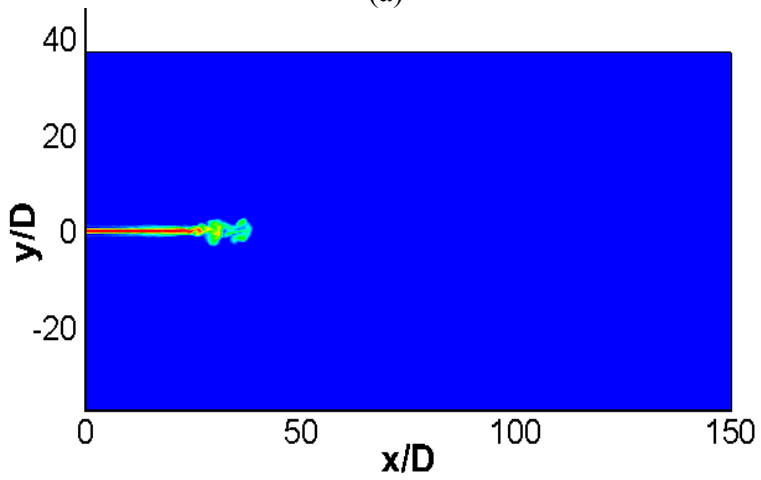

(b)

Figure 5.10. Mixture fraction contours at five time instants: (a) 0.05 ms, (b) 0.1 ms, (c) 0.2 ms, (d) 0.5 ms and (e) 1.0 ms.

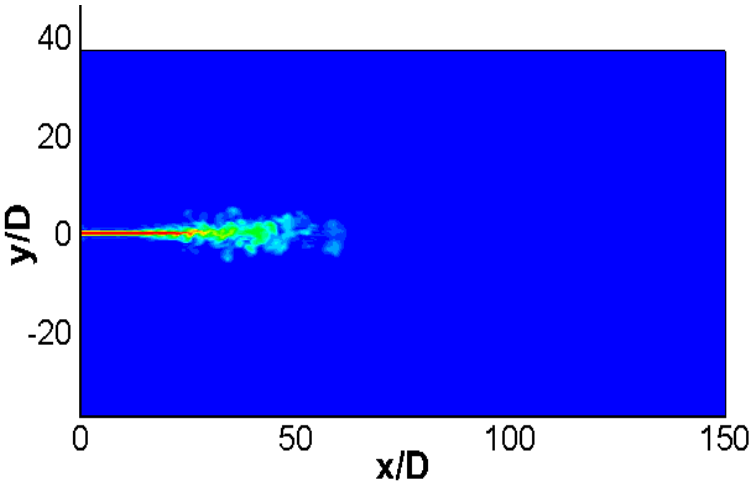

(c)

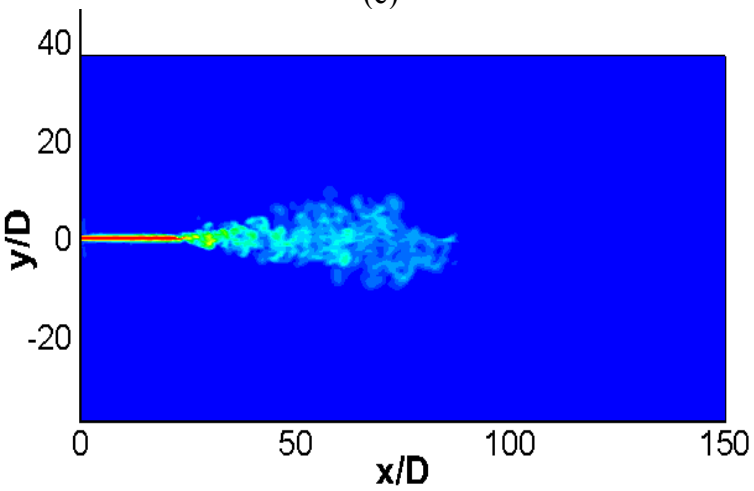

(d)

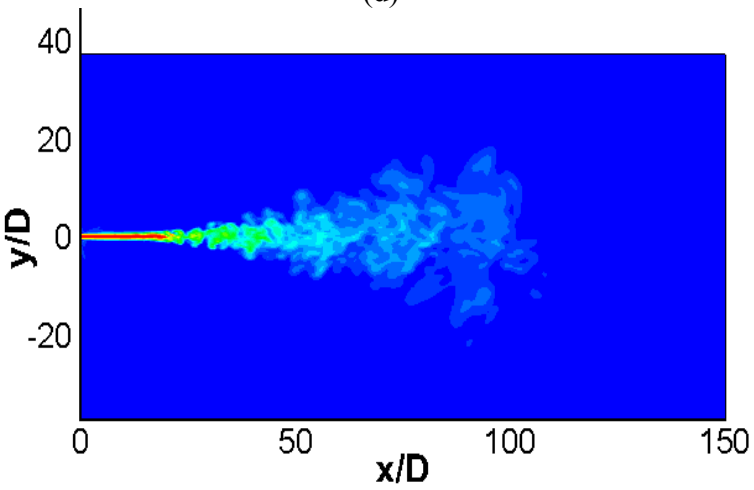

(e)

Figure 5.10. Contd.

The jet-tip penetration can be defined based on the axial variation of either the mixture fraction or the axial velocity. In this study, it is defined as the axial distance at which the instantaneous mixture fraction or the instantaneous axial velocity attains 40% of the steady-state value (Abraham, 1996; Iyer and Abraham, 1997). Figure 5.11 shows the computed penetration based on both these definitions for the subsonic case. The differences between the penetrations computed using the two definitions is not surprising. Recall from Sec. 4.5 that with the ADS model, the turbulent Prandtl number and turbulent Schmidt number are different from unity in regions of high gradients. As a result, momentum and scalar quantities diffuse at different rates. Also shown is the theoretical penetration obtained using incompressible gas jet theory employing the following expression for the jet tip penetration, x_{tip} (Abraham, 1996; Iyer and Abraham, 1997):

$$x_{tip}{}^2 = C_t d(\rho_l / \rho_\infty)^{0.5} U_i t. \tag{5.5}$$

In Eq. (5.5) d is the diameter of the jet, ρ_l and ρ_∞ are the densities of the jet and ambient, U_i is the jet velocity and C_t is an adjustable constant. In this study, the value of C_t is found to be 6.045 for best fit. This is comparable to the value of 5.796 reported by Bajaj et al (2011). It is seen that the computed penetrations based on either definition shows the expected trends with time. The mismatch with the theoretical correlation may arise from the fact that the jet-tip penetration is computed based on the instantaneous contours of the mixture fraction and the axial velocity. If time-averaged values are used, better match is expected. This would, however, require ensemble-averaging multiple simulations in this transient problem. Furthermore, the leading region of the jet may not

have reached quasi-steady state. Figure 5.12 shows similar results for the supersonic case. The trends are found to be similar for both these jets.

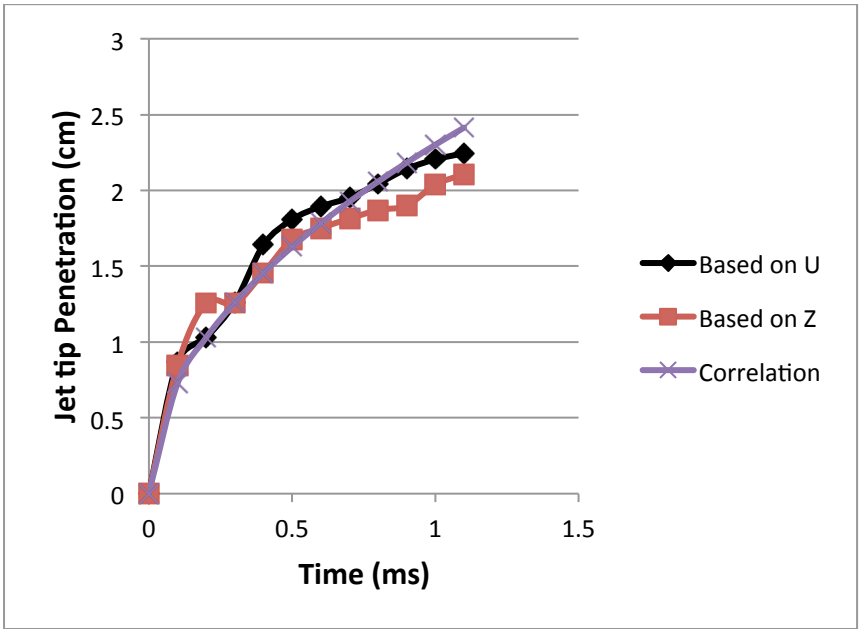

Figure 5.11. Jet-tip penetration as a function of time for the subsonic jet.

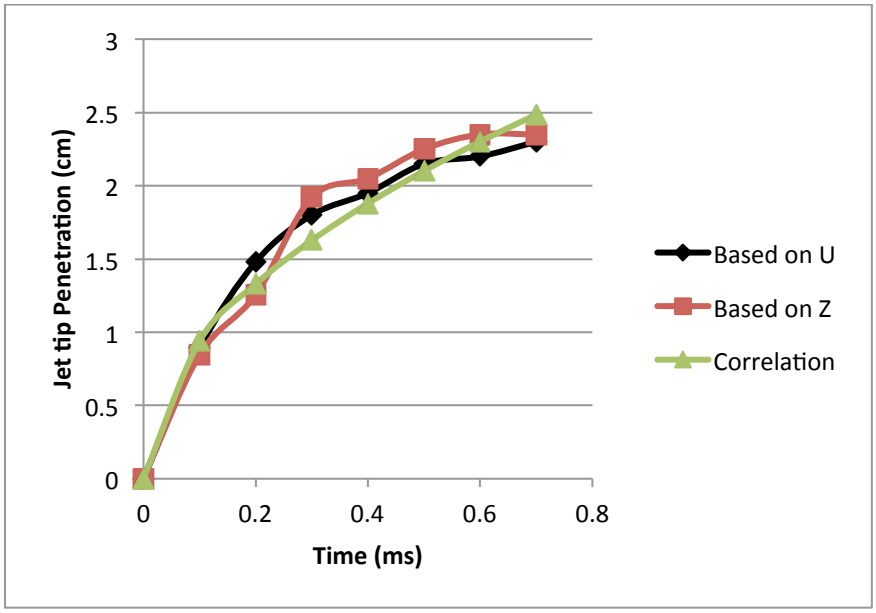

Figure 5.12. Jet-tip penetration as a function of time for the supersonic jet.

The jet half-width $R_{1/2}$ is defined as the radial distance at which the axial velocity attains 50% of the centerline velocity. Figure 5.13 shows the computed $R_{1/2}$ for the subsonic and supersonic jets. It has been shown through numerous experiments (Pope, 2000), that the jet half-width increases linearly with axial distance at a spreading rate in the range of 0.094 - 0.102 (Panchapakesan and Lumley, 1993; Hussein et al., 1994). The computed spreading rate for the jet half-width is 0.096 for the subsonic jet and 0.085 for the supersonic jet. It is seen that the computed spreading rate for the supersonic jet is slightly lower than the experimentally measured values. This is in agreement with the experimental results of Shadow et al. (1990) who showed that the spreading rates for circular jets reduced with increasing inlet Mach numbers for supersonic jets. This could have to do with the fact that the supersonic jet might require more time to become self-similar than the subsonic jet. Nevertheless, the qualitative trends for both the jets are within expected trends

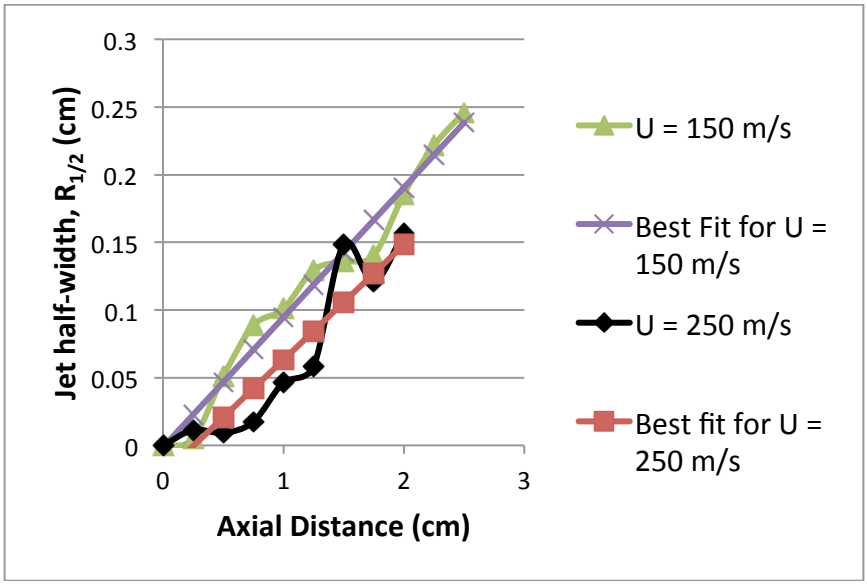

Figure 5.13. Variation of the jet half-width along the axis for the subsonic and supersonic jets.

5.5 Energy Spectrum

A useful method for determining the length scales resolved by any simulation is to determine the turbulent kinetic energy distributed among the eddies of different sizes. This can be performed by converting the results from the physical space to the wave number (spectral) space. The energy spectrum function is the spectral equivalent in the wave number space of the turbulent kinetic energy in the physical space. The method for determining the energy spectrum for homogeneous turbulence is discussed below.

To determine the spatial structures present in a flowfield, the statistical measure that is commonly used is the two-point, one-time auto-covariance, defined by

$$R_{ij}(\mathbf{r},\mathbf{x},t)=\left\langle u_i(\mathbf{x},t)u_j(\mathbf{x}+\mathbf{r},t)\right\rangle. \tag{5.6}$$

In Eq. (5.6), the angular brackets indicate ensemble averaging, and u_i and u_j are the velocity fluctuations. R_{ij}, which is also called as the two-point correlation, is a measure of how strongly the velocity fields at two points separated by a displacement **r** are correlated. Integral length scales can be defined from the two-point correlation as follows.

$$L_{11}(\mathbf{x},t)=\frac{1}{R_{11}(0,\mathbf{x},t)}\int_0^\infty R_{11}(\mathbf{e}_1 r,\mathbf{x},t)dr \tag{5.7}$$

Here, L_{11} is the integral length scale and $\mathbf{e}_1$ is the unit vector in the x direction. For homogeneous turbulence, the two-point correlation, $R_{ij}(\mathbf{r},t)$ is independent of the spatial coordinate, **x**, and the information it contains can be expressed in terms of the wave number spectra. The one-dimensional spectra $E_{ij}(\kappa_1)$ are defined to be twice the one-dimensional Fourier transform of $R_{ij}(\mathbf{e}_1 r_1)$:

$$E_{ij}(\kappa_1) = \frac{1}{\pi}\int_{-\infty}^{\infty} R_{ij}(\mathbf{e}_1 r_1) e^{-i\kappa_1 r_1}\, dr_1 . \tag{5.8}$$

For the diagonal components of the one-dimensional spectra, for eg., E_{11}, Eq. 5.8 can be rewritten as

$$E_{11}(\kappa_1) = \frac{2}{\pi}\int_{0}^{\infty} R_{11}(\mathbf{e}_1 r_1)\cos(\kappa_1 r_1) dr_1 . \tag{5.9}$$

Figure 5.14 shows the typical one-dimensional energy spectrum for isotropic homogeneous turbulence. According to Richardson's energy cascade hypothesis (Pope, 2000), the turbulence can be considered to be composed of eddies of different sizes. The larger eddies are unstable and break up, thus transferring their energies into smaller eddies. This process (energy cascade) continues until the eddies are sufficiently small that the molecular viscosity dissipate the eddies. Three major regions are visible in Fig. 5.14: the large scale energy-containing range, the intermediate scale inertial range, and the small-scale dissipation range. Kolmogorov stated that the statistics of the motion of inertial sub-range and dissipation sub-range are universal. He showed that the slope of the energy spectrum in the inertial sub-range is -5/3 for isotropic turbulence as indicated in Fig. 5.14.

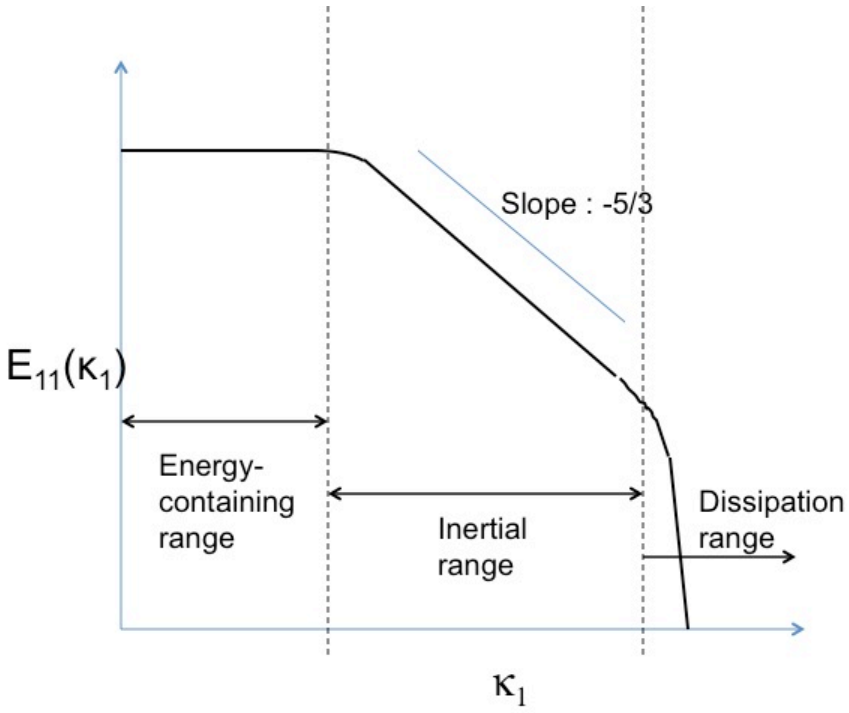

Figure 5.14. Typical turbulence energy spectrum for homogeneous isotropic flows.

Figure 5.15 is a sketch to illustrate how the energy spectrum resolved by an LES simulation would differ from the energy spectrum resolved by a DNS. Recall that the main motivation behind LES is to resolve the large energy-containing scales and model the smaller scales. Thus, as Fig 5.15 shows, the energy spectrum is not accurate at smaller scales, leading to a cutoff wave number κ_c. Above the cutoff wave number, the energy spectrum is not resolved.

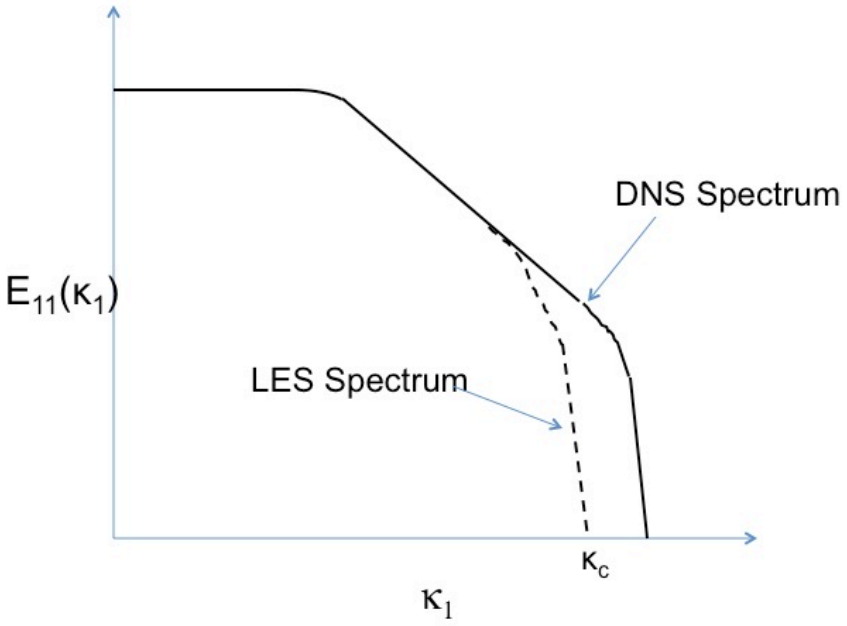

Figure 5.15. Illustration of turbulence energy spectrum resolved by DNS and LES.

Figure 5.16 shows the one-dimensional energy spectrum resolved by the LES for the non-isothermal jet with Ma = 0.8 at an axial location 40 diameters downstream of the inlet boundary. The general shape of the energy spectrum agrees with the expected trend of Fig. 5.15. It is also seen that at very small length scales, the energy spectrum behaves differently from the expected trend. This is because the LES results are not accurate below a cut-off length scale. This length scale is, of course, characterized by the grid size. The intermediate length scale where the energy transfer is dominated by the inertial transfer is characterized by a slope of -5/3 (Pope, 2000). This region is clearly visible in this figure. At smaller scales, the main mode of energy transfer is by viscous dissipation. The slope for this region is not universal, but is shown to be in the range between -3 and -7 (Pope, 2000). In the present study, the dissipation region is characterized by a slope of -5.5, which falls in this range. This shows that the LES model and the grid employed are

capable of resolving the large energy-containing scales, and the correct mode of energy transfer from the large to the small scales.

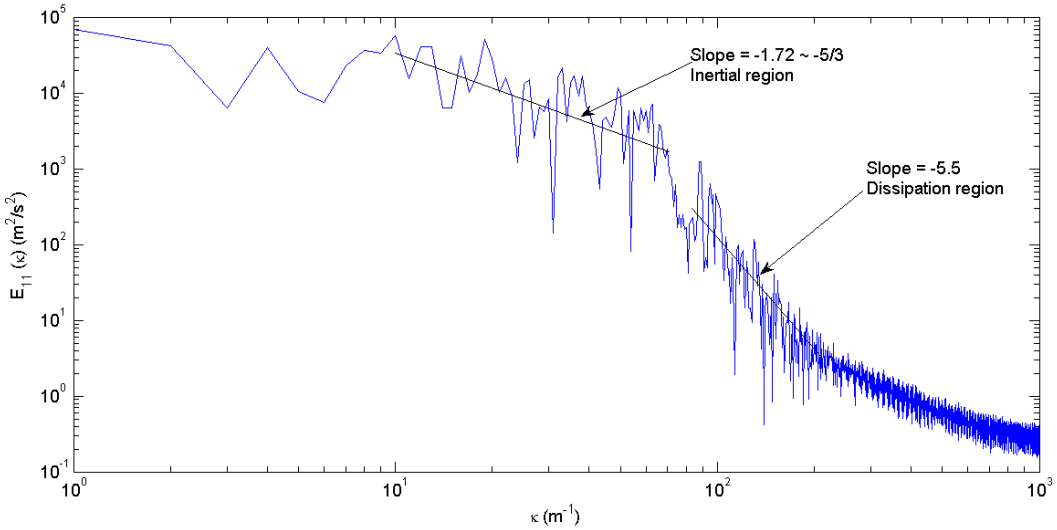

Figure 5.16. Energy spectrum for the non-isothermal jet with Ma = 0.8 at an axial location 40 diameters downstream of the inflow boundary.

5.6 Summary and Conclusions

The LES model described in Chapter 4 is applied in this work to compute non-reacting turbulent jets. Computed results from the simulation of an isothermal jet are compared with experimental and analytical results. It is shown that the computed and measured radial profiles of time-averaged velocities are within 10%. LES simulations were also performed for non-isothermal Re=250,000 and 375,000 jets with nozzle diameter of 200 microns. These jets are closer to diesel jets. It is shown that the tip penetration and dispersion of the jet predicted by LES are within 15% of measured values. The energy spectrum resolved by the LES code shows that the grid resolves 70% of the

total turbulent energy. These results are encouraging and suggest that the LES code can be employed for reacting jet simulations.

6 LARGE EDDY SIMULATION OF REACTING JETS

6.1 Introduction

In this chapter, LES of reacting turbulent jets are discussed. Detailed chemical kinetics is employed and the UFPV model discussed in Chapter 3 within the context of RANS simulations is employed to model the turbulence-chemistry interactions. One important objective is to assess the capability of the model to predict flame lift-off in jets and provide improved understanding of the physics which control lift-off. In Section 6.2, the major differences in the UFPV model implementation in LES from its implementation in RANS are discussed. Section 6.3 discusses the computational domain and numerical grid employed and presents details about the tabulation method adopted for the UFPV model implementation. Section 6.4 discusses the transient development of the flame predicted by LES. The phenomena of ignition, flame development and flame stabilization are examined in detail. In Section 6.5, the differences in jet structure predicted by the reacting and non-reacting simulations (presented in Chapter 5) are discussed. The lift-off height and flame stabilization mechanisms suggested by the LES results are compared with RANS simulation results in Section 6.6, and the reasons for the differences are examined. The chapter concludes in Section 6.7.

6.2 Implementation of the UFPV Model in LES

Section 3.2 discussed the physical understanding underpinning the UFPV model and described its implementation in the RANS code. As discussed in Chapter 4, one of the major differences between the equations solved in RANS simulations and LES is that in LES the equations are obtained by filtering out the smaller scales from the Navier-Stokes equations, whereas the RANS equations are obtained by an ensemble averaging. In LES, modeling is required to include the feedback effect of the smaller (unresolved) scales on the larger (resolved) scales, whereas in RANS the sum effect of all the scales on the mean variables are modeled. The modeling of turbulence-chemistry interactions, however, is similar for large-eddy and RANS simulations. Recall that in the flamelet regime of turbulent non-premixed combustion, i.e. the most prevalent regime of combustion under engine conditions, reactions occur on length and time scales that are shorter than the smallest turbulent scales, i.e. combustion occurs at scales smaller than the Kolmogorov scale (for that matter, what is commonly referred to as DNS usually does not resolve the combustion scales). These scales are not resolved in LES. So, the modeling of the effect of the smaller scales in LES on the flame adopts ideas similar to those in RANS simulations discussed in Section 3.2.

The primary difference in the implementation of the model is in the calculation of the scalar dissipation rate. In RANS simulations, the scalar dissipation rate is calculated based on an empirical correlation involving turbulent kinetic energy, its dissipation rate, and the variance of the mixture fraction (see Eq. (3.1) in Section 3.2) , whereas in LES the definition is not clear. It can be calculated based on the gradients of the resolved

mixture fraction field (see Eq. (5.3) in Section 5.3). Note that, in principle, what is required is the scalar dissipation rate that influences the flame structure. This will certainly include the effects of the larger (resolved) and smaller (modeled) gradients. So, estimating the scalar dissipation rate from the resolved scales alone is an assumption. The errors induced by this assumption need to be examined through DNS. In the present study, δ - PDFs are assumed for the 3 independent variables - mixture fraction Z, scalar dissipation rate χ_{st} and the progress variable C. This is not expected to significantly influence the results as the LES simulations resolve more of the flow field, thereby minimizing the impact of the PDFs on the results.

6.3 Computational Conditions

In the present study, LES are carried out of a jet generated by injecting n-heptane vapor at 373 K into air at 1000 K with a velocity of 150 m/s through an orifice diameter of 200 μm. The computational domain, grid and boundary conditions are the same as those for the non-reacting jet discussed in Section 5.4. The UFPV model is used as the turbulence-chemistry interaction model. A 37-species chemical reaction mechanism developed by Peters et al. (2002) is employed to generate the UFPV libraries. As discussed in Section 6.2, the reaction rates are tabulated as a function of 3 independent variables - mixture fraction Z, scalar dissipation rate χ_{st}, and the progress variable C. For the tabulation, 51 points are used in the Z coordinate, 10 points in χ_{st} coordinate and 21 points in the C coordinate. The accuracy of the resolution adopted has been assessed by

refining the number of points and repeating the computations. RANS simulations were also carried out for comparison with the LES results.

6.4 Results and Discussion

The LES of the jet was carried out until the lift-off height had reached a steady value. This time was found to be about 0.83 ms. Figures 6.1(a) - (f) show the transient evolution of the mixture fraction and temperature profiles for the jet in the central X-Y plane. The different stages of ignition, flame development and flame stabilization are evident in these figures. As the fuel is injected into the domain, it penetrates into the chamber while entraining the hot surrounding air. The mixing of the fuel and hot air leads is followed by the formation of reactive radicals and rise in temperature. The rates of chemical reactions depend primarily on the local pressure, temperature, strain rate and the mixture fraction. In this study, the ignition delay is defined as the first instant at which the maximum temperature in the domain exceeds 1500 K. It is found that for the present LES simulation, the ignition delay is about 0.28 ms.

Figure 6.1 (a) shows the mixture fraction and temperature profiles at a time of 0.29 ms. Ignition is noticeable at the leading edge of the jet. This ignition kernel grows with time as evident by comparing Fig. 6.1 (a) with Fig. 6.1 (b) at 0.33 ms. Meanwhile additional ignition at other points are noticeable at multiple spots in the jet. This is different from the RANS results where an ignition front propagates from the initial ignition location which appears in a rich mixture close to the leading tip toward the stoichiometric mixture fraction surface from where it propagates upstream (see

discussion in Section 3.4). In other words, multiple ignition locations were not observed in RANS. The conditions that favor ignition at multiple points will be discussed later in the section. These ignition kernels develop spatially in time, and then merge to form a continuous flame, as shown in Fig. 6.1 (e). The flame stabilizes at the lift-off location, as shown in Fig 6.1 (f). The lift-off height for this case is seen to be at the approximate axial distance of x/D = 40, i.e. 8 mm. There is no noticeable propagation of the flame upstream and the stabilization occurs at approximately the distance where the furthest upstream ignition occurs.

This flame development predicted by LES is seen to be different from that predicted by RANS in that flame propagation was evident in the RANS simulations. Recall from the discussion in Chapter 3 that the mechanism by which the flame stabilized was attributed to the quenching of ignition reactions at the lift-off height by local scalar dissipation rate which exceeded the ignition scalar dissipation rate. Figures 6.1 (c) to (e) also show the processes of local ignition and extinction at various locations *upstream* of the lift-off height. For example, it is seen that ignition occurs at an axial location of about 30D, but the local strain rates appear to extinguish the ignition kernels. This is discussed in more detail later in the section. It is also interesting to note that because the lift-off height is determined by the ignition scalar dissipation rate which is smaller than the extinction scalar dissipation rate, the likelihood of extinction downstream of the lift-off height where the scalar dissipation rate is smaller than the ignition limit, is small. This suggests that if the process of ignition and flame stabilization are modeled, the steady flamelet libraries alone can predict the combustion process downstream of the lift-off height.

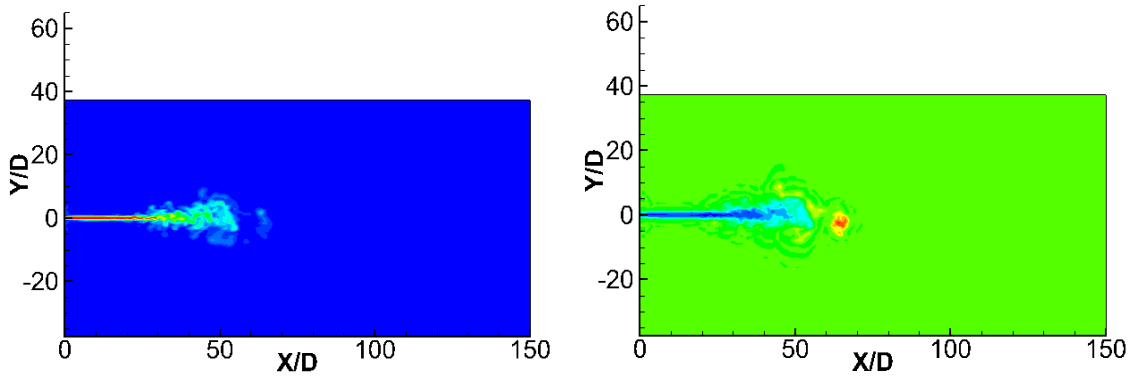

(a)

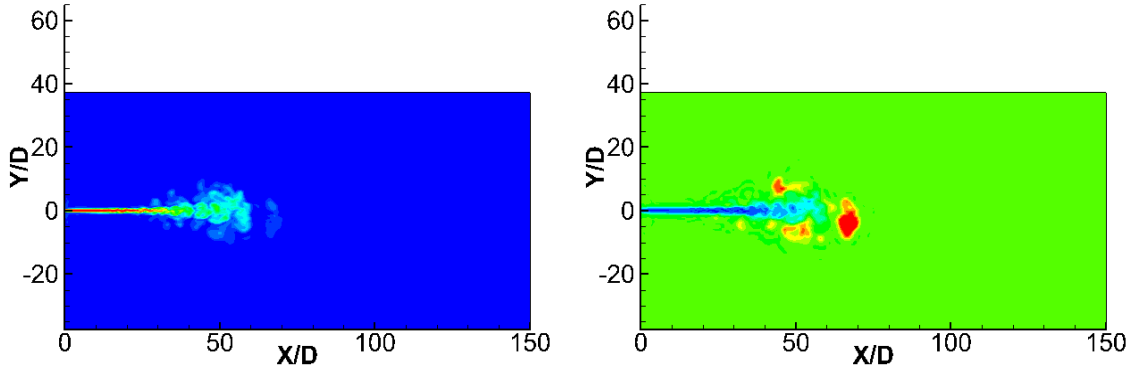

(b)

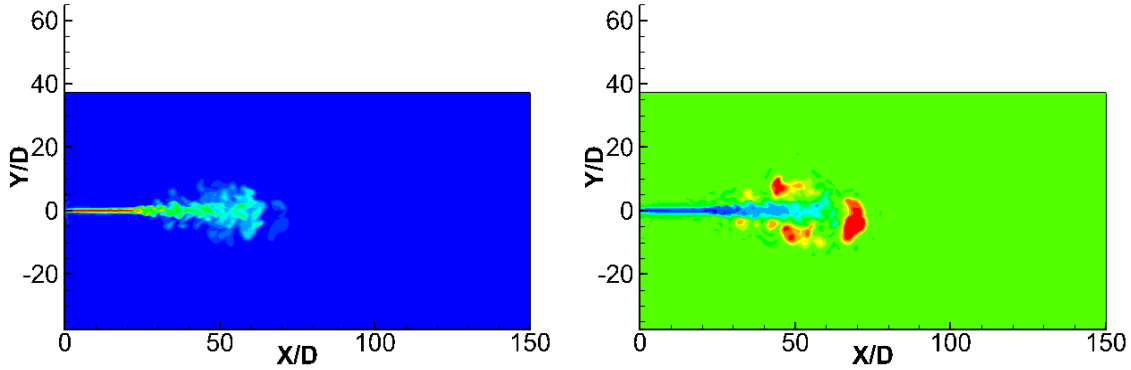

(c)

Figure 6.1. Transient evolution of the mixture fraction and temperature profiles in the central X-Y plane at (a) 0.29 ms, (b) 0.33 ms, (c) 0.36 ms, (d) 0.42 ms, (e) 0.59 ms and (f) 0.83 ms.

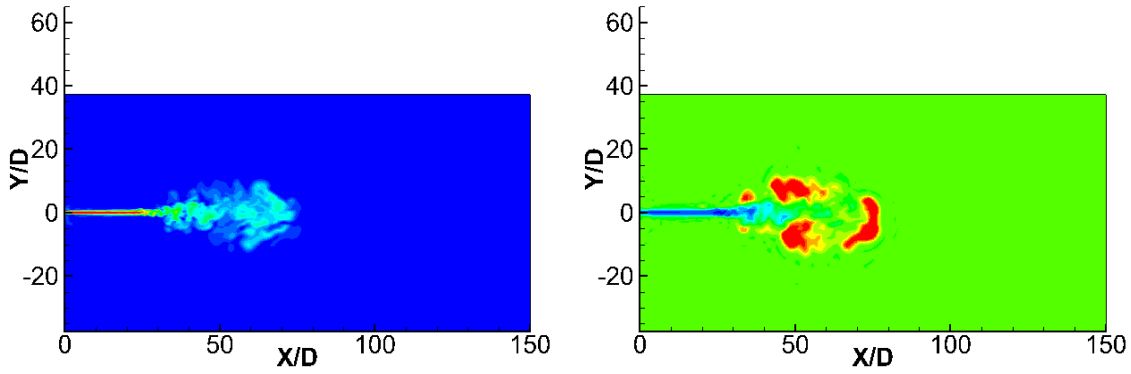

(d)

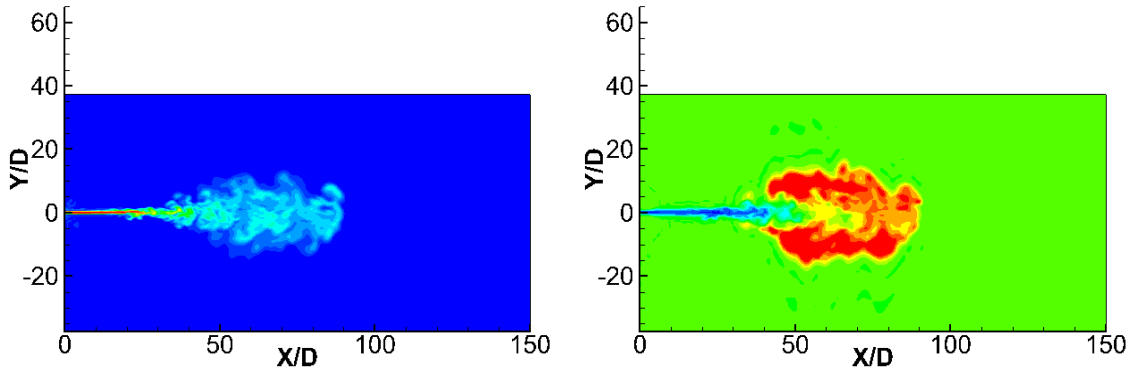

(e)

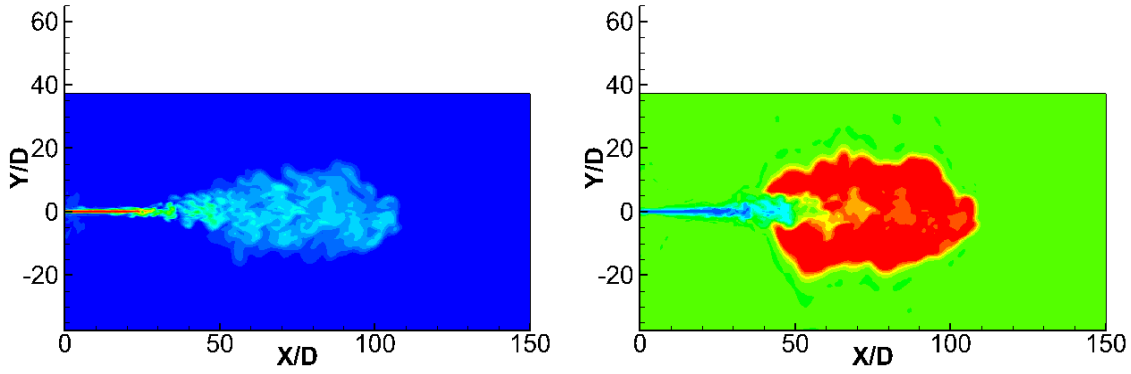

(f)

Figure 6.1. Contd.

The conditions that favor ignition will now be explored in greater detail. Figures 6.2 (a) - (c) show the scalar dissipation rate and mixture fraction values at three of the ignition locations. Also shown is the stoichiometric scalar dissipation rate χ_{st} which is calculated by assuming an error function profile for χ. Recall that χ_{st} is one of the parameters in the UFPV library. Not surprisingly, ignition occurs in slightly rich mixtures (Z~0.068-0.087) with χ_{st} less than the ignition strain rate (which for n-heptane is approximately 50 s^{-1}). This is consistent with the results from RANS in Chapter 3.

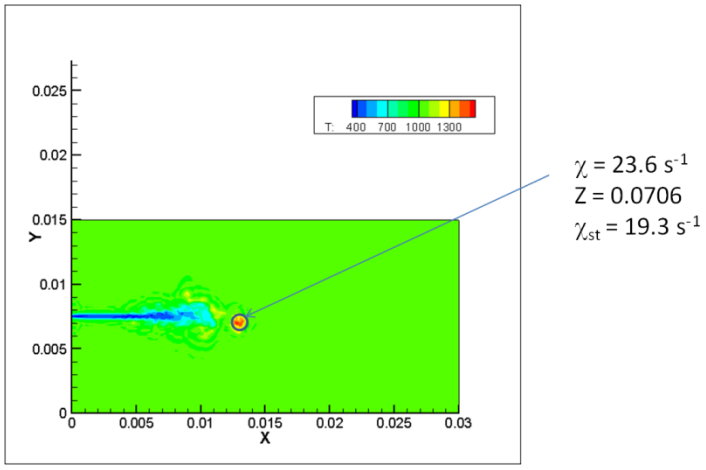

(a)

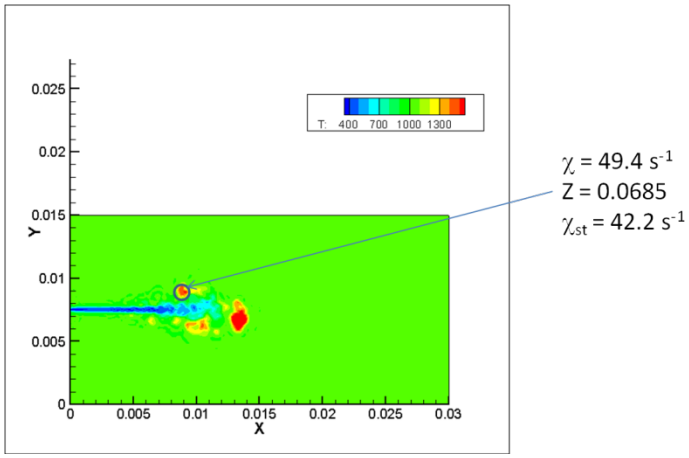

(b)

Figure 6.2. Ignition locations in the central X-Y plane.

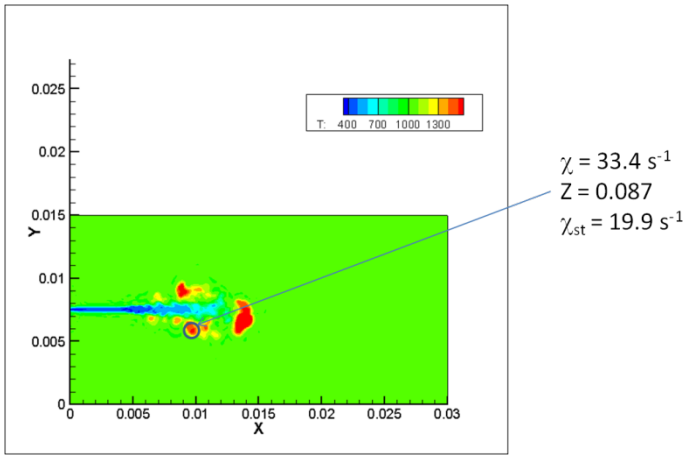

(c)

Figure 6.2. Contd.

More insight into the process of ignition can be gained by examining the T-Z and T-χ scatter plots during the process. Figure 6.3 shows the evolution of T-Z scatter plots at different stages of flame development. Figure 6.3 (a) shows the T-Z scatter at a time of 0.20 ms, i.e. before ignition. The distribution is along the trends expected for a mixing layer of fuel and air at different temperatures. Some of the scatter arises from the use of the ADS model for the subgrid scales. Recall from the discussion in Chapter 4 that the ADS model requires the specification of the turbulent Prandtl and Schmidt numbers at values different from unity in regions of large gradients. Figures 6.3 (b) and (c) show that ignition is initiated in a slightly rich mixture. With increasing time, the ignition location shifts from the rich mixture to an approximately stoichiometric mixture, as the peak temperature locations in Figs. 6.3 (d) and (e) show. This process of ignition front propagation is seen to be very similar to that in RANS (see discussion in Chapter 3).

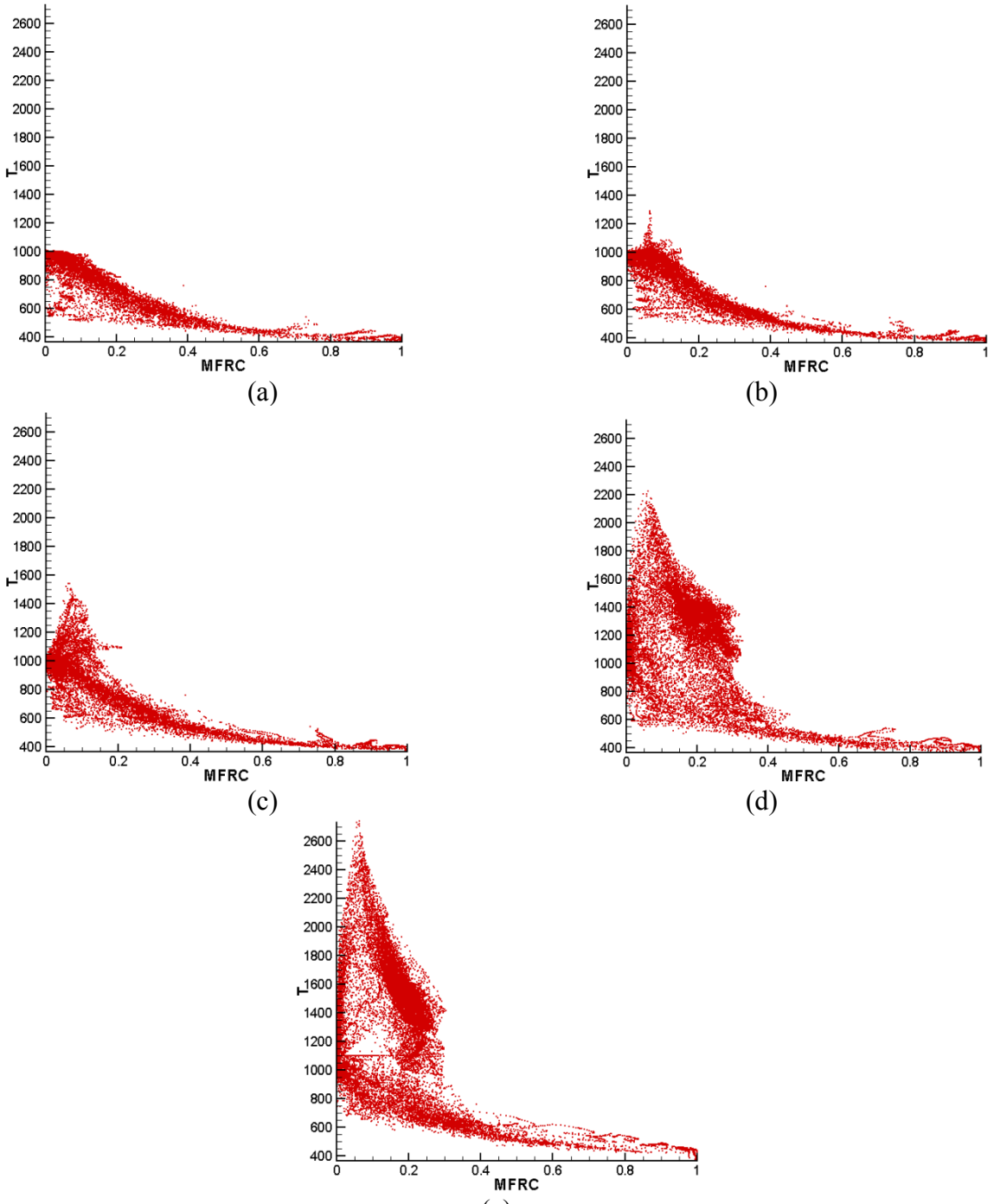

Figure 6.3. T-Z scatter at different stages of flame development (a) 0.20 ms, (b) 0.25 ms, (c) 0.29 ms, (d) 0.59 ms and (e) 0.83 ms (MFRC denotes Z).

Figure 6.4 shows the evolution of T-χ scatter plots at different stages of ignition. Note that values at all points in the domain are shown. Ignition starts to occur at locations where χ is low (< 100 s^{-1}). The temperature at these locations rises with time provided Z is at a suitable value, i.e. slightly rich. The temperatures at higher values of χ rise due to diffusion (see Fig. 6.4). It is also seen that at locations where χ is greater than 500 s^{-1}, the temperature never exceeds 1500 K. This rise in temperature suggests either a weakened flame or rise in temperature arising from heat diffusion alone.

When discussing the results of Figure 6.1, the occurrence of local extinction at locations upstream of the lift-off location was pointed out. Ignition occurs at locations upstream of the lift-off height, but the developing kernels are soon extinguished by the high strain. Figure 6.5 shows the flooded temperature contours and the iso-contour of scalar dissipation rate of value 500 s^{-1}, i.e. close to the extinction scalar dissipation rate of n-heptane, in the central X-Y plane at different time instants between the formation and extinction of these ignition kernels. The ignition kernels are circled in the figure. At t=0.53 ms, ignition kernels appear at an axial location of about 7 mm. As seen in Figure 6.5 (a), the iso-contour of extinction scalar dissipation rate (χ_e) is located close to the ignition kernel. Also note that this kernel is very close to the edge of the potential core of this jet. With increasing time, the turbulent velocity field causes the χ_e contour to start engulfing the ignition kernel as shown in Figs 6.9 (b) to (d). At a time of 0.545 ms, the ignition kernel is seen to be completely extinguished. To examine this phenomenon in greater detail, the T-χ scatter plots at locations close to the local extinction region are discussed next.

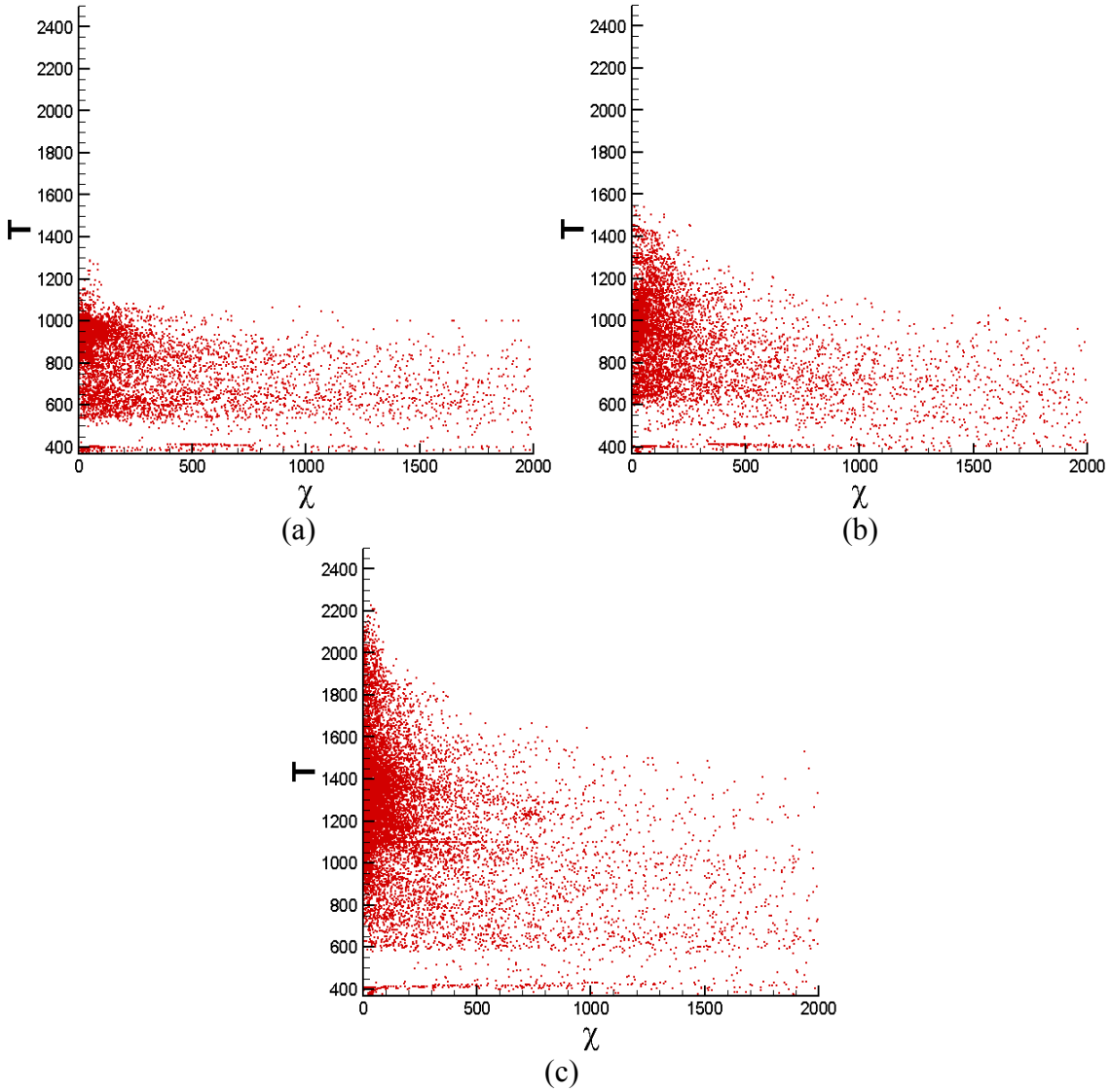

Figure 6.4. T-χ scatter at different stages of ignition (a) 0.25 ms, (b) 0.29 ms and (c) 0.59 ms.

Figure 6.6 shows T-χ scatter plots at axial distances between 6 mm and 8 mm, i.e. the region of interest in the discussion above. Figure 6.6 (a) shows that at 0.53 ms, the highest temperature is above 1600 K in the region where χ is less than the ignition scalar dissipation rate. With increasing time, the highest temperature occurs at higher χ

reflecting the engulfment of the ignition spot by the highly strained flow field. Eventually, the temperature decreases as the reactions are quenched. This discussion highlights the importance of unsteady effects in determining the ignition and extinction processes in the jet.

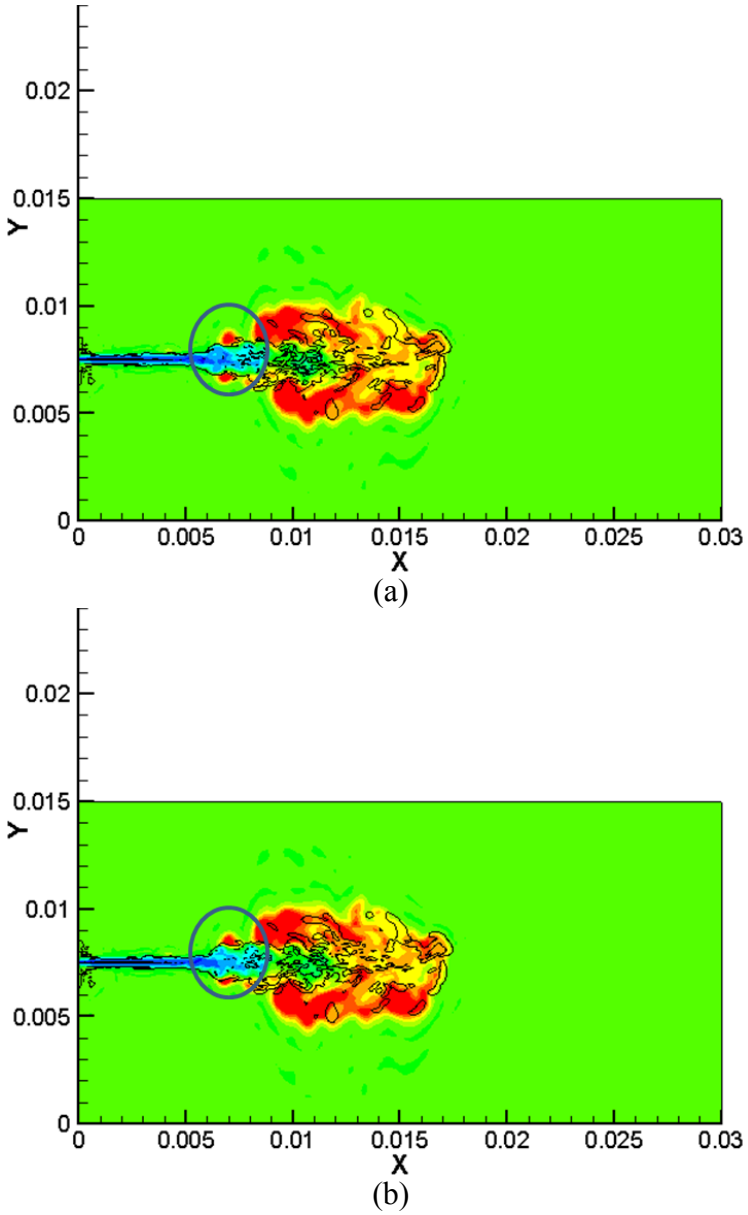

Figure 6.5. Local extinction of ignition spots at locations upstream of the lift off height (a) 0.53 ms, (b) 0.535 ms, (c) 0.54 ms and (d) 0.545 ms.

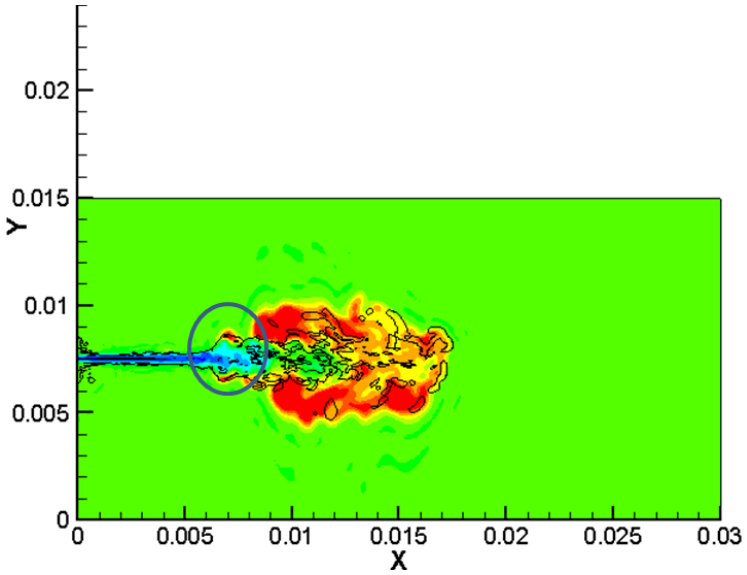

(c)

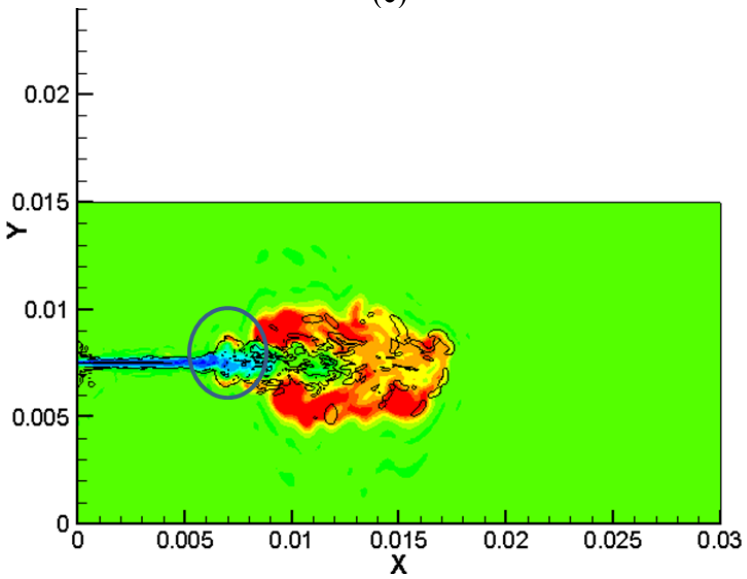

(d)

Figure 6.5. Contd.

It is interesting to examine the formation of product species during the combustion process. Figure 6.7 shows Y_{CO}-Z scatter plots at different times during the flame development. Figure 6.7 (a) shows that CO forms at a mixture fraction of approximately 0.1, i.e. in the rich mixture. As the ignition front and then the flame develop, CO continues to be observed at richer mixture fraction values (Figs. 6.7 (b) -

(d)). Figure 6.8 shows the flooded contours of the CO mass fractions at the final time of 0.83 ms. Figure 6.9 shows the Y_{CO}-T scatter plot at a time of 0.83 ms. It is seen that the peak values of CO are located at regions where temperature lies between 800 and 1800 K.

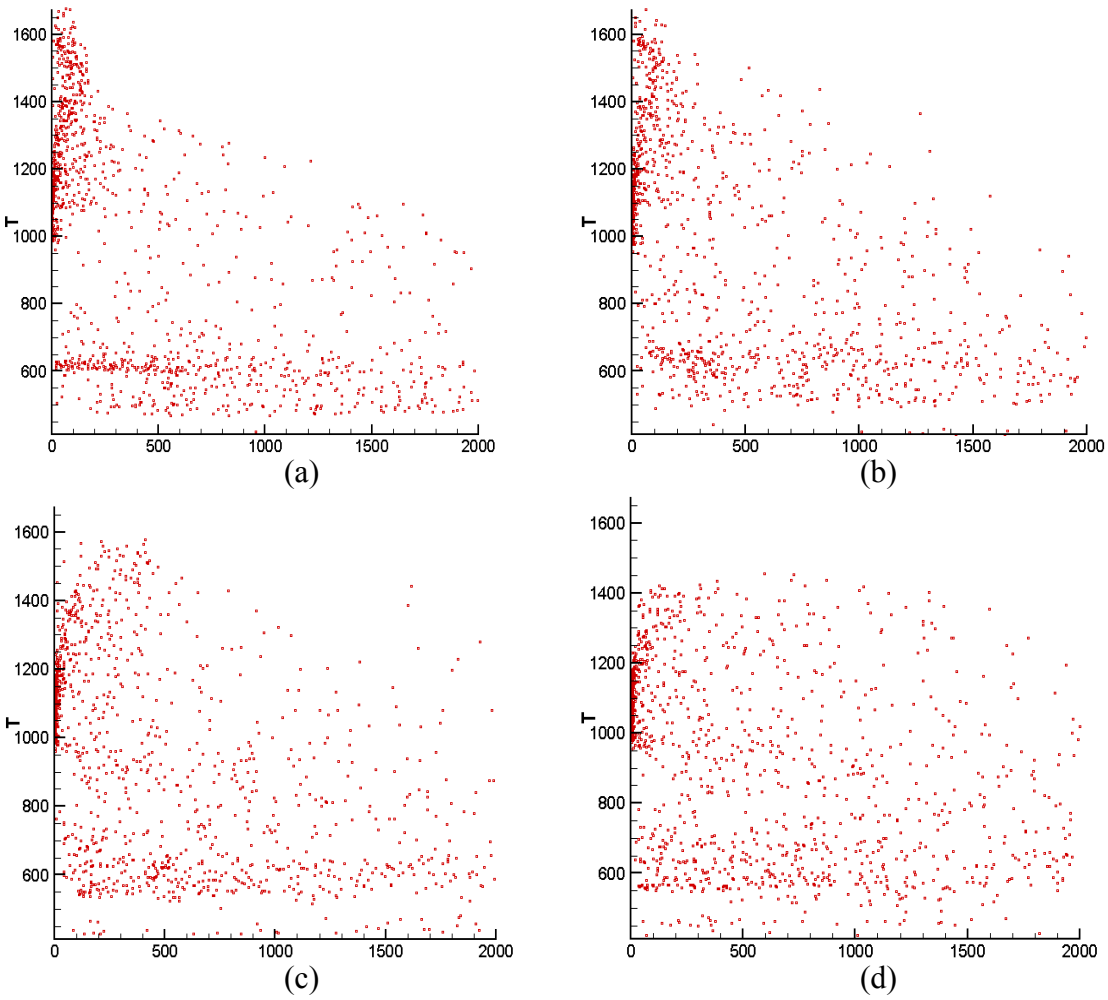

Figure 6.6. T-χ scatter at locations close to the region of local extinction at (a) 0.53 ms, (b) 0.535 ms, (c) 0.54 ms and (d) 0.545 ms.

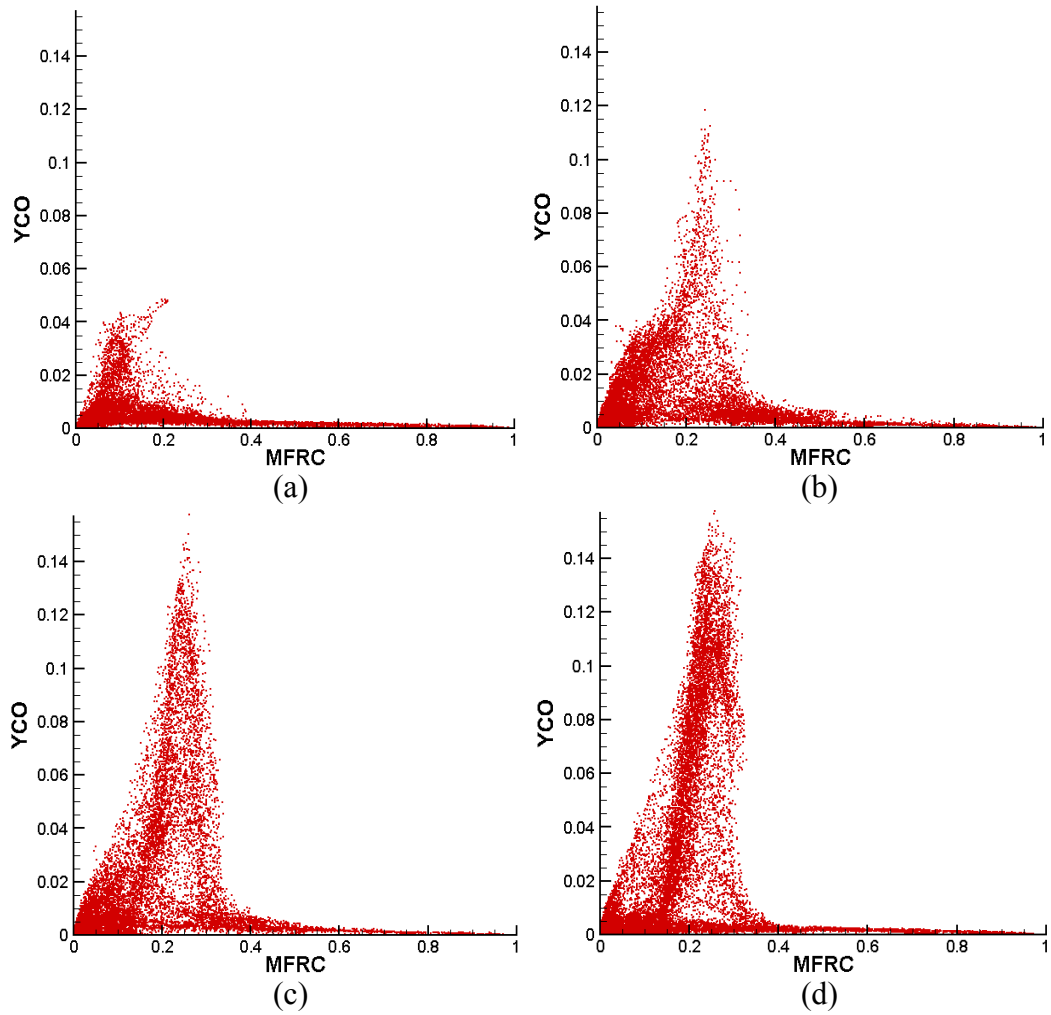

Figure 6.7. Y_{CO}-Z scatter at different stages of flame development (a) 0.29 ms, (b) 0.36 ms, (c) 0.42 ms and (d) 0.59 ms.

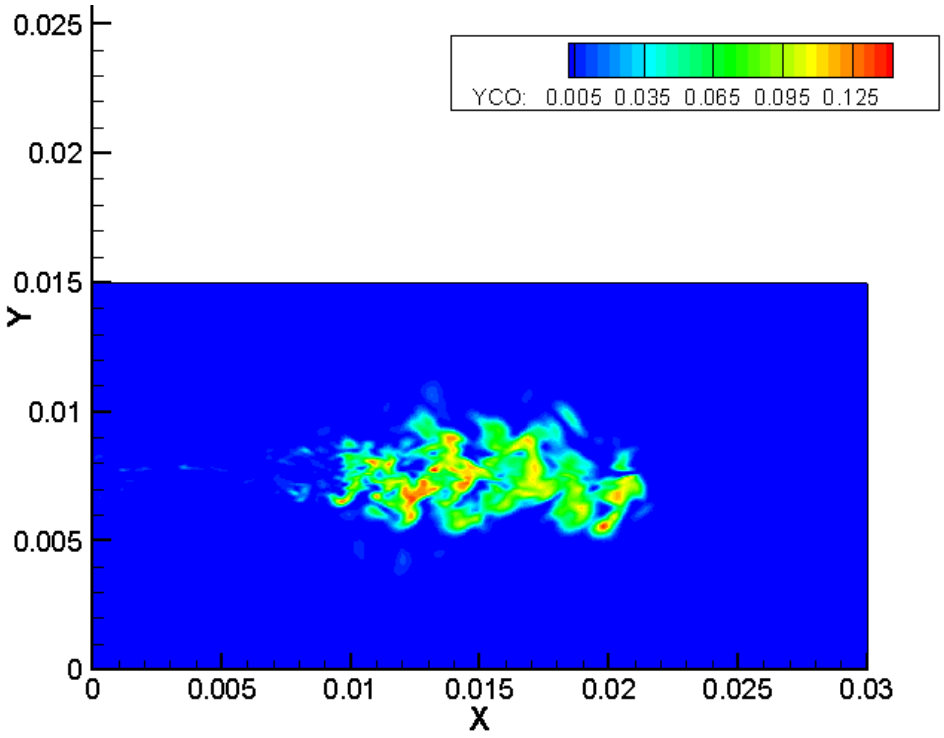

Figure 6.8. Distribution of Y_{CO} in the central X-Y plane at 0.83 ms ASI.

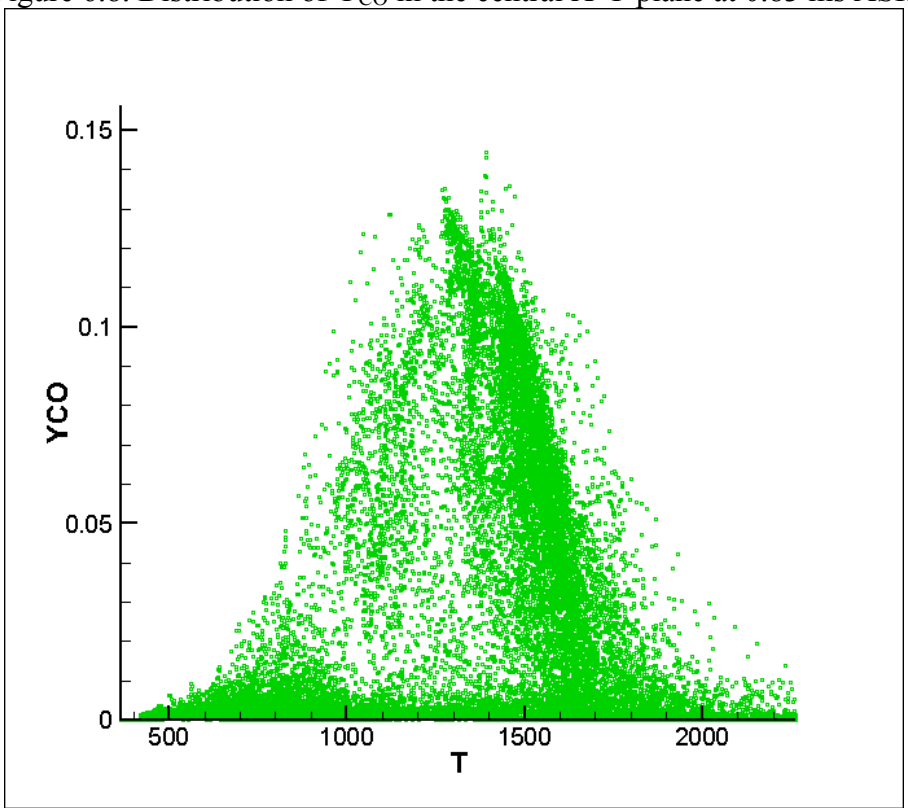

Figure 6.9. Y_{CO} - T scatter at a time of 0.83 ms.

6.5 Comparison Between Reacting and Non-Reacting Results

In this section, the effects of chemical reactions on the jet structure are examined. Figure 6.10 compares the mixture fraction profiles in the central X-Y plane at the same physical time of 0.55 ms. The top half shows the profile from the non-reacting case and the bottom half from the reacting case. There are some noticeable differences, especially in the dispersion of the jet. The half-width for the reacting jet appears to be greater than for the non-reacting jet. This is expected as the rise in temperature can result in thermal expansion. Some of the differences arise from the fact that the comparison is done between instantaneous profiles. It may be easier to draw conclusions between ensemble-averaged profiles.

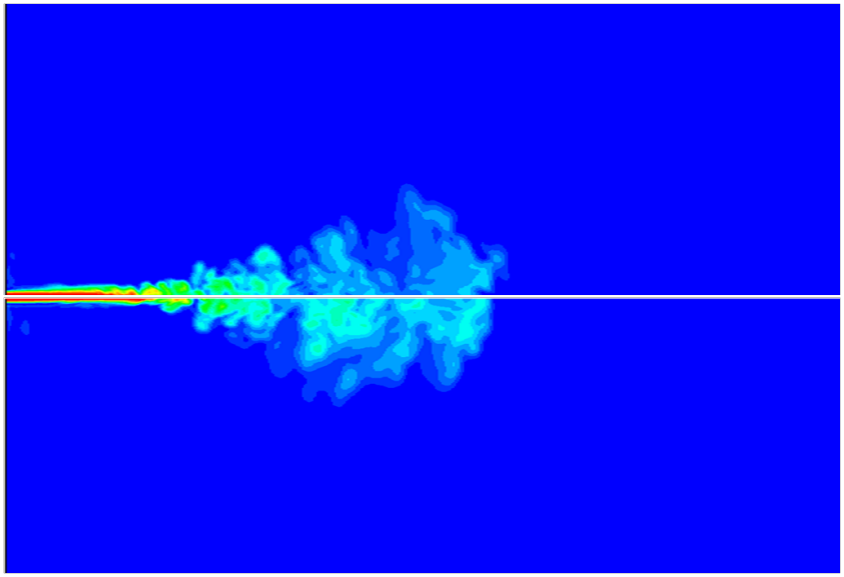

Figure 6.10. Contours of Z from the non-reacting and reacting simulations (Top half: non-reacting simulation; Bottom half: reacting simulation).

Another important parameter which determines the structure of the reacting jet is the distribution of the scalar dissipation rate. Recall that the scalar dissipation rate is an

important variable in the UFPV turbulence/chemistry interaction model. Figure 6.11 compares the iso-contours of the scalar dissipation rate in the central X-Y plane between the non-reacting and reacting jets. The iso-contours shown are for χ of 5, 50 and 500 /s. The top half shows the non-reacting results and the bottom half shows the reacting results. Focusing on the reacting jet, it is seen that large values of χ are interspersed within lower values of χ. It is also seen that qualitatively both the reacting and non-reacting jets show very similar distribution in χ. Figure 6.12 shows the radial distribution of χ at an axial location of 60D. It is seen that the reacting jet shows significantly larger values of χ compared to the non-reacting jet. Recall from the definition of χ that it depends directly on the mixture diffusivity and the mixture fraction gradient. Increase in temperature leads to an increase in diffusivity and hence an increase in χ. The heat release can also increase the mixture fraction gradients, which can again lead to an increase in the scalar dissipation rate. This behavior needs to be examined more closely.

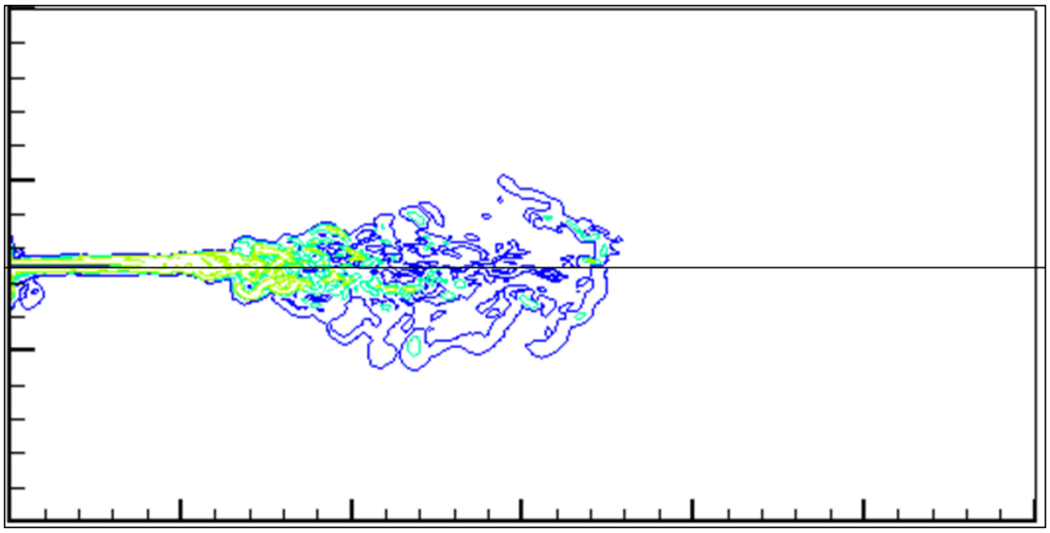

Figure 6.11. Comparison of the iso-contours of χ between the reacting (bottom half) and non-reacting (top half) jets (Blue - χ = 5 s^{-1}, Green - χ=50 s^{-1}, Yellow, χ=500 s^{-1}).

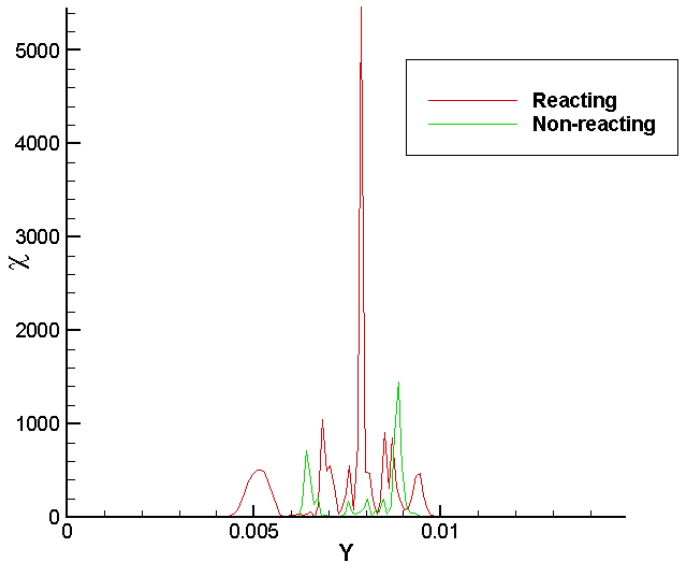

Figure 6.12. Comparison of radial profiles of χ at an axial (X) location of 60 D. Results are shown in the Y-direction, i.e. the direction normal to the axis.

6.6 LES vs. RANS

A RANS simulation was carried out for the same domain and boundary conditions as those of the LES. It was seen that the RANS simulations also resulted in a lifted flame with a lift-off height equal to approximately 1.4 cm, which is greater than that predicted by the LES, i.e. 0.8 cm. Furthermore, the first ignition occurred at around 0.29 ms in the LES whereas it is about 0.65 ms in the RANS simulation. Figure 6.13 compares the mixture fraction fields predicted by the RANS and LE simulations at a time of 0.83 ms. The top half shows the RANS simulation results, and the bottom half shows the LES results. It is encouraging that the jet-tip penetration and dispersion are comparable in the cases. Ensemble-averaging of the LES results are, however, necessary to confirm this. Figure 6.14 compares the temperature profiles. Significant differences are

evident on account of differences in ignition delay. Figure 6.15 compares the steady lift-off heights. As pointed out above, the lift-off height is greater in the RANS simulation. The differences in ignition delay and lift-off height results point to a higher (effective) scalar dissipation rate in the RANS simulation. Recall that the scalar dissipation rate in the RANS simulation is derived from the k-ε model and mixture fraction variance as shown in Eq. (3.4) in Chapter 3 whereas the scalar dissipation rate in the LES is directly obtained from the mixture fraction gradients and local diffusivity. Deriving the scalar dissipation rate from the local gradients takes into consideration only the effect of the larger scales on the gradients and neglects the effect of the unresolved scales. This is fundamentally incorrect and needs to be addressed in future work. As a result, the computed scalar dissipation rate in the LES will be smaller than in the RANS simulation at the corresponding locations.

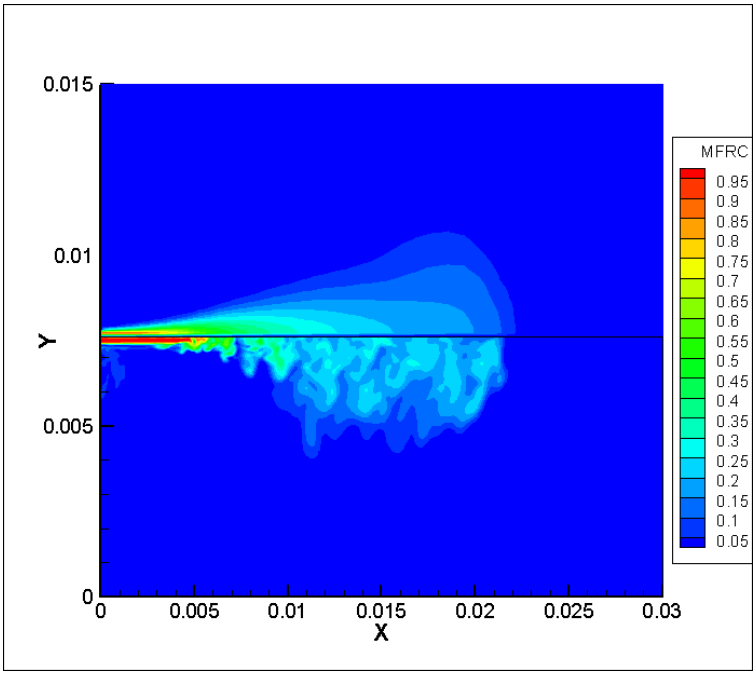

Figure 6.13. Mixture fraction profile in the axial plane at 0.83 ms (Top half - from RANS simulation, Bottom half - from LES simulation).

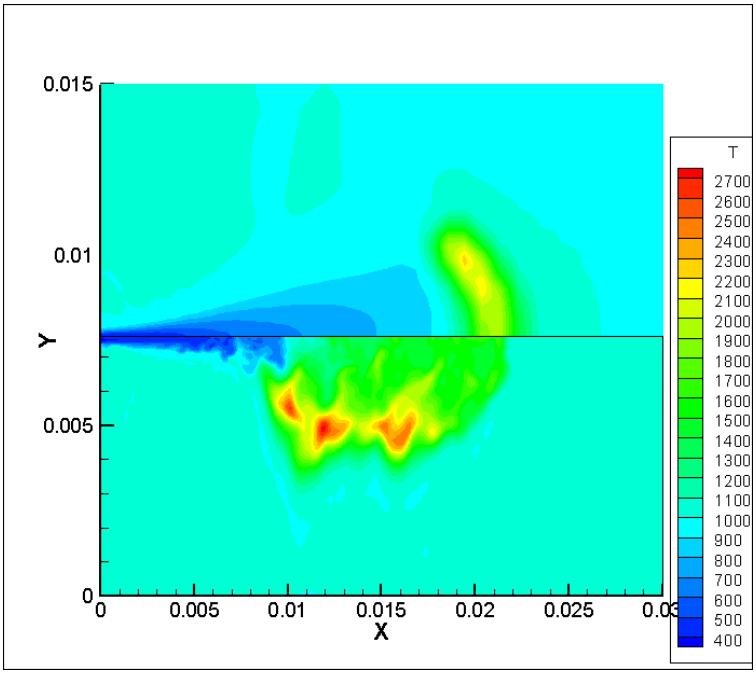

Figure 6.14. Comparison of temperature profiles between LES and RANS at 0.83 ms (Top half - RANS, Bottom half - LES).

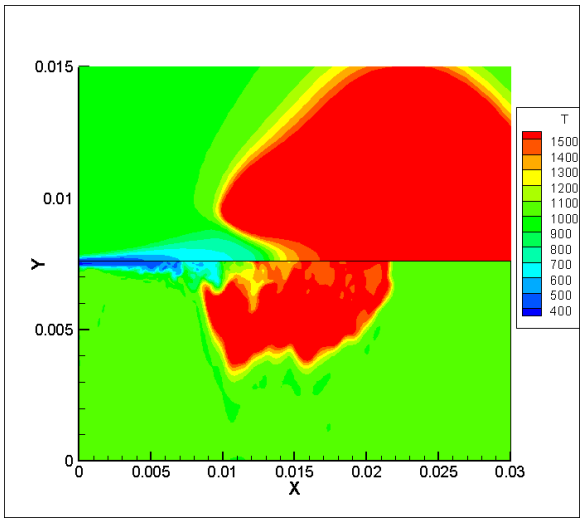

Figure 6.15. Comparison of temperature profiles between LES and RANS (Top half - RANS at 2.0 ms, Bottom half - LES at 0.83 ms).

6.7 Summary and Conclusions

In this chapter, LES results of lifted flames in a turbulent reacting jet are presented. The simulations show the transient evolution of the jet through ignition, flame development and flame stabilization. Ignition occurs at multiple points along the edge of the jet. Analysis shows that the mixture fraction where ignition occurs lies in the rich mixture and scalar dissipation rates at the ignition locations are lower than the ignition scalar dissipation rate. Flames develop from the ignition kernels and merge. The lift-off height is closely approximated by the farthest upstream location in the jet where ignition kernels develop and are not quenched. The transient development of the reacting jet during ignition as revealed by LES differs from RANS simulation results. In Chapter 3, it was shown that the RANS simulation results predict ignition in the rich mixture toward the leading edge of the jet, propagation of an ignition front from the initial ignition point to the stoichiometric surface, and then flame propagation upstream followed by flame stabilization. Both LES and RANS simulations predict that flame stabilization occurs as a result of local scalar dissipation rates exceeding the ignition limit. The lift-off heights are different in the LES and RANS simulations, probably reflecting inaccuracies in the turbulence/chemistry interaction model in the LES. A fundamental evaluation of the turbulence/chemistry interaction model is required. This is the objective of the work discussed in the next chapter.

7 DNS EVALUATION OF THE UNSTEADY FLAMELET PROGRESS VARIABLE MODEL

7.1 Introduction

In this chapter DNS of turbulent reacting and non-reacting mixing layers are used to evaluate the various underlying assumptions and elements of the unsteady flamelet progress variable (UFPV) model used in the LES of reacting jets presented in Chapter 6. The outline for the rest of the chapter is as follows. The computational setup used for the DNS simulations is described in detail in Sec. 7.2. In Sec. 7.3, the modeling of the filtered scalar dissipation rate is discussed. Different models for the filtered scalar dissipation rate and its PDF are evaluated using the DNS database. A model for the variance of the filtered scalar dissipation rate is derived and its performance is assessed. Section 7.4 examines the validity of using "2D" DNS as a means of evaluating LES subgrid-scale models. An important assumption in the UFPV model is that the reactions occur in flamelets. In Sec. 7.5, the validity of this assumption is tested. The UFPV model itself is assessed in Sec. 7.5. Section 7.6 then presents a comparison of the performance of the UFPV model with the perfectly-stirred reactor (PSR) model which is widely employed in LES and RANS because of its simplicity. In Sec. 7.7, non-reacting LES results are used to assess the improved subgrid-scale models. The chapter closes with summary and conclusions in Sec. 7.8.

7.2 Computational Setup

The FLEDS code described in Chapter 4 will be employed for the DNS studies. The effective binary diffusion coefficient model for computing multicomponent species diffusion, using the method of Bird et al. (Bird, Stewart, & Lightfoot, 2007), is employed. Chemical kinetic source terms are computed through an interface with CHEMKIN -like subroutines. The DNS computational domain is initialized using a n-heptane/air mixing layer in a two-dimensional 5 x 5 mm domain (see Fig. 7.1). The fuel-air mixing layer is initialized using a hyperbolic tangent profile in the y-direction using the following equation:

$$s = \left(\frac{s_1+s_2}{2}\right) + \left(\frac{s_1-s_2}{2}\right)\tanh\left(\frac{y-y_c}{\delta}\right), \tag{7.1}$$

where s is the mass fraction of any species at a location y and s_1 and s_2 are the mass fractions of that species in the air and fuel sides, respectively. The variable y_c is the y-coordinate of the center of the mixing layer and δ is the mixing layer thickness. Figure 7.2 shows the distribution of the fuel species as a function of the y-coordinate for δ = 120 μm. In the computations, periodic boundary condition in x-direction and adiabatic slip boundary condition in y-direction are employed. The computational domain is initialized with a turbulent flow field using the method of Fathali et al. (2008) as described in Sec. 4.3. The values of δ, initial pressure and temperature, and the turbulent velocity and length scales used for the simulations will be provided as the different cases are discussed. The turbulent length scale l_0 is selected such that it is smaller than 0.1 times the length of the domain in both the x and y directions. The numerical grid is chosen such

that it is smaller than the Kolmogorov scale and resolves the diffusion flame reaction zone.

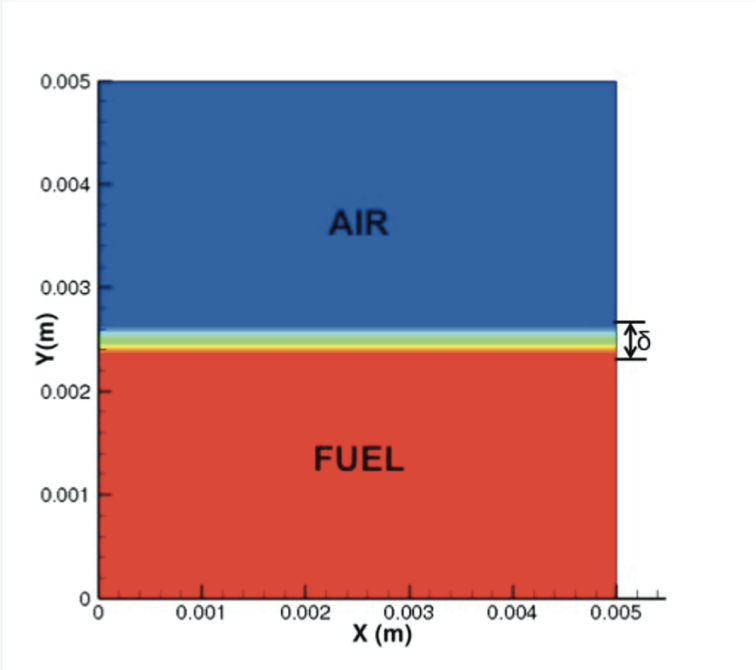

Figure 7.1. The initial mixture fraction field in the computational domain for the 2-D turbulent simulation.

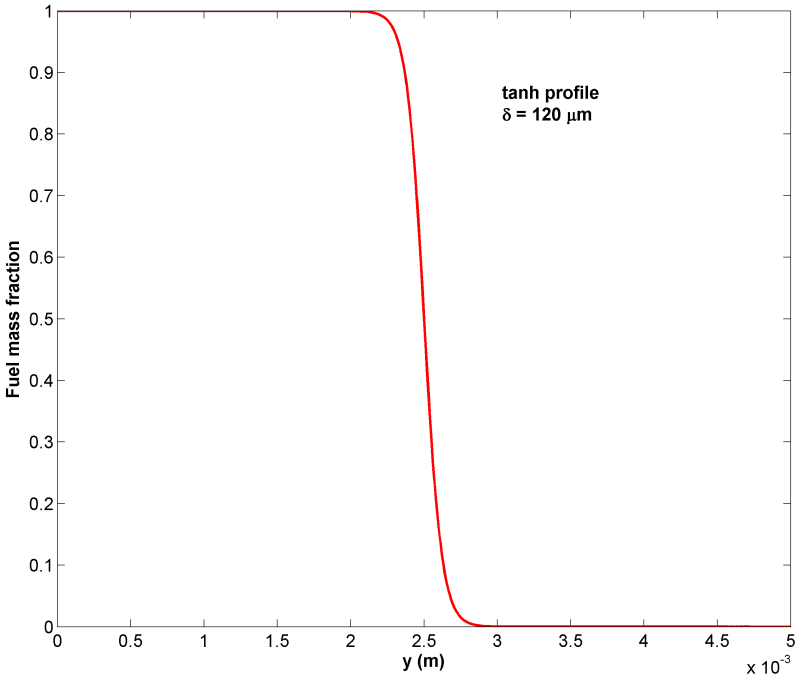

Figure 7.2. Initial fuel mass fraction as a function of the y-coordinate.

7.3 Modeling the Filtered Scalar Dissipation Rate

While the interest in the scalar dissipation rate (χ) in this work is specific to the UFPV model, it is an important variable required in many turbulent combustion models used in RANS and LES. As discussed in Sec. 3.2, χ is defined as

$$\chi = 2D\left|\nabla Z\right|^2, \tag{7.2}$$

where D is the molecular diffusivity. Notice that this fundamental definition cannot be employed in LES (or RANS) because only filtered (or Reynolds-averaged) values of Z are available. In a mixing layer, the functional form of the dependence of χ on Z is typically assumed to follow an error function profile (Peters, 2000; Mukhopadhyay and Abraham, 2012).

$$\chi = \chi_{st}\frac{\exp\left\{-2\left[erfc^{-1}\left(2Z\right)\right]^2\right\}}{\exp\left\{-2\left[erfc^{-1}\left(2Z_{st}\right)\right]^2\right\}}. \tag{7.3}$$

By using this assumption, the value of the scalar dissipation rate at any Z can be related to its value at the stoichiometric mixture fraction, χ_{st}.

In this section, DNS of turbulent mixing layers will be used to examine and evaluate different modeling strategies for the scalar dissipation rate. *Note that parts of this section have been submitted to* ***Combustion Science and Technology*** *and is under review*. Table 7.1 shows the list of simulation parameters, which are used to generate the DNS database. Parametric variations of the mixing layer thickness, δ, and the turbulence intensity, u', are also performed. The case with $u' = 1.0$ m/s and $\delta = 120$ μm is considered

as the *baseline case* in the following discussion. Both non-reacting and reacting simulations are performed for each case. The 37-species mechanism developed by Peters *et al*. (2002) is used as the chemical kinetic mechanism. This mechanism has been employed in several prior studies to study autoignition and flame development under compression-ignition engine conditions (Ameen and Abraham, 2014a; Bajaj et al., 2013; Egüz et al., 2013; Mukhopadhyay and Abraham, 2011; Tap and Veynante, 2005).

Table 7.1. List of simulation parameters employed in this study.

u' (m/s)	**l_0 (μm)**	**δ (μm)**
0.5	500	90,120,240,480
1.0	500	90,120,240,480
2.5	500	90,120,240

Figure 7.3 shows the instantaneous profile of the scalar dissipation rate at a time of 0.7 ms for the (a) non-reacting and (b) reacting baseline case. The regions of high χ are localized to small regions in the computational domain. It is seen that the peak values of scalar dissipation rate is about 500 /s for the non-reacting and reacting mixing layers, but there are more regions of higher scalar dissipation rate in the non-reacting simulation. This is expected as chemical reactions cause an increase in temperature leading to local expansion and thus reduction in the gradients of the mixture fraction. This directly corresponds to a reduction in the scalar dissipation rate (Eq. (7.2)). This is made clearer in Fig. 7.4, which compares the conditionally-averaged scalar dissipation rates, $\langle \chi | Z \rangle$, for the non-reacting and reacting mixing layers at the same time. It can be seen that $\langle \chi | Z \rangle$ is higher for the non-reacting mixing layer for all value of Z.

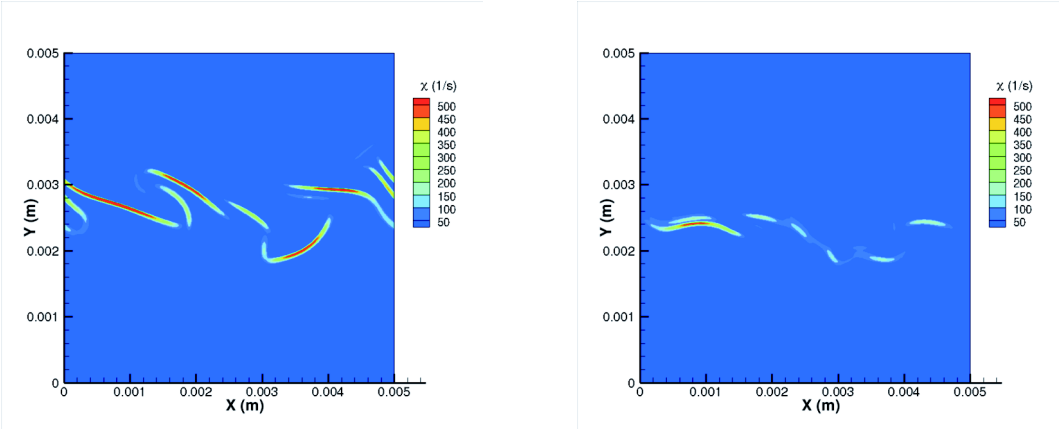

(a) (b)

Figure 7.3. Instantaneous scalar dissipation rate contours at 0.7 ms for (a) non-reacting baseline case, and (b) reacting baseline case.

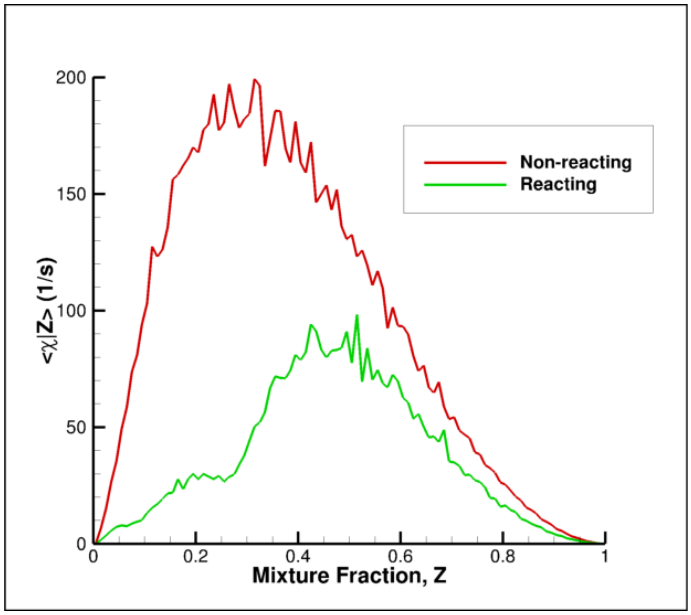

Figure 7.4. Variation of the conditionally-averaged scalar dissipation rate with Z for the non-eracting and reacting baseline cases at 0.7 ms.

For the reacting mixing layer, it is also important to investigate the evolution of χ during the ignition process. Figure 7.5 shows contour plots of χ at 0.20 and 0.30 ms after start of computation. The corresponding temperature contours are shown in Fig. 7.6. The

reason for the bimodal spatial distribution at 0.2 ms will be explained in Sec. 7.5. The heat release causes significant changes in the distribution of χ. As expected, the χ distribution will also depend on the value of the turbulence intensity u'. Figure 7.7 shows the distribution of χ at a time of 0.7 ms for three values of u', 0.5, 1.0 and 2.5 m/s, when the mixture is non-reacting. Not surprisingly, as u' increases, the mixing layer becomes increasingly stretched, leading to larger values of χ.

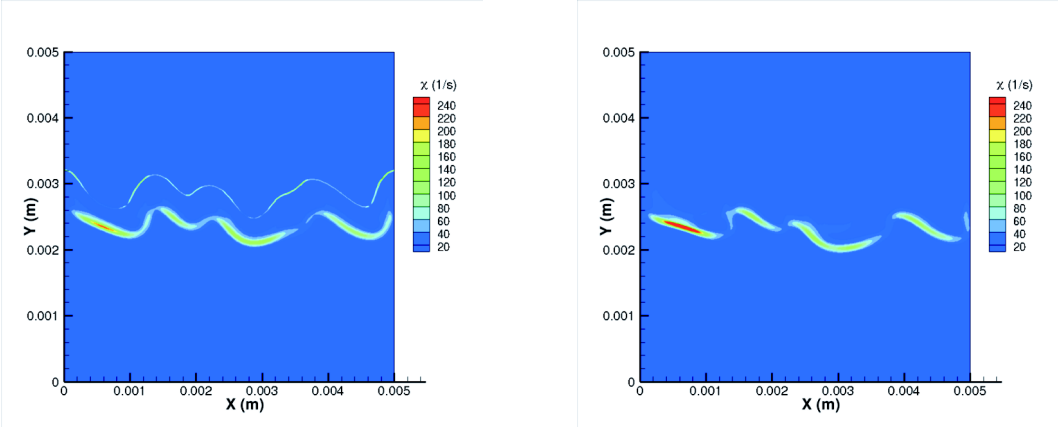

(a) (b)

Figure 7.5. Instantaneous scalar dissipation rate contours for the reacting baseline case during the ignition process at (a) t=0.20 ms and (b) t=0.30 ms.

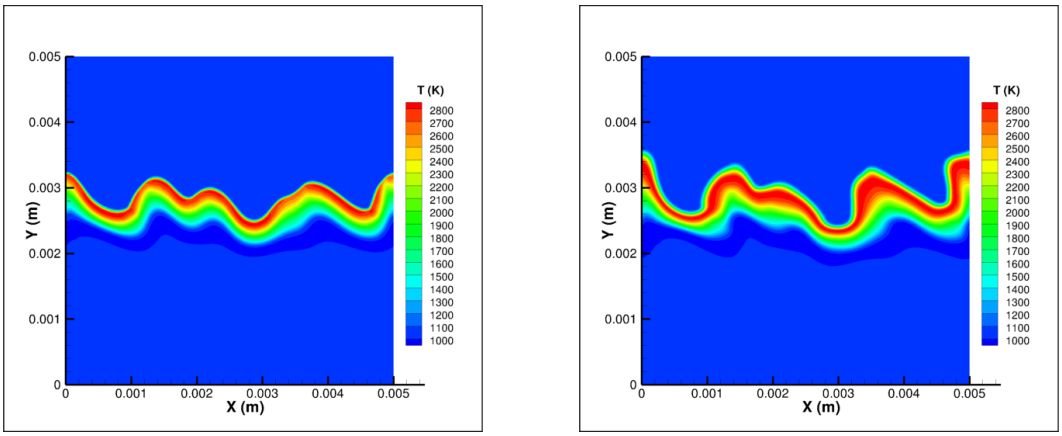

(a) (b)

Figure 7.6. Instantaneous temperature contours for the reacting baseline case during the ignition process at (a) t=0.20 ms and (b) t=0.30 ms.

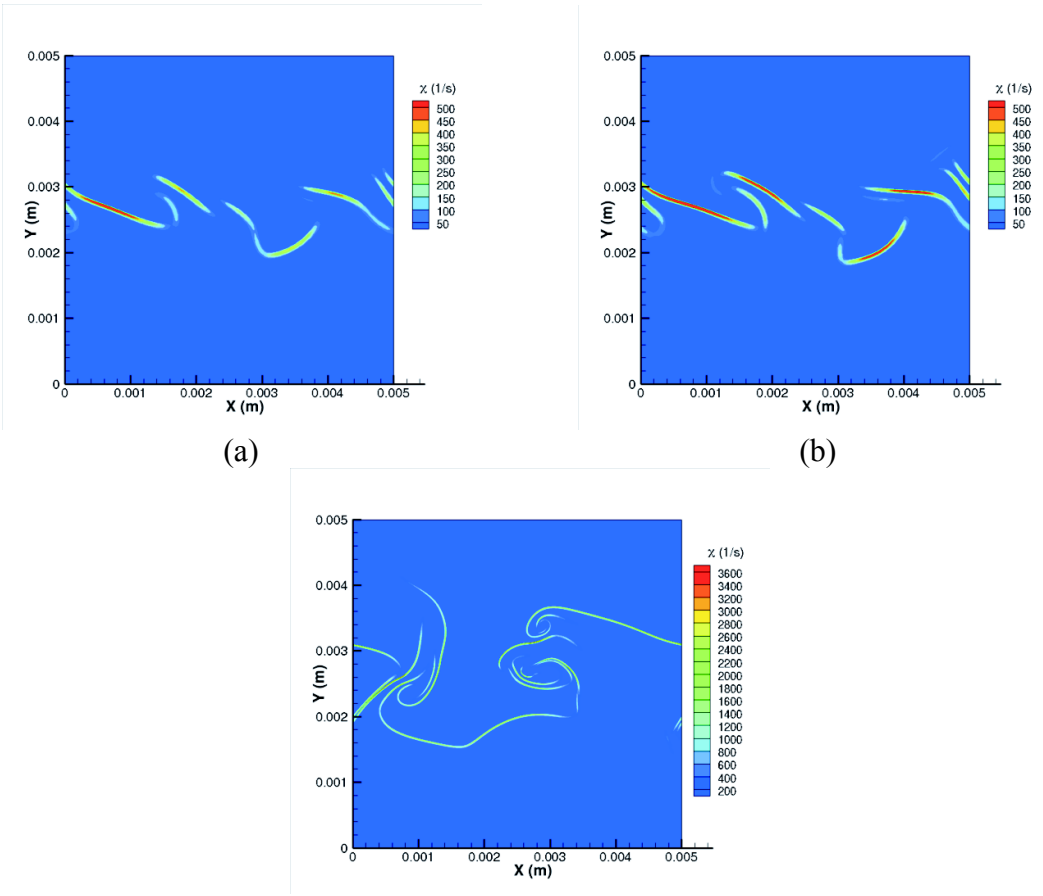

Figure 7.7. Effect of turbulence intensity on the instantaneous scalar dissipation rate contours for the non-reacting baseline case at t=0.7 ms for (a) u'=0.5 m/s, (b) u'=1.0 m/s, and (c) u'=2.5 m/s.

Starting with Eq. (7.2), the filtered scalar dissipation rate is defined as

$$\widetilde{\chi} = \widetilde{2D\left|\nabla Z\right|^2} = 2\widetilde{D}\left|\nabla \widetilde{Z}\right|^2 + \chi_{\text{model}}, \tag{7.4}$$

where χ_{model} is the term to be modeled, and the tilde denotes filtered variables. In this study, several models proposed in the literature for the filtered scalar dissipation rate are evaluated by comparing their performance against DNS results. The models are described below.

The first model that is evaluated is the turbulent diffusivity (TD) model (Girimaji and Zhou, 1996; Pierce and Moin, 2004), given by

$$\chi_{\text{model}} = \chi_{TD} = 2D_T \left|\nabla \tilde{Z}\right|^2, \tag{7.5}$$

where D_T is the sub-grid scale turbulent diffusivity in LES.

In RANS models, the scalar dissipation rate is usually linked algebraically to the variance of the mixture fraction, Z_v (Sanders and Gokalp, 1998). A similar approach can be employed for LES as well. Here, the sub-filter scalar mixing time, $Z_v / \chi_{\text{model}}$, is assumed to be proportional to the sub-filter turbulent timescale, τ, i.e.

$$\chi_{\text{model}} = C \frac{Z_v}{\tau}. \tag{7.6}$$

Based on the choice for the definition of the time-scale τ, different models for the scalar dissipation rate can be derived. Following a method that is commonly employed in RANS simulations when the k-ε model is employed for turbulence, a model can be formulated as proposed by Jimenez et al. (2001) where

$$\chi_{\text{model}} = \chi_{k\varepsilon} = C_{k\varepsilon} \frac{\tilde{\varepsilon}}{\tilde{k}} Z_v, \tag{7.7}$$

and $\tilde{k} = 1/2\left(\widetilde{u_i u_i} - \tilde{u}_i \tilde{u}_i\right)$ is the sub-grid scale kinetic energy, $\tilde{\varepsilon} = \widetilde{\nu\left(\partial u_i / \partial x_j \cdot \partial u_i / \partial x_j\right)}$ is the filtered kinetic-energy dissipation, v is the viscosity, Z_v is the variance of mixture fraction and $C_{k\varepsilon}$ is a model parameter to be determined.

The turbulent time-scale can also be defined as $\tau = 1/|\tilde{S}|$, where $|\tilde{S}|$ the magnitude of the large-scale strain rate tensor can be expressed as $|\tilde{S}| = \left(2\widetilde{S_{ij}}\widetilde{S_{ij}}\right)^{1/2}$ with

$$\widetilde{S_{ij}} = \frac{1}{2}\left(\frac{\partial \widetilde{u_i}}{\partial x_j} + \frac{\partial \widetilde{u_j}}{\partial x_i}\right). \tag{7.8}$$

The strain-rate tensor (SRT) model (Balarac et al., 2008) is defined as

$$\chi_{\text{model}} = \chi_{SRT} = C_{SRT} Z_v |\tilde{S}|, \tag{7.9}$$

where C_{SRT} is a model parameter to be determined.

The turbulent time scale can also be defined as $\tau = k/\Delta^{1/2}$, where Δ is the filter size which is assumed to be equal to the LES grid size. This leads to the subfilter kinetic energy (SKE) model (Schmidt and Schumann, 1989; Balarac et al., 2008) given by

$$\chi_{\text{model}} = \chi_{SKE} = C_{SKE} \frac{Z_v k^{1/2}}{\Delta}, \tag{7.10}$$

where C_{SKE} is a model parameter to be determined. Table 7.2 lists the different models for the filtered scalar dissipation rate that are evaluated in this study.

The DNS database is used to obtain the filtered scalar dissipation rate by explicitly filtering the DNS results using a box filter with different filter sizes ranging from 50 to 500 μm. The scalar dissipation rate models are then analyzed in detail by comparing their accuracy with the DNS values for non-reacting and reacting mixing layers. Among these models, the TD and SRT models are the easiest to implement in LES computations, as there is no need to solve additional transport equations for k and ε.

Table 7.2. List of models for filtered scalar dissipation rate.

	Model	χ_{model}
1	TD model	$\chi_{\text{model}} = \chi_{TD} = 2D_T \left\|\nabla \widetilde{Z}\right\|^2$,
2	k-ε model	$\chi_{\text{model}} = \chi_{k\varepsilon} = C_{k\varepsilon} \frac{\widetilde{\varepsilon}}{\widetilde{k}} Z_v$,
3	SRT model	$\chi_{\text{model}} = \chi_{SRT} = C_{SRT} Z_v \left\|\widetilde{S}\right\|$,
4	SKE model	$\chi_{\text{model}} = \chi_{SKE} = C_{SKE} \frac{Z_v k^{1/2}}{\Delta}$

Note that with the exception of the TD model, an equation for the mixture fraction variance has to be solved. To compare the performance of the models, a normalized error, *E*, is defined similar to the one used by Balarac et al. (2008) and given by

$$E = \frac{\left\langle \left(\chi_{\text{model}} - \left(\widetilde{\chi} - 2\widetilde{D}\left|\nabla \widetilde{Z}\right|^2 \right) \right)^2 \right\rangle}{\left\langle \left(\widetilde{\chi} - 2\widetilde{D}\left|\nabla \widetilde{Z}\right|^2 \right)^2 \right\rangle}, \tag{7.11}$$

where the angular brackets denote an ensemble averaging over all the filtered cells. Note that the term $\left(\widetilde{\chi} - 2\widetilde{D}\left|\nabla \widetilde{Z}\right|^2 \right)$ is the actual quantity estimated from the DNS database. This error norm is a measure of the lack of correlation between the model and the DNS results. A value of *E*=0 implies perfect correlation and as the correlation reduces, *E* increases. The value of the error norm, of course, depends on the model constants. The model constants are selected by minimizing the error norm for the baseline case (u' = 1.0 m/s and δ= 120 μm) over a range of filter sizes and then averaging it across the filter

sizes. For the non-reacting case, the model parameters were found to be $C_{k\varepsilon} = 0.7$, $C_{SRT} = 0.1$ and $C_{SKE} = 0.57$.

Figure 7.8 compares the value of E for the baseline non-reacting case for filter sizes (Δ) varying from 50 to 500 μm. Figure 7.8 shows that the error generally increases with increasing Δ for all the models. The error is negligible when Δ = 50 μm, but increases with increasing Δ. The SKE model performs the best among the 4 models across the range of filter sizes. The performance of the TD model is relatively poor for all the filter sizes. The normalized error for the SKE model is about 0.15 for Δ = 500 μm but about 0.6 for the TD model. In fact, the error norm for the TD model has values that are not very different from using no model. Examining Eqs. (7.4) and (7.5), this suggests that the contribution of the sub-grid scale term (Eq. (7.5)) is relatively small in the TD model. This suggests that the turbulent diffusivity, D_T, which is obtained by the constant-coefficient Smagorinsky model in this study, is being underpredicted. The use of a dynamic Smagorinsky model for the determination of D_T is expected to improve the prediction. Notice that the difference between the two curves (no model vs TD) increases with increasing filter size suggesting that the sub-grid scale contribution does increase as expected. This conclusion is similar to the one made by Balarac et al. (2008). It is also seen that the SRT model performs relatively well under all conditions.

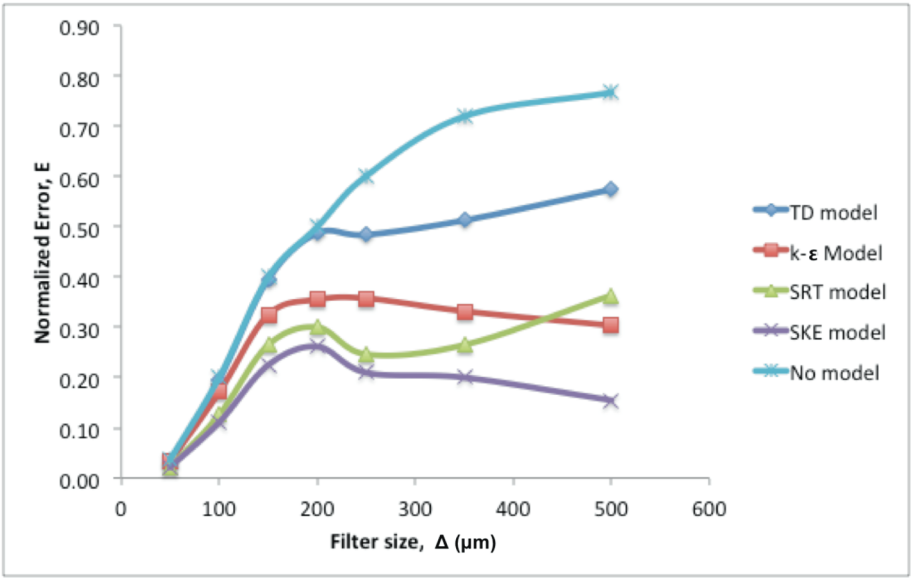

Figure 7.8. Comparison of the different models for filtered scalar dissipation rate for the baseline non-reacting case.

Figure 7.9 makes the same comparison for the reacting baseline case. It is seen that the TD model again performs poorly, showing negligible improvement over using no model. The TD model is used in many LES computations (Ihme et al., 2005; Ihme and Pitsch, 2008; Ihme and See, 2010). When flamelet models are employed together with the TD model, these results suggest that there can be large errors. The SRT and SKE models have the minimum errors across the range of filter widths. Recall that the SKE model had the minimum error for the non-reacting case. For the reacting case, the model parameters were found to be $C_{k\varepsilon} = 0.11$, $C_{SRT} = 0.11$ and $C_{SKE} = 0.45$. While the model parameters for the SRT and SKE model for the reacting cases are within 10% and 20%, respectively, of the values obtained for the non-reacting simulations, the optimum model parameter for the k-ε model is a factor of about seven lower. The reason for this is that in the reacting mixing layer, the increase in temperature leads to higher values of kinematic viscosity, ν, and thus higher values for ε. Since the k-ε model is directly proportional to ε (see Eq.

(7.7)), $C_{k\varepsilon}$ has to be lowered to adjust for the rise in temperature. Note that a temperature-dependent property of the fluid, e.g. ν, appears only in the k-ε model. From this point on, only the SRT and SKE model will be considered for further assessment. The constants derived for the reacting cases are now used to perform further parametric studies by varying mixing layer thickness and turbulence intensity.

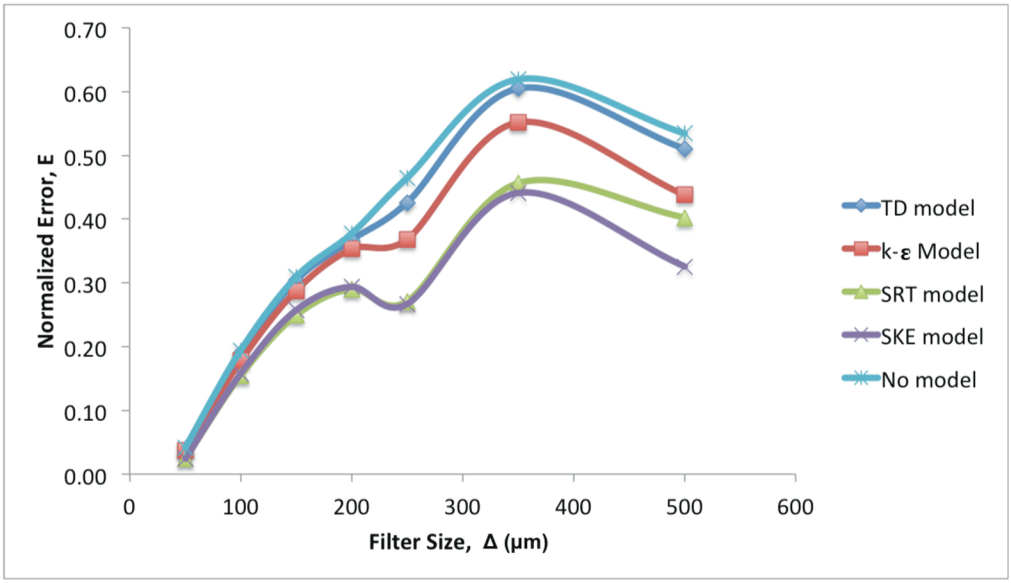

Figure 7.9. Comparison of the different models for filtered scalar dissipation rate for the baseline reacting case.

Figures 7.10 and 7.11 show the effect of the mixing layer thickness on the performance of the SRT and SKE models for the non-reacting and reacting simulations, respectively, for a filter size of 200 μm using the constants determined from the baseline case. Also shown for comparison are the error values obtained without using any model. The general trend from Fig. 7.10 is that as the mixing layer thickness increases, the error *E* reduces. This is expected, as the increase in mixing layer thickness leads to reduction in the gradients in Z and thus lowers the values of the scalar dissipation rate. A similar trend

is observed for Fig. 7.11 for the reacting mixing layers. It can be concluded that both the SRT and SKE models perform equally well for a range of mixing layer thicknesses.

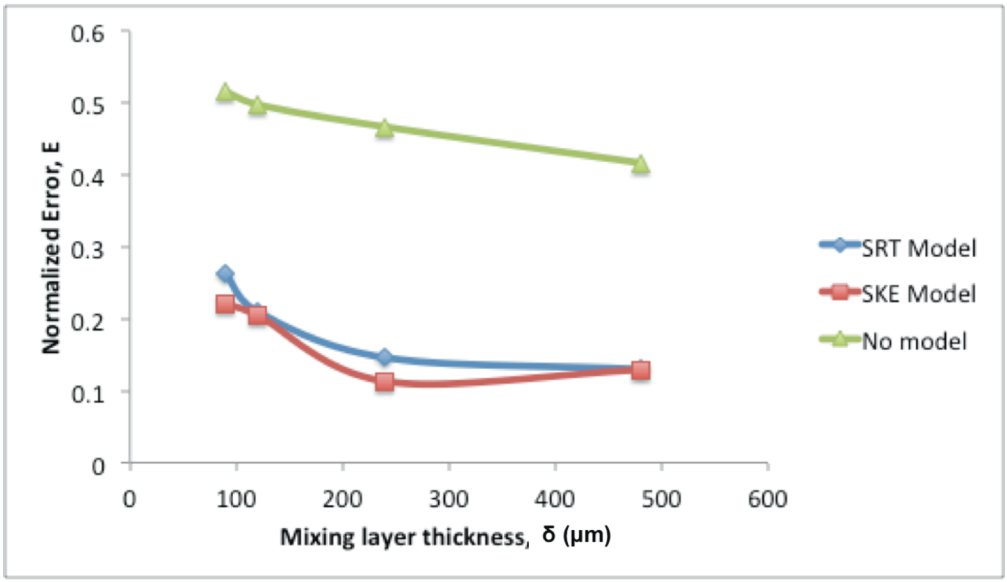

Figure 7.10. Effect of mixing layer thickness (δ) on the performance of the SRT and SKE models for non-reacting mixing layers.

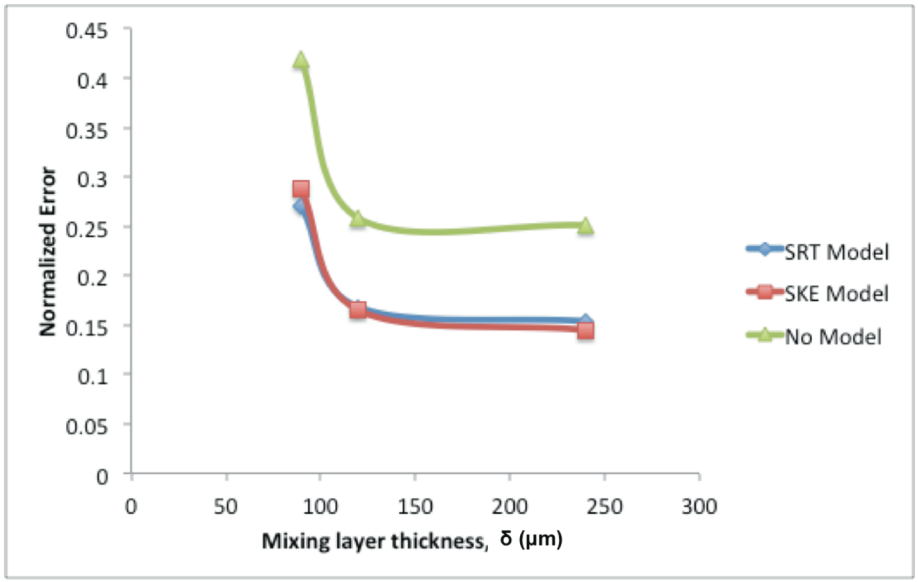

Figure 7.11. Effect of mixing layer thickness (δ) on the performance of the SRT and SKE models for reacting mixing layers.

Figure 7.12 shows the effect of the turbulence intensity on the performance of the SRT model for non-reacting mixing layers. As the turbulence intensity, u', increases, the mixing layer becomes increasingly stretched, leading to larger values of χ. Thus, the error when not using any model for the filtered scalar dissipation rate increases as the turbulence intensity increases. The SRT and SKE models reduce the error to about 50% of that when using no model.

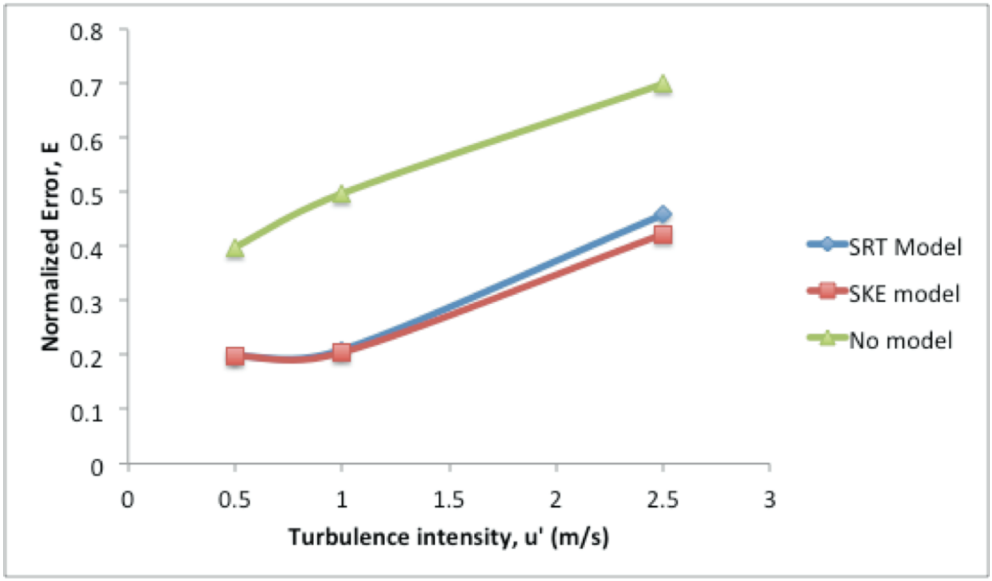

Figure 7.12. Effect of turbulence intensity on the performance of SRT and SKE model for non-reacting mixing layers. Filter size = 200 μm.

It can be concluded that the SRT and SKE models are able to model the filtered scalar dissipation rate relatively well for the wide range of conditions selected in this study. Use of the SKE model, however, requires that a transport equation for the subgrid turbulent kinetic energy has to be solved. Since the differences in performances between these two models are not very significant, the SRT model is the recommended model to be used for LES computations.

7.3.1 Modeling the PDF of Filtered Scalar Dissipation Rate

In addition to the accurate modeling of the filtered scalar dissipation rate $\tilde{\chi}$, the marginal PDF of χ is also required for use in flamelet models (see Eqs. (3.5) and (3.6)). Figures 7.13 and 7.14 show the PDFs obtained from the DNS simulations for the baseline reacting case. When the filter size, Δ, is small, the entire filtered cell can be expected to have an almost uniform value of χ. In other words, the variance of χ can be expected to be very small. Under these conditions, the PDF of χ is expected to behave like a δ-function centered on $\chi=\tilde{\chi}$. Figure 7.13 shows that for Δ=100 μm, the shape of the PDF of χ is similar to a δ-function. It can be expected that when the filter size, Δ, is large, the regions with high χ are localized to a small fraction of the filter size, and the remaining portion have low χ. Hence, the PDF of χ is expected to show a small peak near $\tilde{\chi}$ and a larger peak at a value of χ=0. Figure 7.14 shows that this is indeed the case for Δ=200 μm. Based on the general shapes of these PDFs, two functional forms are used to model the PDF – the exponential PDF and the lognormal PDF. The exponential PDF is given by

$$PDF_{\exp}(\chi)=\frac{1}{\tilde{\chi}}\exp\left(-\frac{\chi}{\tilde{\chi}}\right). \tag{7.12}$$

The lognormal PDF is given by

$$PDF_{LN}(\chi)=\frac{1}{\chi\chi_{\text{var}}^{1/2}(2\pi)^{1/2}}\exp\left(-\frac{\left(\ln\chi-\tilde{\chi}\right)^{1/2}}{2\chi_{\text{var}}}\right), \tag{7.13}$$

where χ_{var} is the variance of the scalar dissipation rate. Figure 7.13 compares the actual PDF with the exponential and lognormal PDF for a filter size of 100 μm. It is seen that the exponential PDF performs well for low values of $\tilde{\chi}$ whereas the lognormal PDF performs well for larger values of $\tilde{\chi}$. The reason for the poor performance of the

lognormal PDF at low values of $\tilde{\chi}$ is that the lognormal PDF always has a value of 0 at χ=0, whereas the discussion above showed that the actual PDF tends to have a non-zero value at χ=0 for low values of $\tilde{\chi}$. Figure 7.14 makes the same comparison for a filter size of 500 μm and the results show that the exponential PDF does better job at this filter size.

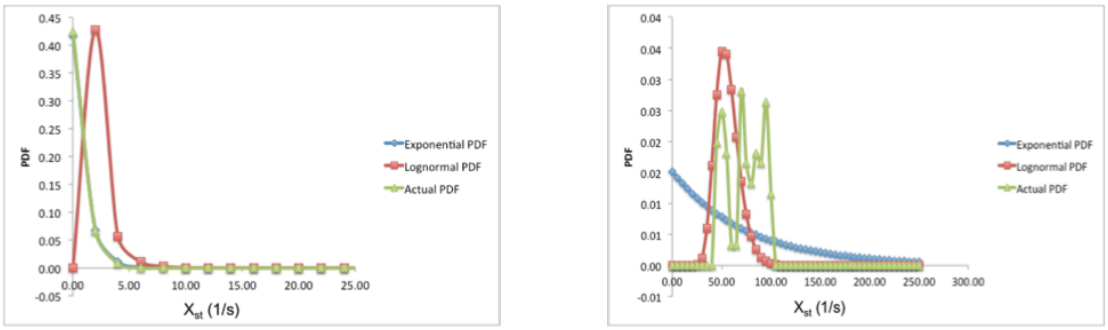

Figure 7.13. Comparison of marginal PDFs for the filtered scalar dissipation rate with the actual PDF for a filter size of 100 μm: (a) $\tilde{\chi}$ = 1.1 s^{-1}, and (b) $\tilde{\chi}$ = 76.3 s^{-1}.

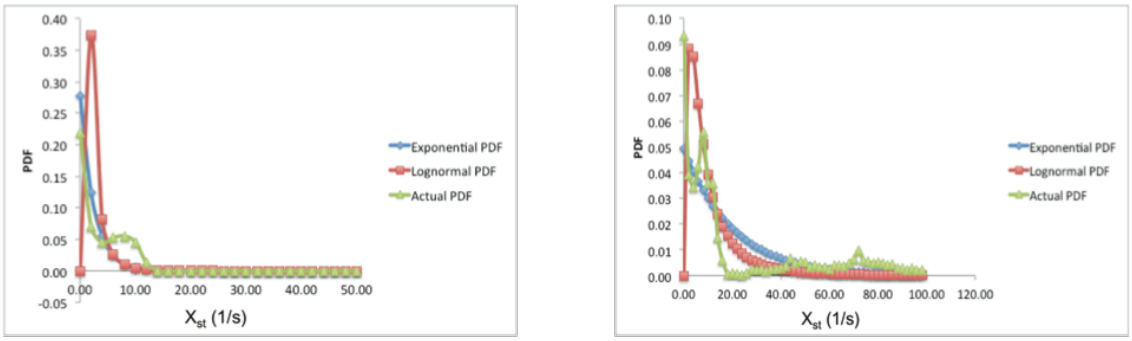

Figure 7.14. Comparison of marginal PDFs for the filtered scalar dissipation rate with the actual PDF for a filter size of 500 μm: (a) $\tilde{\chi}$ = 2.5 s^{-1}, and (b) $\tilde{\chi}$ = 20.1 s^{-1}.

An error norm E_{PDF} can be defined to quantify the performance of the model PDFs as

$$E_{PDF} = \int \left(P(Z) - P_{\text{model}}(Z) \right)^2 dZ, \tag{7.14}$$

where $P(Z)$ is the actual PDF (from DNS database) and $P_{model}(Z)$ is the model PDF. The error norm was calculated for the cases shown in Table 7.1. The range of values of $\tilde{\chi}$, in this set of simulations is from 5 to 50 s^{-1}. A normalized scalar dissipation rate is defined to be

$$\chi_{norm} = \frac{\tilde{\chi}}{\sqrt{\frac{u'^2}{\Delta\delta}}}, \tag{7.15}$$

where u' is the turbulence intensity, l_0 is the integral length scale, Δ is the filter size, and δ is the mixing layer thickness. Because the performance of the model PDF depends on the value of $\tilde{\chi}$, insight can be gained by plotting the error norm as a function of χ_{norm}. Figure 7.15 compares the error norms for the exponential and lognormal PDFs. It is seen that the exponential PDF works better when χ_{norm} is lower than 0.6, and the lognormal PDF works better for larger values. It can be concluded that for low values of Δ and $\tilde{\chi}$, and large values of u', the exponential PDF is the better choice.

7.3.2 Modeling the Scalar Dissipation Rate Variance

When using the SRT or SKE model, a transport equation for the variance of mixture fraction, i.e. Z_v, has to be solved. Knowing Z_v, the variance of the scalar dissipation rate can be modeled as shown below. The variance of the scalar dissipation rate is needed to employ the lognormal PDF. In this section, a simple model is derived for

the variance, which is found to be applicable for all the cases considered here. Using Eq. (7.2), the variance of the scalar dissipation rate can be expressed as

$$\begin{aligned}\chi_{\text{var}} = \widetilde{\chi''^2} &= \widetilde{\left(\chi - \tilde{\chi}\right)^2} \\ &= \overline{\left(2\left(\widetilde{D}+D''\right)\left|\nabla\left(Z+Z''\right)\right|^2 - 2\left(\widetilde{D}+D''\right)\left|\nabla\left(Z+Z''\right)\right|^2\right)} \\ &= \overline{\left(4\widetilde{D}\left(\nabla\widetilde{Z}\bullet\nabla Z''\right)+2D''\left|\nabla\widetilde{Z}\right|^2\right)^2}.\end{aligned} \tag{7.16}$$

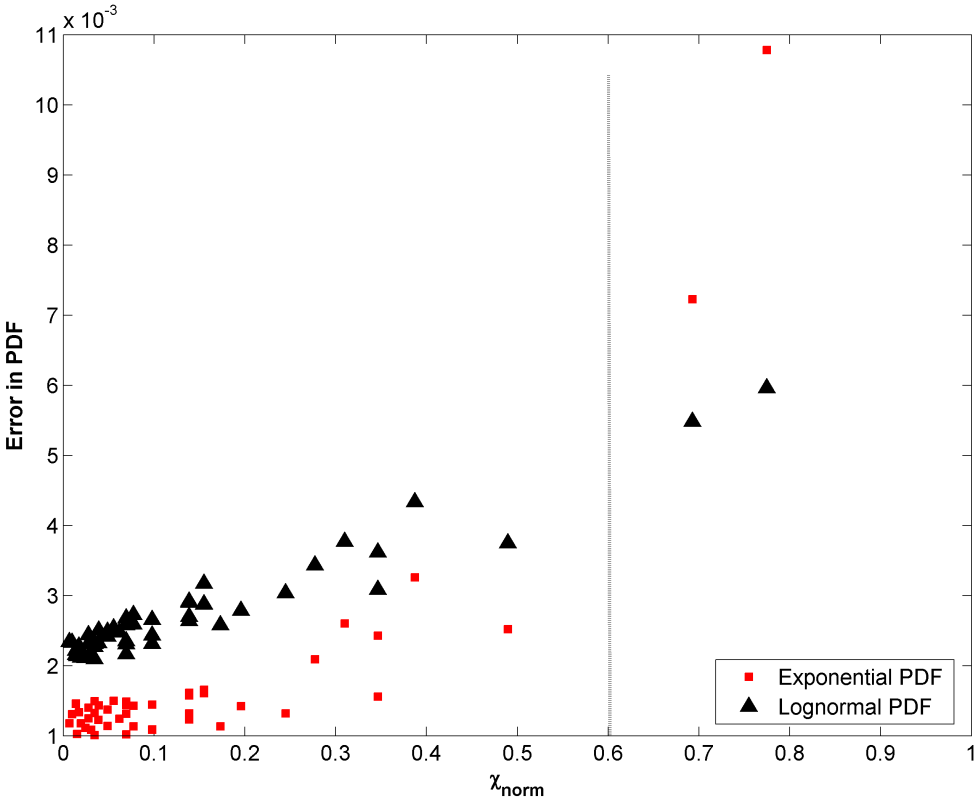

Figure 7.15. Comparison of errors for exponential and lognormal PDFs. The vertical line shows the value of χ_{norm} above which the lognormal PDF is more accurate.

Eq. (7.16) can be expanded to express χ_{var} as a sum of 3 terms as follows:

$$\chi_{\text{var}} = \chi_{\text{var,1}} + \chi_{\text{var,2}} + \chi_{\text{var,3}}, \tag{7.17}$$

where,

$$\chi_{\text{var,1}} = \overline{16\widetilde{D}^2\left(\nabla\widetilde{Z}\cdot\nabla Z''\right)^2} \approx 16\widetilde{D}^2\left|\nabla\widetilde{Z}\right|^2\left|\nabla Z_{sd}\right|^2, \tag{7.18}$$

$$\chi_{\text{var,2}} = \overline{4D''^2\left|\nabla\widetilde{Z}\right|^4}, \text{ and} \tag{7.19}$$

$$\chi_{\text{var,3}} = \overline{16\widetilde{D}D''\left(\nabla\widetilde{Z}.\nabla Z''\right)\left|\nabla\widetilde{Z}\right|^2}. \tag{7.20}$$

In the above expression, Z_{sd} is the square root of Z_v. From the DNS results, it is seen that

$$\chi_{\text{var,2}} + \chi_{\text{var,3}} \approx \chi_{\text{var,1}}. \tag{7.21}$$

Figure 7.16 demonstrates the validity of Eq. (7.21) for a filter size of 200 μm for the reacting baseline case. The reason for this correlation is not known.

Using this approximation, a model for χ_{var} can be given as

$$\chi_{\text{var,model}} = K\chi_{\text{var,1}}, \tag{7.22}$$

where K is a model parameter. In the above expression, the variance of the scalar dissipation rate can be obtained solely based on the values of the filtered mixture fraction, the variance of the mixture fraction and the filtered diffusivity. Figures 7.17 and 7.18

confirm the validity of Eq. (7.22) for filter sizes of 100 and 200 μm, respectively. The model parameter K can be obtained as the slope of the best-fit line. K is found to be in the range of 2-2.3 for all the cases considered in this study. It is worth mentioning that although the slope of K obtained from the linear fit is along expected lines, there are significant departures from the linear correlation especially for large filter sizes as Fig. 7.18 shows.

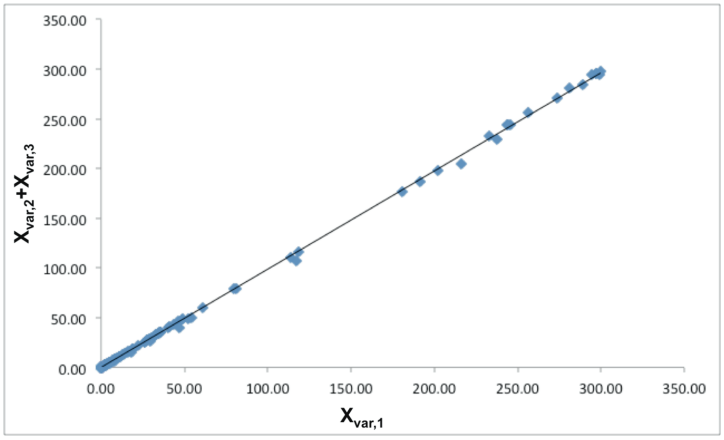

Figure 7.16. Scatter plot to validate the claim made in Eq. (7.21). This plot corresponds to a filter size of 200 μm.

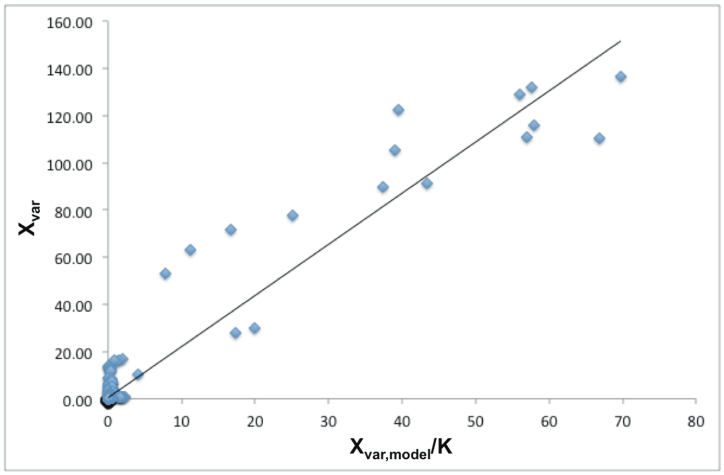

Figure 7.17. Determining the validity of $\chi_{var,model}$ (refer Eq. (7.22)) for filter size of 100 μm. The slope of the best-fit line gives the value of K to be 2.17.

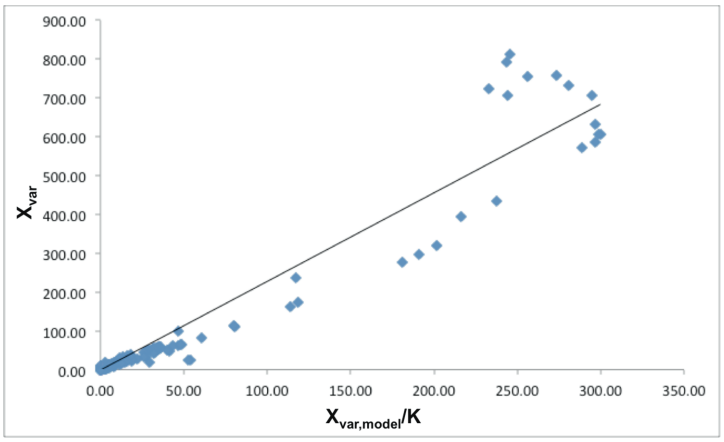

Figure 7.18. Determining the validity of $\chi_{var,model}$ (refer Eq. (7.22)) for filter size of 200 μm. The slope of the best-fit line gives the value of K to be 2.28.

7.3.3 Conclusions

In this study, direct numerical simulations of non-reacting and reacting mixing layers have been carried out to generate databases, which are then employed to assess the accuracy of four models for the filtered scalar dissipation rate in LES. The pressure and temperature conditions selected are relevant to compression-ignited combustion engines. N-heptane, often used as a surrogate for diesel fuel, is used as the fuel in these simulations. The four models assessed are the turbulent diffusivity model, the k-ε model, the strain rate tensor (SRT) model and the sub-filter kinetic energy (SKE) model. An error norm, E, is employed to quantify the differences between the model results and the DNS results. The assessment is carried out for a range of initial mixing layer thicknesses (90 - 480 μm), turbulence intensities (0.5 - 2.5 m/s), and filter widths (50 - 500 μm). Based on the values of the error norm, it is found that the SRT and SKE models perform the best among the models considered for the range of conditions considered. The SRT model is recommended because, unlike the SKE model, it can be used without solving additional transport equations (for the subfilter turbulent kinetic energy). To employ the

model, the probability density function (PDF) of the scalar dissipation rate is required. It is shown that the choice of PDF depended on the value of the filtered scalar dissipation rate – for lower values, an exponential PDF performs well, whereas a lognormal PDF performs better for larger values. A model was also introduced that relates the variance of the scalar dissipation rate to the mean and variance of the mixture fraction. This model is shown to give satisfactory agreement with the DNS results.

These conclusions were arrived at using "2D" DNS. An important question that arises is: is "2D" DNS evaluation adequate? In the next section, this question will be addressed for non-reacting flows.

7.4 Validity of the "2D" DNS

While DNS is not practical for engineering applications, it is a powerful tool to evaluate models that are employed in Reynolds-averaged Navier-Stokes (RANS) solvers and large-eddy simulations (LES). Often the DNS database is generated for canonical problems like the mixing layer discussed in the last section. Even this approach poses computational challenges when Reynolds numbers are high, and it is a common practice, especially for turbulent reacting flows, to perform two-dimensional DNS to evaluate models (Ameen & Abraham, 2014; Ferrer, Lehnasch, & Mura, 2012; Mukhopadhyay & Abraham, 2012; van Oijen, Bastiaans, & de Goey, 2007). 2D DNS have been employed in the past to evaluate turbulence models and turbulence/chemistry interaction models and provide insights into the flow physics. Mastorakos et al. (1997) performed 2D DNS of autoigniting mixing layers to explain the observed dependence of autoignition time on

turbulent time scale, flow length scale and partial premixing. Mastorakos and Bilger (1998) utilized 2D DNS to evaluate a second-order conditional moment closure model for the autoignition of turbulent flows. Van Oijen (2013) analyzed the interaction between ignition chemistry and turbulence in developing mixing layers using 2D DNS. These examples of prior 2D DNS notwithstanding, the fact is that turbulence is inherently three-dimensional in nature. It is questionable whether the results from a 2D DNS can accurately represent the flow features of the turbulent flow. Studies assessing the extent of applicability of 2D DNS for evaluating models are however very few in number especially for flows involving scalar mixing. Sreedhara and Lakshmisha (2002) performed 2D and 3D DNS of autoignition in n-heptane/air mixing layers and studied the differences in the effects of 2D and 3D turbulence on autoignition characteristics. They found that for 2D DNS, the autoignition delay times increased with increase in turbulence intensities whereas experimental evidence and 3D DNS showed the opposing trend. They showed that this difference was due to the fact that the kinetic energy dissipation is more accurately represented in the 3D DNS due to the vortex-stretching phenomenon. It is also important to note that with increasing computational power, some groups are now routinely carrying out 3D DNS of reacting flows (Chen, 2011; Yoo, Luo, Lu, Kim, & Chen, 2013; Yoo, Richardson, Sankaran, & Chen, 2011) on thousands of processors, but these computational resources are not yet readily accessible to most research groups.

Turbulent fuel/air mixing layers are of relevance to many practical applications, e.g. diesel engines, gas turbines, and in process industries. In fact, the turbulent mixing layer is commonly selected as a canonical configuration to study different features of turbulent mixing and to evaluate and propose turbulent sub-grid models for use in large-

eddy simulations (LES) (Sripakagorn, Mitarai, Kosaly, & Pitsch, 2004; Swaminathan & Bilger, 1997). The interest in this work is specific to engine applications where the chamber pressure and temperature are relatively high and where the injection of a hydrocarbon fuel into air results in the generation of turbulent fuel/air mixing layers. While the interest in the engine is in reacting mixing layers, because of the limitations in computational capabilities, the focus is only on non-reacting mixing layers in this study. The thinking is that if there are significant differences in non-reacting mixing layer predictions, the differences are likely to be even greater in reacting mixing layers. *Note that parts of this section have been submitted to the* ***International Journal of Heat and Fluid Flow*** *and is under review*.

For the 3D DNS, periodic boundary conditions are employed in X and Y directions and adiabatic slip boundary conditions in the Z direction (refer to Fig. 7.19). Figure 7.19 also shows the computational grid which was used for the 3D DNS as well as the distribution of the mixture fraction at a time of 0.30 ms. The 2D DNS setup is the same as that shown in Fig. 7.1. The turbulent length scale l_0 is selected to be 500 μm, which is 0.1 times the length of the domain in either X, Y, or Z direction. The initial turbulence intensity u' is selected to be 1.0 m/s which is comparable to the turbulence intensities in an engine just before combustion. The turbulent Reynolds number Re_t defined as $Re_t = u'l_0/\nu$, is approximately 160 in the simulations.

The evolution of the mixture fraction and scalar dissipation rate field predicted by the 2D and 3D DNS are compared and discussed next. The turbulent kinetic energy spectrum and its evolution are examined. Finally, the Smagorinsky model for subgrid

Reynolds stress and models for the filtered scalar dissipation rate and its variance are evaluated using the 2D and 3D DNS results to determine if the conclusions differ. The paper closes with summary and conclusions.

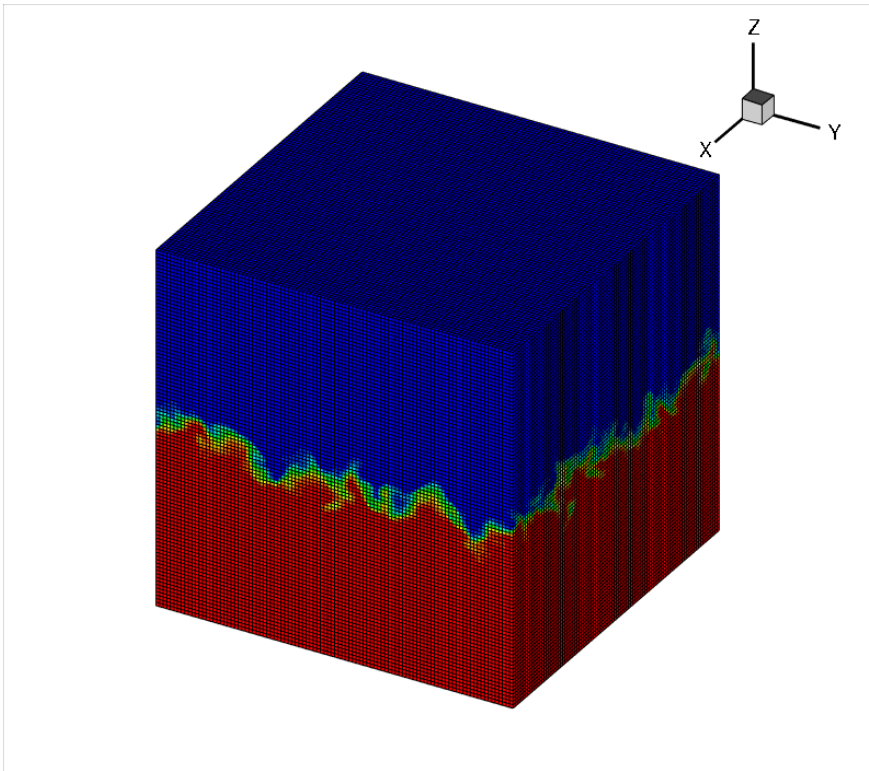

Figure 7.19. Computational Domain for the 3D DNS. Every 5th grid point is shown. The mixture fraction field is shown at a time of 0.3 ms.

7.4.1 Evolution of the Mixture Fraction and Scalar Dissipation Rate Fields

Some qualitative features of the mixing layer are examined first. Figures 7.20 to 7.22 show the distribution of the mixture fraction field in the X-Z plane (see Fig. 7.19) at times of 0.05 ms, 0.3 ms and 0.5 ms after the start of the simulation for the 2D and 3D DNS. Figure 7.20 shows that the qualitative distribution of the mixture fraction fields are similar at an early time of 0.05 ms. Note that this time is much shorter than the eddy turnover time of 0.5 ms. As the mixing layer evolves, and the time becomes comparable

to the eddy turnover time, noticeable differences arise as can be seen in Figs. 7.21 and 7.22. A wider range of gradients is evident in the 3D results. In fact, it is seen that for the 3D DNS, multiple blobs of fuel break away from the mixing layer and are transported to the air side. This phenomenon is not observed in the 2D DNS during the same timeframe. This is significant when employing the DNS results to evaluate turbulent subgrid-scale models for scalar mixing as turbulent transport of scalars could be different when the mixing layer is broken up.

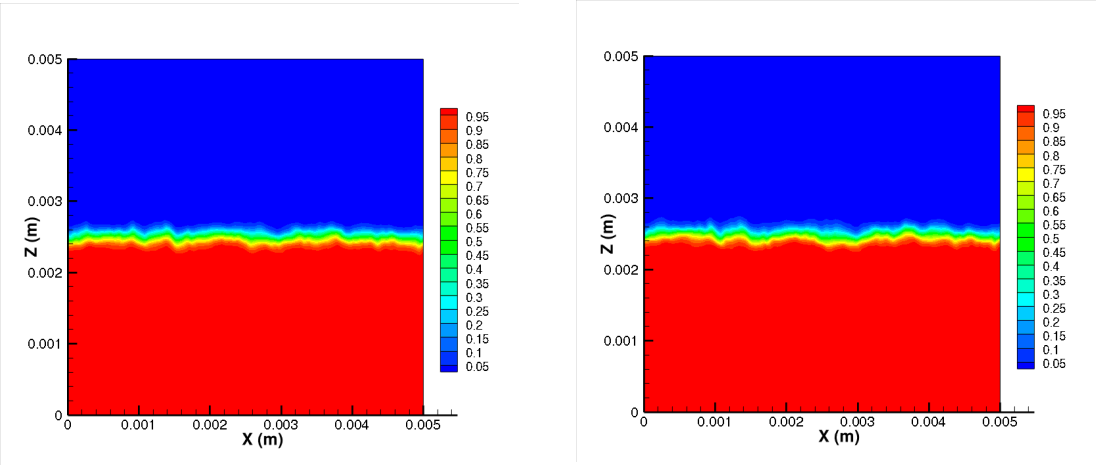

(a) (b)

Figure 7.20. Mixture fraction distribution at a time of 0.05 ms for (a) 2D DNS and (b) 3D DNS.

Figure 7.23 shows the distribution of the scalar dissipation rate contours predicted by the 2D DNS with that of the 3D DNS at a time of 0.5 ms. It is seen that the peak scalar dissipation rates predicted by the 3D DNS are a factor of 2 to 3 greater than that predicted by the 2D DNS. This is made clearer in Fig. 7.24, which compares the scalar dissipation rate, which is conditionally averaged in the mixture fraction space, as a function of Z for the 2D and 3D DNS. It is seen that χ predicted by the 3D DNS are consistently higher than that predicted by the 2D DNS for all values of *Z*. The reason for this is believed to be the vortex stretching phenomena that is observed only for 3D DNS (Pope, 2000;

Tennekes & Lumley, 1972). Vortex stretching is the lengthening of vortices in a three-dimensional flow associated with a corresponding increase in the component of the vorticity in the stretching direction. Vortex stretching is believed to play an important role in the turbulence energy cascade by being the primary mechanism for transferring energy from larger length scales to the smaller length scales. Examining the turbulent energy spectrum can prove useful in determining the effect of this vortex stretching.

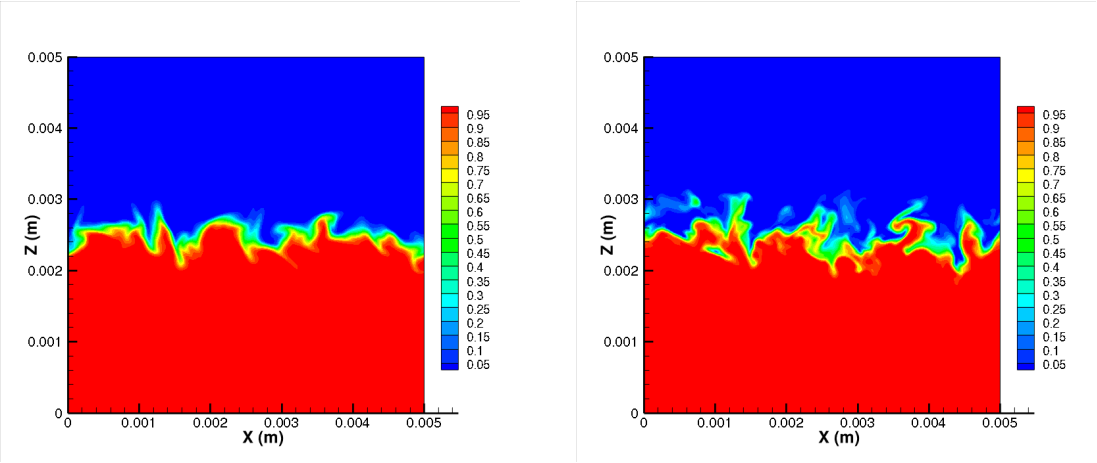

(a) (b)

Figure 7.21. Mixture fraction distribution at a time of 0.30 ms for (a) 2D DNS and (b) 3D DNS.

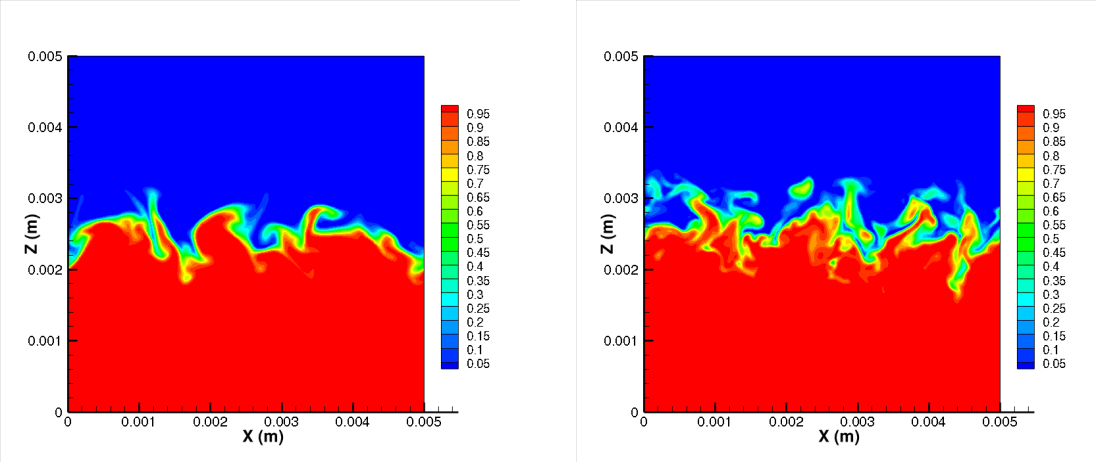

(a) (b)

Figure 7.22. Mixture fraction distribution at a time of 0.5 ms for (a) 2D DNS and (b) 3D DNS.

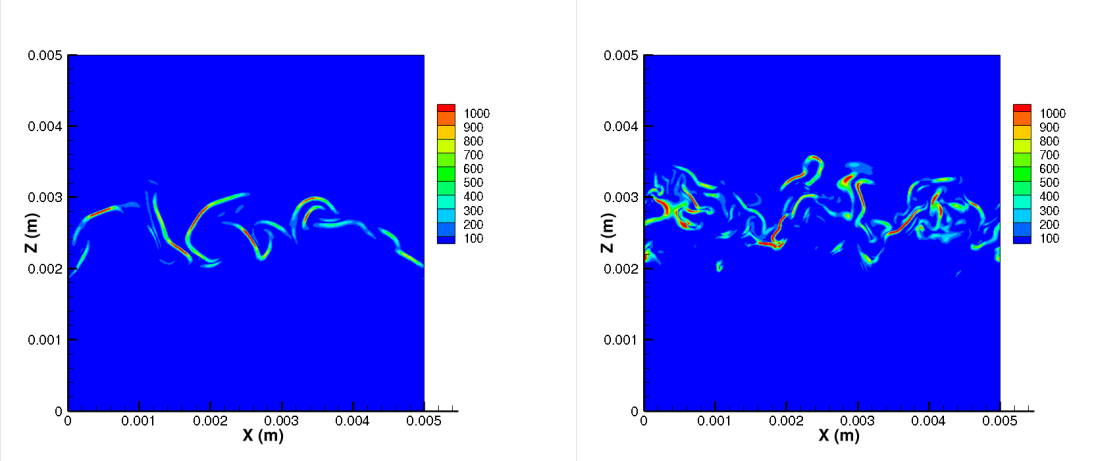

(a) (b)

Figure 7.23. Scalar dissipation rate distribution at 0.5 ms for (a) 2D DNS and (b) 3D DNS.

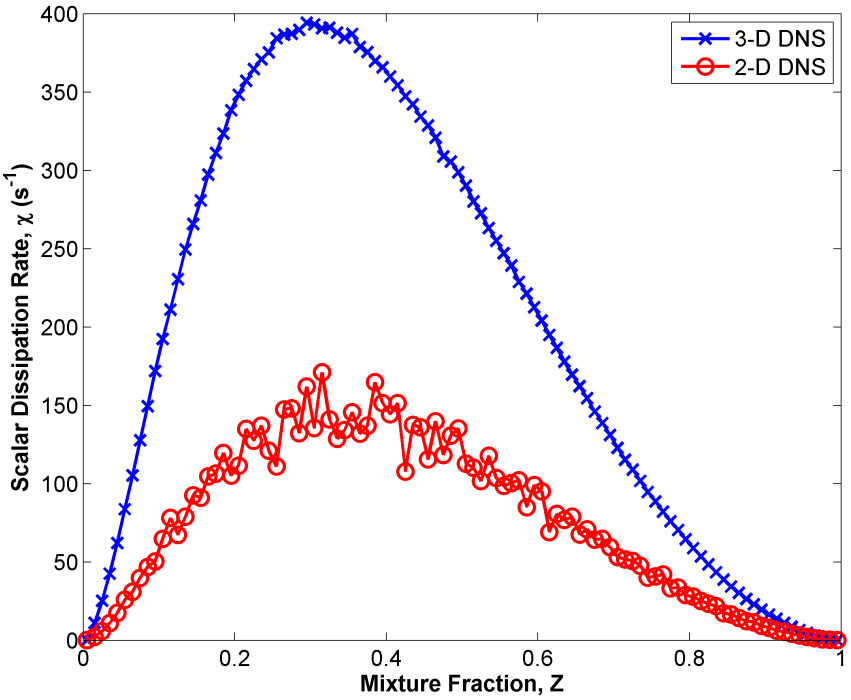

Figure 7.24. Variation of scalar dissipation rate conditionally averaged over Z, as a function of Z for 2D and 3D DNS.

7.4.2 Turbulent Kinetic Energy Spectrum

According to the Kolmogorov hypothesis (Pope, 2000), in any turbulent flow at sufficiently high Reynolds number, the high-wavenumber portion of the velocity spectra exhibit a universal behavior. It has been found that this universal behavior can be expressed as

$$E(k) \propto k^{-\frac{5}{3}}, \tag{7.23}$$

where k is the wave number and $E(k)$ is the energy corresponding to k. This behavior is strictly valid only for homogenous isotropic turbulence. Performing numerical simulations of forced isotropic homogenous turbulence can be used to validate the validity of the present computational code in retaining the spectral characteristics of turbulence. Rosales et al. (2005) performed DNS of homogenous isotropic turbulence. The computational domain was a cubic box with periodic boundary conditions on all sides. The side of the box was 2π m. They solved the compressible form of the Navier-Stokes equations with a sixth-order compact scheme for spatial discretization and a third-order Runge-Kutta method for the time integration. One of their cases where the number of grid points is 128^3 and the kinematic viscosity is equal to 4.491×10^{-3} m^2/s was repeated in this work. The turbulence in the domain was generated using the same procedure that they adopted and with a forcing term in the momentum equation to retain a statistically stationary turbulent field. Figure 7.25 compares the spectra at stationary state from the current simulation (without any mixing layer) with that obtained by Rosales et al. (2005). It can be seen that the general agreement is satisfactory. The differences in behavior at smaller scales is probably on account of the combined effect of

the use of a spatial filter (Lele, 1992) in the current simulation that is implemented to remove spurious small-scale oscillations and round-off errors.

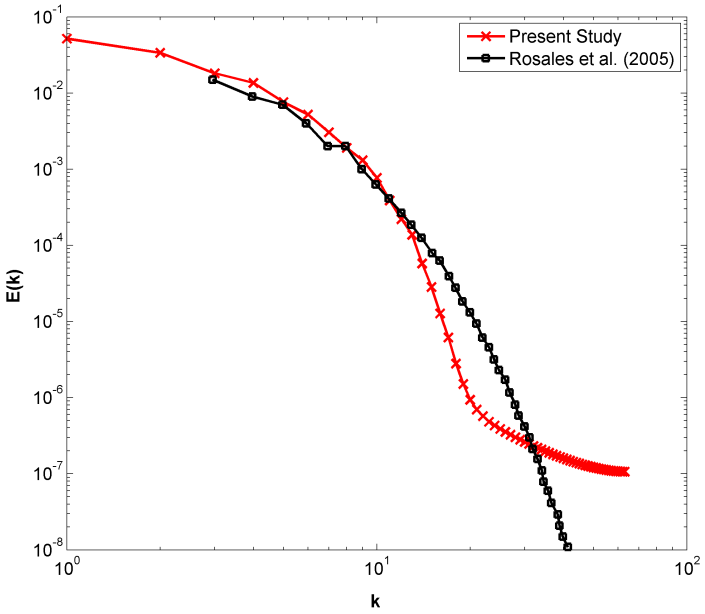

Figure 7.25. Average energy spectra at stationary state for homogenous isotropic turbulence. Also shown are the results from Rosales et al. (2005).

Results will now be shown with the mixing layer present in the domain. Note that the presence of the fuel/air mixing layer implies that the turbulence is not homogeneous or isotropic. Figure 7.26 shows the evolution of the energy spectrum for the 2D DNS at times of 0, 0.1 and 0.5 ms. Figure 7.27 shows the corresponding behavior for the 3D DNS. The domain size and grid size are smaller by three orders of magnitude compared to the simulation discussed in the last paragraph. As a result, the wave numbers are also about three orders of magnitude higher. The significant scatter observed in the energy spectra is due to the fact that the spectrum is generated from one realization of the DNS and there may be insufficient number of data points to carry out the analysis. If an

ensemble averaging is performed over multiple simulations, a smoother spectrum is expected. The energy decays with time, which is expected for homogenous decaying turbulence. As pointed out earlier, the slope of the energy spectrum in the inertial sub-range should be -5/3 for homogeneous isotropic turbulence according to Kolmogorov's hypothesis. Although the turbulence with the mixing layer is neither homogeneous nor isotropic, it is interesting to compare the slopes between the 2D and the 3D. As expected, Figs. 7.26 and 7.27 show that the slopes do not match this theoretical value either for the 2D or the 3D although with increasing time the slope is closer to the theoretical value. One interesting observation is that the turbulence is decaying as evidenced by the reduction in energy as time progresses from 0.1 ms to 0.5 ms. The slight increase in the spectra from a time of 0.0 ms to 0.1 ms for the 3D DNS is thought to be on account of the modifications of the turbulent flow field near the boundaries.

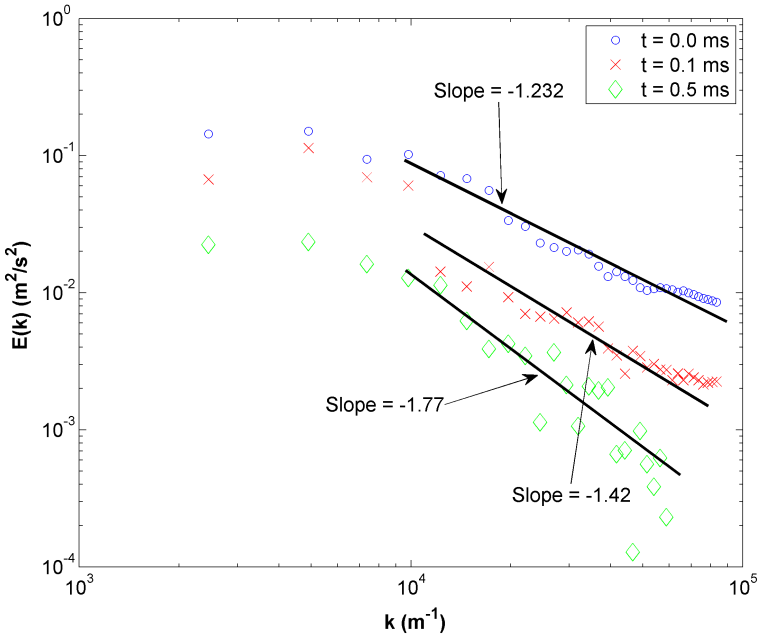

Figure 7.26. Evolution of the turbulent kinetic energy spectrum for the 2D DNS.

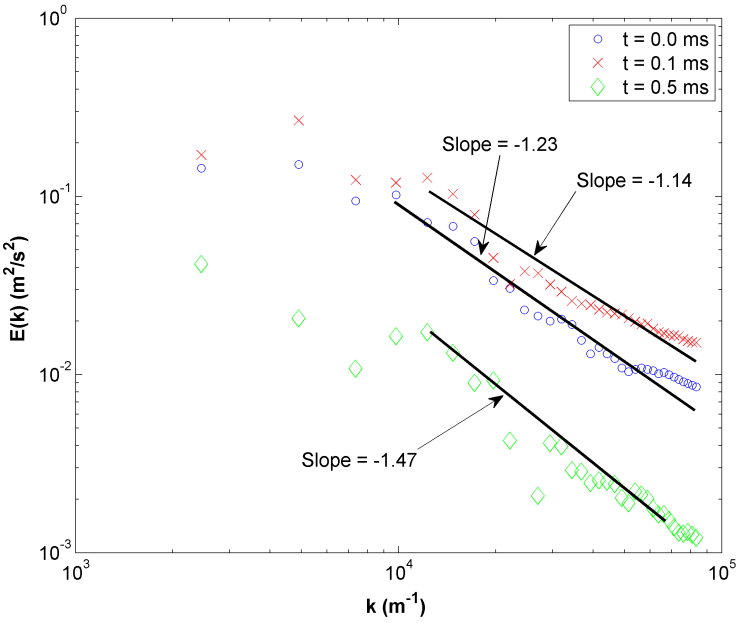

Figure 7.27. Evolution of the turbulent kinetic energy spectrum for the 3D DNS.

7.4.3 Evaluation of the Smagorinsky Model for Subgrid-Scale Stress Using 2D and 3D DNS

The subgrid-scale stress tensor is one of the important terms that require modeling in LES. This term is obtained by filtering the convection term in the momentum equation. It is given by

$$\sigma_{SG,ij} = \bar{\rho}\left(\widetilde{u_i u_j} - \widetilde{u_i}\widetilde{u_j}\right) = \mu_T\left[\left(\frac{\partial \widetilde{u_i}}{\partial x_j} + \frac{\partial \widetilde{u_j}}{\partial x_i}\right) - \frac{2}{3}\frac{\partial \widetilde{u_k}}{\partial x_k}\delta_{ij}\right], \tag{7.24}$$

where μ_T is the subgrid-scale turbulent viscosity and δ_{ij} is the kronecker delta. The most commonly used method for modeling μ_T is the Smagorinsky model given by

$$\mu_T = C\bar{\rho}\Delta^2\left(2\widetilde{S_{ij}}\widetilde{S_{ij}}\right)^{1/2}, \tag{7.25}$$

where $\widetilde{S_{ij}} = \frac{1}{2}\left[\frac{\partial \widetilde{u_i}}{\partial x_j} + \frac{\partial \widetilde{u_j}}{\partial x_i}\right]$, and C is a model constant and Δ is the filter size. In the standard Smagorinsky model, C is taken to be equal to 0.012 (Anders, Magi, & Abraham, 2007; Moin, Squires, Cabot, & Lee, 1991).

The velocity fields obtained from the 2D and 3D DNS results can be explicitly filtered for different filter sizes to determine the applicability of the Smagorinsky model for different filter sizes. In the results shown below, the constant C in Eq. 7.25 is obtained by minimizing the error norm defined as

$$E = \sum\left(\mu_{T,DNS} - \mu_{T,Smag}\right)^2, \tag{7.26}$$

where the summation is carried out over all the filtered cells.

Figure 7.28 shows the optimum value of C for 2D and 3D DNS for a range of filter sizes at times of 0.3 and 0.5 ms. A few interesting observations can be made from Fig. 7.28. The optimum C evaluated from 2D and 3D DNS are significantly different at a time of 0.3 ms. The differences reduce at a later time of 0.5 ms especially for large filter sizes. This could be due to the fact that the energy spectra for the two simulations are significantly different for times earlier than 0.5 ms as shown in Figs. 7.26 and 7.27. Another observation is that for the 3D DNS, C is seen to increase with increase in filter sizes at all times, and asymptotically approach a value of 0.015-0.018. This is well within the range of 0.01 to 0.04 reported in several previous studies (Canuto & Cheng, 1997; Ghosal & Moin, 1995; Moin et al., 1991). This behavior is along expected lines as increasing the filter size leads to a larger contribution of the unresolved scales to the turbulent stress term and hence C has to be increased to model the term accurately. The

behavior of C from the 2D DNS is very different as shown in Fig. 7.28. The changes in the value of C with time are relatively large compared to the results from 3D. In spite of the differences, the values of C predicted by the two simulations become closer as filter size and time increase.

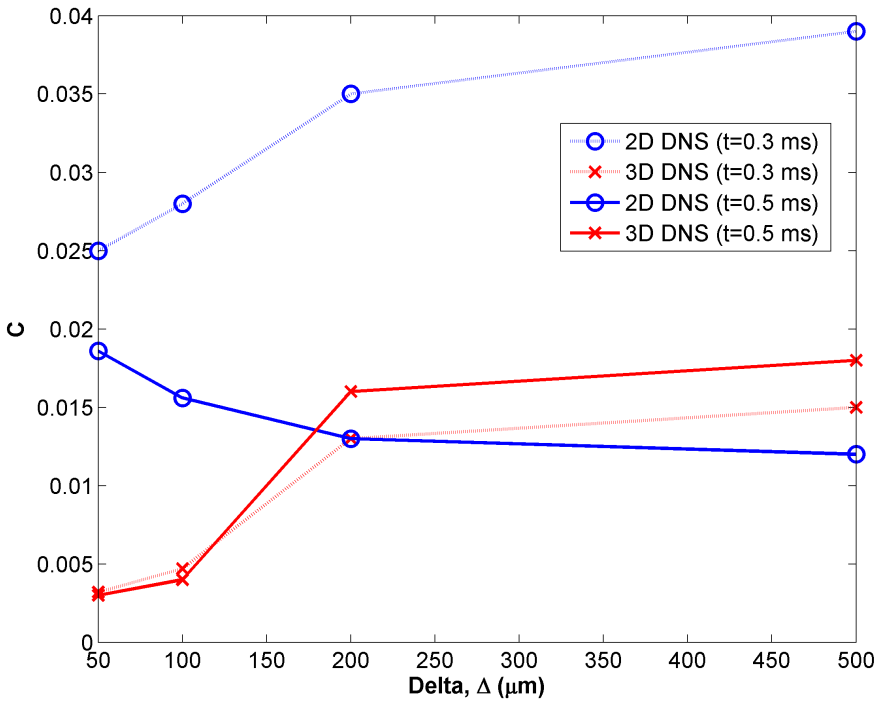

Figure 7.28. Optimum Smagorinsky model constants predicted by 2D and 3D DNS for different filter sizes.

7.4.4 Modeling the Filtered Scalar Dissipation Rate and Variance

Now, the results from the 3D DNS will be used to assess the claims made in Sec. 7.3 regarding the models for the filtered scalar dissipation rate and its variance. The DNS database is used to obtain the filtered scalar dissipation rate by explicitly filtering the DNS results using a box filter with different filter sizes ranging from 50 to 500 microns.

The TD model, SRT model and SKE model are then analyzed in detail by comparing their accuracy with that of the DNS values for the 2D and 3D mixing layers.

Figure 7.29 compares the value of irreducible error for the 2D and 3D DNS as a function of filter size. The irreducible error is here defined as the minimum error that can be obtained for a model by varying the model constant. A few conclusions can be drawn based on this figure. The SKE model performs the best among the 3 models across the range of filter sizes. The performance of the TD model is relatively poor for all the filter sizes. In fact, the error norm for the TD model is close to 1 for filter sizes greater than 50 μm, which implies that using the TD model does not provide much improvement over not using any model. It is also seen that the SRT model also performs relatively well under all conditions. The important observation from Fig. 7.29 is that both the 2D and 3D DNS results lead to the same conclusion – SKE model performs the best followed by the SRT model and then the TD model, although the actual values of the normalized errors are different.

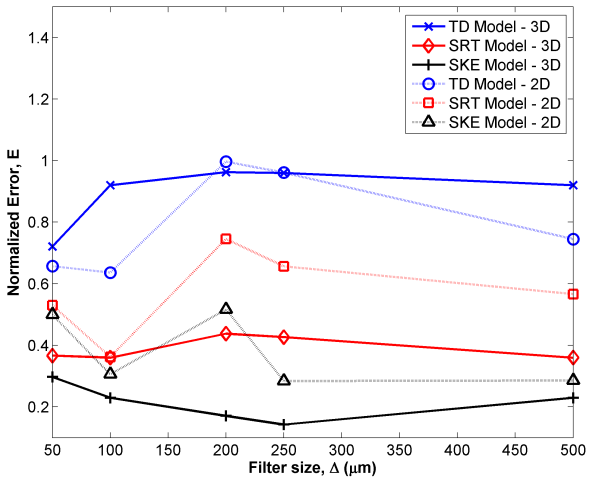

Figure 7.29. Comparison of the different models for the filtered scalar dissipation rate for the 2D and 3D DNS.

In Sec 7.3 a model for the variance of the scalar dissipation rate was proposed based on the 2D DNS. It was given by

$$\chi_{\text{var,model}} = A\widetilde{D}^2\left|\nabla\widetilde{Z}\right|^2\left|\nabla Z_{sd}\right|^2, \tag{7.28}$$

where $\widetilde{D}$ is the filtered diffusivity, $\widetilde{Z}$ is the filtered mixture fraction, Z_{sd} is the square root of the mixture fraction variance, and A is a model constant. Based on the 2D DNS, it was shown that the value of A ranged from 32 to 37 for different filter sizes. The results from the 2D and 3D DNS are now used to assess the accuracy of this value. An error norm for the scalar dissipation rate variance is defined here as

$$E_{var} = \frac{\langle(\chi_{var,model}-\chi_{var})^2\rangle}{\langle(\chi_{var})^2\rangle}. \tag{7.29}$$

The value of A in Eq. (7.28) is obtained by minimizing this error norm. Figure 7.30 compares the value of A for a range of filter sizes for the 2D and 3D DNS. It can be seen that both the 2D and 3D DNS show the same trend – the value of A increases with increasing filter sizes but the values of the constant are different. The 3D DNS results suggest a value that is 10-30 % larger. This result is consistent with the qualitative results shown in Figs. 7.18 to 7.22 where the variation in the scalar dissipation rate was predicted to be noticeably higher in the 3D results.

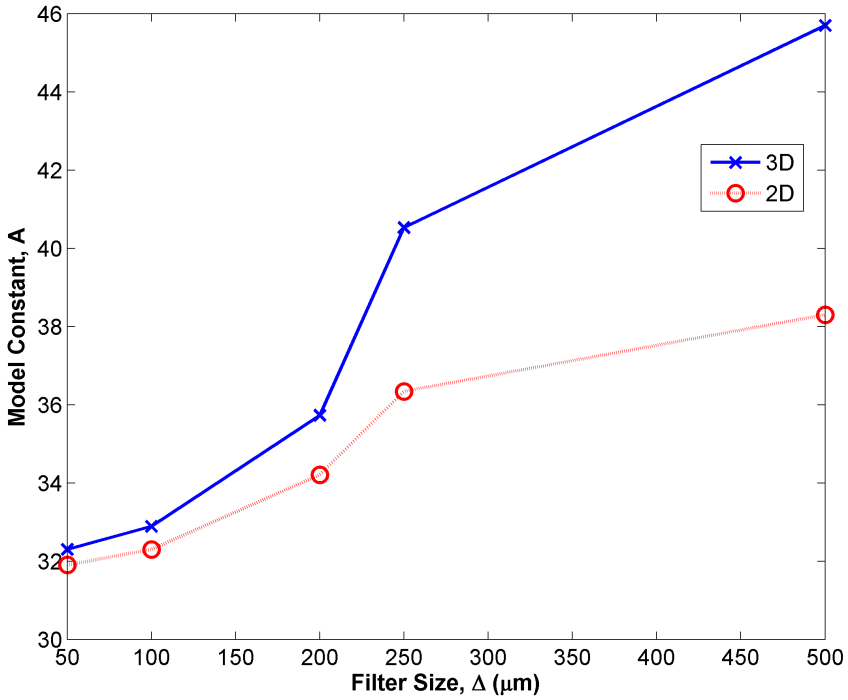

Figure 7.30. Comparison of the model constant, *A*, for the 2D and 3D DNS.

7.4.5 Conclusions

In this study, comparative studies of two-dimensional and three-dimensional DNS of turbulent non-reacting fuel/air mixing layers are carried out. It is found that the evolution of the scalar field and its dissipation rate are noticeably different in the two simulations. It is seen that the three-dimensional velocity fields induce large gradients in the scalar field which can cause breakup of the mixing layer. These differences may arise from the vortex-stretching phenomenon which is captured by the 3D DNS but not the 2D DNS. The evolution of the energy spectrum is also seen to be different for the 2D and 3D DNS. An evaluation of the model constant for the Smagorinsky subgrid scale model leads to values of the constant that lie within the recommended range of 0.01 to 0.04 for both 2D and 3D. The dependence of this constant on filter size and time for 2D and 3D are

different possibly on account of the significant differences in turbulent strain rates and their evolution in time. When the databases are employed to assess the performance of various models for the filtered scalar dissipation rate and its variance, the same conclusion is arrived at regarding the best model. It appears from these simulations that qualitative assessment can be carried out with 2D DNS databases.

Although the conclusions regarding the validity of the "2D" DNS has been assessed only for non-reacting flows, an assumption can be made that similar conclusions can be made about reacting flows as well. This is a reasonable assumption because the presence of chemical reactions is not expected to cause a fundamental difference to the turbulent flow characteristics except at the smallest scales. In the next section, 2D DNS of turbulent reacting mixing layers will be used to assess the validity of the UFPV model as a subgrid-scale combustion model for LES.

7.5 Validity of the Flamelet Model and Improvements in UFPV Implementation

If the chemical reaction scales are short compared to the convection and diffusion scales, the combustion takes place within asymptotically thin layers embedded in the turbulent flow. These layers are called as flamelets. The underlying assumption in the UFPV model is that the structure of the flame is that of a flamelet. Under these conditions, the flame can be assumed to be locally one-dimensional in the mixture fraction (Z) space. Within these reaction zones, which are called as flamelets, the evolution of the species mass fractions are governed by the unsteady flamelet equations given by

$$\frac{\partial \phi}{\partial t} = \frac{\chi}{2}\frac{\partial^2 \phi}{\partial Z^2} + \dot{\omega}_\phi, \tag{7.30}$$

where ϕ is a vector representing the set of all reactive scalars, which includes the temperature and mass fractions of all the species, and $\dot{\omega}_\phi$ is the corresponding source term due to chemical reactions. The symbol χ is the instantaneous scalar dissipation rate defined as

$$\chi = 2D\left|\nabla Z\right|^2, \tag{7.31}$$

where D is the molecular diffusivity and $\left|\nabla Z\right|^2$ is the square of the gradient of mixture fraction. χ is an input parameter for the flamelet model and depends on the mixture fraction distribution inside the flame. In this section, the flamelet assumption is first assessed by comparing the temperature evolution predicted by DNS with that predicted by solving the flamelet equations. *Note that parts of this section have been submitted to* ***Combustion and Flame*** *and is under review*.

The computational setup used to assess the flamelet model is the same as that shown for the turbulent reacting mixing layer shown in Sec. 7.3 (refer to Fig. 7.1). The turbulent length scale l_0 is selected to be 500 μm, which is 0.1 times the length of the domain in either x or y direction. Initial turbulence intensities u' is selected to be 1.0 m/s. The mixing layer thickness, δ, is chosen to be 120 μm. In addition to the 2D turbulent simulations discussed in Sec. 7.3, laminar simulations are also performed in a domain measuring 0.5 mm x 5.0 mm, so it is essentially 1-D in nature. The fuel-air mixing layer

is initialized using a hyperbolic tangent profile in the y-direction as shown in Eq. (7.1) and Fig. 7.2.

Before analyzing the performance of the flamelet model, it is important to study the effect of the grid resolution employed in the laminar simulation on the flame development. Figure 7.31 compares the evolution of the maximum temperature in the domain for grid sizes of 10 μm, 5 μm and 4 μm for the case where the initial temperature is uniform in the domain at 1000 K. As the differences between the 5 μm and 4 μm cases are small, the 5 μm case is employed in the simulations for the one-dimensional laminar and the two-dimensional DNS. The effect of resolution is made clearer in Fig. 7.32, which shows the temperature distribution in mixture fraction space for times of 0.15 and 0.2 ms. It is interesting to note that the Kolmogorov length scale for the turbulent case described in the previous section is 11 μm. So, for the reacting DNS, the grid size of 5 μm resolves both the turbulent scales and the reacting mixing layer.

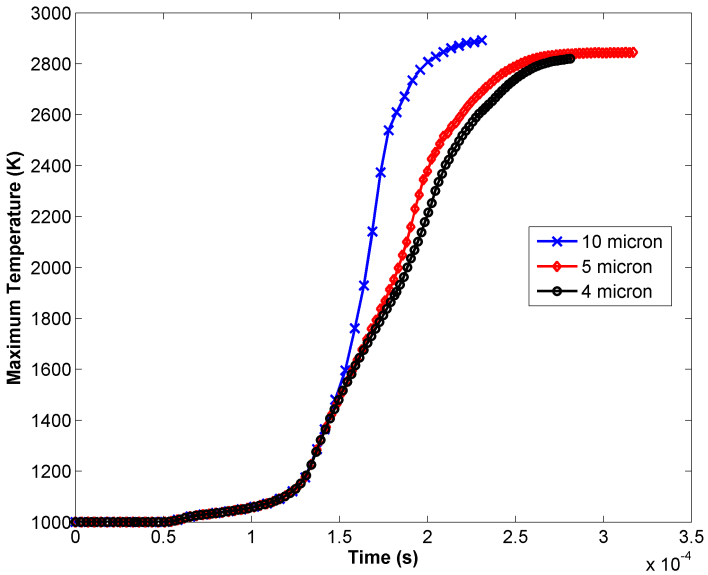

Figure 7.31. Evolution of the maximum temperature in the domain for the laminar simulation with grid sizes of 10 μm, 5 μm and 4 μm.

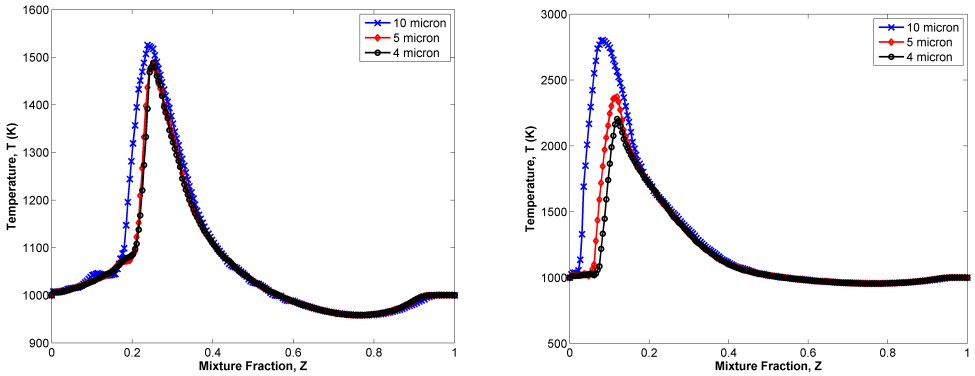

(a) (b)

Figure 7.32. Distribution of temperature in mixture fraction space for the laminar simulation at times of (a) 0.15 ms and (b) 0.20 ms.

7.5.1 Validity of the "Flamelet" Approximation

Comparing the temperature evolution predicted by DNS with that predicted by solving the flamelet equations (Eq. (7.30)) is used to test the validity of the flamelet assumption. To solve the flamelet equations the distribution of the scalar dissipation rate,

χ, in the Z-space has to be prescribed. The approach used in UFPV model implementations is to use a constant functional form for χ, usually an error-function profile, which is discussed later in Sec. 7.5.2. However, to test whether the flame behaves like a flamelet, it is more appropriate to solve the flamelet equations using the actual unsteady χ profiles obtained from the DNS.

Figure 7.33 shows the scalar dissipation rate plotted as a function of mixture fraction at different times during the flame development for the laminar simulation. There is very little change in the scalar dissipation rate prior to autoignition. Subsequently, the scalar dissipation rate profile changes considerably as the temperature rises and the flame develops. The heat release due to chemical reactions, which raises temperature and reduces density, causes local expansion, which leads to local reduction in the scalar dissipation rate. The effect of expansion is to reduce $|\nabla Z|^2$ in Eq. (7.31). On the other hand, the increase in temperature increases the diffusivity D in Eq. (7.31) and this can lead to increase in χ if the effect is greater than that of local expansion. An increase in scalar dissipation rate can lead to increased diffusion of active radicals near the flame front and thus faster flame development. The flamelet model utilizing a constant functional form may not capture this behavior.

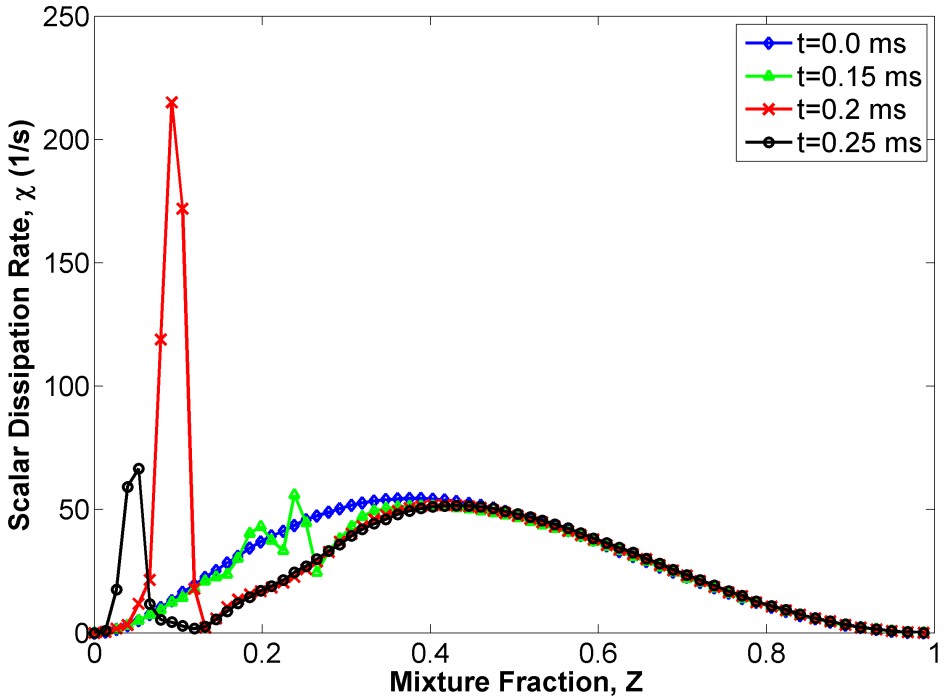

Figure 7.33. Evolution of scalar dissipation rate profiles for the laminar simulation.

The χ profiles from the laminar simulation are tabulated as a function of time and employed in solving the flamelet equations. This approach for solving the flamelet equations is henceforth referred to as the corrected flamelet model. Figures 7.34 (a) – (d) compares the performance of the corrected flamelet model with that of the laminar simulations for the uniform temperature case. DNS of a developing turbulent flame are also carried out with the turbulent conditions described in the previous section. The conditionally-averaged temperature profiles from the turbulent simulations (DNS) are also shown in Fig. 7.34. A few interesting observations can be made regarding Fig. 7.34. Firstly, the temperature profiles obtained from the laminar simulation and the conditionally-averaged temperature profiles from the turbulent simulation agree closely at all times. This validates one of the primary assumptions of the flamelet model for the conditions considered here – the turbulent flow field does not affect the internal structure

of the flame. For higher levels of turbulence, when the Kolmogorov scales are comparable to smaller than the reaction zone thickness, this observation may not hold. The other observation is that the corrected flamelet model predictions agree very closely with the laminar and DNS predictions. In fact, the error is found to be less than 5 % at all times and, as expected, the agreement is very close at steady-state.

From the discussion in this section, it can be concluded that the flamelet assumption is a valid approximation – the flame development predicted by solving the flamelet equations reproduces the flame development predicted by DNS, provided an accurate description of χ is prescribed. However, the approach discussed here of using the χ from the laminar simulations is not very practical. In the next section, the methodology used in the UFPV model for prescribing χ is critically assessed.

7.5.2 Validity of the UFPV Model Implementation

The UFPV model that was employed in the RANS and LES results shown in this study was discussed in Sec. 3.2. It was shown that the scalar dissipation rate, χ, is an important variable used in flamelet models. The functional form of the dependence of χ on the mixture fraction, Z, is typically assumed to follow an error function profile (Peters, 2000; Mukhopadhyay and Abraham, 2012) that is assumed to be independent of time, i.e.,

$$\chi = \chi_{st} \frac{\exp\{-2[erfc^{-1}(2Z)]^2\}}{\exp\{-2[erfc^{-1}(2Z_{st})]^2\}}. \tag{7.32}$$

By using this assumption, the value of the scalar dissipation rate at any Z can be related to its value at the stoichiometric mixture fraction, χ_{st}.

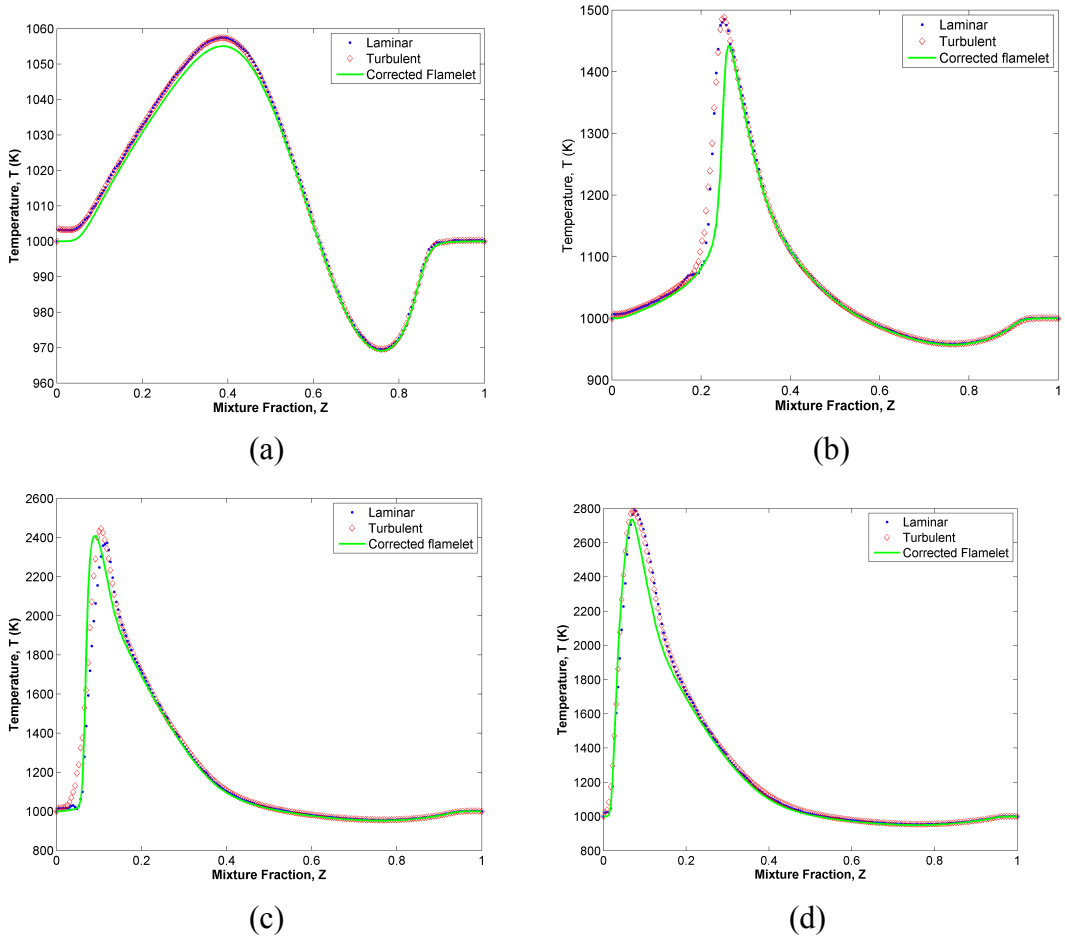

Figure 7.34. Comparison of the temperature profiles predicted by the corrected flamelet model with that predicted by the laminar and turbulent reacting mixing layers at times of (a) 0.10 ms, (b) 0.15 ms, (c) 0.20 ms and (d) 0.25 ms.

To test the validity of this approximation, the flamelet equations (Eq. (7.30)) are solved with the constant functional form for χ given by Eq. (7.32). Figures 7.35 (a) – (d) compares the temperature profiles as a function of the mixture fraction Z at four times during the flame development for the uniform temperature case. In addition to the

temperature evolution for the single flamelet, also shown are the temperature evolution obtained for multiple flamelets. The solution with the multiple flamelets is obtained by solving the flamelet equations for stoichiometric scalar dissipation rates, χ_{st}, ranging from 1 s^{-1} to 200 s^{-1}. The temperatures obtained from this solution are then tabulated as a function of Z, time, and χ_{st}. This look-up table is then employed to determine the temperature in the laminar simulations (Venugopal and Abraham, 2007). Figure 7.35 (a) shows that when the rise in temperature is relatively small, i.e. about 10% higher than the initial value, the flamelet and laminar predictions are within 1%. Figure 7.35 (b) shows that the differences increase to about 10% when the rise in temperature is about 50%, i.e. to 1500 K from 1000 K, and Fig. 7.35 (c) shows even larger differences. In fact, Fig. 7.33 (c) shows that the "ignition front" propagates faster toward the steady-state flame profile than predicted by the flamelet. Figure 7.35 (d) shows that there are noticeable differences even at 0.25 ms at which time the laminar simulation has already reached steady-state. Another interesting observation is that the differences between the solutions obtained using a single flamelet and using multiple flamelets increases with time. The reason for this is that heat release due to chemical reactions causes the scalar dissipation rate in the laminar simulation to change significantly in the reaction zone, as was shown in Sec 7.5.1. In principle, a single flamelet should be sufficient in the laminar simulation. However drastic spatial and temporal changes in the value of the scalar dissipation rate results in temperature profiles from different flamelets being mapped at values of Z that are not very different. This results in significant deviations in temperature. It should be noted that the multiple flamelet formulation is the most commonly used approach to model combustion in LES and RANS codes (Bajaj et al., 2013; Ihme and Pitsch, 2008;

Ihme and See, 2010). In any case, it can be concluded that the flamelet model in the present form, with error function profiles for the scalar dissipation rate, is inadequate in predicting the flame development even in the absence of turbulence.

Although the corrected flamelet approach discussed in Sec. 7.5.1 leads to improved predictions, it is not a very practical as it requires solving an autoigniting laminar mixing layer to generate the scalar dissipation rate profiles which is then used as in input for the flamelet model. Multiple laminar simulations will have to be performed with varying mixing layer thicknesses to use the corrected flamelet model for a practical simulation. It would be more practical to incorporate the change in scalar dissipation rate á priori without performing the laminar simulations. Equation (7.31) shows that the scalar dissipation rate can change due to changes in the mixture-fraction diffusivity, D, and changes in the mixture fraction gradient $|\nabla Z|$.

Figure 7.36 shows the evolution of χ, D, $|\nabla Z|^2$, and the density from the laminar simulation. Figure 7.36 (a) shows that the largest change in χ occurs between the times of 0.15 and 0.20 ms. During the same time frame, the change in diffusivity, D, is much larger than the change in $|\nabla Z|^2$ as shown in Figs. 7.36 (b) and 7.36 (c). Figure 7.36 (c) shows the evolution of the square of the mixture fraction gradient $|\nabla Z|^2$, during the flame development process. Chemical reactions cause local expansion, which leads to reduction in the mixture fraction gradient. From a purely physical argument, it may be assumed that the reason for the change in the mixture fraction gradient is the change in the local density. $|\nabla Z|$ can be assumed to be directly proportional to the local density. Local

expansion causes the density in the flame region to reduce, which causes the iso-lines of mixture fraction to become further apart and thus lead to reduction in $|\nabla Z|$. However, Fig. 7.36 (d) shows that this effect is not felt locally. Indeed, the reduction in $|\nabla Z|$ does correspond to reduction in the local density up to 0.15 ms. Beyond this time, the relationship does not hold. The heat release due to chemical reactions leads to the generation of expansion waves that give rise to this highly transient behavior in the mixture fraction gradients. In any case, it was concluded from the previous discussion that changes in the diffusivity, *D*, is the most important reason for the changes in χ. The diffusivity, *D*, is strongly dependent on temperature and weakly dependent on the species mass fractions. This strong effect of changing diffusivity on the evolution of χ suggests that an improved flamelet model may be one which accounts for the change in scalar dissipation rate due to change in *D*. A new model is proposed, henceforth referred to as *diffusivity-modified flamelet model*, given by

$$\chi_{model} = \chi_{st} \frac{\exp\left\{-2\left[erfc^{-1}(2Z)\right]^2\right\}}{\exp\{-2[erfc^{-1}(2Z_{st})]^2\}} \frac{D}{D_0}, \tag{7.33}$$

where D_0 is the initial diffusivity for Z=0 in the flamelet simulation.

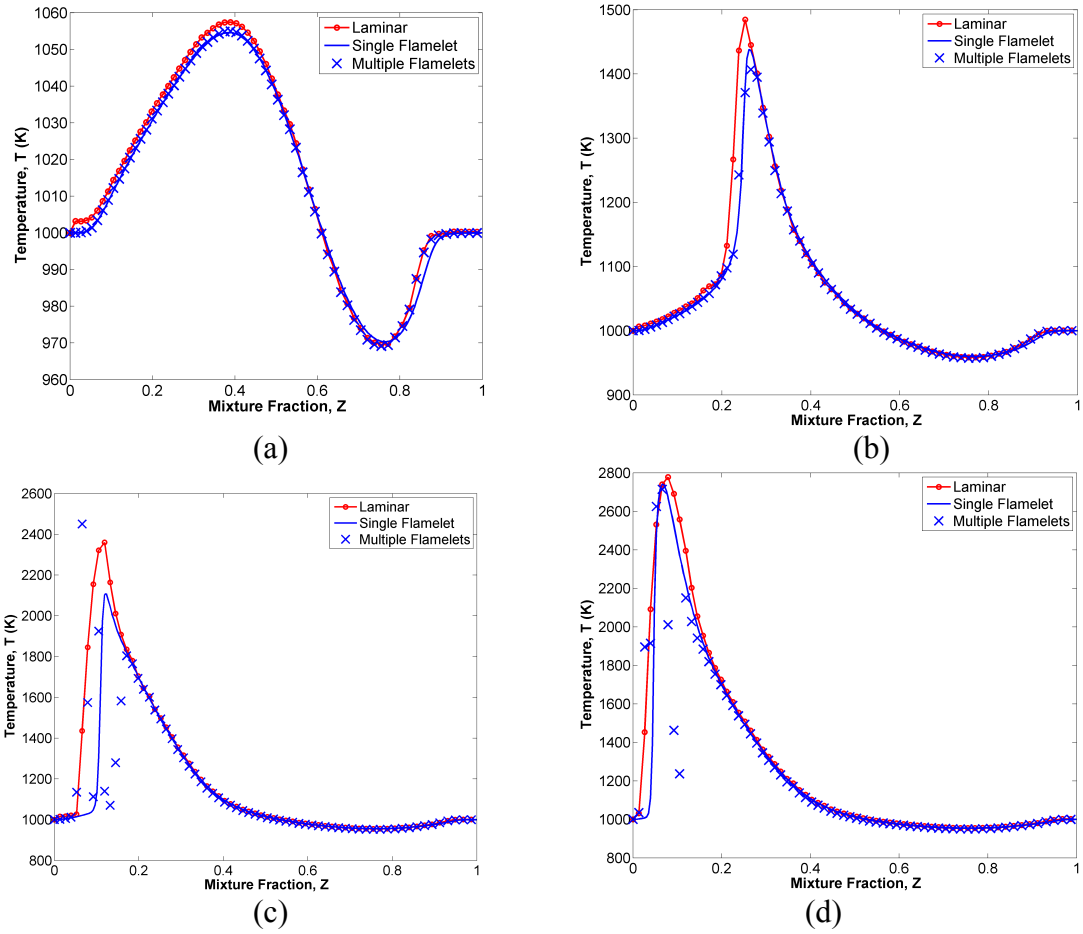

Figure 7.35. Comparison of the temperature profile from the laminar simulation with that from the single flamelet and multiple flamelets at (a) 0.1 ms, (b) 0.15 ms, (c) 0.2 ms, and (d) 0.25 ms.

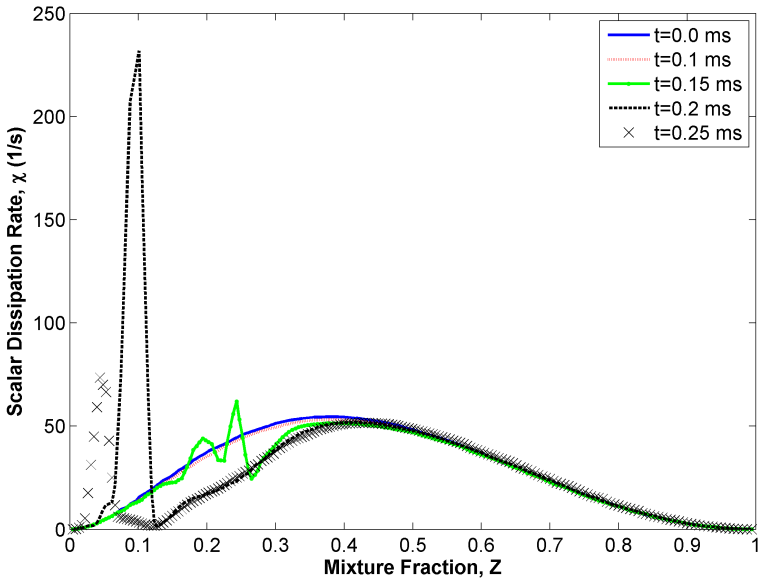

(a)

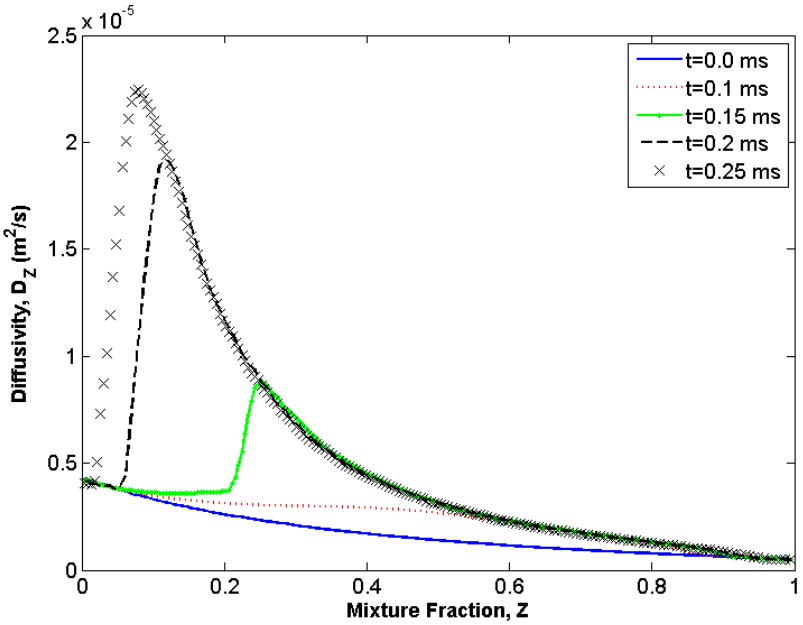

(b)

Figure 7.36. Evolution of (a) scalar dissipation rate, χ , (b) diffusivity, D, (c) square of the mixture fraction gradient, and (d) density for the laminar case.

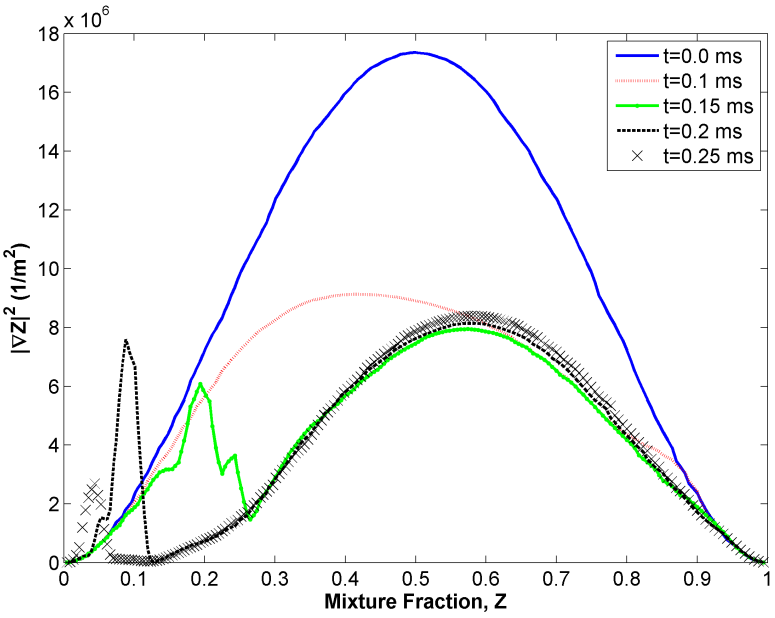

(c)

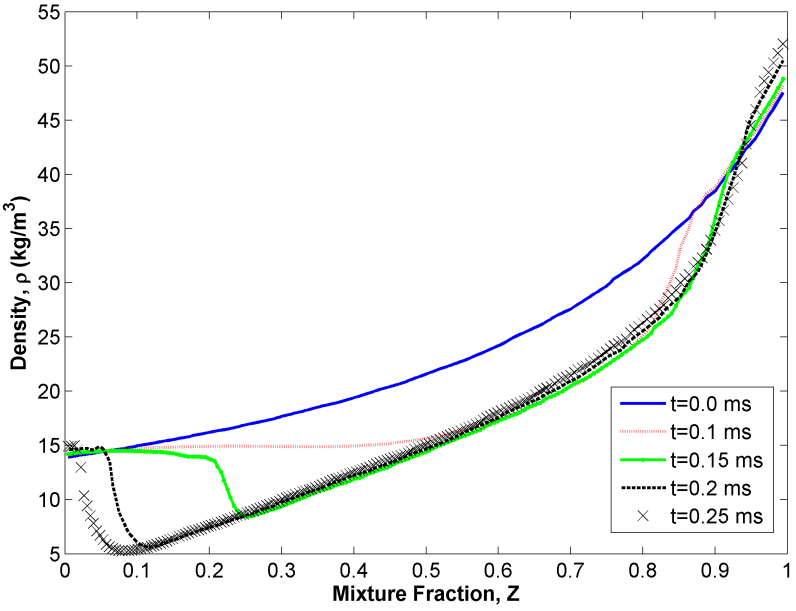

(d)

Figure 7.36. Continued.

Figures 7.37 compare the evolution of the scalar dissipation rate profiles predicted by the *diffusivity-modified model* with that predicted by the DNS. It can be seen that this model is able to account for the increase in χ in the high-temperature region accurately where temperature has risen and chemical reactions are predominant. Consider Fig. 7.37 (b) when the rise in temperature is about 500 K (see Fig. 7.34 (b)) and the ignition front is located at about a mixture fraction value of about 0.3. The ignition front is defined as the region where there is a sharp gradient in temperature on the lean side, which is the direction in which the developing front is propagating. In this region, the diffusivity in the diffusivity-modified model can be seen to rise from about 80 /s to about 180 /s. This change is more than the change in the laminar simulation, in part because during this early stage the expansion causes the gradient of mixture fraction to decrease. Subsequently, the increase in diffusivity corresponds closer to the rise in diffusivity in the laminar simulation in the mixture fraction space where the flame front is propagating (compare with temperature profiles in the corresponding figures in Fig. 7.34 at the same time).

Figure 7.38 compares the evolution of temperature profiles predicted by DNS with that predicted by the diffusivity-modified flamelet model and the single flamelet with the error function profile. It can be seen that the new model leads to significantly improved prediction of temperature profile and it is comparable to the predictions obtained using the corrected flamelet model (refer to Fig. 7.34) and the laminar simulation. The errors in the temperature profile are higher than that predicted by the corrected flamelet model, but it is still within 10 % and the errors are limited to regions of high temperatures. It can be concluded that diffusivity-modified flamelet model shows an

improvement over the traditional approach of using a constant functional form in solving the flamelet equations. The additional advantage of this model is that it can be easily incorporated into the traditional tabulation framework that is used when flamelet models are employed in RANS simulations (Bajaj et al., 2013) and LES (Ihme and Pitsch, 2008; Ihme and See, 2010, Ameen and Abraham, 2014a).

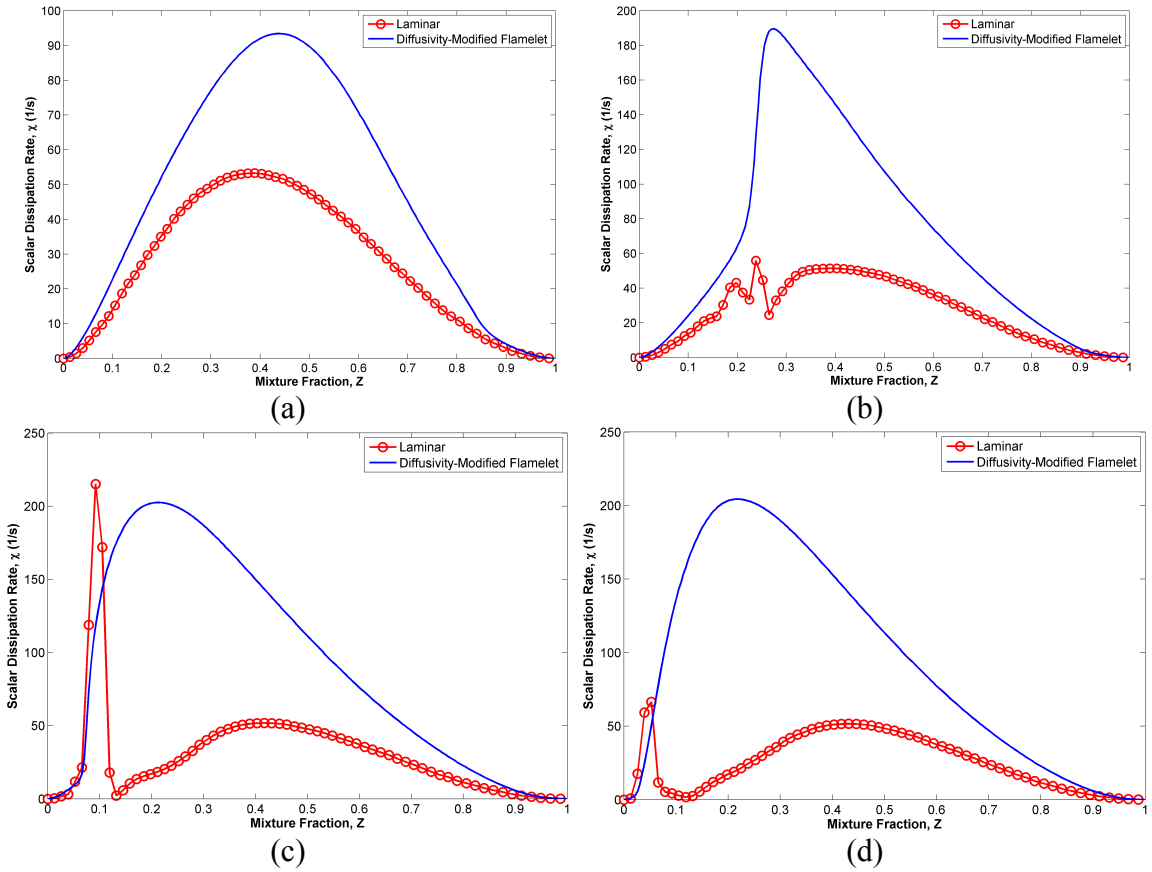

Figure 7.37. Comparison of the scalar dissipation rate profiles for the diffusivity-corrected model with that for the laminar simulations at (a) 0.1 ms, (b) 0.15 ms, (c) 0.2 ms, and (d) 0.25 ms.

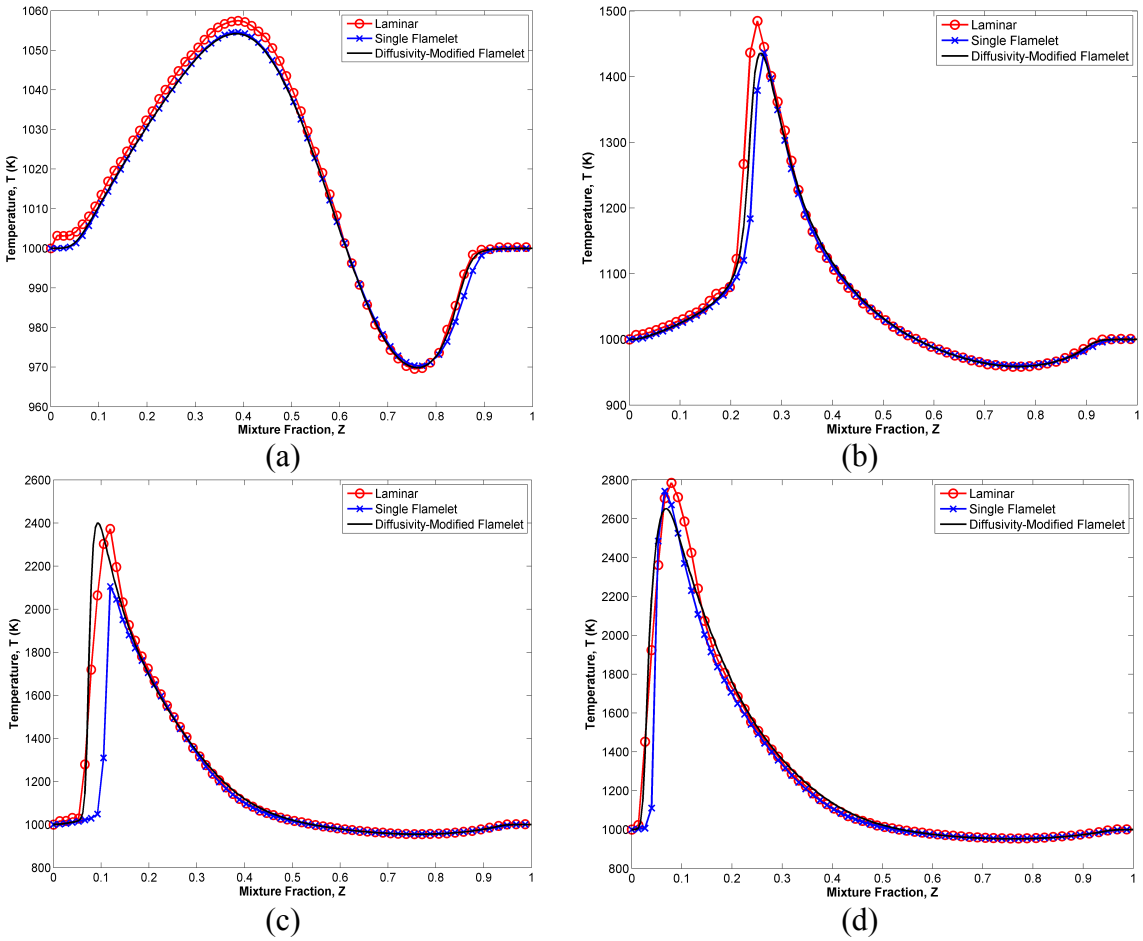

Figure 7.38. Comparison of the temperature profiles for the diffusivity-corrected model with that for the laminar simulations at (a) 0.1 ms, (b) 0.15 ms, (c) 0.2 ms, and (d) 0.25 ms.

7.5.3 Conclusions

In this study, one-dimensional laminar simulations and two-dimensional turbulent DNS are carried out of an autoigniting n-heptane/air mixing layer. The results are employed to assess the accuracy of an unsteady flamelet model in predicting the flame development. A constant functional form (error function) representation of the scalar dissipation rate is employed in the unsteady flamelet simulation. It is shown that the flamelet model predictions differ significantly from the laminar simulation and DNS results during the flame development process following autoignition. Differences arise

from the use of the constant functional form for the scalar dissipation rate profiles. The laminar and turbulent simulations show that during the flame development, the rise in temperature resulting from heat release leads to significant changes in the scalar dissipation rate profiles on account of changes in molecular diffusivity and thermal expansion. It is shown that solving the unsteady flamelet equations using the time-dependent scalar dissipation rate profiles obtained from the laminar simulations leads to less than 5% difference in the temperature profiles. This confirms that the origin of the difference between the solutions does, in fact, arise from the use of the constant error-function profile. Since using time-dependent scalar dissipation rate profiles from laminar simulations is not computationally feasible for practical applications, a new model is proposed to modify the error function profile to account for the change in temperature. It is shown that changes in diffusivity, D, is the major cause of the change in the scalar dissipation rate. In the newly proposed diffusivity-corrected flamelet model, the increase in scalar dissipation rate due to increased diffusivity at high temperatures is accounted for. This model shows significant improvements over the traditional flamelet approach and the differences in the temperature profiles are found to be limited to 10%. It can be concluded that the flamelet model using constant functional forms for the scalar dissipation rate will lead to significant differences in the unsteady flame development whereas the diffusivity-corrected flamelet model is a viable alternative to the traditional flamelet approach.

In the next section, the performance of the UFPV model is compared with that of the perfectly-stirred reactor (PSR) model.

7.6 Comparison of UFPV and PSR Models

In prior work, the perfectly-stirred reactor (PSR) model (Lucchini, D'Errico, Ettorre, & Ferrari, 2009; Pei, Hawkes, & Kook, 2011; Som & Aggarwal, 2010), the unsteady flamelet progress variable (UFPV) model with á-priori PDFs (Bajaj, Ameen, & Abraham, 2013), flamelet-generated manifolds (Bekdemir, Somers, & de Goey, 2011), conditional moment closure (CMC) models with á- priori PDFs (Wright, Depaola, Boulouchos, & Mastorakos, 2005), and transported PDF (Pei, Hawkes, & Kook, 2013) models have been evaluated as subgrid-scale combustion models for diesel engine applications. In this section, the performance of the PSR model and the UFPV model as turbulent combustion models for diesel engine conditions are evaluated. These two models are more common in RANS simulations and LES of engine combustion (Hu, Jhavar, Singh, Reitz, & Rutland, 2007; Hu & Rutland, 2006; Kong & Reitz, 2002). The computational setup used to assess the flamelet model is the same as that shown for the turbulent reacting mixing layer shown in Sec. 7.3 (refer to Fig. 7.1 and table 7.1). *Note that parts of this section have been submitted to* ***Fuel*** *and is under review*.

7.6.1 Evolution of Turbulent Reacting Mixing Layer

In this section, the evolution of the turbulent reacting mixing layer from the DNS will be examined in detail. For this purpose, a formation rate, $\dot{\omega}_C$, is defined as the sum of the reaction rates of the major products – CO_2, CO, H_2O and H_2 – i.e.,

$$\dot{\omega}_C = \dot{\omega}_{CO2} + \dot{\omega}_{CO} + \dot{\omega}_{H_2O} + \dot{\omega}_{H_2}. \tag{7.34}$$

Figure 7.39 shows the evolution of the maximum temperature in the domain, T^{Max}, and the maximum formation rate, $\dot{\omega}_C^{Max}$, as a function of time for the baseline case (u'=1.0 m/s and δ=120 microns). A two-stage ignition process is seen with $\dot{\omega}_C^{Max}$ initially showing a peak at about 0.07 ms and then showing larger peak at 0.15 ms. This two-stage ignition behavior has been observed for n-heptane flames (Mukhopadhyay & Abraham, 2011). The variation of T^{Max} follows that of $\dot{\omega}_C^{Max}$ in that the rate of increase of T^{Max} is highest when $\dot{\omega}_C^{Max}$ is high. By 0.3 ms, the formation rate reaches steady values that are much lower than the peak values observed during ignition. After this time, the maximum temperature is also steady.

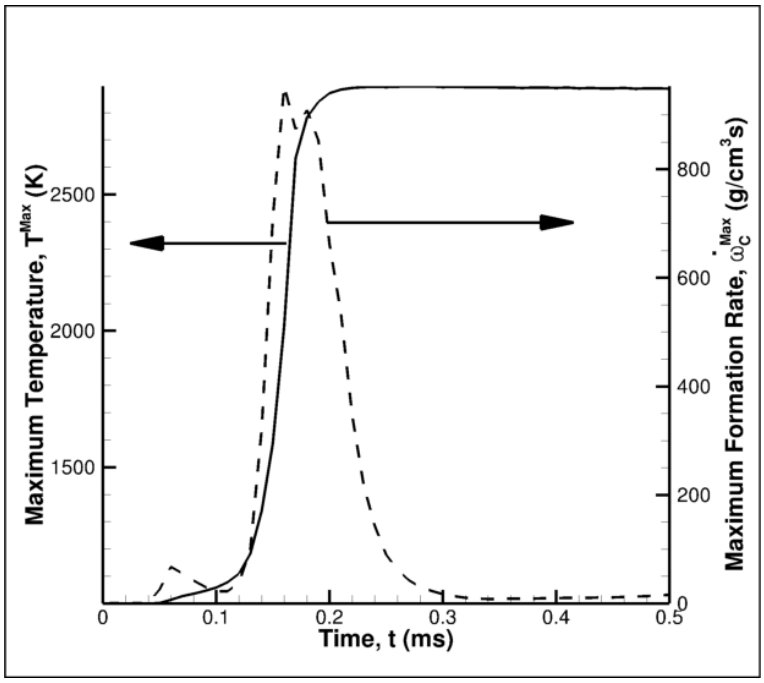

Figure 7.39. Evolution of maximum temperature and maximum formation rate in the domain as a function of time for the baseline case (u'=1.0 m/s, δ=120 microns).

In addition to looking at the maximum formation rate, $\dot{\omega}_C^{Max}$, it is also important to understand the spatial distribution of $\dot{\omega}_C$. Figure 7.40 shows the contours of $\dot{\omega}_C$ in the

computational domain for the baseline case at times of 0.1, 0.15, 0.2, 0.25 and 0.5 ms. Notice that these times are selected to evaluate the flame structure at times before, during, and after the autoignition process (refer to Fig. 7.37). Figure 7.40 (a) shows that at a time of 0.1 ms, which is just after the first stage of autoignition, the formation rates are lower than 20 g/cm^{3}s. After the second-stage of ignition is initiated, the formation rates increase exponentially as shown in Fig. 7.40 (b) and Fig. 7.40 (c). It is seen that the peak formation rates increased from 20 g/cm^{3}s at 0.1 ms to 650 g/cm^{3}s at 0.15 ms. Another interesting observation is that the thickness of the reaction zone reduces considerably during the same timeframe. For the purpose of the discussion that follows, a reaction zone thickness is defined based on the average thickness of a layer where the formation rate is within 10% of the maximum value of the formation rate. Figure 7.41 shows the evolution of the reaction zone thickness as a function of time for the baseline case. It can be seen that the reaction zone thickness reduces from approximately 275 μm at 0.1 ms to 30 μm at 0.15 ms.. After the flame temperature reaches steady values, the formation rates reduce to 15 g/cm^{3}s and the reaction zone thickness increases to approximately 200 μm, as shown in Figs. 7.40 (e) and 7.41. The observation that the formation rates are highly localized in physical space, especially during the early flame development, makes the evaluation of subgrid-scale combustion models challenging.

Figure 7.42 shows the distribution of the formation rates, conditionally averaged on Z, in the mixture fraction (Z) space at different times during the flame development. It is seen that the formation rates are localized in the mixture fraction space. This is not surprising given that they are also localized in physical space as discussed earlier. An ignition front propagation is also observed which shows the location of the peak

formation rate shifting from a rich mixture of Z=0.2 at a time of 0.15 ms to a stoichiometric mixture with Z=0.06 at a time of 0.2 ms. Once the flame has stabilized at the stoichiometric mixture fraction, the combustion appears to be mixing-controlled as is well known for diffusion flames.

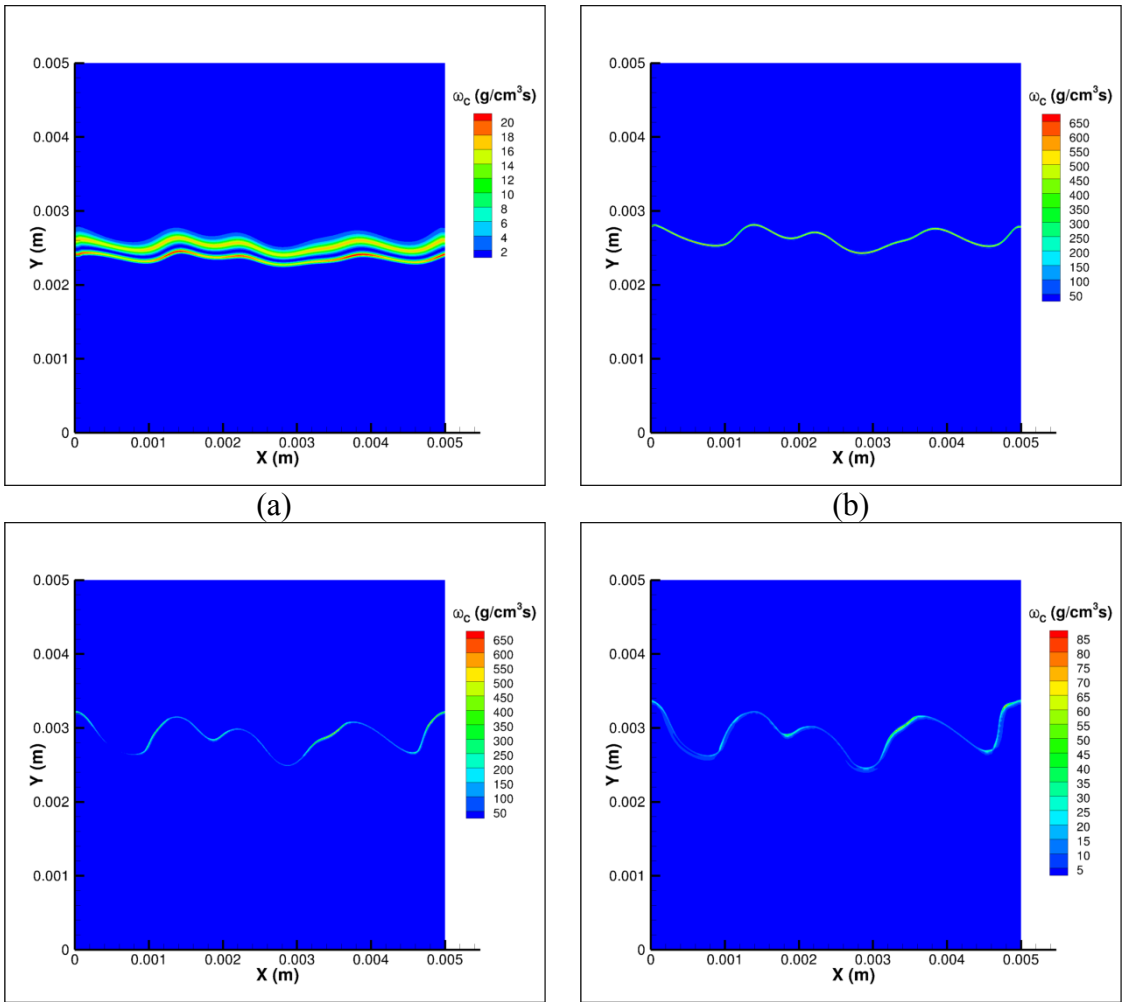

Figure 7.40. Evolution of $\dot{\omega}_C$ contours for the baseline case (u'=1.0 m/s and δ=120 microns) at (a) 0.1 ms, (b) 0.15 ms, (c) 0.2 ms, (d) 0.25 ms, and (e) 0.5 ms.

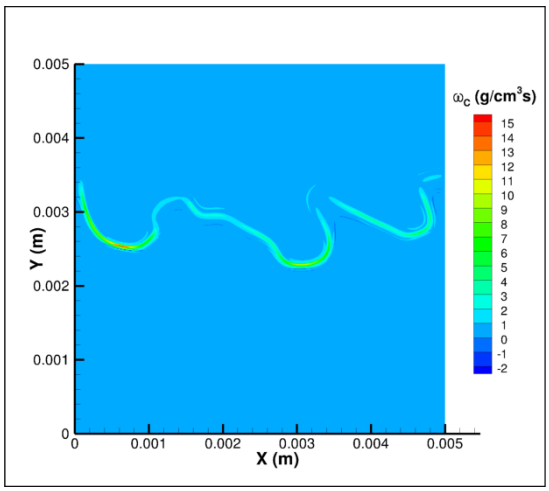

(e)

Figure 7.41. Contd.

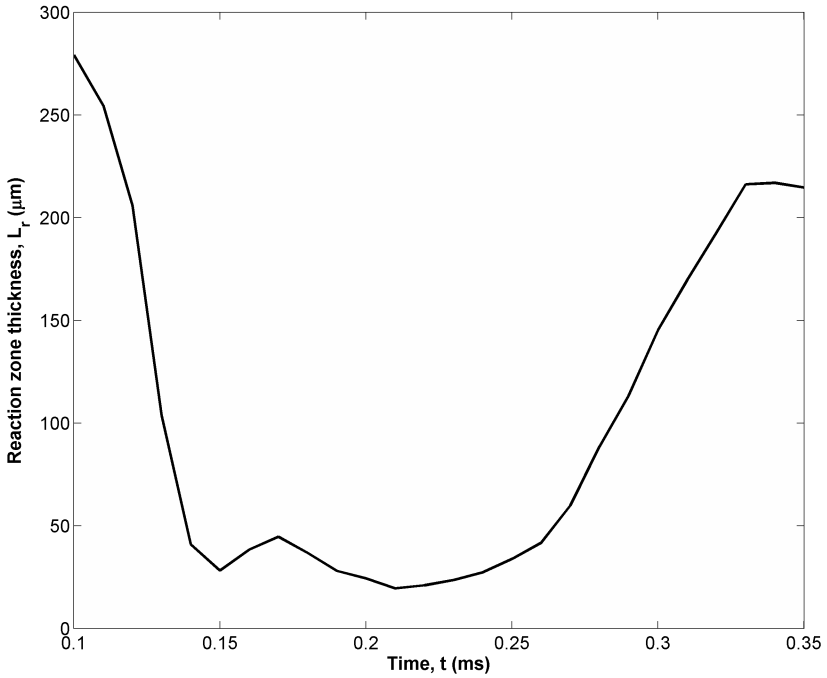

Figure 7.42. Evolution of the reaction zone thickness, L_f, as a function of time for the baseline case (u'=1.0 m/s and δ=120 microns).

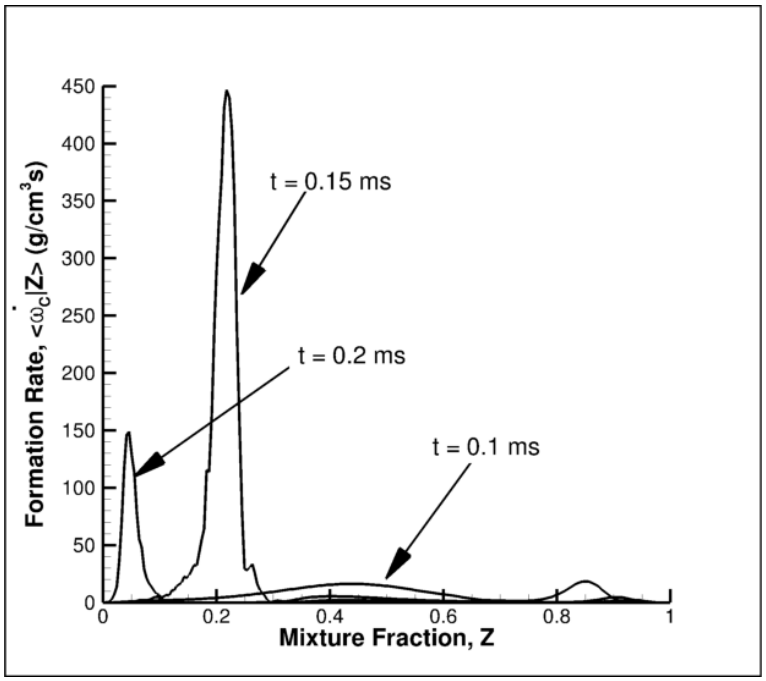

Figure 7.43. Distribution of conditionally-averaged instantaneous formation rates in the Z-space at different times during the flame development for the baseline case (u'=1.0 m/s and δ=120 microns).

The purpose of subgrid-scale combustion models is not to predict the instantaneous formation rates, but rather the filtered formation rates. The filtered formation rates can be directly obtained from the DNS results by explicitly filtering the DNS solution with different filter sizes. In this study, the conventional top-hat filter was used for filtering the DNS results. Figure 7.43 shows the distribution of filtered formation rates as a function of Z for different filter sizes at a time of 0.15 ms. Since the reaction zone thickness is comparable to the DNS grid size at this time, filtering the results reduces the formation rates considerably and makes the reaction zone thicker in the physical as well as the mixture fraction space. In the subsequent sections, two well-known turbulent combustion models – the PSR model and the UFPV model - will be

evaluated for their ability to reproduce the filtered formation rates for a range of conditions.

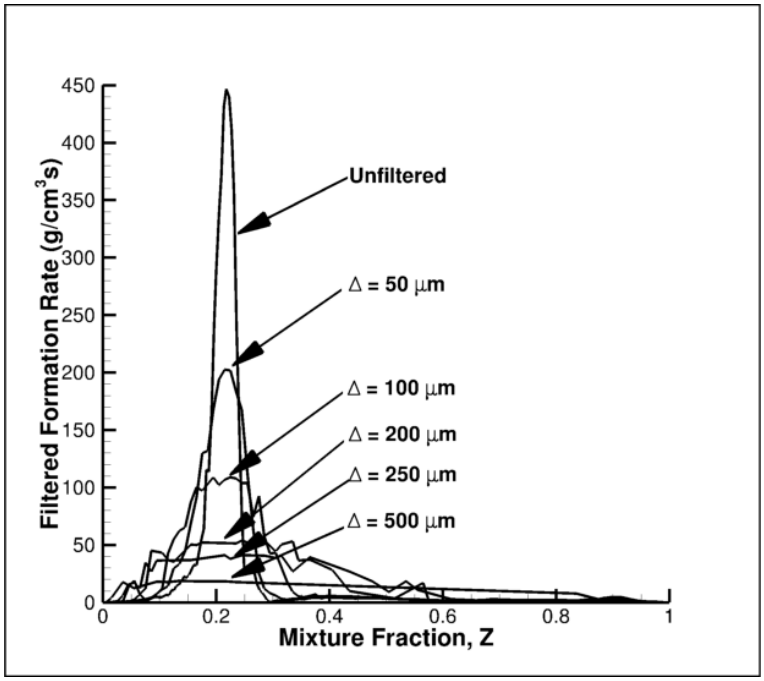

Figure 7.44. Distribution of filtered formation rate as a function of Z for the baseline case (u'=1.0 m/s, δ=120 microns) at a time of 0.15 ms.

7.6.2 Description of Subgrid-Scale Combustion Models

The perfectly stirred reactor (PSR) model is one of the simplest turbulent combustion models to implement. Each computational cell is assumed to be a closed homogenous reactor, and the filtered reaction rate is assumed to be equal to the Arrhenius reaction rate in the cell. In other words, the effect of turbulence is disregarded completely. The PSR model is given by

$$\widetilde{\dot{\omega}_{i,PSR}}\left(\tilde{T}, \tilde{Y}_1, \tilde{Y}_2, \ldots\right) = \dot{\omega}_i(T, Y_1, Y_2, \ldots), \tag{7.35}$$

where $\widetilde{\dot{\omega}_{i,PSR}}$ is the reaction rate predicted by the PSR model, $\dot{\omega}_i$ is the Arrhenius reaction rate, T is the temperature, Y_i is the mass fraction of species i, and the tilde denotes the Fávre-averaged quantities.

The UFPV model implementation details were discussed in Sec. 3.2. The unsteady flamelet equations (Eq. (7.30)) are solved for different values of χ_{st} and the solution is tabulated as a function of three independent variables Z, χ_{st} and Λ, where Λ is called the progress variable and it is an indicator of how far the reactions have progressed in the flamelet. These models are only valid if a single flamelet is present in an LES computational cell. Typically, there is a probability that each computational cell contains multiple flamelets, and the filtered reaction rate in a computational cell is given by averaging the reaction rate over all these flamelets.

$$\widetilde{\dot{\omega}_\phi} = \int\int\int \dot{\omega}_\phi P(Z, \chi_{st}, \Lambda) dZ d\chi_{st} d\Lambda = \int\int\int \dot{\omega}_\phi P(Z) P(\chi_{st}) P(\Lambda) \tag{7.36}$$

In the above equation, $P(Z, \chi_{st}, \Lambda)$ is the joint-PDF of Z, χ_{st} and Λ, and P(Z), P(χ_{st}) and P(Λ) are the marginal PDFs of Z, χ_{st} and Λ respectively. The implicit assumption is made that these 3 variables are statistically independent so that the joint PDF can be written as the product of the marginal PDFs. Mukhopadhyay and Abraham (2012) have verified this assumption for reacting mixing layers. In this study, a beta PDF is employed for Z and delta PDFs for χ_{st} and Λ.

7.6.3 Comparison of the Sub-grid-Scale Combustion Models

Figure 7.44 compares the formation rate predictions of the PSR model and the UFPV model with that of the DNS at a time of 0.15 ms for filter sizes of 100 μm and 200 μm as a function of filtered Z. Also shown, for reference, is the formation rate predicted by a single flamelet without the use of any PDF. While not shown here, the result from the single flamelet matches the DNS results if no filter size is used. The single flamelet

result is shown only to highlight the reduction in the peak rate as a result of filtering. The filtered DNS result is obtained as the density-averaged reaction rate per unit volume in the filtered cell. The PSR rate is obtained as the reaction rate calculated as a function of the filtered temperature and species concentrations (refer to Eq. (7.35)). The UFPV model results are obtained using Eq. (7.36). The PSR model is seen to perform reasonably well at this time for a filter size of 100 μm (Fig. 7.44 (a)). One possible reason for the superior results from the PSR model is that the effect of turbulence is not felt at this early time of 0.15 ms by the evolving mixing layer. Note that the turbulent time scale defined as u'/l_0 for the baseline case is 0.5 ms. Since the PSR model neglects the effect of the turbulence on chemistry, this model is expected to perform well during the early time. Furthermore, the early stage of ignition occurs over a wider range of Z values. It can be seen from Fig. 7.44 (a) that the DNS (non-filtered) results show significant formation rates between Z of 0.15 and 0.3. The corresponding physical thickness will also be relatively large. This is, as opposed, to an infinitesimally thin flame. If the reaction zone thickness is relatively large, the PSR model is expected to perform well. When the filter size is increased to 200 μm, the differences between the PSR model predictions and the UFPV model predictions decrease relative to the DNS results. The marginal PDF (Eq. (7.36)) for the mixture fraction used in the UFPV model is the beta PDF. The performance of the beta PDF is known to be poor for small filter sizes (Mukhopadhyay & Abraham, 2012). This improvement in the performance of the beta PDF with increasing filter size could be the reason for the improved performance of the UFPV model for the filter size of 200 μm.

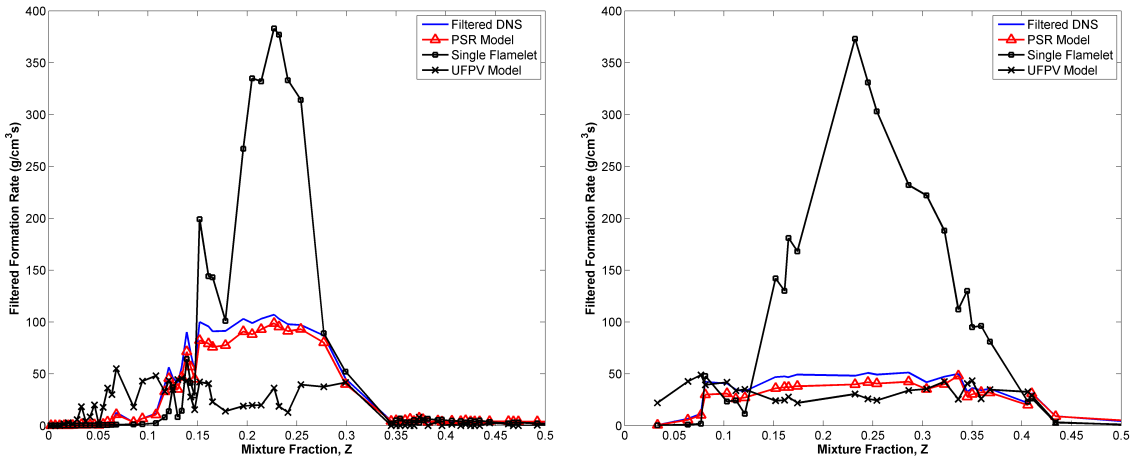

Figure 7.45. Comparison of the predictions of PSR model and the UFPV model with DNS results for the baseline case (u'=1.0 m/s, δ=120 microns) at a time of 0.15 ms for filter sizes of (a) 100 μm, and (b) 200 μm.

In the last paragraph, it was stated that the performance of the PSR model is expected to deteriorate with time at later times as the effect of turbulence is increasingly felt by the reaction zone. Figure 7.45 compares the filtered formation rates predicted by the PSR and the UFPV models at times of 0.20 ms and 0.25 ms after the start of the simulation for a filter size of 100 μm. At these times, the peak temperatures are close to the steady-state peak temperatures (refer to Fig. 7.39). It can be seen that at both times, the formation rates predicted by the PSR model are much higher than the filtered DNS rates. Recall that at 0.15 ms, the PSR formation rates agreed closely with the filtered DNS results (refer to Fig. 7.44(a)). By 0.2 ms, the peak formation rate predicted by the PSR model is 7 times higher than the DNS formation rate (refer to Fig. 7.45(a)) and it becomes 12 times greater at 0.25 ms (refer to Fig. 7.45(b)). On the other hand, the UFPV model predictions agree closely with the filtered DNS rates at both 0.2 and 0.25 ms.

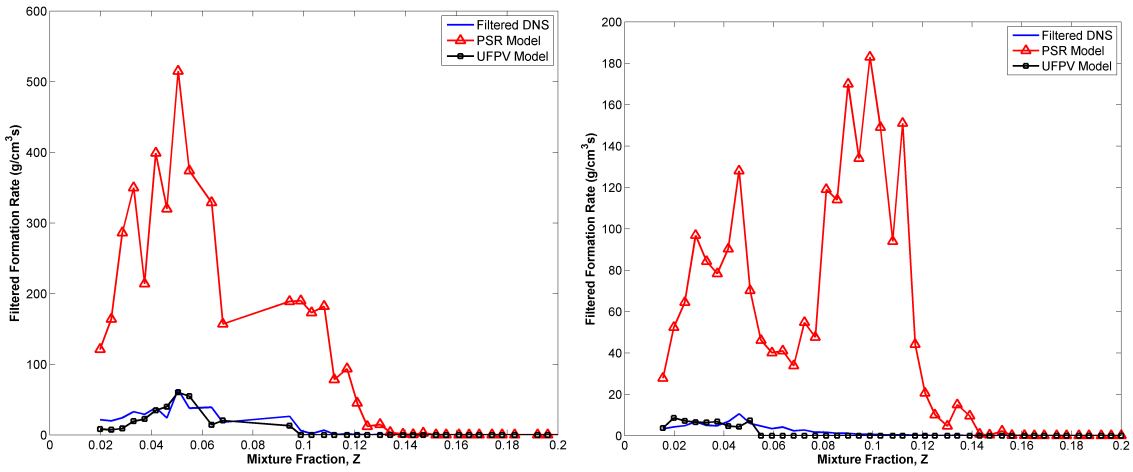

Figure 7.46. Comparison of the predictions of PSR model and the UFPV model with DNS results for the baseline case (u'=1.0 m/s, δ=120 microns) for a filter size of 100 μm at times of (a) 0.2 ms and (b) 0.25 ms.

To quantify the performance of these models, a normalized error E is defined as

$$E = \frac{|\dot{\omega}_{C,model} - \dot{\omega}_{C,DNS}|}{|\dot{\omega}_{C,DNS}|}, \tag{7.37}$$

where $\dot{\omega}_{C,model}$ is the formation rate predicted by the model and $\dot{\omega}_{C,DNS}$ is the formation rate obtained by filtering the DNS results. Figure 7.46 compares the value of E for the PSR model and the UFPV model for the baseline case as a function of filter size. Notice that the error is on a logarithmic scale. The performance of both the models deteriorates in general as the filter size increases. This is expected, as increasing filter sizes leads to the reaction zone being increasingly under-resolved. The slight decrease in error for the UFPV model when the filter size increased from 50 to 100 μm is because of the improved performance of the beta PDF at larger filter sizes. However, it is seen that the PSR model error increases more sharply and beyond a filter size of 200 μm, the UFPV model is seen to perform better.

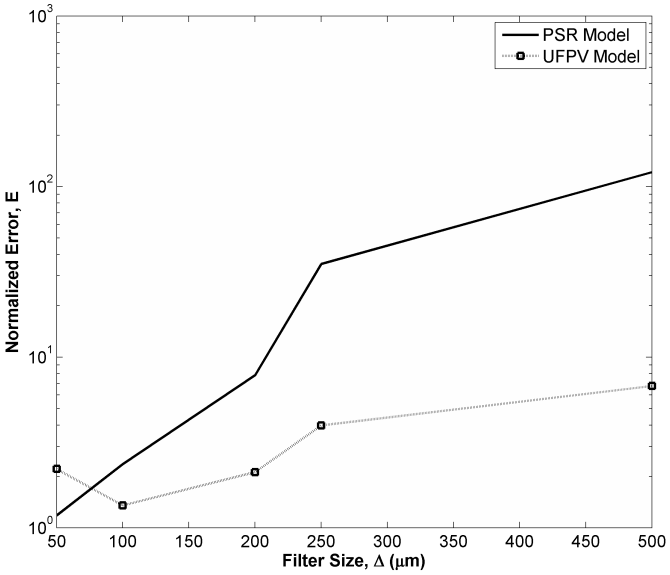

Figure 7.47. Comparison of the normalized errors of the PSR model and the UFPV model as a function of the filter size for the baseline case (u'=1.0 m/s, δ=120 microns) at a time of 0.2 ms.

Figure 7.47 compares the normalized errors for the two models as a function of time for the baseline case with a filter size of 100 μm. As previously suggested, the PSR model performance is expected to deteriorate with increasing time as the effect of turbulence on the evolving reaction zone increases with time. This is evident in Fig. 7.47 as the error with the PSR model increases significantly after a time of about 0.2 ms and becomes almost 20 times higher than the UFPV model error by a time of 0.5 ms.

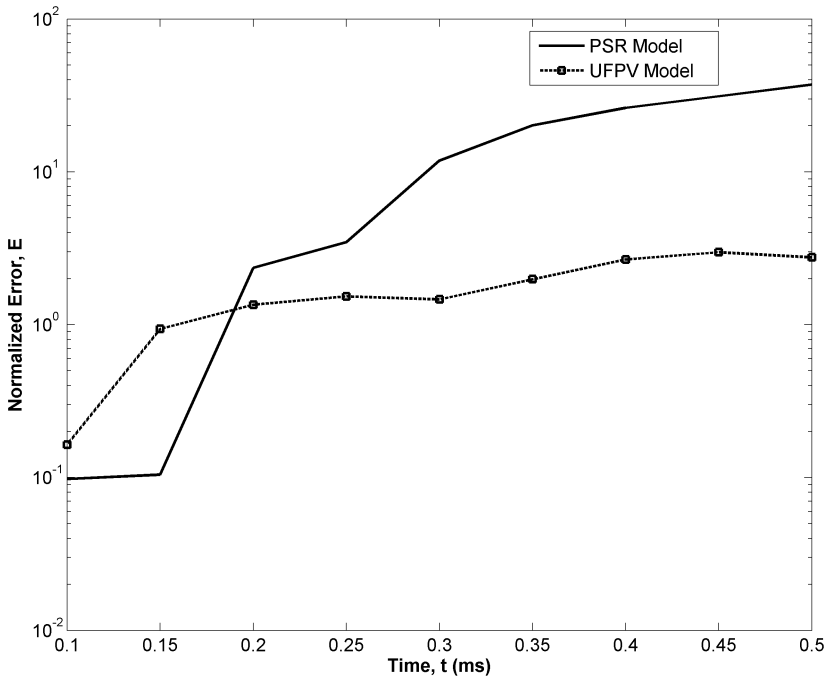

Figure 7.48. Comparison of the normalized errors of the PSR model and the UFPV model as a function of time for the baseline case (u'=1.0 m/s, δ=120 microns) for a filter size of 100 μm.

Mixing layer thickness (δ) is an indicator of the reaction zone thickness. So, a normalized filter size is here defined as Δ/δ, which indicates the relative size of the LES cell with respect to the reaction zone thickness. In this study, turbulent reacting mixing layer simulations were performed for δ of 90 μm, 120 μm and 240 μm. Figure 7.48 compares the normalized errors for the PSR and the UFPV model as a function of the normalized filter size at a time of 0.2 ms. It can be seen that the performance of the PSR model deteriorates rapidly with increasing filter size, whereas the UFPV model error is approximately independent of the filter size. It can be seen that the PSR model performs better when the filter size is smaller than about 0.5 times the mixing layer thickness, whereas the UFPV model is the superior model for larger filter sizes.

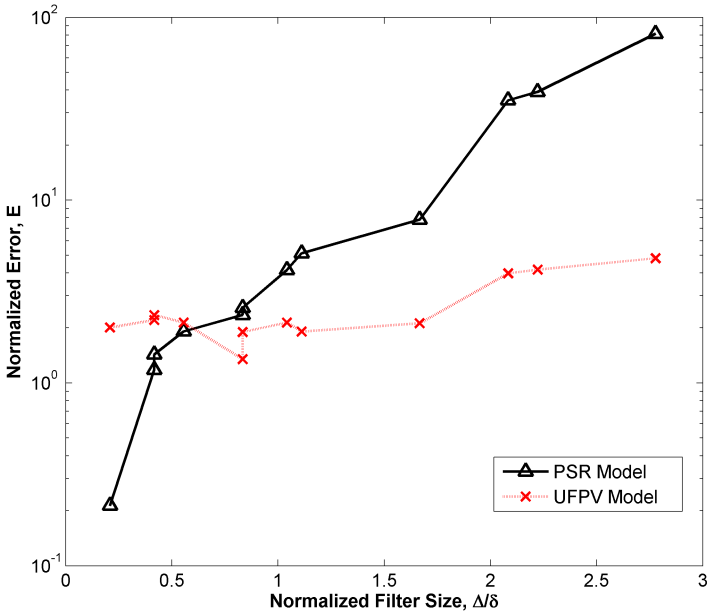

Figure 7.49. Comparison of the normalized errors of PSR and UFPV models as a function of the normalized filter size at a time of 0.2 ms.

It was suggested above that one of the reasons for the superior behavior of the PSR model at earlier times is due to the fact that the effect of turbulence on the reaction zones is not fully felt at earlier times. To confirm this hypothesis, two additional simulations were made with turbulent velocity scales u' = 0.5 m/s and u' = 2.5 m/s in addition to the baseline case which had u' = 1.0 m/s. A normalized time can then be defined as $\tau = tu'/l_0$, which is an indicator of the extent of the turbulence on the reaction zone. The larger the value of τ, the larger is the effect of turbulence on the reaction zone, and based on the previous arguments, the worse the PSR model performance is expected to be.

Figure 7.49 compares the normalized errors of the PSR and UFPV model as a function of τ. For ease of analysis, a uniform filter size of 100 μm is used for all the points. It can be seen that the PSR model performs better for τ less than about 0.4. This

conclusion is valid irrespective of the turbulent velocity scale u'. This shows that at times less than 0.4 times the turbulent time scale in an initial laminar mixing layer evolving under the influence of turbulence, the need for a turbulence-chemistry interaction model is not significant, and reasonably accurate results can be obtained even with the PSR model. However, this conclusion is only valid when the filter sizes are small suggesting that if the LES grid is fine enough, no turbulence-chemistry interaction model is necessary during the early stages of combustion. However, the prediction of flame development after the initial ignition period requires the use of a turbulent combustion model.

7.6.4 Conclusions

In this section, direct numerical simulations of autoigniting mixing layers that evolve under the influence of a turbulent flow field are carried out and the DNS results are used to evaluate two subgrid-scale combustion models – the perfectly stirred reactor (PSR) model and the unsteady flamelet progress variable (UFPV) model. It is shown that during ignition, i.e. early stage of combustion, the PSR model performs better than the UFPV model for small filter sizes because the beta-PDF that is employed in the UFPV model does not represent the PDF well (for small filter sizes). The reason why the PSR model performs better during the early stage of combustion is specific to the setup in this work where a laminar mixing layer evolves in a turbulent flow field. In the early stage, the mixing layer is not fully turbulent. The performance of the PSR model deteriorates rapidly as filter sizes are increased and at later times, i.e. after ignition. The UFPV model, on the other hand, performs reasonably well at all times and for all filter sizes.

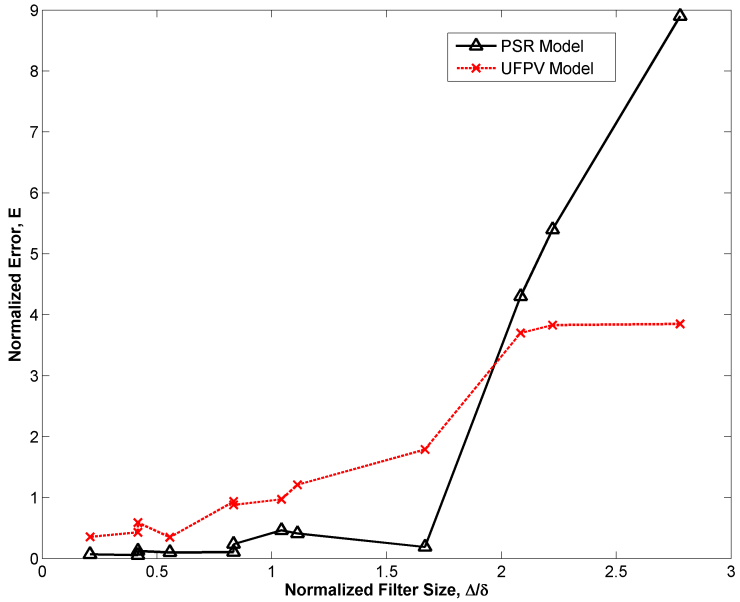

Figure 7.50. Comparison of the normalized errors of the PSR and the UFPV models as a function of normalized time, τ. A uniform filter size of 100 μm is chosen.

7.7 À-posteriori Evaluation of Improved Subgrid-scale Models

7.7.1 Introduction

In this section, the improved subgrid-scale models proposed in this chapter are evaluated using LES. Non-reacting LES is performed using conditions described in Sec. 6.3. The non-reacting LES data is used to compare the predictions using the original models with that of the proposed models. In addition to the transport equations for the momentum, species and energy, a transport equation for the mixture fraction variance, $\widetilde{Z''^2}$, is also solved. Note that the variance is required for the strain rate tensor (SRT) model for scalar dissipation rate. The mixture fraction variance transport equation (Ihme and See, 2010) is given by

$$\bar{\rho}\widetilde{D}_t\widetilde{Z''^2} = \nabla.\left(\bar{\rho}\tilde{\alpha}\nabla\widetilde{Z''^2}\right) + 2\bar{\rho}D_T\left|\nabla\tilde{Z}\right|^2 - \frac{C_{Z_1}\bar{\rho}D_T}{\Delta^2}\widetilde{Z''^2}, \tag{7.38}$$

where $\tilde{\alpha}$ is the filtered thermal diffusivity, D_T is the turbulent diffusivity, Δ is the LES grid size, and C_{Z_1} is a model constant which is assumed to be equal to 4.0. Figure 7.50 shows the distribution of time-averaged $\widetilde{Z''^2}$ in the computational domain at a time of 1.45 ms. The time-averaging was performed between 1.0 ms and 1.45 ms. This implies that the results are meaningful only in that part of the jet which has reached quasi steady-state at 1.0 ms. It can be seen that $\widetilde{Z''^2}$ is highest near the orifice and decays rapidly in both the axial and radial directions. This is made clearer in Figs. 7.51 and 7.52 which shows the axial and radial variations of $\widetilde{Z''^2}$, respectively. Figure 7.51 shows the presence of a peak in the $\widetilde{Z''^2}$ distribution at an axial location of 0.001 m. This is downstream of the location, 0.0002 m, of the random vortex ring (refer to Sec. 4.9) that is used to trigger the transition to turbulence. $\widetilde{Z''^2}$ rapidly decays with axial distance due to viscous dissipation. Figure 7.52 shows that $\widetilde{Z''^2}$ also decays radially and its behavior is consistent with the spreading of the jet.

The subgrid-scale models are evaluated by comparing the earlier model results with the proposed model results. Section 7.7.2 compares the filtered scalar dissipation rate predicted by the TD (turbulent diffusivity) model with that predicted by the SRT model. In Sec. 7.7.3, the performance of the exponential and lognormal PDFs are compared and evaluated.

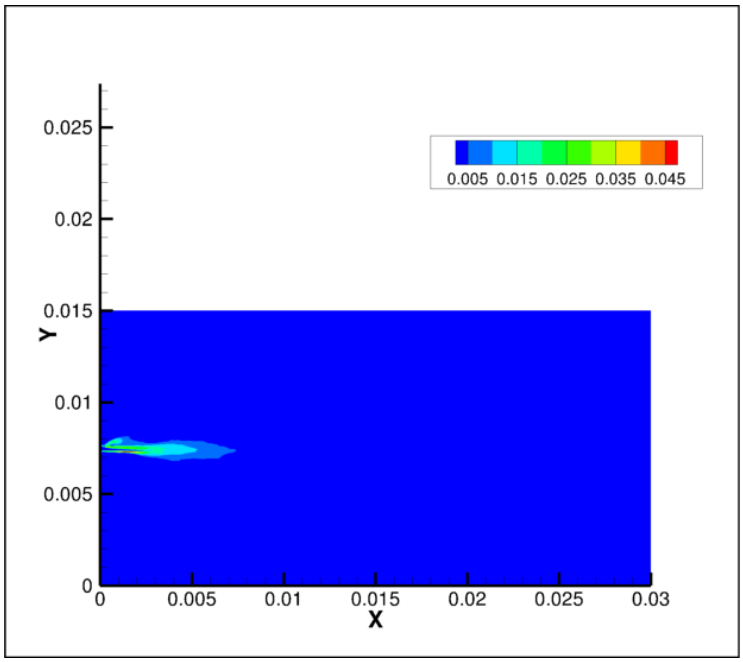

Figure 7.51. Distribution of time-averaged mixture fraction variance in the computational domain at a time of 1.45 ms.

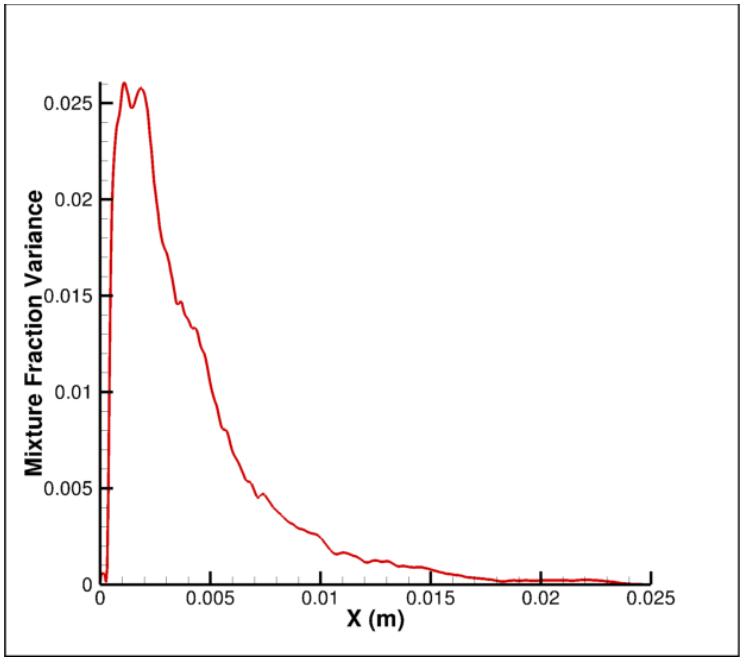

Figure 7.52. Axial variation of time-averaged mixture fraction variance at a time of 1.45 ms.

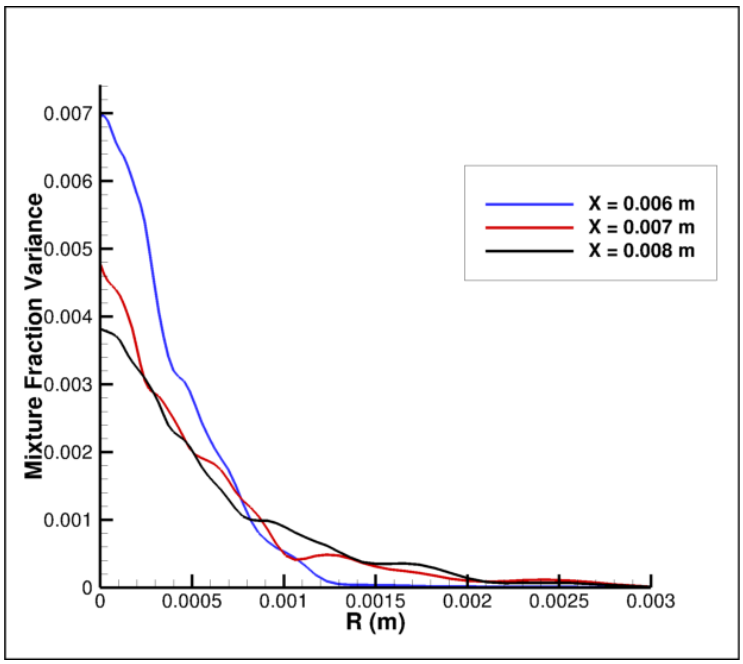

Figure 7.53. Radial variation of mixture fraction variance at axial locations of 0.006 m, 0.007 m, and 0.008 m at a time of 1.45 ms.

7.7.2 Comparison of TD and SRT Models

In Sec. 7.3, four models for the filtered scalar dissipation rate were described and their performance was compared using DNS data. It was shown that the commonly used TD model (Eq. (7.5)) performs relatively poorly and the SRT model (Eq. (7.9)) is a better alternative. Recall that the TD model was employed in the computations discussed in Chapter 6. The non-reacting LES data is used to compare the scalar dissipation rates predicted by the TD and SRT models and the impact of the predictions on reacting LES is discussed.

Figure 7.53 compares the axial variation of the filtered scalar dissipation rate predicted by the TD model and the SRT model. The scalar dissipation rate computed without using any model is also shown for comparison. Note that the y-axis is in logarithmic scale. It is seen that the SRT model consistently predicts higher values than

the TD model. Note that the TD model predictions are different from those using no model only at locations very close to the orifice. Recall that it was pointed out in Sec. 7.3 when assessing the various models using the DNS database that the contribution of the subgrid-scale component in the TD model is relatively small. Figure 7.53 also shows the region where the mixture fraction lies between 0.03 and 0.1. Note that this is the band within which reactions are likely to be most intense. It can be seen that in this region, although the SRT model predictions are much higher (a factor of 5 to 10 higher) than the TD model predictions, the scalar dissipation rates predicted by all the models (1-10 /s) are well within the ignition scalar dissipation rate which is approximately 60 /s for this mixture (see Secs. 3.5 and 6.4). So, it is expected that both models will predict the presence of a flame at these locations although the flame predicted using the SRT model is expected to be weaker. In addition, the large differences in the scalar dissipation rate at upstream locations are expected to influence the low-temperature chemical reactions and the soot precursor formation rates and lead to differences in predictions of ignition delay and pollutants.

Figure 7.54 compares the radial variation of the scalar dissipation rates predicted by the TD and SRT models at an axial location of 0.006 m. In the region between the Z=0.03 and Z=0.1 isolines, the differences are still considerable, although, as pointed out above, the scalar dissipation rates predicted by both models are below the ignition scalar dissipation rate. Thus, the same explanations given in the previous paragraph apply – the steady flame structure predicted by both these models might be similar. The fluctuations that are evident in the plot arises from the presence of large scale eddies. The time

averaging over a period of 0.45 ms is not sufficient to remove the local and instantaneous fluctuation effects.

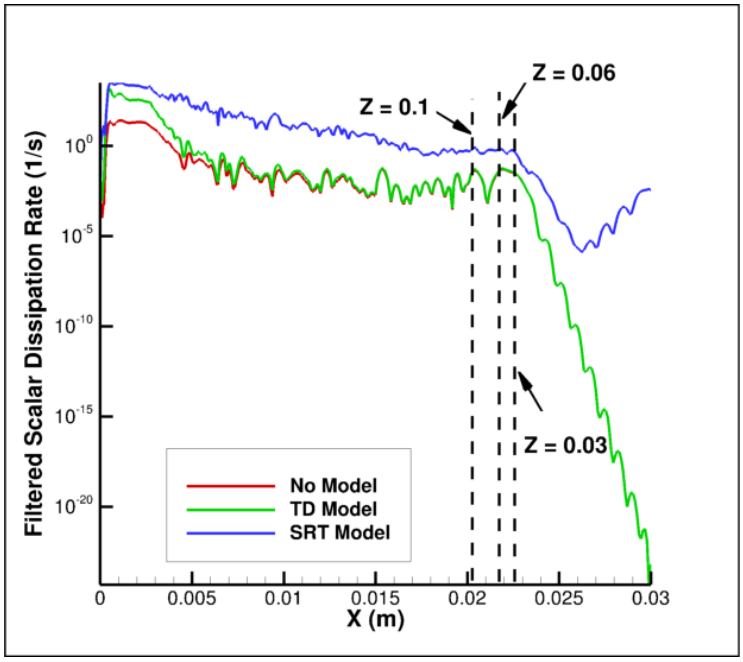

Figure 7.54. Axial variation of the filtered scalar dissipation rate at a time of 1.45 ms using no model, TD model and SRT model.

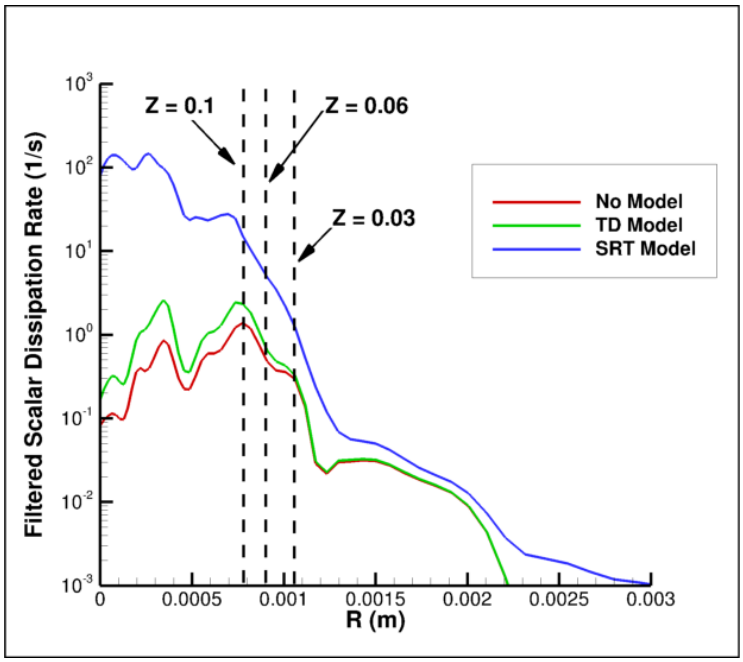

Figure 7.55. Radial variation of the filtered scalar dissipation rate at an axial location of 0.006 m at a time of 1.45 ms using no model, TD model and SRT model.

7.7.3 PDF of Scalar Dissipation Rate

In Sec. 7.3, it was shown that the PDF of the scalar dissipation rate could be represented by an exponential PDF or a lognormal PDF depending on the value of the filtered scalar dissipation rate. In order to evaluate the effect of the scalar dissipation rate PDF, the non-reacting LES data is used to predict the steady-state temperature profiles employing a steady flamelet library. Figure 7.55 compares the radial variation of the temperature with and without the scalar dissipation rate PDF. The criterion based on the normalized scalar dissipation rate for selecting the PDF is not applied here. In other words, the exponential and lognormal PDFs are applied everywhere in two separate analysis. It is seen that employing a PDF for the scalar dissipation rate leads to temperature rise in regions which did not ignite when a PDF is not employed. When a PDF is not employed, ignition occurs only in regions where the scalar dissipation rate is lower than the ignition scalar dissipation rate. The use of a PDF implies that there is a finite probability for the region to ignite even when the filtered scalar dissipation rate is high. Figure 7.55 also shows that the lognormal PDF leads to larger temperature than the exponential PDF. This difference arises because the variance of the mixture fraction is relatively high in this region and leads to a broader lognormal PDF. In practice, the exponential PDF would be employed in some regions and the lognormal PDF in others. In the region under consideration where the LES grid size is about 100 μm and the scalar dissipation rate values are about 50-70 /s, the lognormal PDF is the likely PDF of choice. It is also important to point out that examination of results further downstream, beyond an axial distance of 0.006 m, shows negligible effect of the PDFs because the scalar dissipation rates are much smaller than the ignition scalar dissipation rates.

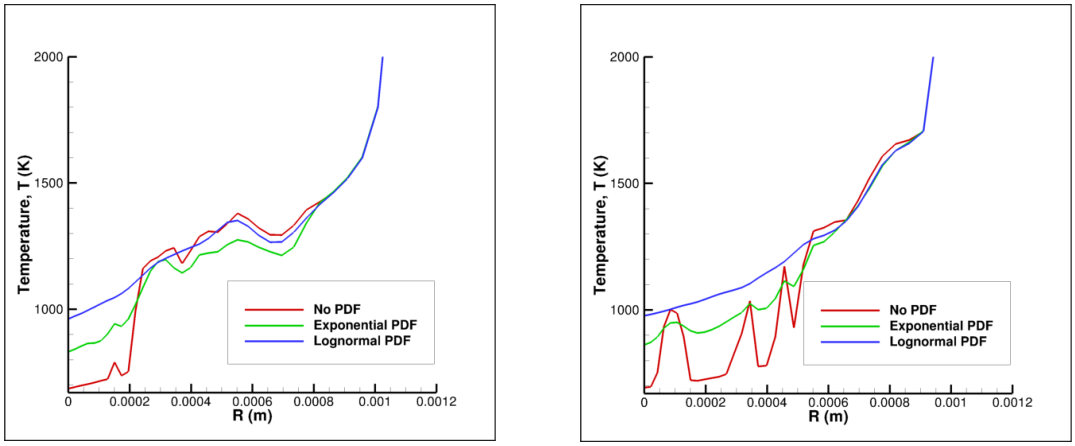

(a) (b)

Figure 7.56. Radial variation of the steady-state temperature at axial locations of (a) 0.003 m and (b) 0.004 m.

7.7.4 Conclusions

In this section, the improved subgrid-scale models proposed in Sec. 7.3 are evaluated by employing data from non-reacting LES. It is shown that although the SRT model consistently predicts higher scalar dissipation rate values than the TD model, the differences between the two models are small in the combustible region. This is expected to cause the steady-state temperatures predicted by these two models to be similar. Differences in the very near field of the jet, i.e. upstream of about 30 diameters, in the prediction of scalar dissipation rate can, however, lead to differences in ignition delay and pollutant formation. In regions of the jet where the scalar dissipation rate is of the order of the ignition scalar dissipation rate, the use of a PDF for scalar dissipation rate is likely to show higher temperature than when a PDF is not employed due to finite probability of scalar dissipation rate being lower than the ignition scalar dissipation rate. In the downstream region of the jet, i.e. greater than about 30D, the scalar dissipation rates are much lower than the ignition scalar dissipation rate and the use of a PDF is not

of consequence. These conclusions are made on the basis of evaluation of non-reacting LES results and have to be assessed for reacting LES.

7.8 Summary and Conclusions

In this chapter, DNS of reacting and non-reacting turbulent mixing layers are performed to evaluate the applicability of the unsteady flamelet progress variable (UFPV) model as a subgrid-scale combustion model for use in LES. While the focus is on LES, much of the work is also applicable to RANS simulations. The DNS results are employed to assess the accuracy of four models for the filtered scalar dissipation rate in LES. It is shown that the turbulent diffusivity (TD) model that is commonly employed in LES to model the filtered scalar dissipation rate lead to large errors. The strain rate tensor (SRT) and subgrid kinetic energy (SKE) models perform the best among the models considered, for the range of conditions considered. The SRT model is recommended because, unlike the SKE model, it can be used without solving additional transport equations. This study is carried out using two-dimensional (2D) "DNS". Comparative studies of 2D and 3D DNS of turbulent non-reacting fuel/air mixing layers are carried out. It appears from these simulations that qualitative assessment of subgrid-scale models can be carried out with 2D DNS databases. The DNS results are also employed to assess the accuracy of an unsteady flamelet model in predicting the flame development. It is shown that the flamelet model predictions differ significantly from the laminar simulation and DNS results during the flame development process following autoignition. Differences arise from the use of the constant functional form for the scalar dissipation rate profiles. It is

shown that changes in diffusivity, D, is the major cause of the change in the scalar dissipation rate. In the newly proposed diffusivity-corrected flamelet model, the increase in scalar dissipation rate due to increased diffusivity at high temperatures is accounted for. This model shows significant improvements over the traditional flamelet approach and the differences in the temperature profiles are found to be limited to 10%. DNS results are used to evaluate two subgrid-scale combustion models – the perfectly stirred reactor (PSR) model and the unsteady flamelet progress variable (UFPV) model. It is shown that during ignition, i.e. early stage of combustion, the PSR model performs better than the UFPV model for small filter sizes because the beta-PDF that is employed in the UFPV model does not represent the PDF well (for small filter sizes). The reason why the PSR model performs better during the early stage of combustion is specific to the setup in this work where a laminar mixing layer evolves in a turbulent flow field. In the early stage, the mixing layer is not fully turbulent. The performance of the PSR model deteriorates rapidly as filter sizes are increased and at later times, i.e. after ignition. The UFPV model, on the other hand, performs reasonably well at all times and for all filter sizes. The improved subgrid-scale models are evaluated by using data from non-reacting LES. It is shown that the newly proposed models for the filtered scalar dissipation rate and its PDF causes significant differences in the steady-state flame structure as well as the pollutant predictions.

8 SUMMARY, CONCLUSIONS AND FUTURE WORK

8.1 Summary and Conclusions

This work has focused on developing and assessing the tools that would aid in improving the modeling of reacting diesel jets. The review of prior literature presented in Chapter 2 showed that the understanding of turbulence/chemistry interactions in reacting diesel jets is incomplete. Much of the prior work in modeling of diesel jets and combustion in diesel engines has employed RANS models. These models are fundamentally incapable of identifying the role of various turbulent scales on mixing and turbulence/chemistry interactions. LES, on the other hand, can capture the effect of the larger scales on mixing and turbulence/chemistry interactions. Irrespective of whether RANS simulation or LES is employed, the inadequacy of turbulence/chemistry interactions models is a serious limitation. In this work, the unsteady flamelet progress variable (UFPV) model is evaluated in detail through RANS simulations, LES, and DNS.

As a starting point, RANS simulations of a set of reacting diesel jets which had been experimentally studied at Sandia National Laboratories are carried out. The work is described in Chapter 3. This work was carried out in collaboration with Mr. Chetan Bajaj, a student who graduated with his MSME in 2012. It had been shown in work carried out prior to the work of Bajaj and Ameen (2012) that the ensemble-averaged structure of the vaporizing diesel jet can be captured with RANS models (Abraham and Pickett, 2010;

Bajaj et al., 2011). The computed results reproduce the measured penetration is within about 10%, dispersion within about 20%, and axial and radial profiles of mixture fraction within about 20%. The work described in Chapter 3 demonstrated that the RANS model can capture the measured ignition delay and flame lift-off height within about 25%. The computations also suggested a mechanism for transient flame development, starting with ignition in the rich mixture toward the leading tip of the jet followed by ignition front propagation toward the stoichiometric surface, flame propagation upstream along the stoichiometric surface, and flame stabilization at the height where the local scalar dissipation rate at the stoichiometric surface matched the ignition scalar dissipation rate. The accuracy of the details is, however, difficult to assess from RANS results. For example, the roles played by the range of scales and unsteady effects on flame structure are difficult to model. LES are required to provide further insight.

As part of the thesis work of Dr. Jonathan Anders (2006), an LES code (FLEDS – Flow, Large-Eddy, Direct Simulation) had been developed and it had subsequently been assessed for accuracy by Anders et al. (2007) and Venugopal (2008, 2009). These simulations were however of isothermal jets and focused on the near-field (within 25 orifice diameters) of the jet. In the work of Venugopal (2008, 2009), the focus was on quasi-steady jets. In the present work, the interest is in transient developing reacting non-isothermal jets. This gives rise to some numerical and modeling challenges. Chapter 4 describes the numerical algorithm and subgrid-scale models employed. Through iterative studies, it was determined that an Artificial Diffusivity Scheme (ADS) model is suited for the studies in the present work because of the presence of sharp gradients.

Results from application of FLEDS to non-reacting turbulent diesel jets are presented in Chapter 5. The structure of the transient developing jet is described. Comparisons of computed and measured radial velocity profiles and penetration reveal that the LES model is able to reproduce these variables within an accuracy of about 20%. However, this conclusion is based on comparisons of instantaneous LES results with ensemble-averaged experimental results. These initial results are encouraging. The computed energy spectrum agrees qualitatively with the well-known turbulence energy spectrum. Some of the quantitative aspects of the energy spectrum are also reproduced quite well.

FLEDS is then applied to carry out LES of reacting jets. This requires the implementation of the UFPV model. The scalar dissipation rate required in the UFPV model is approximated from the gradient of the local resolved mixture fraction. The effect of the subgrid scales is modeled using a turbulent diffusivity approximation. Note that many prior studies have shown that this approximation may not be valid under all conditions. Nevertheless, some interesting observations are made from the preliminary results. Ignition occurs in the rich mixture as in the RANS simulations. Unlike the RANS results, ignition occurs at multiple points. Flames develop from these multiple points and they merge into a continuous sheet along the stoichiometric surface. The flame stabilization plane is the upstream location beyond which ignition can no longer occur or if it does occur, the kernels are quenched by large strain.

The accuracy of the subgrid combustion model employed for RANS and LES is assessed in Chapter 7 using DNS of turbulent reacting mixing layers. Note that ignition, flame development, and heat release in a diesel jet occurs through chemical reactions in a

mixing layer. It is shown that the turbulent diffusivity (TD) model for the subgrid-scale scalar dissipation rate does not perform well under diesel engine conditions. Recall that this model was employed in the LES presented in Chapter 6. A detailed evaluation of the DNS results shows that the Strain Rate Tensor (SRT) model is a better approximation for the subgrid-scale scalar dissipation rate. DNS results are used to determine the optimal model constants for the SRT model. The additional advantage of SRT model is that no additional transport needs to be solved and, hence, it can be easily implemented. The DNS results are also used to determine the PDF of the scalar dissipation rate. It is found that when the grid size is comparable to the scalar mixing layer thicknesses, a lognormal PDF worked the best, whereas for larger grid sizes, an exponential PDF performs better. A new model for the variance of the scalar dissipation rate is also proposed and shown to perform well under all conditions.

Chapter 7 also addresses the question of whether the flame behaves like a "flamelet" in a diesel jet. It is shown that the flame development predicted by the flamelet approximation is slower than what is observed from DNS. This is due to the fact that the flamelet model does not incorporate the effect of flame expansion due to heat release and increased species diffusivities caused by temperature rise. An improved *diffusivity-modified flamelet model* is proposed which incorporates the effect of heat release in the flamelet model. This model is shown to predict the flame development more accurately than the traditional flamelet approach.

Chapter 7 also compares the performance of the UFPV model with the Perfectly Stirred Reactor (PSR) model, which is a commonly used approach in LES of reacting

flows. It is shown that the UFPV model performs much better than the PSR mode for grid sizes and turbulence intensities commonly encountered in diesel engines.

À-posteriori evaluation of the improved subgrid-scale models are carried out using non-reacting LES results. It is shown that the scalar dissipation rate predicted by the SRT model is, as expected, greater than that predicted by the TD model. This is consequential in the near-field of the jet where it can influence flame temperature, low-temperature chemistry and pollutant precursor reaction rates. The scalar dissipation rate values decrease below the ignition scalar dissipation rate beyond about 30 orifice diameters and the impact of the differences in the scalar dissipation rates on the flame temperature is expected to be small in this region. Employing a PDF for the scalar dissipation rate affects temperature in the near-field but not in the far-field where the scalar dissipation rate and its variance are relatively small.

8.2 Future Work

While this work has made significant contributions to the development and application of a turbulence/chemistry interaction model that can employed in RANS simulations and LES of turbulent reacting diesel jets, much work remains to be done. These can be broadly summarized into five parts.

8.2.1 3D DNS of Reacting Mixing Layers

In Chapter 7, 2D and 3D DNS of non-reacting turbulent mixing layers are performed and the results are used to evaluate LES subgrid-scale models. It is shown that

although the qualitative predictions from both the studies are similar, the effect of vortex stretching that is only captured in 3D DNS leads to higher gradients and scalar dissipation rates. Hence, the model coefficients suggested from these two simulations are different. 3D DNS of autoigniting diesel flames is currently not feasible with the available computational resources. With increasing availability of large-scale computational resources, 3D DNS may become feasible in the near future. For example, the Titan supercomputer (CRAY XK-7) at ORNL currently has 560,000 cores. The maximum number of cores employed in the computations in this work is 4096. Increasing the number of cores requires dramatic improvements in the scalability of the code, improved visualization techniques, and data (I/O) management. It will be worthwhile to revisit the conclusions of Sections 7.5 and 7.6 using 3D DNS.

8.2.2 LES of Reacting Diesel Jet with Improved Subgrid-Scale Models

Chapter 7 presented à-priori analysis of subgrid-scale combustion models for reacting diesel jets using DNS of mixing layers. LES have to be performed with the improved unsteady flamelet progress variable (UFPV) model and improved models for the mean, variance and PDF of the scalar dissipation rate discussed in Chapter 7. Quantitative and qualitative comparisons of the LES results with experimental measurements have to be carried out. Recall that the LES presented in Chapter 6 are carried out for lower Reynolds numbers than in the diesel jets for which measurements are available. The limitation is related to the computational issues discussed in the last sub-section (8.2.1).

8.2.3 Additional LES Work Including Pollutants

An interesting utility of the UFPV model is that it can be easily extended to include models for soot and NO chemistry. RANS simulations are currently being carried out by Ms May Yen in the research group to extend the work of Chapter 3 to include soot and NO (Yen and Abraham, 2013, 2014). Yen and Abraham (2014) repeated the cases explained in Section 3.4 (refer to Table 3.1) including soot and NO models and compared the predicted soot volume fractions and NO mass fractions with the experimental measurements. Figure 8.1 compares the predicted and measured soot volume fractions for a few of the cases shown in Table 3.1. It can be seen that the UFPV model is able to predict the locations of peak soot volume fractions accurately. The qualitative change in total soot in the domain with changing conditions is also reproduced well by the model although the quantitative soot predictions are off by an order of magnitude. LES simulations can be performed with the extended UFPV model with soot and NO incorporated to study this in more detail. In particular, there is interest in determining if the lift-off height can be correlated to the soot (and NO) formation in the jet. The RANS simulations suggest that this correlation is not universal.

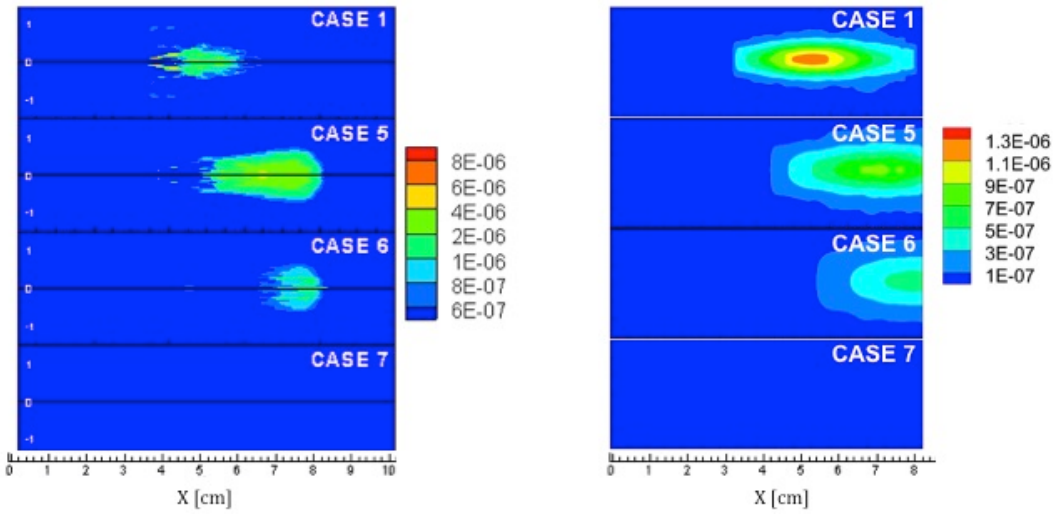

Figure 8.1. Comparison of predicted and measured soot volume fractions. Left image shows the predicted results and the right image shows the measured results. The cases correspond to the cases mentioned in Table 3.1 (Yen and Abraham, 2014).

8.2.4 Reduced Chemical Kinetic Mechanisms

One of the challenges with the reacting simulations is the significant computational overhead on account of the use of multistep chemical kinetic mechanisms. Many of the reacting computations are carried out with a 37-species, 74-step mechanism for n-heptane oxidation. While the complexity of this mechanism is significantly reduced relative to comprehensive mechanisms with 550 species and 2450 elementary reactions (Curran et al., 1998), it is still computationally intensive in LES and DNS. The development of simpler mechanisms which can represent the chemistry with adequate accuracy is critical. This is even more challenging when practical fuels are considered. This is an area that requires additional work. A preliminary study was done as part of this work and this is discussed in Appendix A.

8.2.5 Application in Engines

The extension of these computational tools and subgrid-scale models to engines is challenging for multiple reasons. These include the need to use fine grid resolution, extend the flamelet model to a chamber where pressure is changing, model flame-wall interactions, and model jet-jet interactions. Furthermore, in diesel engines, radiation heat transfer is expected to be important. The inclusion of radiation heat transfer in a rigorous way in an engine simulation has not been attempted. Most computational studies incorporating the effect of radiation heat transfer in diesel engine combustion neglect turbulence/radiation interactions (Abraham and Magi, 1997). For these reasons, the modeling of in-cylinder combustion in diesel engines is likely to remain somewhat qualitative and only useful when combined with corresponding experimental work. True predictive capability is still elusive.

LIST OF REFERENCES

LIST OF REFERENCES

Abraham, J., (1996). Entrainment Characteristics of Transient Gas Jets, *Numerical Heat Transfer* 30(4):347–364.

Abraham, J., (1997). What is Adequate Resolution in the Numerical Computations of Transient Jets? *SAE Transactions* 106:141-155.

Abraham, J., and Magi, V., (1997). Comparisons of Transient Jets: RNG k-ε model Versus Standard k-ε Model, *SAE Transactions* 106(3):1442–1452.

Abraham, J., and Pickett, L., (2010). Computed and Measured Fuel Vapor Distribution in a Diesel Spray, *Atomization and Sprays* 20:241–250.

Abraham, J., Bracco, F. V., and Reitz, R. D., (1985). Comparisons of computed and measured premixed charge engine combustion, *Combustion and Flame* 60:309-322.

Abramovich, G. N., and Schindel, L., (1963). *The Theory of Turbulent Jets*, The MIT Press, Cambridge, MA.

Ameen, M.M., and Abraham, J., (2014a). RANS and LES Study of Lift-Off Physics in Reacting Diesel Jets, *SAE Technical Paper* 2010-01-1118.

Ameen, M.M., and Abraham, J., (2014b). Evaluation of scalar dissipation rate sub-models for modeling unsteady reacting diesel jets, *Combustion Science and Technology* (under review).

Anand, M. S., and Pope, S. B., (1987). Calculations of premixed turbulent flames by pdf methods, *Combustion and Flame* 67:127-142.

Anders, J. W., Magi, V., and Abraham, J., (2007). Large-eddy simulation in the near field of a transient multicomponent gas jet with density gradients. *Computers and Fluids* 36:1609-1620.

Anders, J. W., Magi, V., and Abraham, J., (2008). A Computational Investigation of the Interaction of Pulses in Two-Pulse Jets, *Numerical Heat Transfer, Part A: Applications* 54(11):999-1021.

Anders, J.W., (2006). *Turbulence and Residual Gas Effects in Pulsed Diesel Jets*, PhD Thesis, Purdue University, West Lafayette, IN.

Anders, J.W., Magi, V., and Abraham, J., (2007). Large-eddy simulation in the near-field of a transient multi-component gas jet with density gradients, *Computers and Fluids* 36:1609–1620.

Aneja, R., and Abraham, J., (1998). Comparisons of Computed and Measured Results of Combustion in a Diesel Engine, *SAE Paper* 980786.

Arregle, J., Lopez, J. J., Garcia, J. M., and Fenollosa, D., (2003). Development of a Zero-Dimensional Diesel Combustion Model. Part 1: Analysis of the Quasi-Steady Diffusion Combustion Phase, *Applied Thermal Engineering* 23(11):1301-1317.

Bajaj, C., Abraham, J., and Pickett, L.M., (2011). Vaporization Effects on Transient Diesel Spray Structure, *Atomization and Sprays* 21(5):411-426.

Bajaj, C., (2012). *Computational Investigations of Ignition and Flame Lift-Off in Diesel Jets*, MSME Thesis, Purdue University, West Lafayette, IN.

Bajaj, C., Ameen, M., and Abraham, J., (2013). Evaluation of an unsteady flamelet progress variable model for autoignition and flame lift-Off in diesel jets, *Combustion Science and Technology* 185:454-472.

Balarac, G., Pitsch, H., and Raman, V., (2008). Development of a dynamic model for the subfilter scalar variance using the concept of optimal estimators, *Physics of Fluids* 20, 035114.

Balarac, G., Raman, V., and Pitsch, H., (2008). Modeling of the subfilter scalar dissipation rate using the concept of optimal estimators, *Physics of Fluids* 20, 091701.

Bekdemir , C., Somers, L. M. T., de Goey, L. P. H., Tillou, J., and Angelberger, C., (2013). Predicting diesel combustion characteristics with Large-Eddy Simulations including tabulated chemical kinetics, *Proceedings of the Combustion Institute* 34:3067–3074.

Bekdemir, C., Rijk, E., Somers, B., de Goey, P., and Albrecht, B., (2010). On the Application of the Flamelet Generated Manifold (FGM) Approach to the Simulation of an Igniting Diesel Spray, *SAE Technical Paper* 2010-01-0358.

Bekdemir, C., Somers, L.M.T., and de Goey, L.P.H., (2011). Modeling diesel engine combustion using pressure dependent Flamelet Generated Manifolds, *Proceedings of the Combustion Institute* 33:2887–2894.

Bhattacharjee, S., and Haworth, D.C., (2013). Simulations of transient n-heptane and n-dodecane spray flames under engine-relevant conditions using a transported PDF method, *Combustion and Flame* 160:2083–2102.

Bilger, R. W., (1993). in *Turbulence and Molecular Processes in Combustion* (Takeno, T., *Ed.*), Elsevier, Amsterdam, pp. 267–285.

Bilger, R.W., Pope, S.B., Bray, K.N.C., and Driscoll, J.F., (2005). Paradigms in turbulent combustion research, *Proceedings of the Combustion Institute* 30:21-42.

Bird, R.B., Stewart, W.E., and Lightfoot, E.N., (2007). *Transport Phenomena*, 2nd ed, John Wiley & Sons, Inc.

Blakeman, P.G., Chiffey, A.F., Phillips, P.R., Twigg, M.V., and Walker, A.P., (2003). Developments in Diesel Emission Aftertreatment Technology, *SAE Technical Paper* 2003-01-3753.

Bogey, C. and Bailly, C., (2004). A family of low dispersive and low dissipative explicit schemes for flow and noise computations, *Journal of Computational Physics* 194: 194-214.

Bogey, C., Bailley, C. and Juve, D., (2003). Noise Investigation in a High Subsonic Moderate Reynolds Number Jet using a Compressible Large Eddy Simulation, *Theoretical & Computational Fluid Dynamics* 16:273-297.

Bracco, F., (1985). Modeling of Engine Sprays, *SAE Transactions* 94:144-167.

Byggstoyl, S., and Magnussen, B. F., (1983). A model for flame extinction in turbulent flow, *4th Symp. Turbulent Shear Flows*, pp.10.23-10.38.

Candel S., Veynante D., Lacas F., Maistret E., Darabiha N., and Poinsot T., (1990). Coherent flamelet model: applications and recent extensions, *Recent Advances in Combustion Modeling* 6:19-64.

Canuto, V.M., and Cheng, Y., (1997). Determination of the Smagorinsky–Lilly constant C_S. *Physics of Fluids* 9, 1368.

Cao, L., Bhave, A., Su, H., Mosbach S., Kraft, M., Dris, A., and McDavid, R. M., (2009). Influence of Injection Timing and Piston Bowl Geometry on PCCI Combustion and Emissions, *SAE Technical Paper* 2009-01-1102.

Chen, J.H., (2011). Petascale direct numerical simulation of turbulent combustion—fundamental insights towards predictive models. *Proceedings of the Combustion Institute* 33:99–123.

Chen, Y.-C., and Bilger R. W., (2000). Turbulence and scalar transport in premixed Bunsen flames of lean hydrogen/air mixtures, *Proceedings of the Combustion Institute* 28: 521-528.

Chomiak, J., and Karlsson, A., (1996). Flame Lift-off in Diesel Sprays, *26th Symposium (International) on Combustion* pp. 2557-2564.

Clemens, N.T. and Paul, P.H., (1995). Effects of Heat Release on the Near Field Flow Structure of Hydrogen Jet Diffusion Flames, *Combustion and Flame* 102:271-284.

Cook, A. W., and Riley, J. J., (1998). Subgrid Scale Modeling for Turbulent Reacting Flows, *Combustion and Flame* 112:593-606.

Cook, A. W. and Cabot, W. H., (2004). A high-wavenumber viscosity for high-resolution numerical methods, *Journal of Computational Physics* 195:594-601.

Curran, H. J., Gaffuri, P., Pitz, W. J., and Westbrook, C. K., (1998). A Comprehensive Modeling Study of n-Heptane Oxidation, *Combustion and Flame* 114:149-177.

Dahms, R. N., Manin, J., Pickett, L. M., and Oefelein, J. C., (2013). Understanding high-pressure gas-liquid interface phenomena in Diesel engines, *Proceedings of the Combustion Institute* 34:1667-1675.

Davidson, P.A., (2004). *Turbulence: An Introduction for Scientists and Engineers.* OUP Oxford.

Deardoff, J.W., (1966). The Counter-Gradient Heat Flux in the Lower Atmosphere and in the Laboratory, *Journal of Atmospheric Sciences* 23:503-506.

Deardoff, J.W., (1971). On the magnitude of the subgrid scale eddy coefficient, *Journal of Computational Physics* 7:120-133.

De Bruyn Kops, S.M., Riley, J.J., Kosály, G., and Cook, A.W., (1998). Investigation of modeling for non-premixed turbulent combustion. *Flow, Turbulence and Combustion* 60(1):105-122.

Dec, J.E., (1997). A Conceptual Model of DI Diesel Combustion Based on Laser Sheet Imaging, *SAE Paper* 970873.

Domingo, P., and Vervisch, L., (1996). Triple flames and partially premixed combustion in autoignition of non-premixed turbulent mixtures, *Proceedings of the Combustion Institute* 26:233-240.

Dukowicz, J. K.,(1980). A Particle–fluid Numerical Model for Liquid Sprays, *Journal of. Computational Physics* 35(2):229–253.

Egüz, U., Leermakers, C.A.J., Somers, L.M.T., and De Goey, L.P.H., (2013). Premixed charge compression ignition combustion modelling with a multi-zone approach including inter-zonal mixing. *Proceedings of the Institute of Mechanical Engineers Part D Journal of Automobile Engineering* 227:1313–1324.

Eickhoff, H., Lenze, B., and Leuckel, W., (1984). Experimental Investigation on the Stabilization Mechanism of Jet Diffusion Flames, *Proceedings of Combustion Institute* 20:311-316.

Erlebacher, G., Hussaini, M. Y., Speziale, C. G., and Zang, T. A., (1990). On the Large-Eddy Simulation of Compressible Isotropic Turbulence, *ICASE Report* pp.90-76, ICASE/NASA Langley Research Center.

Fathali, M., Klein, M., Broeckhoven, T., Lacor, C., and Baelmans, M., (2008). Generation of turbulent inflow and initial conditions based on multi-correlated random fields, *International Journal of Numerical Methods in Fluids* 57:93–117.

Fellouah, H., Ball, C.G., and Pollard, A., (2009). Reynolds number effects within the development region of a turbulent round free jet, *International Journal of Heat and Mass Transfer* 52:3943-3954.

Ferrer, P.J.M., Lehnasch, G., Mura, A., (2012). Direct numerical simulations of high speed reactive mixing layers, in: *Journal of Physics: Conference Series*. p. 12004.

Fiedler, H.E., (1998). Control of free turbulent shear flows, in: *Flow Control: Fundamentals and Practices* (M.G. El-Hak, A. Pollard, J.P. Bonnet (Eds.)), Springer-Verlag, Germany, pp. 335–429.

Flynn, P.F., Durret, R.P., Hunter, G.L., zurLoye, A.O., Akinyemi, O.C., Dec, J.E., and Westbrook, C.K., (1999). Diesel Combustion: An Integrated View Combining Laser Diagnostics, Chemical Kinetics, and Empirical Validation, *SAE Technical Paper* 1999-01-0509.

Gago, C. F., Garnier, F., and Utheza, F., (2003). Direct Testing of Subgrid Scale Models in Large-Eddy Simulation of a Non-Isothermal Jet, *International Journal for Numerical Methods in Fluids* 42:999-1026.

Germano, M., Piomelli, U., Moin, P., and Cabot, W., (1991). A Dynamic Subgrid-Scale Eddy Viscosity Model, *Physics of Fluids* 3:1760-1765.

Ghosal, S., and Moin, P., (1995). The Basic Equations for the Large Eddy Simulation of Turbulent Flows in Complex Geometry, *Journal of Computational Physics* 118:24-37.

Gill, S., (1951). A Process for the Step-by-Step Integration of Differential Equations in an Automatic Computing Machine, *Proceedings of the Cambridge Philosophical Society* 47:96-108.

Girimaji, S.S. and Zhou, Y., (1996). Analysis and modeling of subgrid scalar mixing using numerical data. *Physics of Fluids* 8, 1224.

Givi, P., (1989). Model-free Simulations of Turbulent Reactive Flows, *Progress in Energy and Combustion Science* 15:1-107.

Günther, R., Horch, K., and Lenze, B. (1981). *First Specialist Meeting (International) of the Combustion Institute*, pp. 117-122.

Halstead, M. P., Kirsch, L. J., Quinn C. P., (1977). The autoignition of hydrocarbon fuels at high temperatures and pressures - fitting of a mathematical model, *Combustion and Flame* 30:45-60.

Han, Z., Uludogan, A., Hampson, G. J., and Reitz, R. D., (1996). Mechanism of Soot and NOx Emission Reduction Using Multiple-Injection in a Diesel Engine, *SAE Paper* 960633.

Hasselbrink, E.F., Jr. and Mungal, M.G., (1998). Observations of the Stabilization Region of Lifted Non-Premixed Methane Transverse Jet Flames, *Proceedings of the Combustion Institute* 27:1167-1173.

Heywood, J., (1988). *Internal Combustion Engine Fundamentals*, McGraw Hill, Inc., New York.

Hilbert, R., and Thévenin, D., (2002). Autoignition of turbulent non-premixed flames investigated using direct numerical simulations, *Combustion and Flame* 128:22–37.

Hinze, J. O., (1975). *Turbulence*, McGraw Hill, Inc., New York.

Hiroyasu, H., and Arai, M., (1990). Structure of Fuel Sprays in Diesel Engines, *SAE Paper* 900475.

Horch, K., (1978). PhD Thesis, Universitat Karlsruhe, FRG.

Hori, T., Kuge, T., Senda, J., and Fujimoto, H., (2007). Large eddy simulation of diesel spray combustion with eddy-dissipation model and CIP method by use of KIVALES, *SAE Technical Paper* 2007-01-0247.

Hoshiya, M. (1972), Simulation of Multi-Correlated Random Processes and Application to Structural Vibration Problems, *Proceedings of JSCE* 204:121–128.

Hu, B., Jhavar, R., Singh, S., Reitz, R., Rutland, C.J., (2007). Combustion Modeling of Diesel Combustion with Partially Premixed Conditions, *SAE Technical Paper* 2007-01-0163.

Hu, B., and Rutland, C.J., (2006). Flamelet Modeling with LES for Diesel Engine Simulations. *SAE Technical Paper* 2006-01-0058.

Huang, Y., (2000). *Experimental Studies of Impulsively-Started Liquid into-Gas and Gas-into-Gas Turbulent Jets*, PhD Thesis, Princeton University, Princeton, NJ.

Hussein, H.J., Capp, S.P., and George, W.K., (1994). Velocity measurements in a high-Reynolds-number, momentum-conserving, axisymmetric, turbulent jet, *Journal of Fluid Mechanics* 258:31-75.

Ihme, M., and Pitsch, H., (2008a) Prediction of extinction and re-ignition in nonpremixed turbulent flames using a flamelet/progress variable model 1. A priori study and presumed PDF closure. *Combustion and Flame* 155:70-89.

Ihme, M., and Pitsch, H., (2008b). Modeling of radiation and NO formation in turbulent non-premixed flames using a flamelet/progress variable formulation, *Physics of Fluids* 20, 055110

Ihme, M., and See, Y.C., (2010). Prediction of Autoignition in a Lifted Methane/Air Flame Using an Unsteady Flamelet/Progress Variable Model, *Combustion and Flame* 157:1850-1862.

Ihme, M., Cha, C. M., and Pitsch, H., (2005). Prediction of local extinction and re-ignition effects in non-premixed turbulent combustion using a flamelet/progress variable approach, *Proceedings of the Combustion Institute* 30:793–800

Iyer, V. A., Post, S. L., and Abraham, J., (2000). Is the Liquid Penetration in Diesel Sprays Mixing Controlled?, *Proceedings of Combustion Institute* 28(1):1111–1118.

Iyer, V., and Abraham, J., (1997). Penetration and Dispersion of Transient Gas Jets and Sprays, *Combustion Science and Technology* 130:315-334.

Iyer, V., and Abraham, J., (2003). An Evaluation of a Two-Fluid Eulerian-liquid Eulerian-gas Model for Diesel Sprays, *ASME Journal of Fluids Engineering* 125:660–669.

Iyer, V., and Abraham, J., (2005). Two-Fluid Modeling of Spray Penetration and Dispersion under Diesel Engine Conditions, *Atomization and Sprays* 15:249-269.

Jimenez, C., Ducros, F., Cuenot, B. and Bedat, B. (2001) Subgrid scale variance and dissipation of a scalar field in large eddy simulations. *Physics of Fluids* 13, 1748.

Kaario, O., (2000). Comparison Between Single-Step and Two-Step Chemistry in a Compression Ignition Free Piston Engine, *SAE Technical Paper* 2000-01-2937.

Kalghatgi, G.T., (1984). Lift-off Heights and Visible Lengths of Vertical Turbulent Jet Diffusion Flames in Still Air, *Combustion Science and Technology* 41:17-29.

Kärrholm, F.P., Tao, F., and Nordin, N., (2008). Three-Dimensional Simulation of Diesel Spray Ignition and Flame Lift-Off Using OpenFOAM and KIVA-3V CFD Codes, *SAE Technical Paper* 2008-01-0961.

Kawai, S., and Lele, S. K., (2008). Localized artificial diffusivity scheme for discontinuity capturing on curvilinear meshes, *Journal of Computational Physics* 227:9498-9526.

Kawai, S., Shankar, S.K., and Lele, S.K., (2010). Assessment of localized artificial diffusivity scheme for large-eddy simulation of compressible turbulent flows, *Journal of Computational Physics* 229:1739-1762.

Kee, R.J., Rupley, F.M., Miller, J.A., Coltrin, M.E., Grcar, J.F., Meeks, E., Moffat, H.K., Lutz, A.E., Dixon-Lewis, G., Smooke, M.D., Warnatz, J., Evans, G.H., Larson, R.S, Mitchell, R.E., Petzold, L.R., Reynolds, W.C., Caracotsios, M., Stewart, W.E., and Glarborg, P., (1999). *CHEMKIN Collection, Release 3.5*, Reaction Design, Inc., San Diego, CA.

Kempf, A., Malalasekera, W., Ranga-Dinesh, K.K.J., and Stein, O., (2003) Large Eddy Simulations of Swirling Non-premixed Flames With Flamelet Models: A Comparison of Numerical Methods, *Flow, Turbulence and Combustion* 81(4):523 – 561.

Kim, S.H., and Pitsch, H., (2005). Conditional filtering method for large-eddy simulation of turbulent nonpremixed combustion, *Physics of Fluids* 17, 105103.

Klein, M., Sadiki, A., and Janicka J. (2003). A Digital Filter Based Generation of Inflow Data for Spatially Developing Direct Numerical or Large Eddy Simulations, *Journal of Computational Physics* 186:652–665.

Klimenko, A. Y., (1990). Conditional Moment Closure and Diffusion in Conserved Scalar Space, *ECOLENScientific Research Lab. Paper*, Moscow, Russia.

Klimenko, A. Y., and Bilger, R. W., (1992). Relationship between Conserved Scalar pdfs and Scalar Dissipation in Turbulent Flows, *Charles Kolling Report* TNF101, University of Sydney.

Knudsen, E., Richardson, E.S., Doran, E.M., Pitsch, H., and Chen, J.H. (2012) Modeling scalar dissipation and scalar variance in large eddy simulation: Algebraic and transport equation closures, *Physics of Fluids* 24, 055103.

Kong, S.-C., and Reitz, R.D., (1993). Multidimensional Modeling of Diesel Ignition and Combustion Using Multistep Kinetics Models, *Journal of Engineering for Gas Turbines and Power* 115(4):781-789.

Kong, S.-C., and Reitz, R.D., (2002). Use of Detailed Chemical Kinetics to Study HCCI Engine Combustion With Consideration of Turbulent Mixing Effects, *Journal of Engineering for Gas Turbines and Power* 124:702–707.

Kuleshov, A. S., (2009). Multi-Zone DI Diesel Spray Combustion Model for Thermodynamic Simulation of Engine with PCCI and High EGR Level, *SAE International Journal of Engines* 2:1811-1834.

Kwon, J., Seo, J., Lee, D., and Huh, K., (2011). Zero-Dimensional Simulation of Diesel Engine Combustion and Emissions Based on CMC Model and Skeletal Reaction Mechanism, SAE *International Journal of Engines* 4(1):964-975.

Kyle, D., Sreenivasan, K., (1993). The instability and breakdown of a round jet variable-density jet, *Journal of Fluid Mechanics* 249:619–664.

Labs, J. and Parker, T. (2003). Diesel fuel spray droplet sizes and volume fractions from the region 25 mm below the orifice, *Atomization and Sprays* 13:45–62.

Labs, J. and Parker, T. (2006). Two-dimensional droplet size and volume fraction distributions from the near-injector region of high-pressure diesel sprays, *Atomization and Sprays*, 16:843–855.

Lee, S., Lele, S.K., and Moin P. (1992). Simulation of Spatially Evolving Turbulence and the Applicability of Taylor's Hypothesis in Compressible Flow, *Physics of Fluids A* 4(7):1521–1530.

Lee, K., and Abraham, J., (2011). *Spray Applications in Internal Combustion Engines*, in Handbook of Atomization and Sprays: Theory and Application (N. Ashgriz (ed.)), pp. 777-810.

Lele, S.K. (1992) Compact finite difference schemes with spectral-like resolution. *Journal of Computational Physics* 103:16-42.

Lesieur, M., and Metais, O., (1996). New Trends in Large-Eddy Simulations of Turbulence. *Annual Review of Fluid Mechanics* 28:45-882.

Lesieur, M., Metais, O., and Comte, P., (2005). *Large-Eddy Simulations of Turbulence*, Cambridge University Press, New York.

Lilly, D. K., (1992). A proposed modification of the Germano subgridscale closure method, *Physics of Fluids A* 4:633-636.

Liu, S., Hewson, J. C., Chen, J. H., and Pitsch, H., (2004). Effects of Strain Rate on High-Pressure Non-premixed n-Heptane Autoignition in Counterflow, *Combustion and flame* 137: 320-339.

Lu, T., and Law, C.K., (2005). A directed relation graph method for mechanism reduction, *Proceedings of the Combustion Institute* 30:1333–1341.

Lu, T., and Law, C.K., (2006). Linear time reduction of large kinetic mechanisms with directed relation graph, *Combustion and Flame* 144:24-36.

Lu, T., and Law, C.K., (2008). Strategies for mechanism reduction for large hydrocarbons: n-heptane, *Combustion and Flame* 154:153-163.

Lu, T., and Law, C.K., (2009). Toward accommodating realistic fuel chemistry in large-scale computations, *Progress in Energy and Combustion Science* 35:192-215.

Lu, T., Ju, Y., and Law, C.K., (2001) Complex CSP for chemistry reduction and analysis, *Combustion and Flame* 126:1445–1455

Lucchini, T., D'Errico, G., Ettorre, D., Ferrari, G., (2009). Numerical Investigation of Non-Reacting and Reacting Diesel Sprays in Constant-Volume Vessels, *SAE Technical Paper* 2009-01-1971.

Lund, T.S., Wu, X., and Squires, K.D., (1998). Generation of Turbulent Inflow Data for Spatially-Developing Boundary Layer Simulations, *Journal of Computational Physics* 140:233–258.

Lundgren, T.S., (1969). Model Equation for Nonhomogeneous Turbulence, *Physics of Fluids* 12:485-497.

Maas, U., Pope, S.B., (1992) Laminar flame calculations using simplified chemical kinetics based on intrinsic low-dimensional manifolds, *Combustion and Flame* 88:239–264.

Madnia, C. K., and Givi, P., (1993). Direct Numerical Simulation and Large Eddy Simulation of Reacting Homogeneous Turbulence, *Large Eddy Simulations of Complex Engineering and Geophysical Flows*, Cambridge, UK, Cambridge University Press, pp. 315–346.

Magi, V., Iyer, V., and Abraham, J., (2001). The k-ε Model and Computed Spreading Rates in Round and Plane Jets, *Numerical Heat Transfer A* 40:317-334.

Magnussen, B.F., and Hjertager, B.J., (1976). On Mathematical Modeling of Turbulent Combustion, *16th Symposium (International) on Combustion* 719-729.

Marble, F. E., and Broadwell. ,E., (1977). The coherent flame model for turbulent chemical reactions, *Project SQUID Technical Report* TRW-9-PU.

Mastorakos, E., Baritaud, T.A., Poinsot, T.J., (1997). Numerical simulations of autoignition in turbulent mixing flows, *Combustion and Flame* 109, 198–223.

Mastorakos, E., Bilger, R.W., (1998). Second-order conditional moment closure for the autoignition of turbulent flows, *Physics of Fluids* 10, 1246.

McNutt, D. G., (1981). M.S. Thesis, Massachusetts Institute of Technology.

Moin, P., Squires, K., Cabot, W., and Lee, S., (1991). A Dynamic Subgrid-Scale Model for Compressible Turbulence and Scalar Transport, *Physics of Fluids, A* 3:2746-2757.

Moin, P., and Kim, J., (1982). Numerical investigation of turbulent channel flow, *Journal of Fluid Mechanics* 118:341-377.

Mukhopadhyay, S., (2011). *Ignition and Early Flame Development in Stratified-Charge Mixtures*, PhD Thesis, Purdue University, West Lafayette.

Mukhopadhyay, S., and Abraham, J., (2011). Influence of Compositional Stratification on Autoignition in n-heptane/Air Mixtures, *Combustion and Flame* 158(6):1064-1075.

Mukhopadhyay, S., and Abraham, J., (2012). Evaluation of an unsteady flamelet progress variable model for autoignition and flame development in compositionally stratified mixtures, *Physics of Fluids* 24, 075115.

Müller, C.M., Breitbach, H., and Peters, N., (1994). Partially-premixed Turbulent Flame Propagation in Jet Flames, *Proceedings of the Combustion Institute* 25:1099-1106.

Müller, W., Ölschlegel, H., Schäfer, A., Hakim, N., and Binder, K., (2003). Selective Catalytic Reduction – Europe's NOx Reduction Technology, *SAE Technical Paper* 2003-01-2304.

Muniz, L., and Mungal, M.G., (1997). Instantaneous Flame Stabilization Velocities in Lifted Jet Diffusion Flames, *Combustion and Flame* 111:16-31.

Natarajan, B., and Bracco, F. V. (1984). On Multidimensional Modeling of Auto-Ignition in Spark-Ignition Engines, *Combustion and Flame* 57:179-197.

Nguyen, T. V., and Pope, S. B., (1984). Monte Carlo calculations of turbulent diffusion flames, *Combustion Science and Technology* 42:13-45.

O'Rourke, P. J., (1981). *Collective Drop Effects on Vaporizing Liquid Sprays*, PhD Thesis, Princeton University, Princeton, NJ.

O'Rourke, P., and Amsden, A., (1987). The TAB Method of Numerical Calculation of Spray Droplet Breakup, *SAE Paper* 872089.

Oldenhof, E., Tummers, M., van Veen, E.H., Roekaerts, D.J.E.M., (2010). Ignition kernel formation and lift-off behavior of jet-in-hot-coflow flames. *Combustion and Flame* 157, 1167–1178.

Panchapakesan, N., Lumley, J., (1993). Turbulence measurements in axisymmetric jets of air and helium. Part 1. Air jet, *Journal of Fluid Mechanics* 246:197–223.

Patterson, M. A., Kong, S.-C., Hampson, G. J., and Reitz, R.D., (1994). Modeling the Effects of Fuel Injection Characteristics on Diesel Engine Soot and NO_x Emissions, *SAE Paper* 940523.

Pawlak, G., Cruz, C. M., Bazan, C. M., and Hrdy, P. G., (2007). Experimental characterization of starting jet dynamics, *Fluid Dynamics Research* 39:711–730.

Pei, Y., Hawkes, E.R., and Kook, S., (2011). *Modelling n-heptane spray and combustion in conventional and low-temperature diesel engine conditions*, Australian Combustion Symposium, pp. 90–93.

Pei, Y., Hawkes, E.R., and Kook, S., (2013). Transported probability density function modelling of the vapour phase of an n-heptane jet at diesel engine conditions. *Proceedings of the Combustion Institute* 34:3039–3047.

Peters, N. and Williams, F.A., (1983). Lift-Off Characteristics of Turbulent Jet Diffusion Flames, *The American Institute of Aeronautics and Astronautics Journal* 21:423-429.

Peters, N., (1984). Laminar Diffusion Flamelet Models in Non-Premixed Turbulent Combustion, *Progress in Energy and Combustion Science* 10:319-339.

Peters, N., (1986). Laminar Flamelet Concepts in Turbulent Combustion, *Proceedings of Combustion Institute* 21:1231–1250.

Peters, N., (2000). *Turbulent Combustion*, Cambridge University Press, Cambridge, UK.

Peters, N., Paczko, G., Seiser, R., and Seshadri, K., (2002). Temperature Cross-over and Non-thermal Runaway at Two-stage Ignition of n-heptane. *Combustion .and Flame* 128:38-59.

Pickett, L.M., and Siebers, D. L., (2004). Soot in Diesel Fuel Jets: Effects of Ambient Temperature, Ambient Density and Injection Pressure, *Combustion and Flame* 138:114-135.

Pickett, L.M., Siebers, D.L., and Idicheria, C.A., (2005). Relationship Between Ignition Processes and Flame lift-off Length in Diesel Fuel Jets, *SAE Technical Paper* 2005-01-3843.

Pierce, C., Moin, P., (2001). The progress variable approach for large eddy simulation of turbulent combustion, TF- Report 80, Flow Physics Division, Mechanical Engineering Department, Stanford University, Stanford, CA.

Pierce, C. D., and Moin, P., (2004). Progress-Variable Approach for Large-Eddy Simulation of Non-premixed Turbulent Combustion, *Journal of Fluid Mechanics* 504:73-97.

Pitsch, H., (2006). Large-eddy Simulation of Turbulent Combustion, *Annual Review of Fluid Mechanics* 38:453-483.

Pitsch, H., and Ihme, M., (2005). An Unsteady/Flamelet Progress Variable Method for LES of Non-premixed Turbulent Combustion, *The American Institute of Aeronautics and Astronautics Journal* 2005-557

Pitsch, H., Barths, H., and Peters, N., (1996). Three-Dimensional Modeling of NOx and Soot Formation in DI Diesel Engines Using Detailed Chemistry Based on the Interactive Flamelet Approach, *SAE Paper* 962057.

Pitsch, H., Chen, M., and Peters, N. (1998) Unsteady flamelet modeling of turbulent hydrogen-air diffusion flames. Symp. (Int.) Combust., 27, 1057.

Pitsch, H., Riesmeier, E., and Peters, N., (2000). Unsteady Flamelet Modeling of Soot Formation in Turbulent Diffusion Flames, *Combustion Science and Technology* 158:389-406.

Pitsch, H., Wan, Y.P., and Peters, N., (1995). Numerical Investigation of Soot Formation and Oxidation under Diesel Engine Conditions, *SAE Paper* 952357.

Pitts, W.M., (1989). Assessment of Theories for the Behavior and Blowout of Lifted Turbulent Jet Diffusion Flames, *Proceedings of the Combustion Institute* 22:809-816.

Poinsot, T. J., and Lele, S. K., (1992). Boundary Conditions for Direct Simulations of Compressible Viscous Flows, *Journal of Computational Physics* 101:104-129.

Poinsot, T., Veynante, D., and Candel, S., (1991). Quenching Processes and Premixed Turbulent Combustion Diagrams, *Journal of Fluid Mechanics* 228:561-606.

Pope, S.B., (1976). The probability approach to the modeling of turbulent reacting flows, *Combustion and Flame* 27:299-312.

Pope, S.B., (1981a). A Monte Carlo method for the PDF equations of turbulent reactive flow, *Combustion Science and Technology* 25:159-174.

Pope, S. B., (1981b). Transport equation for the joint probability density function of velocity and scalars in turbulent flow, *Physics of Fluids*, 24:588-596.

Pope, S. B., (1985). PDF methods for turbulent reactive flows, *Progress.in Energy and Combustion Science* 11:119-192.

Pope, S. B., (1990). Computations of turbulent combustion: progress and challenges, Invited Plenary Lecture, *Proceedings of the Combustion Institute* 23:591-612.

Pope, S. B., (1997). Computationally efficient implementation of combustion chemistry using in situ adaptive tabulation, *Combustion Theory and Modeling* 1:41-63.

Pope, S. B., (2000), *Turbulent Flows*, Cambridge University Press, New York.

Post, S., Iyer, V., and Abraham, J., (2000). A Study of Near-field Entrainment in Gas Jets and Sprays under Diesel Conditions, *Journal of Fluids Engineering* 122:385-395.

Qi, Y., Liu, H., Midkiff, K., and Puzinauskas, P., (2010). A Feasible CFD Methodology for Gasoline Intake Flow Optimization in a HEV Application Part 1: Development and Validation, *SAE Technical Paper* 2010-01-2239.

Reddy, H., (2011). *Numerical Studies of Turbulence Effects on Developing Flames in Lean Methane/Air Homogeneous Mixtures*, PhD Thesis, Purdue University, West Lafayette.

Reitz, R. D., and Bracco, F. V., (1983). Global Kinetics and Lack of Thermodynamic Equilibrium, *Combustion and Flame* 53:141-144.

Reitz, R., (1987). Modeling Atomization Processes in High-Pressure Vaporizing Sprays, *Atomization and Spray Technology* 3:309–337.

Rosales, C., and Meneveau, C., (2005). Linear forcing in numerical simulations of isotropic turbulence: Physical space implementations and convergence properties, *Physics of Fluids* 17, 095106.

Ruetsch, G, R., Vervisch, L., and Linan, A., (1995). Effects of heat release on triple flame, *Physics of Fluids* 7, 1447.

Rutland, C.J., (2011). Large-eddy simulations for internal combustion engines - a review, *International Jornal of Engine Research* 12:421–451.

Saddoughi, S., and Veeravalli , S. V., (1994). Local isotropy in turbulent boundary layers at high Reynolds numbers, *Journal of Fluid Mechanics* 268:333-372.

Sagaut, P., and Meneveau, C., (2005). *Large eddy simulation for incompressible flows: an introduction*, Springer.

Şahin, Z., and Durgun, O., (2008). Multi-zone Combustion Modeling for the Prediction of Diesel Engine Cycles and Engine Performance Parameters, *Applied Thermal Engineering* 28:2245-2256.

Sanders, J.P.H., and Gokalp, I., (1998). Scalar dissipation rate modelling in variable density turbulent axisymmetric jets and diffusion flames. *Physics of Fluids* 10, 938.

Sayeed, M., Magi, V., and Abraham, J., (2011). Enhancing the Performance of a Parallel Solver for Turbulent Reacting Flow Simulations, *Numerical Heat Transfer, Part B: Fundamentals* 59(3):169-189.

Schlichting, H., (1979). *Boundary Layer Theory*, McGraw-Hill, Inc., New York.

Schmidt, H., and Schumann, U. (1989). Coherent structure of the convective boundary layer derived from large-eddy simulations, *Journal of Fluid Mechanics* 200:511-562.

Seiser, H., Pitsch, H., Seshadri, K., Pitz, W. J., and Curran, H. J., (2000). Extinction and Autoignition of n-Heptane in Counterflow Configuration, *Proceedings of the Combustion Institute* 28:2029-2037.

Senecal, P.K., Pomraning, E., and Richards K. J., Briggs, T. E., Choi, C. Y., McDavid R. M., and Patterson, M. A., (2003). Multidimensional Modeling of Direct Injection Diesel Spray Liquid Length and Flame Lift-off Length Using CFD and Parallel Detailed Chemistry, *SAE Technical Paper* 2003-01-1043.

Seshadri, K., Lu, T., Herbinet, O., Humer, S., Niemann, U., Pitz, W.J., and Law, C.K., (2009) Experimental and kinetic modeling study of extinction and ignition of methyl decanoate in laminar non-premixed flows, *Proceedings of the Combustion Institute* 32:1067–1074

Siebers, D. L., (1998). Liquid-phase Fuel Penetration in Diesel Sprays, *SAE Paper* 980809.

Siebers, D.L., and Higgins, B. S., (2001). Flame Lift-Off on Direct Injection Diesel Sprays under Quiescent Conditions, *SAE Technical Paper* 2001-01-0530.

Siebers, D.L., Higgins, B.S., and Pickett, L.M., (2002). Flame Lift-off on Direct Injection Diesel Fuel Jets: Oxygen Concentration Effects, *SAE Technical Paper* 2002-01-0890.

Shinozuka, M., (1972). Simulation of Multivariate and Multidimensional Random Processes, *The Journal of the Acoustical Society of America* 49(1):357–367.

Smagorinsky, J., (1963). General circulation experiments with the primitive equations I. The basic experiment, *Monthly Weather Review*, 91:99–164.

Som, S., and Aggarwal, S.K., (2010). Effects of primary breakup modeling on spray and combustion characteristics of compression ignition engines, *Combustion and Flame* 157:1179–1193.

Spalding, D. B., (1971). Mixing and chemical reaction in steady confined turbulent flames, *Symposium (International) on Combustion* 13:649-657.

Sreedhara, S., and Lakshmisha, K.N., (2002). Autoignition in a non-premixed medium: DNS studies on the effects of three-dimensional turbulence, *Proceedings of the Combustion Institute* 29:2051–2059.

Sripakagorn, P., Mitarai, S., Kosaly, G., and Pitsch, H., (2004). Extinction and reignition in a diffusion flame: a direct numerical simulation study. *Journal of Fluid Mechanics* 518:231–259.

Subramaniam, S., and O'Rourke, P. J., (1998). *Numerical convergence of the KIVA-3 code for sprays and its implications for modeling*, Los Alamos Laboratory Report UR-98-5465, Los Alamos, NM, 1998.

Swaminathan, N., and Bilger, R.W., (1997). Direct Numerical Simulation of Turbulent Nonpremixed Hydrocarbon Reaction Zones Using a Two-step Reduced Mechanism, *Combustion Science and Technology* 127:167–196.

Takahashi, F. and Goss, L.P., (1992). Near Field Turbulent Structures and the Local Extinction of Jet Diffusion Flames, *Proceedings of the Combustion Institute* 24:351-359.

Tao, F., and Chomiak, J., (2002). Numerical Investigation of Reaction Zones Structure and Flame Lift-Off of DI Diesel Sprays with Complex Chemistry, *SAE Technical Paper* 2002-01-1114.

Tap, F.A., and Veynante, D., (2005). Simulation of Flame Lift-Off on a Diesel Jet Using a Generalized Flame Surface Density Modeling Approach, *Proceedings of the Combustion Institute* 30:919-926.

Tennekes, H., and Lumley, J.L., (1972). *A First Course in Turbulence*. MIT Press.

Thomas, L.H., (1949). *Elliptic Problems in Linear Difference Equations over a Network*, Columbia University Press, New York.

Tow, T. C., Pierpont, D. A., and Reitz, R. D., (1994). Reducing Particulate and NOx Emission by Using Multiple Injections in a Heavy Duty D.I. Diesel Engine, *SAE Paper* 940897.

Van Oijen, J.A., (2013). Direct numerical simulation of autoigniting mixing layers in MILD combustion, *Proceedings of the Combustion Institute* 34:1163–1171.

Van Oijen, J.A., Bastiaans, R.J.M., de Goey, and L.P.H., (2007). Low-dimensional manifolds in direct numerical simulations of premixed turbulent flames, *Proceedings of the Combustion Institute* 31:1377–1384.

Vanquickenborne, L., and van Tiggelen, A., (1966). The Stabilization Mechanism of Lifted Diffusion Flames, *Combustion and Flame* 10:59-69.

Venugopal, R., and Abraham, J., (2007). A Review of Fundamental Studies Relevant to Flame Lift-off in Diesel Jets, *SAE Technical Paper* 2007-01-0134.

Venugopal, R., (2008) *Numerical Simulations of Flame Dynamics in the Near-field of High-Reynolds Number Jets*, PhD Thesis, Purdue University, West Lafayette.

Venugopal, R., and Abraham, J., (2008). A 2-D DNS investigation of extinction and reignition dynamics in nonpremixed flame-vortex interactions, *Combustion and Flame* 153:442–464.

Veynante, D., Lacas, O., Boudier, P., Dillies, B., and Samaniego, J. M., (1992). *The Coherent Flamelet Model for Propulsion Applications*, Ft. Belvoir Defense Technical Information Center FEB.

Veynante, D., and Vervisch, L., (2002). Turbulent Combustion Modeling, *Progress in Energy and Combustion Science* 28:193–266.

Viggiano, A., and Magi, V., (2004). A 2-D Investigation of n-Heptane Autoignition by Means of Direct Numerical Simulation, *Combustion and Flame* 137:432-443.

Wilcox, D. C., (2006). *Turbulence Modeling for CFD*, La Canada, CA: DCW Industries, Inc., Chap. 4.

Winklhofer, E., Ahmadi-Befrui, B., Wiesler, B., and Cresnoverh, G., (1992). The Influence of Injection Rate Shaping on Diesel Fuel Sprays—An Experimental Study, *Proceedings of the Institute of Mechanical Engineers, Part D: Journal of Automobile Engineering* 206:173–183.

Wright, Y., Depaola, G., Boulouchos, K., and Mastorakos, E., (2005). Simulations of spray autoignition and flame establishment with two-dimensional CMC, *Combustion and Flame* 143, 402–419.

Wu, K.-J., Reitz, R.D., and Bracco, F.V. (1986). Measurements of drop sizes at the spray edge near the nozzle in atomizing liquid jets, *Physics of Fluids* 29:941–951.

Yen, M., and Abraham, J., (2013). Modeling Lifted Diesel Jets: Insights into the Correlation between Flame Lift-Off Height and Soot Formation, *8th US National Combustion Meeting*, Utah, paper no. 070IC-0133.

Yen, M., and Abraham, J., (2014). Soot and NO Modeling in Reacting Diesel Jets with an Unsteady Flamelet Progress Variable Model, *submitted to Proceedings of the Institute of Mechanical Engineers, Part D: Journal of Automobile Engineering*.

Yoo, C.S., Luo, Z., Lu, T., Kim, H., and Chen, J.H., (2013). A DNS study of ignition characteristics of a lean iso-octane/air mixture under HCCI and SACI conditions. *Proceedings of the Combustion Institute* 34:2985–2993.

Yoo, C.S., Richardson, E.S., Sankaran, R., and Chen, J.H., (2011). A DNS study on the stabilization mechanism of a turbulent lifted ethylene jet flame in highly-heated coflow, *Proceedings of the Combustion Institute* 33, 1619–1627.

Yoshizawa, A., (1986). Statistical theory for compressible turbulent shear flows, with the application to subgrid modeling, *Physics of Fluids A* 29:2152–2164.

APPENDIX

APPENDIX

Skeletal Reduction of Chemical Reaction Mechanisms using DRG

A.1 Introduction

Reaction mechanisms are an integral part of any combustion simulation. Detailed mechanisms have been widely used for accurate and detailed descriptions of chemically reacting flows. However, for large combustion simulations, such as involving turbulence or complex geometries, the use of reduced mechanisms is essential to reduce the computational time.

In general, there are two major types of mechanism reduction - skeletal reduction and time scale analysis. In skeletal reduction, unimportant species and reactions are removed from the mechanism based on the consideration that the effect of its removal on the major species, like fuel, oxidizer and pollutants, are minimized. Time scale analysis is based on making Quasi-steady state assumptions for highly reactive radicals and partial equilibrium assumptions for fast reactions. Both these methods lead to a sufficiently small reaction mechanism which can then be utilized for realistic combustion simulations. The major examples of skeletal reduction are sensitivity analysis, Directed Relation Graph (DRG) method (Lu and Law, 2005), DRG with Error Propagation (DRGEP), and

DRG with Sensitivity Analysis (DRGASA) (Lu and Law, 2009). Sensitivity analysis is one of the earliest method for reducing reaction mechanisms, in which the errors induced by removing each species from the mechanism is analyzed by obtaining the Jacobian matrix of the species coupling. This method is very time-consuming for large mechanisms.

A.2 DRG Method: Background and Algorithms

Since most conventional methods for mechanism reduction involve time consuming operations on sensitivity or Jacobian matrices, the reduction time of such methods typically scales as a cubic function of the size of the mechanism, and as such the reduction rapidly becomes unaffordable when the number of species becomes larger than a few hundred. The method of DRG is based on linear-time operations (Lu and Law, 2006), such that the reduction time scales linearly with the number of species. DRG can efficiently handle overly large mechanisms and is most suitable to apply as the first step in mechanism reduction to quickly bring down a large mechanism to a small size that can be further analyzed by other methods. DRG is a mathematical concept which is used to denote a set of directionally connected nodes. In the context of chemical reactions, the nodes correspond to the species present in the reaction mechanism. The DRG method was originally proposed by Lu and Law (Lu and Law, 2005; 2009) to efficiently reduce large detailed mechanisms. In this method, the species couplings are mapped to a graph and strongly coupled species are identified by graph searching algorithms (Lu and Law, 2006). The major species of interest are first identified (e.g., fuel, oxidizer, and pollutants). The species which are weakly coupled to the major species are considered

unimportant and removed from the mechanism. The efficiency and accuracy of DRG has been demonstrated for n-heptane and isooctane, for which the detailed LLNL (Lawrence Livermore National Laboratories) mechanisms were reduced from 561 species to 188 species (Lu and Law, 2008), and from 857 to 233 species (Lu and Law, 2006), respectively, with less than 20% error. For the even larger mechanism of methyl decanoate, it was reduced from 3036 to 125 species with approximately 20% error (Seshadri et al., 2009).

According to the DRG method, an arrow exists from species *A* to species *B*, only if the removal of species B from the mechanism directly induces significant error in the production rate of A. To quantify the influence of species *A* on species *B*, the following parameter is defined

$$r_{AB} = \frac{\sum_{i=1}^{I} |\nu_{A,i}\omega_i \delta_{Bi}|}{\sum_{i=1}^{I} |\nu_{A,i}\omega_i|}, \tag{A.1}$$

where *I* is the number of reactions, ω_i is the reaction rate of reaction *i* and $\nu_{A,i}$is the net stoichiometric coefficient of species *A* in reaction *i*. δ_{Bi} is equal to 1, if the reaction *i* contains species *B*, and is zero otherwise. The parameter, r_{AB}, represents the error introduced in the production rate of species *A* by the removal of species *B*. If the threshold value r_{AB} is greater than ε, then a directed arrow exists from species A to B. The major steps involved in the reduction of a reaction mechanism using DRG are summarized below.

- Graph construction: For each pair of species (*A*,*B*) in the reaction mechanism, an arrow is introduced between them if the parameter defined by Eq. (A.1) exceeds the threshold value.

- Graph search: Starting with the major species, such as fuel or oxidizer, species coupled directly or indirectly to these species can be obtained by a graph searching algorithm. The Depth First Search (DFS) method is seen to be best suited for this. The species which are not coupled to the major species are eliminated from the mechanism.
- Elimination of reactions: The reactions which contain the eliminated species are eliminated from the mechanism.

The above steps constitute the algorithm for mechanism reduction using the DRG method. Reaction mechanisms with decreasing number of species can be obtained by increasing the value of the threshold parameter.

To obtain a skeletal mechanism valid over a range of conditions, a group of points are sampled from the parametric space for typical applications. Typically, the homogenous systems of Perfectly Stirred Reactor (PSR) and autoignition are chosen, as these are chemistry-controlled phenomena, and the computational times are smaller than diffusive systems of laminar flame propagation as well as counterflow ignition and extinction. For each application, a sub-skeletal mechanism can be obtained for each sampling point. The union of all these mechanisms will produce a skeletal mechanism, which is valid at every sampling point for the conditions of interest. The resulting skeletal mechanism can then be further reduced by time-scale reduction. This can be accomplished by eliminating species with short time scales by approximating them to be in steady state. The removal of the short time scales effectively reduces the stiffness of the system as well as the number of differential equations. The short time scales can be identified by several methods, such as those of intrinsic low dimensional manifold (Maas

and Pope, 1992) and computational singular perturbation (CSP) (Lu et al., 2001). These systematic approaches involve the evaluation and manipulation of Jacobian matrices, which can be very time consuming for large mechanisms.

A.3 Skeletal Mechanism for n-Heptane using DRG method

In this work, the performance of the DRG method for reducing detailed mechanisms was tested by using the detailed mechanism of n-heptane containing 561 species and 2539 reactions (Curran et al., 1998). A C++ code was written to implement the DRG algorithm presented in the previous section. The code uses the chemkin input file of the detailed mechanism, and produces a new chemkin file for the reduced mechanism. This code is given in Sec. A.5. A sequence of reduced mechanisms with varying accuracies was produced by varying the threshold parameter in the DRG code. The performance of this mechanism was tested by comparing the autoignition time with the detailed mechanism. The results are summarized below.

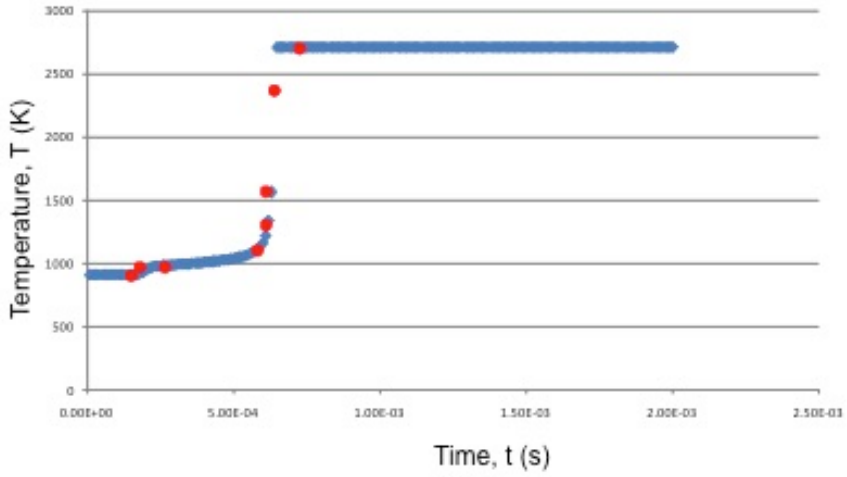

Figure A.1. Selecting the configuration points for DRG reduction.

To use the DRG method, a set of sampling points have to be obtained which gives the rates of each reaction in the mechanism. The flamelet code with zero diffusion was used to produce these configuration points. The temperature rise for n-heptane at an equivalence ratio of 1 at an initial temperature of 900 K and a pressure of 40 bar is shown in Fig. A.1. The red crosses indicate the configuration points selected for applying the DRG procedure.

Table A.1. Skeletal mechanisms obtained using DRG.

Time for configuration points, t	**Temperature, K**	**Number of species retained in the sub-skeletal mechanism**		
		ε=0.1	**ε=0.15**	**ε=0.2**
1.00E-04	900.0	109	70	52
2.00E-04	943.9	101	63	11
3.00E-04	980.4	101	51	36
5.00E-04	1010.6	107	68	38
7.00E-04	1115.3	50	40	30
7.40E-04	1289.9	64	40	36
7.50E-04	1435.8	64	53	41
7.60E-04	2393.4	74	57	37
7.70E-04	2700.5	55	51	50
8.10E-04	2705.3	72	67	64
No. of species in the skeletal mechanism		**195**	**146**	**113**
No. of reactions in the skeletal mechanism		**883**	**702**	**515**

The DRG was applied at each configuration point, and the sub-skeletal mechanisms obtained were combined to produce a skeletal mechanism. Different skeletal mechanisms are obtained by changing the threshold parameter. The results are summarized in Table A.1. As seen in table A.1, three different mechanisms were obtained by successively increasing the value of the threshold parameter ε. The performance of these different mechanisms are compared with the detailed mechanism by running the flamelet code with these mechanisms. The results for a temperature of 900 K, pressure of 40 bar and an equivalence ratio of 1 is shown in Fig. A.2. In addition to the skeletal mechanisms shown in Table A.1, the 160 species mechanism developed by Seiser et al. (2000) is also compared with the detailed mechanism. It is clear from the figure that the 146 species mechanism obtained by choosing ε to be 0.15 performs the best among the 3 mechanisms. Its performance is comparable to the performance of the 160 species mechanism reported in the literature. Surprisingly, the 195 species mechanism performs worse than the 146 species mechanism. The third mechanism consisting of 113 species obtained by taking ε to be 0.2 is seen to significantly under-predict the ignition delay.

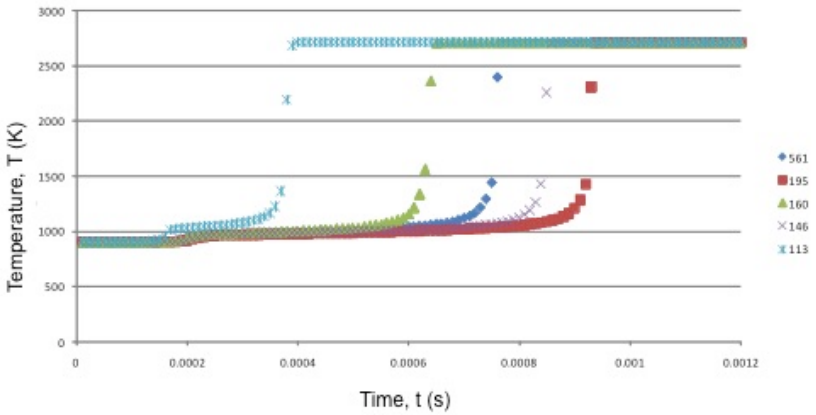

Figure A.2. Comparison of the different mechanisms for Φ=1, T=900K and P=40 bar

The results for equivalence ratio of 0.51 and 1.46 are shown in Figs. A.3 and A.4 respectively. For the low equivalence ratio of 0.51, the 146 species mechanism is seen to match the ignition delay predicted by the detailed mechanism very closely, whereas the other two mechanisms perform poorly. For the equivalence ratio of 1.46, the performance of the 146 species mechanism is worse than the 160 species mechanism. To test these mechanisms further, the simulations were repeated for a higher initial temperature of 1000K by keeping the pressure at 40 bar. The results are shown in Fig. A.5. For this case, the 146 species and the 195 species mechanisms predict approximately the same ignition delay.

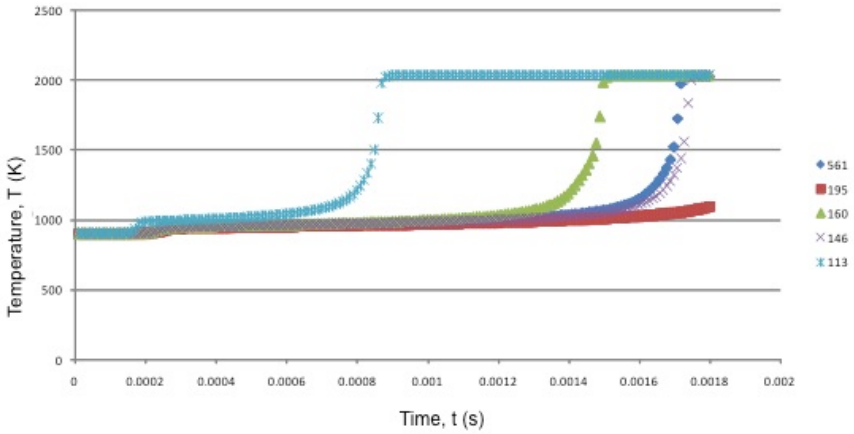

Figure A.3. Comparison of the different mechanisms for Φ=0.51, T=900K and P=40 bar.

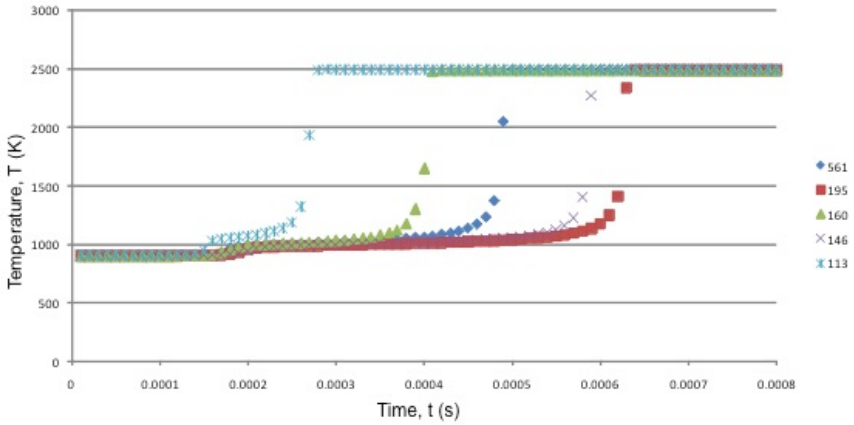

Figure A.4. Comparison of the different mechanisms for Φ=1.46, T=900K and P=40 bar.

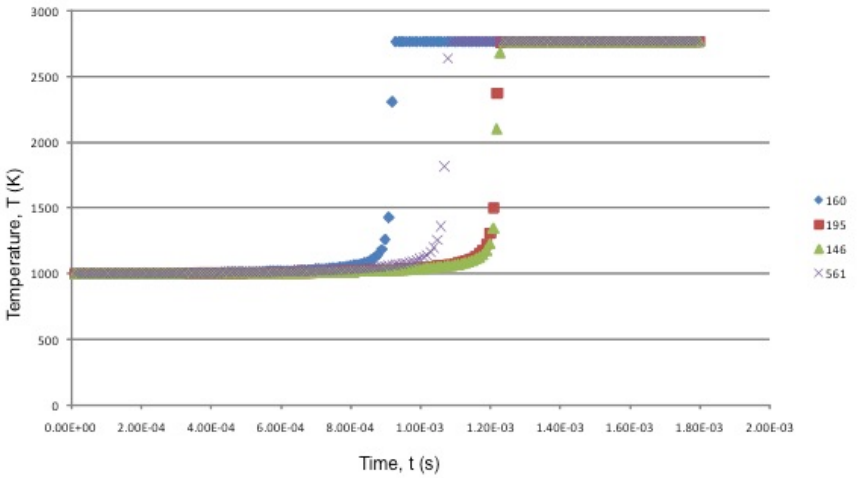

Figure A.5. Comparison of the different mechanisms for Φ=1, T=1000K and P=40 bar.

The results above have been obtained by selecting the configuration points uniformly over the simulation time as depicted in Fig. A.1. Other strategies were also adopted by restricting the configuration points to the low-temperature region only, the medium-temperature region only, or the high-temperature region only. In each of these cases, a sequence of mechanisms was obtained with decreasing number of species. The results were similar to the results shown previously. As ε is increased beyond 0.15, the performance of the resulting mechanism was very poor.

From the above results, it is clear that skeletal mechanisms which perform reasonably well over a variety of conditions can be obtained from the detailed mechanism using the DRG method. The shortcoming is that, as the size of the mechanism is reduced further using DRG, the predictions with the skeletal mechanisms become unreliable. In the exercise above, the successful mechanisms were still too large to be used feasibly for direct or large eddy simulation. To get reduced mechanisms of reasonable size suited for direct and large eddy simulations, the DRG method must be used in association with other reduction techniques as outlined in Lu et al. (2005).

A.4 Conclusions

The DRG method was used to develop skeletal mechanisms for n-heptane oxidation starting from a detailed mechanism. The performance of these mechanisms was tested using autoignition simulations. It was found that DRG method is not able to provide highly reduced mechanisms which are accurate. As suggested by the developers of the DRG method, this method should always be used in association with other methods like time-series analysis to effectively reduce the mechanism to the smallest possible size. In this work, skeletal and reduced mechanisms obtained using such analysis and reported in the literature are employed for RANS simulations, LES, and DNS.

A.5 C++ Code for DRG Reduction

```
//drg.cpp - reduce the reaction mechanism given the reaction rates and
//          the threshold parameter

#include <iostream>
#include <cmath>
#include <vector>
#include <fstream>

#define SPEC 600
#define REAC 1900
#define WHITE 0
#define GRAY 1
#define BLACK 2

using namespace std;

int vert_stat[SPEC];

struct adj
{
      int elem;
      long double rAB;
};

void DFSvisit(vector<struct adj> *adjlist, int u)
{
      vert_stat[u]=BLACK;
      vector<adj>::iterator iter;
```

```
	int i;
	//int counter=0;
	iter=adjlist[u].begin();
	for(; iter!=adjlist[u].end(); iter++){
		//counter ++;
		i=(*iter).elem;
		if(vert_stat[i]==WHITE){
			DFSvisit(adjlist,i);
		}
	}
}

int main()
{
	ifstream fin1("stoich.inp");
	ifstream fin2("rrate.inp");
	ofstream fout("Adj_list.out");
	vector<adj> adjlist[SPEC]; //Adjacency lists
	vector<adj>::iterator iter; //iterator for accessing vector
//	vector<int>::size_type

	int a,ireac,nspec,p;
	a=ireac=nspec=p=0;
	int sto[REAC][SPEC]={0};  //stoichiometric coefficients
	long double wdot[REAC]; //reaction rates
	long double reps=0.1;   //threshold value

	for(int i=0; i<REAC; i++){
		fin1 >> ireac;
		fin1 >> nspec;
		for(int j=0;j<nspec;j++){
			fin1 >> p;
			fin1 >> sto[i][p-1];
		}
	}

	double b,c;
	for(int i=0; i<REAC; i++){
		fin2 >> a >> c >> b;
		wdot[i]=c-b;
	}
	cout<<wdot[1];

	int dBi=0;
	struct adj newsp;
	long double rABd, rABn;
	int rcount;

	for(int j=0; j<SPEC; j++){
		for(int k=0; k<SPEC; k++){
			rcount=0;
			if(j!=k){
				rABd=rABn=0.0;
				for(int i=0; i<REAC; i++){
					if(sto[i][j]!=0){
```

```
                                    rcount++;
                                    newsp.elem=k;
                                    dBi=0;
                                    if(sto[i][k]!=0) dBi=1;
                                    rABd+=fabs(wdot[i]*sto[i][j]);
                                    rABn+=fabs(wdot[i]*sto[i][j]*dBi);
                              }
                        }
                  }
                  if(rcount!=0){
                              newsp.rAB=rABn/rABd;
                              if(newsp.rAB>reps)
adjlist[j].push_back(newsp);
                  }
            }
      }

      for(int i=0; i<SPEC; i++){
            cout << endl<< i <<"\t";
            iter=adjlist[i].begin();
            for(; iter!=adjlist[i].end(); iter++){
                  cout << (*iter).elem << "," << (*iter).rAB << "\t";
            }
      }

      fout << "EPS = " << reps << endl;
      for(int i=0; i<SPEC; i++){
            fout << endl<< i <<"\t";
            iter=adjlist[i].begin();
            for(; iter!=adjlist[i].end(); iter++){
                  fout << (*iter).elem << "\t";
            }
      }
//    Graph search with DFS
      for(int i=0; i<SPEC; i++)
            vert_stat[i]=WHITE;
      DFSvisit(adjlist,0); //C7H16
      DFSvisit(adjlist,4); //O2

//    Print list of retained species
      fout << endl << endl << "MAJOR SPECIES : " << 0;
      fout << endl << "LIST OF RETAINED ELEMENTS";
      for(int i=0; i<SPEC; i++)
            if(vert_stat[i]==BLACK) fout << endl << i;
      cout<<endl;

//    Delete reactions
      int reac_cnt=0;
      int reac_flag[1540]={0};
      for(int i=0; i<REAC; i++){
            for(int j=0; j<SPEC; j++){
                  if((vert_stat[j]==WHITE)&&(sto[i][j])){
                        reac_flag[i]=1;
                        reac_cnt++;
                        break;
```

```
                }
            }
        }
        fout<<endl<<endl<<"REACTIONS DELETED = " << reac_cnt;
        for(int i=0; i<REAC; i++)
            if(!reac_flag[i]) fout<<endl<<i;
        return 0;
}
```

A.6 C++ Code for Combining the Sub-skeletal Mechanisms

```
//combine.cpp - combine the reaction lists produced by drg.cpp for
//              different configuration points, and produce the
//              chem.inp file for the resulting skeletal mechanism
#include <iostream>
#include <fstream>
#include <string>
#include<iomanip>

#define REAC 1900
#define SPEC 600

using namespace std;
int main()
{
      ifstream fin1("spec1.inp");
      ifstream fin2("spec2.inp");
      ifstream fin3("spec3.inp");
      ifstream fin4("spec4.inp");
      ifstream fin5("spec5.inp");
      ifstream fin6("spec6.inp");
      ifstream fin7("spec7.inp");
      ifstream fin8("spec8.inp");
      ifstream gin("elemname.inp");
      ifstream gin1("stoich.inp");
      ifstream hin("reactions.inp");
      ofstream fout("comblist.out");
      ofstream hout("reactionlist.out");
      hout.setf(ios::left);

      int splist[160]={0};
      int sto[REAC][SPEC]={0};
      int a;
      char elem[15];
      char eleml[160][15]={};
      while(!fin1.eof())
      {
            fin1 >> a;
            splist[a]=1;
      }
      while(!fin2.eof())
      {
            fin2 >> a;
            splist[a]=1;
```

```
}
while(!fin3.eof())
{
	fin3 >> a;
	splist[a]=1;
}
while(!fin4.eof())
{
	fin4 >> a;
	splist[a]=1;
}
while(!fin5.eof())
{
	fin5 >> a;
	splist[a]=1;
}
while(!fin6.eof())
{
	fin6 >> a;
	splist[a]=1;
}
while(!fin7.eof())
{
	fin7 >> a;
	splist[a]=1;
}
while(!fin8.eof())
{
	fin8 >> a;
	splist[a]=1;
}
while(!gin.eof())
{
	gin >> a;
	gin >> elem;
	strcpy_s(eleml[a-1],elem);
}
int j=0;
for(int i=0; i<SPEC; i++){
	if(splist[i]==1)
	{
		j++;
		fout << j << "\t" << eleml[i] << endl;
	}
}
fout << "Number of elements:\t" << j;

int ireac,nspec,p;
ireac=nspec=p=0;
for(int i=0; i<REAC; i++){
	gin1 >> ireac;
	gin1 >> nspec;
	for(int j=0;j<nspec;j++){
		gin1 >> p;
		gin1 >> sto[i][p-1];
```

```
            }
      }

      int reac_cnt=0;
      int reac_flag[REAC]={0};
      for(int i=0; i<REAC; i++){
            for(int j=0; j<SPEC; j++){
                  if((splist[j]==0)&&(sto[i][j])){
                        reac_flag[i]=1;
                        reac_cnt++;
                        break;
                  }
            }
      }
      fout<<endl<<endl;
      fout<<"REACTIONS DELETED = " << reac_cnt;
      for(int i=0; i<REAC; i++)
            if(!reac_flag[i]) fout<<endl<<i+1;

//WRITE OUT chem.inp FILE
//ELEMENTS
      hout << "ELEMENTS" << endl;
      hout << "N  C  H  O " << endl;
      hout << "END" << endl;
//SPECIES
      hout << "SPECIES";
      int tcount=0;
      for(int i=0; i<SPEC; i++){
            if(splist[i]){
                  if(tcount%5==0)
                        hout << endl << setw(16) << eleml[i];
                  else
                        hout << setw(16) << eleml[i];
                  tcount++;
            }
      }
      hout << endl << "END" << endl;
//REACTIONS
      hout << "REACTIONS" << endl;
      int reacno=0;
      string str;
      string str1("=");
      string str2("/");
      string str3("DUPLICATE");
      size_t found,found1;
      char reacline[256];
      while(!hin.eof()){
            hin.getline(reacline,256);
            str=reacline;
            found=str.find(str1);
            if(found!=string::npos){
                  if(reac_flag[reacno]==0){
                        hout << str << endl;
                  }
                  reacno++;
```

```
            }
            found1=str.find(str2);
            if(found1!=string::npos){
                  if(reac_flag[reacno-1]==0)
                        hout << str << endl;
            }
            found1=str.find(str3);
            if(found1!=string::npos){
                  if(reac_flag[reacno-1]==0)
                        hout << str << endl;
            }
      }
      hout << "END";
      return 0;
}
```

VITA

VITA

Muhsin Ameen obtained his Bachelor of Technology degree in Mechanical Engineering from the National Institute of Technology Calicut (NITC), Calicut, India, in 2008. Muhsin was awarded the gold medal at NIT Calicut, for being the top rank holder both in the Department of Mechanical Engineering and in the Institute for the undergraduate (BTech) program for the period 2004-2008. At NITC, he worked on discrete modeling of nanofluids using molecular dynamics, and this work led to one archival journal publication and one conference paper. He joined the Indian Institute of Science (IISc), Bangalore, India for the Master of Science (MS) program and graduated in May 2010. While at IISc, he worked on turbulent combustion modeling of premixed systems using RANS simulations. This work led to one archival journal publication and one conference paper. He was the top-rank holder at IISc for the period 2008-2010 in Mechanical Engineering. At IISc, he also received the GE scholarship for the period 2008-2010. He joined Purdue University in August 2010 to pursue his PhD in Professor Abraham's research group in the School of Mechanical Engineering. His PhD work has focused on the LES simulations of lifted flames in turbulent reacting jets. His PhD work has resulted in one journal paper published, four papers in review for publication in various journals, and eight (six refereed) conference papers. At Purdue, he has been the recipient of a John Zink fellowship for the year 2012 and a Lambert Teaching fellowship for the year 2013. His awards include:

1. Lambert Teaching Fellow for the year 2013.
2. John Zink scholar for the year 2012.
3. GE scholar for the year 2008-2010.

4. Top rank holder at the Indian Institute of Science, Bangalore, India, during Master of Science (MS) in Mechanical Engineering.
5. Gold Medalist at the National Institute of Technology Calicut, Kerala, India, for being the top rank holder both in the Department of Mechanical Engineering and in the Institute for the undergraduate (BTech) program.

Upon completing his PhD, Muhsin would be joining the Energy Systems division at Argonne National Laboratory as a postdoctoral appointee.

LIST OF PUBLICATIONS

LIST OF PUBLICATIONS

Refereed Journal Publications

Ameen, M.M., and Abraham, J., Á-priori Evaluation of Subgrid-Scale Combustion Models for Diesel Engine Applications, *Submitted to Fuel, November 2014*

Ameen, M.M., and Abraham, J., A Comparison of "2D" and 3D DNS of Turbulent Fuel/Air Mixing Layers under Engine Conditions, *Submitted to International Journal of Heat and Fluid Flow, November 2014.*

Ameen, M.M., Magi, V., and Abraham, J. An Improved Unsteady Flamelet Model for Turbulence/Chemistry Interactions, *Submitted to Combustion and Flame, October 2014.*

Ameen, M.M., and Abraham, J. Evaluation Of Scalar Dissipation Rate Sub-Models For Modeling Unsteady Reacting Diesel Jets, *Submitted to Combustion Science and Technology, July 2014*.

Bajaj. C., Ameen, M.M., and Abraham, J., (2013). Evaluation of an unsteady flamelet progress variable model for autoignition and flame lift-off in diesel jets, *Combustion Science and Technology* 185:454-472, 2013.

Ameen, M. and Ravikrishna, R.V., (2011). An EDC-based turbulent premixed combustion model, *Combustion Theory and Modeling*, 15(5):607-622.

Ameen, M., Prabhul, K., Sivakumar, G., Abraham, P.P., Jayadeep, U.B. and Sobhan,C. B., (2010). Molecular Dynamics Modeling of Latent Heat Enhancement in Nanofluids, *International Journal of Thermophysics* 31(6):1131-1144.

Conference Publications

Ameen, M. and Abraham, J., (2014). RANS and LES Study of Lift-Off Physics in Reacting Diesel Jets, *SAE Technical Paper* 2014-01-1118.

Ameen, M., Magi, V., and Abraham, J., Flame Dynamics in the Lift-Off Region of Diesel Jets, *Australian Combustion Symposium 2013*, University of Western Australia, Australia, November 2013.

Ameen, M., Magi, V., and Abraham, J., Modeling the transient structure of reacting diesel jets using large eddy simulation, *8th U. S. National Combustion Meeting*, May 19-22, 2013

Anders, J., Ameen, M, Magi, V. and Abraham, J., Mixing Mechanism of Pulsed Jets with Applications to Fuel Delivery in Combustion Applications, *18th Australasian Fluid Mechanics Conference*, Launceston, Australia, December 2012

Ameen, M, Bajaj, C., Yen, M. and Abraham, J., Inferences about the mechanism of flame stabilization in the near-field of diesel jets, *18th Australasian Fluid Mechanics Conference*, Launceston, Australia, December 2012

Bajaj, C., Ameen, M. and Abraham, J., Modeling the Transient Structure of Non-Reacting and Reacting Diesel Sprays, *ICLASS 2012, 12th Triennial International Conference on Liquid Atomization and Spray Systems*, Heidelberg, Germany, September 2012.

Bajaj, C., Ameen, M. and Abraham, J., Computed and Measured Ignition Delay and Flame Lift-off in Diesel Jets, *Spring Technical Meeting of the Central States Section of the Combustion Institute*, Dayton, USA, April 2012.

Bajaj, C., Ameen, M. and Abraham, J., Computed and Measured Ignition Delay and Flame Lift-Off in Diesel Jets, *Proceedings of the Australian Combustion Symposium*, Newcastle, Australia, November 2011.

Ameen, M., Reddy, L.K. and Ravikrishna, R.V., A Modified EDC-based Approach for Modeling Turbulent Premixed Combustion, *8th Asia-Pacific Conference on Combustion*, Hyderabad, India, 2010.

Sobhan, C.B., Ameen, M. and Abraham, P.P., Numerical Modeling of Micro Fin Arrays using Slip Flow and Temperature Jump Boundary Conditions, *1st ASME Micro/Nanoscale Heat Transfer Conference*, Tainan, Taiwan, January 2008.